Norwegian University of Life Sciences
Faculty of Science and Technology

Philosophiae Doctor (PhD)
Thesis 2020:51

Scattering and Absorption in Nano- and Microstructured Media

Spredning og absorpsjon i media med nano- og mikrostrukturer

Maren Anna Brandsrud

Scattering and Absorption in Nano- and Microstructured Media

Spredning og absorpsjon i media med nano- og mikrostrukturer

Philosophiae Doctor (PhD) Thesis

Maren Anna Brandsrud

Norwegian University of Life Sciences
Faculty of Science and Technology

Ås, 2020

Thesis number: 2020:51
ISSN: 1894-6402
ISBN: 978-82-575-1717-5

Abstract

When electromagnetic radiation interacts with objects of the same wavelength as the radiation, the objects can act as resonators and strong scattering effects appear. The goal of this PhD project has been to understand better scattering effects and resonances in small particles and their relation to absorption properties. The thesis considers two application areas, namely (i) absorption efficiency of optically thin solar cells and (ii) absorption spectra from infrared microspectrocopy of biological cells and tissues. These two application areas consider two different wavelength regions, the visible light and the infrared radiation. However, since the illuminated objects are of the same size as the wavelengths for both applications, similar phenomena are present and the same approaches can be used to obtain a better understanding of the underlying mechanisms.

In the field of optically thin solar cells, nano-structured surfaces are used to enhance absorption properties in the absorptive layers. Different mechanisms have been explained in the literature for explaining the rationale behind the enhancement effects. The thesis uses ray models to obtain a deeper understanding of enhancement of absorption in the scattering of electromagnetic radiation at small particles. An exact ray theory was developed by use of a semi-classical theory to connect ray dynamics to the appearance of resonances. By carefully attaching phases to infinitely many rays, the reflection, transmission and absorption properties could be described exactly. The attached phases ensure that the wave nature of light, the resonance structure, is described. The ray model was validated against exact electromagnetic theory and by measured data of a film of SiN_x. The resonances in thin films were further investigated for layered systems. The study shows how resonances in the absorptive layers increase the amount of absorbed radiation in a thin film. By structuring these absorptive films, i.e. by attaching non-absorptive films to it, it was shown that a resonance in the non-absorptive film increases absorption as well.

In infrared microscopy of biological cells and tissues, scattering hinders the interpretation of chemical absorbance in measured spectra. The spectroscopist is at a loss to decide if radiation was lost due to scattering or due to absorption by the sample. Thus, the interpretation of band ratios referring to different chemical constituents can be biased. Since in the case of infrared microscopy, biological cells are at the same size as the wavelengths employed. Therefore the same scattering phenomena and resonant structures appears as in light scattering at nano-structured solar cells. In the case of spherical or quasi-spherical objects such as biological cells, the scattering is the so-called Mie-type scattering. Advanced methods have been developed to retrieve the pure absorbance spectra from these measured spectra. However, it is not clear how shape deviation from a spherical shape affects scattering features in Mie scattering such as the so-called wiggles and ripples in the extinction efficiency. In this thesis, the extinction efficiency of a gradually deformed circular scatterer was evaluated. Further the scattering behavior was investigated by classical ray dynamics. The results indicate that sample deformation with chaotic scattering has an accelerating effect on the disappearance of Mie ripples, while deformation that is connected to regular scattering removes the ripples at a slower rate.

Sammendrag

Når elektromagnetisk stråling interagerer med objekter som har samme størrelse som strålingens bølgelengde, kan objektene fungere som resonatorer og sterke spredningseffekter kan oppstå. Målet med dette doktorgradsprosjektet har vært å forstå spredningseffekter og resonanser i små partikler og hvordan de påvirker absorpsjonsegenskaper. Oppgaven tar for seg to bruksområder: (i) absorpsjon av lys i optisk tynne solceller og (ii) absorpsjon av infrarød stråling i mikrospektroskopi av biologiske celler og vev. Disse to bruksområdene betrakter to ulike bølgelengdeområder, synlig lys og infrarød stråling. Siden objektene har samme størrelse som bølgelengdene for begge bruksområdene, er lignende feonomener til stede og de samme tilnærmingene kan brukes for å få en bedre forståelse av de underliggende mekanismene.

For optisk tynne solceller kan nanostrukturerte overflater brukes til å forbedre absorpsjonsegenskapene i de absorberende lagene. I litteraturen har ulike mekanismer blitt brukt for å forklare den økte absorpsjonen. I opgaven er det brukt strålemodeller for å få en dypere forståelse for økt absorpsjon og spredning av elektromagnetisk stråling av små partikler. En eksakt stråleteori ble utviklet ved bruk av semiklassisk teori ved å koble stråler til eksistensen av resonanser. Ved å tilordne faser på korrekt måte til uendelig mange stråler, kan refleksjons-, transmisjons- og absorpsjonsegenskapene beskrives nøyaktig. Fasene sikrer at lysets bølgenatur, resonansstrukturen, blir beskrevet. Strålemodellen ble validert mot eksakt elektromagnetisk teori og med målte data fra en SiN$_x$-film

Resonansene i tynne filmer ble videre undersøkt. Studien viser hvordan resonanser i de absorberende lagene øker mengden absorbert stråling i en tynn film. Ved å strukturere disse absorberende filmene ved å feste ikke-absorberende filmer til den, ble det vist at en resonans i den ikke-absorberende filmen også øker absorpsjonen.

Ved infrarød mikrospektroskopi av biologiske celler og vev, vil spredning av den infrarøde strålingen kunne føre til mistolkningen av kjemisk absorbans i målte spektre. For spektroskopisten er det usikkert om strålingen går tapt på grunn av spredning eller på grunn av absorpsjon i prøven. Dermed kan tolkningen av forholdene mellom absorpsjonsbåndene, som refererer til forskjellige kjemiske bestanddeler, være misvisende. For infrarød mikrospektroskopi er biologiske celler i samme størrelse som bølgelengden til strålingen. Derfor kan de samme spredningsfenomenene og resonansstrukturene som i lysspredning ved nanostrukturerte solceller vises. Når det gjelder sfæriske eller tilnærmet sfæriske objekter som biologiske celler, er spredningen Mie-liknende spredning. Avanserte verktøy er utviklet for å finne absorbansspektra fra de målte spektrene. Det er imidlertid ikke klart hvordan en endring fra en sfærisk form påvirker spredningstrekk som de såkalte ‘ripples’ og ‘wiggles’ i Mie-spredningen. I denne oppgaven undersøkte vi spredningen til et gradvis deformert sirkulært objekt. Videre ble spredningen undersøkt ved klassisk stråledynamikk. Resultatene indikerer at endring av form til en form som gir kaotisk spredning gjør at ‘ripples’ forsvinner raskere enn om den endrede formen gir regulær spredning.

Preface

The work presented in this thesis was carried out from 2016 to 2020 at the Faculty of Science and Technology (REALTEK) at the Norwegian University of Life Sciences (NMBU). Throughout the whole period I was part of the BioSpec Norway group. My PhD position was funded by the Norwegian Research Council through the project no 250678: “Development of a new ray model for understanding between dielectric spheres for photovoltaics with higher efficiency”. The PhD has been supervised by main supervisor Achim Kohler, together with Reinhold Blümel, Rozalia Lukacs, Erik Marstein and Espen Olsen.

First of all, I would like to thank Achim. I am thankful for all supervision, patience and time. This journey would not be the same without your guidance. I am grateful for all the possibilities you have given me, all trips we have had and the social gatherings. I look forward to continuing to work together with you!

Further I would like to thank Reinhold, for all the answers to any kind of questions, and for guidance in research and paper writing. I would also like to thank you for the possibility to visit you several times in US and for your visits at Ås.

Rozalia, you have been the project manager of the project. I am thankful for you giving me the opportunity to start my PhD in your project. Many thanks for guidance, trips and good conversations. I would also like to thank Espen and Erik; you have the knowledge from the field of solar cells and have given important inputs for discussions and paper writing.

I would like to thank all my friends in the BioSpec group. It is well-known that dark days exist during the PhD journey, but you always brighten up the day. Eivind, you have been my partner in crime on the project. Your technical support made my life much less complicated. A lot of good memories from conferences and trips, but also from everyday life in Ås. It has been a pleasure to work together with you. Johanne, thank you for all the good conversations and happy memories. Our collaboration, within research and teaching, on social gatherings and trips, have always been followed by a lot of go-ahead spirit, a lot of laugh and exciting results. I am looking forward to the continuation! I could continue to thank everyone in the BioSpec group; you have been very important for me these years: From bottom of my heart, I am so happy to have got to know all of you!

Further I would like to thank Aurora! I am so grateful that you moved into our office when you started your PhD. Thank you for always listening when I needed someone and for always giving a smile when needed.

Last, but not least, my friends and family back home, thanks for our good times together. You have been my break from the PhD-life and given me the possibility to focus on other things. Especially thanks to my mom, my dad and my sister Inger Johanne and to Ole-Johan. Without your support, encouragement and love, it would not have been possible to finalize this work.

Maren Anna Brandsrud

Ås, July 2020

Norwegian University
of Life Sciences

BioSpec
Norway

Contents

List of Papers

Paper I

[1] M.A. Brandsrud, E. Seim, R. Lukacs, A. Kohler, E.S. Marstein, E. Olsen, and R. Blümel. Exact ray theory for the calculation of the optical generation rate in optically thin solar cells. *Physica E: Low-dimensional Systems and Nanostructures*, 105:125–138, 2019

Paper II

[2] M.A. Brandsrud, R. Blümel, R. Lukacs, E. Seim, E.S. Marstein, E. Olsen, and A. Kohler. An exact ray model for oblique incident light on planar films. Submitted to *Physica E*, under review

Paper III

[3] M.A Brandsrud, R. Blümel, R. Lukacs, E. Seim, E.S. Marstein, E. Olsen, and A. Kohler. Resonance structures in layers of planar films. To be submitted to *Physica E*

Paper IV

[4] M.A Brandsrud, R. Blümel, J. Solheim, and A. Kohler. Validity of mie theory for infrared spectroscopy of biological cells. Submitted to *Scientific Reports*

Additional Scientific Work

Papers

[5] E. Seim, A. Kohler, R. Lukacs, M.A. Brandsrud, E.S. Marstein, E. Olsen, and R. Blümel. Chaos: A new mechanism for enhancing the optical generation rate in optically thin solar cells. *Chaos: An Interdisciplinary Journal of Nonlinear Science*, 29(9):093132, 2019

[6] E. Seim, A. Kohler, R. Lukacs, M.A. Brandsrud, E.S. Marstein, E. Olsen, and R. Blümel. Wave chaos enhanced light-trapping in optically thin solar cells. *Journal not decided*, being written

Conference Proceedings

[7] M.A. Brandsrud, R. Lukacs, R. Blümel, E. Seim, E.S. Marstein, E. Olsen, and A. Kohler. Optimized solar cells based on changes in resonance structure as a function of the refractive index and the thickness. In *Physics, Simulation, and Photonic Engineering of Photovoltaic Devices VIII*, volume 10913, pages 109–130. International Society for Optics and Photonics, 2019

[8] E. Seim, A. Kohler, R. Lukacs, M.A. Brandsrud, E.S. Marstein, E. Olsen, and R. Blümel. Chaos: a new mechanism for enhancing the optical generation rate in optically thin solar cells. In Alexandre Freundlich, Laurent Lombez, and Masakazu Sugiyama, editors, *Physics, Simulation, and Photonic Engineering of Photovoltaic Devices VIII*, volume 10913, pages 213 – 221. International Society for Optics and Photonics, SPIE, 2019

[9] M.A. Brandsrud, R. Blümel, J. Solheim, E.A. Magnussen, E. Seim, and A. Kohler. Does chaotic scattering affect the extinction efficiency in quasi-spherical scatterers? In *Biomedical Spectroscopy, Microscopy, and Imaging*, volume 11359, page 113590C. International Society for Optics and Photonics, 2020

Oral Presentations

- ⋆ M.A. Brandsrud, R. Lukacs, R. Blümel, E. Seim, E.S. Marstein, E. Olsen, and A. Kohler. Optimized solar cells based on changes in resonance structure as a function of the refractive index and the thickness. Presented at: *SPIE Photonics West* 2019-02-01–2019-02-06
- ⋆ E. Seim, A. Kohler, R. Lukacs, M.A. Brandsrud, E.S. Marstein, E. Olsen, and R. Blümel. Wave chaos: A new mechanism for enhancing the absorption cross section of optically thin solar cells. Presented at: *Norwegian Solar Cell Conference* 2019-05-20–2019-05-21
- ⋆ M.A. Brandsrud, R. Blümel, J. H. Solheim, E. Magnussen, E. Seim, and A. Kohler. Does chaotic scattering affect the extinction efficiency in quasi-spherical scatterers? Presented at: *SPIE Photonics Europe Digital Forum* 2020-04-06–2020-04-10

Poster Presentations

- ⋆ M.A. Brandsrud, A. Kohler, R. Blümel, E. Seim, and R. Lukacs. The importance of coupling between spheres for the efficiency enhancement of periodically structured solar cells. Presented at: *Norwegian Solar Cell Conference* 2017-05-09–2017-05-10
- ⋆ E. Seim, A. Kohler, R. Blümel, M.A. Brandsrud, and R. Lukacs. Light trapping by structured surfaces in the regular and chaotic scattering regime. Presented at: *Norwegian Solar Cell Conference* 2017-05-09–2017-05-10
- ⋆ E. Seim, A. Kohler, R. Lukacs, M.A. Brandsrud, E.S. Marstein, E. Olsen, and R. Blümel. Chaos: A new mechanism for enhancing the optical generation rate in thin-film solar cells. Presented at: *SPIE Photonics West* 2019-02-01–2019-02-06
- ⋆ M.A. Brandsrud, R. Lukacs, R. Blümel, E. Seim, E.S. Marstein, E. Olsen, and A. Kohler. Two-dimensional ray theory for optically thin solar cells. Presented at: *Norwegian Solar Cell Conference* 2019-05-20–2019-05-21
- ⋆ M.A. Brandsrud, E. Seim, J.H. Solheim, R. Blümel, and A. Kohler. Does chaotic scattering affect the extinction efficiency in quasi-spherical scatterers? Presented at: *BioSpecMLC* 2019-04-18–2019-08-21

Chapter 1

Introduction

1.1 Motivation

The interaction of electromagnetic radiation with objects, which have a size that is of the same order as the wavelength, has occupied physicists for a long time [18, 19]. In this regime, strong scattering and resonance effects appear. As other authors before, we will designate this regime in this thesis as scattering at small particles [18]. Scattering effects in small particles, such as for example spherical particles, are rich and have been explained for example as interference phenomena or resonances such as whispering gallery modes in spherically shaped particles [18, 20, 21]. When objects are absorbing, absorption may affect scattering and vice versa. It is known that standing waves in a spherical resonator enhance the field in the resonator, a mechanisms that may induce increased absorption [20–22].

Scattering and absorption of light at small particles, is relevant for different applications. The scattering and absorption properties are valid for all wavelengths regions. In the visible the condition is fulfilled for scattering at nano-structures and particles, while in the infrared the condition is fulfilled when the size of the particles is in the micrometer range as is true for cells and tissues. In this work we focused on two application areas. The first application is **optically thin solar cells** with surface structures, where the surface structures are approximately of the same size as the wavelength of the incoming light. The purpose of these surface structures have been to increase the absorption of light in the energy-converting material below the nano-structured surfaces. It has been previously shown that surface structures with increased scattering of light gives increased absorption of light in optically thin solar cells [23–26].

Due to the reduced thickness compared with conventional solar cells, optically thin solar cells are expected to be cheaper due to reduced material costs. However, the efficiency of optically thin solar cells are in general lower than the conventional, crystalline silicon solar cells [27, 28]. In order to utilize as much as possible of the power of the incoming radiation in a solar cell, long optical absorption lengths are needed. Especially, silicon solar cells require optimization of absorption properties in the near-infrared region. In the case of silicon, up to a few hundred micron path lengths are needed to obtain total absorption of the incoming radiation. However, state-of-the-art optically thin solar cells have thicknesses below one micrometer and have thus thicknesses that are much lower than a few hundred microns. Structured surfaces redirect light into the energy converting material resulting in longer path lengths and thus better absorption properties [29, 30]. Both ordered structures and random structured surfaces have been evaluated in order to evaluate light trapping of solar cells [30–35]. When absorption properties are enhanced by nano-structured surfaces, thinner solar cells can be produced with comparable absorption properties as thicker solar cells with no surface structuring.

Both numerical experiments and practical validations have shown that the absorption of light can be enhanced by nano-structures at the surface of the optically thin solar cell. The absorption enhancement has been explained by several mechanisms: (i) Numerical computation of the electromagnetic field, e.g. finite difference time domain calculations, have shown that the near-field can be enhanced by resonances such as whispering gallery modes in spherical nano-particles on surfaces of thin solar cells. The near-field enhancement has been interpreted as the cause for an increased absorption of incoming solar radiation. (ii) Surface structures that re-direct the light into the absorptive layer, called light trapping, has been investigated as a cause for the enhancement of the absorption. Finally, (iii) when for example nano-spheres are arranged in a lattice, waveguide modes may couple. The coupling of the regularly organized nano-particles is expected to increase the field locally and this effect may also increase the absorption of light in the thin-film solar cells. [21, 30, 36–38].

The second application area is **infrared microspectroscopy** of biological cells and tissues. In infrared microspectroscopy of cells and tissues, the samples are also at the same size as the wavelength. While infrared microspectroscopy is performed to non-destructively perform a chemical and structural analysis of intact cells and tissues, scattering affects the absorbance properties of the materials, leading to skewed band ratios rendering the interpretation of the results difficult [39, 40]. By evaluating the absorbance of the sample as a function of wavelength, the chemical composition of the sample can be found. Different molecular bonds absorb light of a specific wavelength. The peaks in absorbance spectra are explained as the fingerprint of the sample [41].

The enhanced scattering effects in spectroscopy are therefore generally a hurdle for the spectroscopist. Since absorption bands are skewed and non-Lambert-Beer type absorption is present, the interpretation of measured data is difficult. In infrared microspectroscopy measurements, the aim is to quantify chemical compounds in the sample by estimating the loss of radiation transmitting through the sample.

However, since extinction of the radiation is not only caused by absorption, but in addition by scattering, it is hard for a spectroscopist to quantify the pure chemical absorption properties of the material. In addition, absorption properties of the sample lead to fluctuations of the real part of the refractive index, which causes further distortions of chemical absorption bands. Therefore, in the field of infrared spectroscopy of cells and tissues, sophisticated algorithms have been developed to retrieve pure absorption signatures from highly scatter-distorted spectra [42–47].

There are various ways to achieve a better understanding of absorption phenomena in solar cells and spectroscopy and how they are affected by scattering in resonances:

- **Use of exact electromagnetic theory**
  Idealized systems such as perfect spheres and infinitely extended films can be solved by exact electromagnetic theory [18,19,48]. By use of the electromagnetic boundary conditions, the exact behavior of the electromagnetic wave can be found. The exact wave solutions can be found for a stack of films by the transfer matrix method, which has been used to study photovoltaic devices [49–51]. Within the field of spectroscopy, exact wave calculations have been used to derive a model for mid-IR micro-spectroscopy for homogeneous layered samples [52, 53]. The Mie theory has been used to understand scattering and estimate parameters, such as size and refractive index, of spherical samples [20, 54–57]. Advanced algorithms have been developed to retrieve pure absorbance spectra from quasi-spherically shaped particles such as cells [42–46] Rasskazov et al. presented a scattering correction algorithm for cylinders, which is based on the exact Mie theory for cylinders [47]. In the field of infrared spectroscopy, approximation formulae developed by van de Hulst [18] have been used to model scattering and absorption in highly scatter-distorted spectra [42–47]. The van de Hulst approximation formulae describe interference phenomena well, while shape resonances are not described. It is therefore interesting to investigate the validity of the employed Mie formalisms in the field of infrared spectroscopy of cells and tissues.

- **Use of full numerical wave calculations**
  Full wave calculations and electromagnetic wave propagation have been used extensively in the field of solar cells to model the absorption efficiency of solar cells. Grandidier et al. [21,23,58] have shown that whispering gallery modes in spherical SiO_2 surface structures increases the spectral current density. It is further shown how the reflection can be reduced and the light trapping enhanced by adding structures on top of the thin film solar cells [33, 38, 59]. However, the rational behind the enhancement mechanisms is difficult to decode in advanced numerical calculations. Full numerical calculations of the electromagnetic field have also been used within spectroscopy. Davis et al., e.g., demonstrate the diffraction and scattering effects in heterogeneous layered samples [60].

- **Use of a ray model in the classical limit of short wavelength**
  Classical ray tracing has been used to investigate structured solar-cell systems as well. Classical ray tracing does not take the wave nature of the light into account, but is a good approximation when the size parameters of the system are much larger than the wave length of the light [61–65]. In these cases it can be used to estimate the absorption enhancement properties of surface-structured solar cells. For systems where the wavelength of the radiation is comparable with the size of the objects these methods are doomed to fail, since they do not take into account the wave nature of the light.

While in the field of thin-film solar cells efficiency enhancement has been investigated by ray models and wave calculations, the connection between these models is poorly understood. Ray models in the field of solar cells are purely classical ray models that were used to explain the absorption of light by structured solar cells in the short-wavelength limit. When the size of the scatterer matches the size of the wavelength, resonance structures occur and it is highly interesting to investigate if these resonance structures can also be described in a ray picture. The role of resonance structures are not well understood in the infrared spectroscopy of cells and tissues. While the Mie formalism exhibits clear resonance structures, they are not observed in most real measurements of biological cells.

1.2 Objective

The main objective of this work was to contribute to a better understanding of absorption and scattering properties of electromagnetic radiation by scatteres when the size of the scatterers is of the same order as the wavelength.

The objective has been divided into subgoals:

- In the field of semiclassics, which connects classical dynamics and quantum wave dynamics, powerful methods, so-called ray models, have been developed for the interpretation of quantum wave phenomena. These tools have been used in the field of microlasers, and to understand the dynamics in molecular and atomic systems. One of the aims of this thesis is to investigate if these ray models can be transferred to electromagnetic wave systems, and if they can contribute to obtain a deeper understanding of absorption enhancement due to scatter phenomena.
- Ray models in the field of semiclassics have been proven to be especially useful for the investigation of chaotic quantum systems. Thus, another objective of this thesis is to investigate if ray models can be used to interpret chaotic electromagnetic scattering systems.
- The role of resonances due to shape parameters of the object has been discussed frequently in the literature on surface-structured solar cells. It is

important within the field of infrared microspectroscopy as well, in order to understand the effect of scattering phenomena on the measured spectra. Therefore, we wanted to understand the relation between resonances and absorption enhancement. It is especially interesting to see if the appearance of resonances is causally related to absorption enhancement and how shape parameters of an object govern the appearance of resonances and thereby absorption properties.

1.2.1 Organization of the thesis: Introduction and relation to the papers

Resonance phenomena that occur when electromagnetic radiation impinges on a scatterer that has a size at the same scale as the wavelength of the electromagnetic radiation, are exactly described by electromagnetic theory. We start in section 2.1 by introducing the reader to methods used in electromagnetic theory to describe the scattering and absorption of electromagnetic radiation at small particles. Both, for applications in nano-structured thin-film solar cells and infrared mirospectroscopy it is important to be able to quantify the absorption properties. We therefore introduce the reader in section 2.2 to the quantities absorption, scattering and extinction efficiency as they are calculated in the field of solar cells and in spectroscopy. In this context, we will also introduce approximation formulae for extinction efficiencies as they have been frequently used in infrared microspectroscopy of cells and tissues. Finally we will introduce the reader briefly to the use of ray models for describing electromagnetic scatter problems and the use of ray dynamics for evaluating if a system is chaotic or not. The description of rays is kept short since detailed introductions can be found in Paper I [1], Paper II [2] and Paper IV [4]. Paper I [1] and Paper II [2] present an exact ray model for systems consisting of films for both normal and oblique incident light and meet thereby the first subgoal of the thesis. While Paper I [1] and Paper II [2] focus on applications in the field of thin-film solar cells, the results are of rather generic nature. The ray models presented in these papers are validated by comparing the ray models with exact electromagnetic theory and with experimental data. Paper IV [4] deals with an application in infrared microspectroscopy. We investigate the presence and absence of resonances, so called ripples, which are predicted by Mie theory in infrared absorbance spectra. We evaluated their presence and absence in the electromagnetic field by exact and numerical simulations and classical ray tracing. We investigate how scattering properties, i.e. regular or chaotic scattering, effects the resonances in the scatterer. These investigations meet both the second and third subgoals. In Paper III [3], we investigate one-dimensional systems in order to evaluate how the resonance structure in both absorptive and non-absorptive layers affects the absorption properties of a system. Paper III meets the third subgoal.

Chapter 2

Theory and Methods

2.1 Electromagnetic theory for scattering and absorption at small particles

2.1.1 Describing scattering and absorption requires the dual nature of light

In this work we consider three-dimensional electromagnetic systems that are invariant in one or two dimensions and which are effectively one- or two-dimensional systems. In order to describe the wave phenomena which occur in these systems, e.g. when light is propagating towards an object as illustrated in Fig.2.1, we use either exact theory or numerical approaches. When light is impinging on an object, it is either scattered off, transmitted through or absorbed by the object as shown in Fig. 2.1. Since most scattering objects are absorbing as well, we use the term scatterer also in cases when we consider absorption phenomena.

Figure 2.1 illustrates a typical situation for scattering and absorption at small particles. Due to conservation of energy, the intensity of the incoming radiation I_0 is conserved and given by the sum of the intensity of the scattered radiation I_s, the intensity of the absorbed radiation I_a and the intensity of the transmitted radiation I according to

$$I_0 = I_s + I_a + I. \tag{2.1}$$

When the wavelength of the incoming electromagnetic wave is of the same order as the size of the scatterer, resonances may occur. The resonances are caused by standing waves in the scatterer. In case of a film, standing waves appear, when an integer number of wavelengths match two times the width of the film. In the case

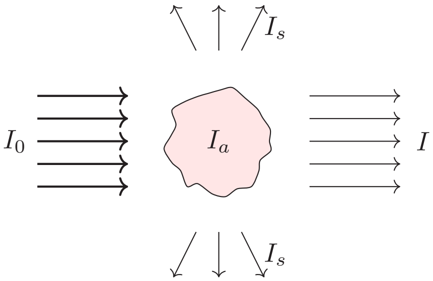

Figure 2.1: Electromagnetic radiation of intensity I_0 is propagating towards an object. The incoming light is either scattered off (I_s), transmitted through (I) or absorbed (I_a) by the object.

of a circular or spherical scatterer, resonances are created when an integer number of wavelengths fits approximately inside the circumference of the scatterer. The standing wave creates an increased electric field inside the scatterer which leaks to the outside of the scatterer [66]. An important part of the thesis concerns understanding how these resonances contribute to the absorption enhancement in different situations such as light absorption in nano-structured solar cells or absorption of infrared radiation in cells and tissues as in infrared microspectroscopy. When establishing an electromagnetic model, we therefore need to consider both scattering properties and absorption properties of light. These two properties are explained by the dual nature of light. Light can be described as electromagnetic *waves*, as Maxwell did in the 19th century. The wave nature of light describes the propagation of light and explains its interference properties. Quantum physics introduced the particle interpretation of light. The particle is called a *photon* and was introduced by Einstein in the beginning of the 20th century. The particle nature of light was needed to explain how matter can absorb energy in the form of electromagnetic radiation. We describe later in this section, how absorption properties are incorporated in the electromagnetic theory.

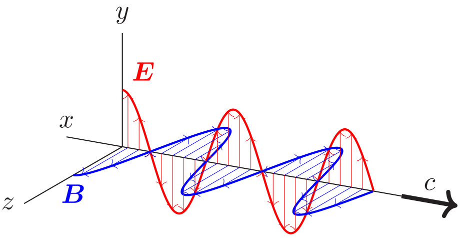

Figure 2.2: The electric (E) and magnetic (B) field vectors in a linear polarized electromagnetic wave. The fields are normal to each other and to the propagation direction. The wave is propagating in x-direction with a speed equal to c.

In the electromagnetic theory, electromagnetic radiation consists of an electric and a magnetic field. The electric and the magnetic field are normal to each other and to the propagation direction as shown in Fig. 2.2. Electromagnetic radiation in vacuum satisfies

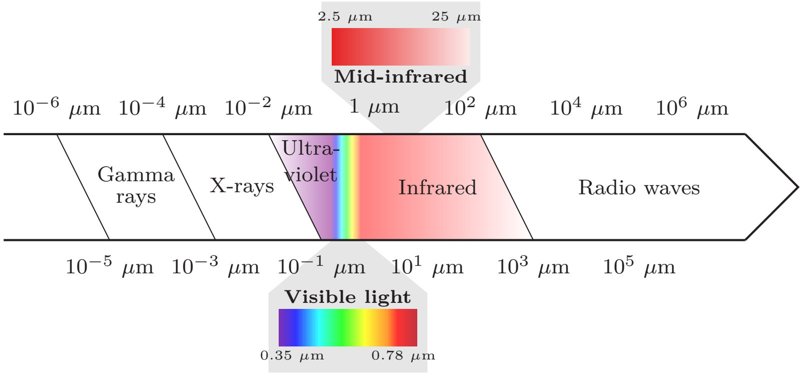

Figure 2.3: The electromagnetic spectrum is divided into different spectral ranges depending on the wavelength, i.e. the energy of the electromagnetic radiation. This thesis considers both the visible region from 0.35 μm-0.78 μm and the mid-infrared region ranging from 2.5 μm-25 μm.

the wave equation,

$$\nabla^2 U = \frac{1}{c^2}\frac{\partial^2 U}{\partial t^2}, \tag{2.2}$$

where U is the electromagnetic field, i.e. either the E- or B-field and c is the speed of light. Electromagnetic radiation is classified according to the wavelength in vacuum as shown in Fig. 2.3. The wavelength ranges of the electromagnetic radiation considered in this work are the visible and mid-infrared region of the electromagnetic spectrum. The visible range is considered for applications of enhancement of electromagnetic radiation in optically thin solar cells, while the mid-infrared range is considered for application of mid-infrared spectroscopy. The mid-infrared range considered is approximately from 2.5 to 25 micrometers.

The speed of electromagnetic radiation in vacuum is independent of wavelength, and it is found to be approximately $c = 3 \cdot 10^8 \,\frac{\mathrm{m}}{\mathrm{s}}$. The speed is reduced in media, and the ratio between c and the speed of light in media is the refractive index of the media, m.

The behavior of electromagnetic radiation is described exactly by Maxwell's equations. In case of no free charge and no free current and a linear, homogeneous medium, Maxwell's equations are given by

$$\nabla \cdot \mathbf{E} = 0, \tag{2.3}$$

$$\nabla \cdot \mathbf{B} = 0, \tag{2.4}$$

$$\nabla \times \mathbf{E} = -\frac{\partial \mathbf{B}}{\partial t}, \tag{2.5}$$

$$\nabla \times \mathbf{B} = \mu\varepsilon\frac{\partial \mathbf{E}}{\partial t}, \tag{2.6}$$

where $\mathbf{E}$ and $\mathbf{B}$ are the electric and magnetic field, ε is the permittivity and μ is the permeability. The permittivity is given by $\varepsilon = \varepsilon_r\varepsilon_0$, where ε_r is the dielectric constant of the material and ε_0 is the permittivity of vacuum ($\varepsilon_r = 1$ for vacuum). The permeability is given by $\mu = \mu_r\mu_0$ where μ_r is the relative permeability of the material and μ_0 is the permeability of vacuum ($\mu_r = 1$ for vacuum) [48].

The materials investigated in this work are linear, homogeneous media where $\mu_r = 1$. The refractive index, m, is related to the dielectric constant by

$$m = \sqrt{\varepsilon_r\mu_r}. \tag{2.7}$$

Both μ_r and ε_r are wavelength dependent. The refractive index m can be used to describe absorption properties of matter as we will see in the following.

In 1905, Einstein laid the foundation for the understanding of the absorption of light by matter. His seminal work on the photoelectric effect of 1905 prepared the ground for the interpretation of light as particles, photons, with a discrete energy [67–69]. Photons are stable, chargeless, massless elementary particles that exist only at speed c. The energy of the photon can be quantized by energy levels of electrons, atoms and molecules. The energy is dependent on the wavelength of the corresponding electromagnetic radiation and is given by

$$E_f = hf, \tag{2.8}$$

where h is Planck's constant and f is the frequency of the waves. The frequency f is given by $f = \frac{c}{\lambda}$, where c is the speed of light and λ is the wavelength. Einstein's theory laid among other contributions the foundation for the *Quantum mechanics*, which at the end of the 1920's was a well-verified theory due to the work of Bohr, Born, Heisenberg, Schrödinger, De Broglie and others [67]. As mentioned previously, quantum mechanics and the particle nature of light describe the interaction between light and matter. In addition to the particle nature of light, discrete energy levels of atoms, molecules etc. are needed in order to understand absorption properties of materials. In general a photon that impinges on an object, is redirected and scattered. However, when the energy of the incoming photon matches the energy gap between energy levels of the atom, molecule, crystal etc. with which the photon interacts, the photon can be absorbed. The absorbed energy may be emitted as a photon of the same energy, where emission can in principle take place in any direction, it can be converted into electric current as in thin film solar cells, it can be converted into thermal energy, etc..

While the particle nature of the light describes the interaction between light and matter, i.e. the absorption and emission of light, we often use a semi-classical picture of absorption, e.g. by the Lorentz model, when describing the scattering and absorption of electromagnetic radiation in matter. In the Maxwell theory, the absorption properties of materials are described by the imaginary part of the refractive index m. The imaginary part of the refractive index can either be calculated or measured. For calculations, different models can be applied. To describe the absorption properties of dielectric molecules, the Lorentz models can be used. The absorption properties of solar cell materials, i.e. semiconductor materials, are described by the band gap of the material. Beer-Lambert law can be used to describe the absorption [27,54]. The absorption properties of materials are incorporated as the imaginary part n_i of the refractive index m according to

$$m = n_r + in_i, \tag{2.9}$$

where n_r is the real part of m which describes the refraction properties of the material and n_i the imaginary part which describes the absorption properties [48,67,68]. We will see later how the imaginary part of the refractive index can be related to measured absorption properties of materials.

2.1.2 Approaches for solving the electromagnetic problems

All electromagnetic problems considered in this thesis are scattering problems concerning small particles, where the small particles are homogeneous with respect to the refractive index (see Fig.2.4).

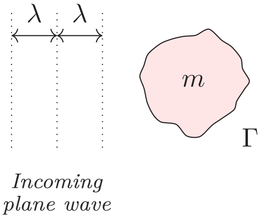

Figure 2.4: An electromagnetic plane wave of wavelength λ is propagating towards the small particle. The particle is homogeneous and has a refractive index m. The particle is separated from the surroundings by the boundary Γ.

To solve the problems exactly, the wave equation

$$\nabla^2 U = \frac{m^2}{c^2}\frac{\partial^2 U}{\partial t^2}, \tag{2.10}$$

has to be solved for all areas with constant refractive index m while in addition, electromagnetic boundary conditions are imposed on the boundary. At a boundary Γ (see Fig. 2.4), the E- and B-fields are discontinuous. The discontinuity is described by Maxwell's equations (Eqs. 2.3-2.6). The electromagnetic boundary conditions in case of no free charge or free current at the surface are given by

$$\varepsilon_1 E_1^{\perp} = \varepsilon_2 E_2^{\perp}, \tag{2.11}$$

$$\vec{E}_1^{\|} = \vec{E}_2^{\|}, \tag{2.12}$$

$$B_1^{\perp} = B_2^{\perp}, \tag{2.13}$$

$$\frac{1}{\mu_1}\vec{B}_1^{\|} = \frac{1}{\mu_2}\vec{B}_2^{\|}, \tag{2.14}$$

where the subscripts 1 and 2 indicate the two different materials. The superscript $\perp$ and $\|$ indicate the components perpendicular and parallel to the boundary [48].

Electromagnetic problems are in general three-dimensional problems, since electromagnetic fields are vector fields (Fig. 2.2). However, when the electric field is normal to the plane of incidence, i.e. when light is perpendicular polarized, the intrinsically three-dimensional problem can be simplified and scalar wave theory can be used to describe the effectively two-dimensional scattering system. The plane of incidence is described as the plane which is formed by the propagation vector and the normal to the boundary [48]. By use of scalar wave theory, we can reduce the three dimensional electromagnetic problem to a scalar one- or two dimensional problem. Then our system satisfies boundary conditions which are equivalent to the corresponding quantum mechanical boundary conditions, i.e. that wave function and the first derivative of the wave function both are continuous across the boundary. [70].

For special shapes of the objects, such as films or spheres, exact solution can be found for the problems. In the case of more complex systems, numerical methods are used. Many different and powerful numerical approaches and software packages have been developed to describe the propagation and absorption of electromagnetic radiation. Techniques which solve electromagnetic problems numerically are for example the Finite Difference Time Domain (FDTD) method, the Finite Element Method (FEM) and Rigorous Coupled Wave Analysis (RCWA) [71, 72]. Solvers based on these techniques are available as commercial software and are used within several fields. In this work, FDTD by the commercial program Lummerical [73] and FEM by Comsol's wave optics module [74] were used in order to evaluate various electromagnetic problems. In addition to the use of commercial software packages, an algorithm based on the Green function was developed in this thesis for initial investigations, for gaining a deeper understanding and for comparison with commercial software packages. The developed algorithm, is a scalar wave method finding a solution of the Helmholtz equation by the use the Green function method. Below we present the Green function method that was used at the beginning of the thesis work to achieve a better understanding of the physics in light scattering at small particles. We further compare the Green function results with commercial solvers. We finally introduce shortly the Gaussian beam method method, which was used to study the interaction of a finite beam and a small particle.

Greens function method

For simplification and without loss of any generality, a two-dimensional system that is described by the scalar wave function was considered. This is for several cases is a good approximation. The solution of the scalar Helmholtz equation for an arbitrary potential is found by the Lippmann-Schwinger equation with the free two-dimensional Green function [75]. For periodic potentials [76], the Green function was combined with the Bloch ansatz [77, 78], which allowed us to treat infinite surfaces. While the method allowed to choose an arbitrary but periodic structure, we focused on periodic structures with circular shapes (disks) and disks placed on an energy converting material. The investigated systems are effectively two dimensional and equivalent to three-dimensional infinite cylinders.

In order to investigate the effectively two-dimensional systems, we searched for a solution of the time-independent wave equation for the given potential

$$-\Delta\psi(\vec{r}) + k^2 m^2(\vec{r})\psi(\vec{r}) = 0 \tag{2.15}$$

where $\vec{r}$ is the position vector, $m(\vec{r})$ is the index of refraction, k is the the angular wavenumber, which is related to the wavelength, λ, by $k = \frac{2\pi}{\lambda}$. The wave function $\psi(\vec{r})$ is calculated in the potential $V(\vec{r})$ given by

$$V(\vec{r}) = k^2 v(\vec{r}), \tag{2.16}$$

where $v(\vec{r}) = 1 - m(\vec{r})$.

A solution of the problem can be obtained by solving the Lippmann-Schwinger equation [75]

$$\psi(\vec{r}) = \varphi(\vec{r}) - \int G(\vec{r}, \vec{r'}, k)V(\vec{r})\psi(\vec{r'})d^2\vec{r'}, \tag{2.17}$$

where $\varphi(\vec{r})$ is the wave function of the incoming wave and $\psi(\vec{r})$ is the wave function in the potential $V(\vec{r})$.

In our simulations, the incoming wave is given by a plane wave. $G(\vec{r}, \vec{r'}, k)$ is the Green function for the free Helmholtz equation [79]. The Green function is given by

$$G(\vec{r}, \vec{r'}, k) = \frac{i}{4}H_0^{(+)}(k|\vec{r'} - \vec{r}|), \tag{2.18}$$

where $H_0^{(+)}$ is the Hankel function of the first kind and zero order [79]. The Lippmann-Schwinger approach, Eq. 2.18, gives us the possibility to investigate an arbitrary potential.

When the arbitrary potential is periodic, as shown in Fig 2.5, the Bloch ansatz can be applied to the Green function [70].

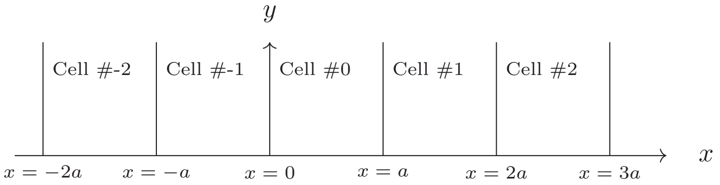

Figure 2.5: A periodic two-dimensional potential of width a.

The solution of the Helmholtz equation is given by

$$\psi(\mathbf{r}) = u(\mathbf{r})e^{i\mathbf{br}} \tag{2.19}$$

where $\mathbf{b}$ is the Bloch momentum and $u(\mathbf{r})$ has the same period as the crystal lattice with $u(\mathbf{r}) = u(\mathbf{r} + \mathbf{a})$ [70, 77, 78]. It gives us the possibility to investigate infinite periodic potentials [76]. For a potential that is periodic in x-direction as shown in Fig. 2.5, the Bloch momentum is equal the x-component of the angular wavenumber of the incoming wave. This can be found by requiring that the incoming wave also satisfies the Bloch condition.

We can compute the wave function in cell number 0 in Fig. 2.5 by the Lippmann-Schwinger equation. In this case we have to use the Lattice Green function [76] given by

$$\tilde{G}(k, \mathbf{r}_0, \mathbf{r'}_0) = \sum_{M=-\infty}^{\infty} G(k, \mathbf{r}_0, \mathbf{r'}_0 + M\mathbf{a})e^{i\mathbf{b}\cdot\mathbf{Ma}} \tag{2.20}$$

where M is the cell number. The Green function method has several limitations which the optimized commercial software packages can handle. The accuracy of the Greens Function method decreases as the differences between refractive index of the materials evaluated increases. The simulations are time and memory consuming. In the following section we present the comparison of the Green function method with commercial software packages, which was done as initial work in the thesis.

Comparison between Green function methods, FDTD and analytical solutions

In order to determine the precision of our Green Function method and of the commercial software tool, we compared in total three approaches for a disk: (i) the algorithm based on the Green function method, (ii) an FDTD-based electromagnetic simulator [73] and (iii) the analytical Mie solution. The radius of the disk was chosen to be 500 nm and the refractive index as 1.2. By evaluating the three plots of the absolute squares of the wave functions in Fig. 2.6 visually, the three approaches give the same field for a disk.

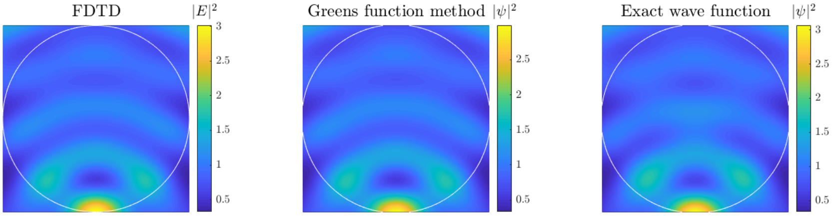

Figure 2.6: The absolute square of the field is shown for the scattering of a plan electromagnetic wave at a disk using three different approaches for the calculation of the field. The disk has a radius of 500 nm and a refractive index of 1.2. The surrounding square has a refractive index equal to 1. The incoming plane wave is propagating from the top and has a wavelength of 615 nm. In (a) the absolute square of the perpendicular polarized electric field for the system calculated by FTDT [73] is shown, (b) shows the absolute square of the wave function found by the Green function method and (c) shows the absolute square of the exact wave function of the system.

The three approaches were further compared by evaluating the value of the absolute square of the field in a given grid. The FDTD calculations were performed using a resolution of 200 x 200. The simulation by the Green function method was accomplished with a 100 x 100 grid. We compared the field in points with the same x- and y-values. Field deviations are shown in Tab. 2.1, where the comparison is done pairwise for the three different approaches.

Table 2.1: An element-wise comparison for the three approaches. The calculations correspond to the situation for which the absolute square of the field is presented in Fig. 2.6. Here we evaluate the root mean squared error, RMSE, calculated pairwise between the three approaches. Comparing the FDTD and the method based on the Green function, we find a relatively low RMSE, while the comparison of the two numerical approaches with the exact solution, reveals a larger error.

Methods compared	**RMSE**
FDTD and Greens function method	0.0044
FDTD and Exact solution	0.0615
Exact solution and Greens Function Method	0.0617

The difference between the simulations from FDTD and the Green function differ by an RMSE = 0.0044. The numerical programs differ both with a RMSE equal to 0.06 when comparing them with the exact solution.

Illuminating an object with a finite beam - the Gaussian Beam

In order to evaluate the scattering and absorption properties of an object that is illuminated by a beam with finite width, we can propagate a Gaussian beam towards the surface of the object and let it transmit the surface and propagate in the object. As before we consider a two-dimensional problem without losing any generality of our findings. The Gaussian beam is, in contrast to a plane wave, a radiation source of finite width.

The transverse profile of the optical intensity of a Gaussian beam can be described by a Gaussian function [80]. The spot radius of the beam is defined as the distance from the center of the beam with maximum value E_0 to where the value of the electric field has dropped to $\frac{E_0}{e}$ or $\sim 0.37E_0$ [67].

Figure 2.7 shows a Gaussian beam of spot size 5 μm propagating towards a film of refractive index 1.84 and a thickness of 75 μm. The angle of incidence is 50°. The refractive index of the outer material (i.e. the triangles left and right of the film) is 1.0. Figure 2.7 shows how the refracted beam changes direction and also how the beam is reflected several times inside the film.

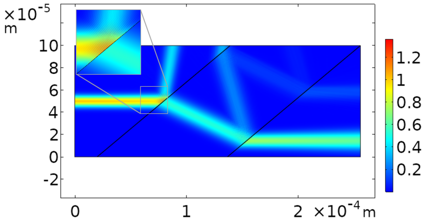

Figure 2.7: A Gaussian beam propagating towards a film of thickness 75 μm with an angle of incidence equal to 50°. The refractive index of the film is 1.84.

2.2 Quantification of scattering and absorption by electromagnetic theory

2.2.1 Scattering and absorption in one-dimensional systems

An infinite film with normal incident light is an effectively one-dimensional system. The incoming radiation is either back scattered by the film (reflected), absorbed by the film or transmitted through the film as shown in Fig. 2.8. The reflected, absorbed and transmitted electromagnetic radiation can be found analytically with

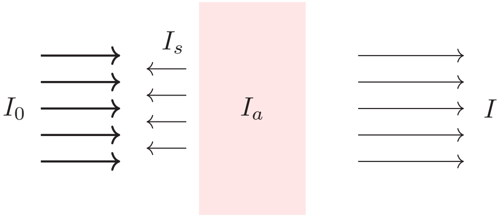

Figure 2.8: Electromagnetic radiation of intensity I_0 is propagating towards an infinite film. Part of the radiation is scattered backwards described by the scattered intensity I_s, part of the radiation is absorbed by the film described by the absorbed radiation I_a, part of the radiation is transmitted through the film described by the intensity I.

the help of the electromagnetic boundary conditions (Eqs. 2.11-2.14) or by scalar wave theory.

In the case of a one-dimensional system as in Fig. 2.8, where a plane wave is propagating with normal incidence, reflection, absorption and transmission properties of the system can be described by scalar wave theory. The incoming wave (ψ_0), reflected wave (ψ_r) and transmitted wave (ψ_t) are given by

$$\psi_0(x) = e^{ikx}, \tag{2.21}$$

$$\psi_r(x) = re^{-ikx}, \tag{2.22}$$

$$\psi(x) = te^{ikx}. \tag{2.23}$$

The incoming plane wave with wavelength λ and amplitude one is propagating in positive x-direction. The angular wavenumber k is related to the wavelength by $k = \frac{2\pi}{\lambda}$. r and t are the reflection and transmission amplitude. The amount of absorbed light, the *absorption efficiency*, is given by

$$\sigma_a = 1 - R - T, \tag{2.24}$$

where $R = |r|^2$ is the reflection probability and $T = |t|^2$ is the transmission probability [48, 70].

As shown in Paper I [1], The absorption efficiency for an arbitrary one-dimensional system can also be given by

$$\sigma_a = 2k \int n_i(x) n_r(x) |\psi(x)|^2 \, \mathrm{d}x \,, \tag{2.25}$$

where k is the angular wavenumber, n_r and n_i are the real and imaginary parts of the refractive index, respectively. The product of the absorption efficiency and the spectral weighting term gives the *optical generation rate*, G_{opt} [81]. Where the spectral weighing describes the spectral radiance as a function of wavelength. [27].

2.2.2 Scattering and absorption in two- and three-dimensional systems

Arbitrary two- and three-dimensional systems cannot be solved analytically. The two-dimensional systems considered in this thesis correspond to three dimensional problems that are invariant in the third dimension. These systems can be evaluated by numerical approaches as described in Sec. 2.1.2. In the case of a three-dimensional system, the power $\Theta(\lambda)$ that is absorbed by a volume V is calculated by performing the following integral over the volume V:

$$\Theta(\lambda) = \frac{1}{2\hbar} \int \mathrm{Im}\{\varepsilon_r\} |E|^2 dV, \tag{2.26}$$

where $\hbar$ is the reduced Planck constant, ε_r is the dielectric constant of the media and E is the electric field in the scatterer [81, 82].

For special situations, such as an infinite film, a cylindrical or spherical scatterer, the electromagnetic problem can be solved analytically. The theory of light scattering and absorption by a sphere was developed by Gustav Mie in 1908 [18, 19].

Infinite film

In the case of a plane wave propagating towards an infinite film as shown in Fig. 2.9, the field is invariant along the boundary [48,68]. The behavior of the a plane wave propagating towards material is of considerable interest within both the field of optically thin solar cells and IR spectroscopy. For layered optically thin solar cells this knowledge can be used to decrease the surface reflection and increase the field inside the absorptive film. The minimization of reflection, i.e. antireflection coatings, are a widely explored field [51, 67, 83, 84]. Within spectroscopy this knowledge is valuable when the scattering and absorption of radiation from layered samples is considered [85].

For a thin film, we can derive Snell's law from the boundary conditions. This is illustrated in Fig. 2.9, where the boundary conditions require that the y-component of wave vector $\vec{k}$ is equal on both sides of the boundary. At the boundary at $x = 0$, this is expressed by

$$k \sin\theta_0 = k \sin\theta_r = mk \sin\theta. \tag{2.27}$$

The angular wavenumber k is the magnitude of $\vec{k}$ in vacuum and mk is the angular wavenumber inside the film. θ_0, θ_r and θ are the angles of incidence, reflection and refraction as indicated in Fig. 2.9. Eq. 2.27 is Snell's law.

With Snell's law in Eq. 2.27 and the electromagnetic boundary conditions (Eqs. 2.11-2.14) at hand, we can derive the exact expressions for the reflection and transmission amplitudes for both parallel and perpendicular polarized light.

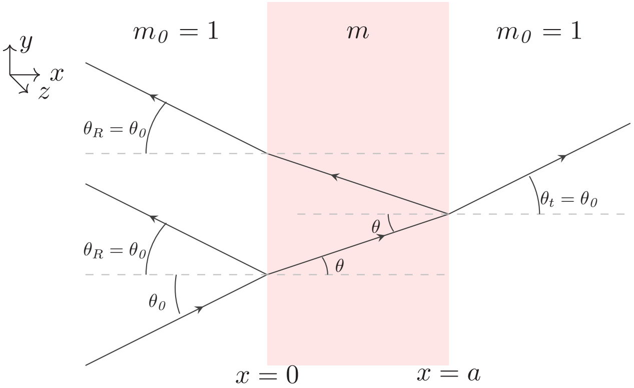

Figure 2.9: The model system consists of a single film of thickness a and a refractive index m. In front of the film, the refractive index is $m_0 = 1$, i.e. the refractive index of vacuum. A plane wave is propagating towards the film in the xy-plane with an angle of incidence θ_0. The angle of reflection, θ_R, is equal to θ_0. The angle of refraction, θ, can be found by Snell's law. For the transmitted ray behind the film, the direction of the angle of the transmitted ray is $\theta_t = \theta_0$.

The two-dimensional film system in Fig. 2.9, is as discussed above, invariant in y-direction. Therefore, the resonances in the system are parallel to the film boundaries, i.e. the standing waves occur as parallel stripes in y-direction inside the film. A resonance takes place in the case where an integer number of wavelengths fits into the thickness of the film.

In the case of an absorptive material, the wave vector inside the film is complex

$$\vec{k_I} = m\vec{k} = \vec{k_{I,r}} + i\vec{k_{I,i}}, \tag{2.28}$$

where $\vec{k_{I,r}}$ and $\vec{k_{I,i}}$ are the real and imaginary parts of the wave vector. The wave vector outside the film is, as before, real. In order to fulfil the requirement presented in Eq. 2.27, $\vec{k_{I,r}}$ and $\vec{k_{I,i}}$ need to have different directions and the resulting electromagnetic wave is said to be *inhomogeneous*. The direction of $\vec{k_{I,r}}$ can be found by

$$\vec{k} \cdot \vec{r} = \vec{k_{I,r}} \cdot \vec{r}, \tag{2.29}$$

at the boundary. $\vec{k}$ is the wave vector in the non-absorptive region and $\vec{k_{I,r}}$ is the real part of the wave vector inside the film. $\vec{r}$ is the position vector. Due to the fact that the wave vector outside the film is real, the direction of $\vec{k_{I,i}}$ is normal to the boundary [68]. The reflection and transmission amplitudes can be found by the electromagnetic boundary conditions, Eqs. 2.11-2.14.

In the case of an absorptive film, the absorption efficiency is found by using the same expression as for the one-dimensional problem for an infinite film, Eq. 2.24.

Infinite cylinder and sphere

In the case of an infinite cylinder or a sphere, the electromagnetic field can be described by Mie theory [18, 19]. Mie type-scattering phenomena have great importance both in the field of nano-structured optically thin solar cells and within the field infrared spectroscopy of biological materials.

Figure 2.10, shows how an incident plane wave of intensity I_0 is either absorbed by a circular object, scattered off or transmitted through the circular object.

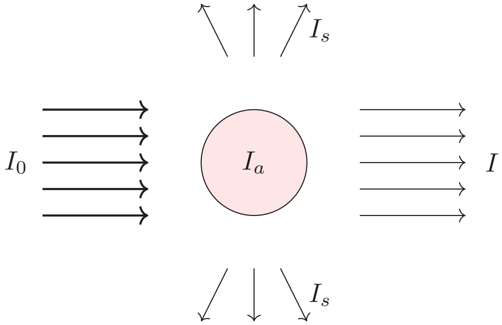

Figure 2.10: Electromagnetic radiation of intensity I_0 is propagating towards a cylinder-shaped object. The incoming radiation is be either scattered off (I_s), transmitted through (I) or absorbed by (I_a) the object.

A commonly, dimensionless quantity used to quantify the share of the electromagnetic radiation that is extinguished from the forward direction, is the extinction efficiency, Q_{ext} [18]. The extinction efficiency is defined by

$$Q_{ext} = \frac{4\pi}{k^2}\frac{1}{g}\,\mathrm{Re}[S(0)], \tag{2.30}$$

where k is the angular wavenumber, g is the geometrical cross section of the scatterer and $S(0)$ is the amplitude function in forward direction [18].

The extinction efficiency is related to the absorption efficiency (Q_{abs}) and scattering efficiency (Q_{sca}) by the following relation

$$Q_{ext} = Q_{abs} + Q_{sca}. \tag{2.31}$$

Q_{ext}, Q_{abs} and Q_{sca} can be found directly from Mie Theory for a sphere and for an infinite cylinder. For the situation where a cylinder is evaluated, we have to take the polarization of the E-field into account [18]. Figure 2.11 shows Q_{ext} as a function of wavenumber for a sphere (black line) and the two polarization directions (green and red line). The radius of the sphere and the cylinder is 10 μm

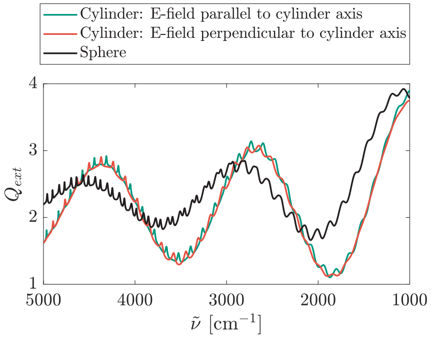

Figure 2.11: The extinction efficiency Q_{ext} for an infinite cylinder (green and red line) and for a sphere (black line) with radius 10 μm and a refractive index of 1.3. The blue and red line corresponds to the two polarization directions. [18]

and the refractive index is 1.3. The selected wavenumber interval corresponds to wavelengths from 2 μm to 10 μm, i.e. the wavelengths and the size of the scatterer are of the same magnitude and we would expect resonances.

For all the three situations described in Fig. 2.11, we observe that the lines oscillate around two. This phenomenon is called the extinction paradox [18]. We observe that Q_{ext} consists of long-range oscillations and sharp, narrow oscillations. The long-range oscillations are called wiggles. The narrow, sharp oscillations are the ripples. They are caused by standing waves, i.e., resonances, inside the sphere also called *whispering gallery modes* [20].

In this thesis, we considered cylindrical objects where the electric field is parallel to the cylinder axis and the propagation direction is perpendicular to the cylinder axis (green line in Fig. 2.11). In this case, the extinction, scattering and absorption efficiencies are given by

$$Q_{ext} = \frac{2}{ka} \sum_{n=-\infty}^{\infty} \mathrm{Re}(b_n), \tag{2.32}$$

$$Q_{sca} = \frac{2}{ka} \sum_{n=-\infty}^{\infty} |b_n|^2, \tag{2.33}$$

and

$$Q_{abs} = Q_{ext} - Q_{sca}, \tag{2.34}$$

where k is the angular wavenumber of the incoming plane wave and a is the radius of the cylinder. The coefficients b_n are given by

$$b_n = \frac{\tan \beta_n}{\tan \beta_n - i}, \tag{2.35}$$

and the $\tan \beta_n$ are given by

$$\tan \beta_n = \frac{mJ_n'(mka)J_n(ka) - J_n(mka)J_n'(ka)}{mJ_n'(mka)N_n(ka) - J_n(mka)N_n'(ka)}, \tag{2.36}$$

where m is the refractive index of the cylinder, J_n is the nth order Bessel function of the first kind and N_n is the nth order Bessel function of second kind (Neumann function).

In the case where the electric field is parallel to the cylinder axis, the situation is equivalent to a two-dimensional scalar wave problem where a plane wave is propagating towards a circular scatterer. An exact description of the field inside and outside the scatterer can be given. Details are given in the appendix of Paper IV [4].

Figure 2.12 shows an example of a whispering gallery mode for a cylinder. The radius of the cylinder is 10 μm and the refractive index is 1.8.

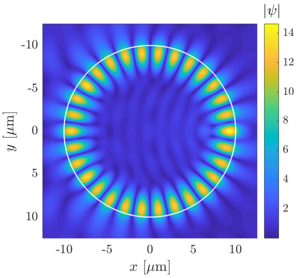

Figure 2.12: The norm of the wave function is plotted for a whispering gallery mode. The radius of the disk is 10 μm and the index of refraction is 1.8. The incident radiation is a plane wave with wavenumber 1643.5 cm^{-1}, an amplitude equal to one, propagating from the left. The wavenumber of the incident plane wave is chosen to coincide with the wavenumber of a ripple, which corresponds to a whispering gallery mode.

2.2.3 Approximation of the extinction efficiency

Van de Hulst presents in his book 'Light scattering at small particles' [18] an approximation for the extinction efficiency, Q_{ext}, for spherical scatterers. The approximation is found by evaluating the interference of undisturbed rays and rays that experience a phase lag due to the distance the wave has travelled trough the sphere with a refractive index m. The van de Hulst approximation for Q_{ext} for a sphere of radius 10 μm and a refractive index of 1.3 is shown together with the Mie solution in Fig. 2.13.

Figure 2.13 shows how the van de Hulst approximation explains the wiggle structure of the extinction efficiency. The ripples are not modelled by the van de Hulst

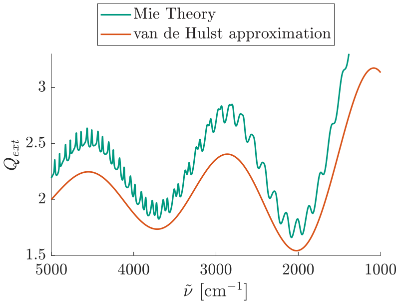

Figure 2.13: The extinction efficiency for a sphere of radius 10 μm and a refractive index of 1.3. The green line indicates the exact extinction efficiency (described by Mie Theory) and the red line is the van de Hulst approximation for Q_{ext}.

approximation. The approximation is found by evaluating Eq. 2.30, where the amplitude function $S(0)$ is found by calculating the phase lag a ray experiences when it penetrates a spherical scatterer. By use of the same procedure, approximation formulas for the extinction efficiency of scatterers with other shapes can be found as well. In Paper IV [4], the approximation of Q_{ext} is calculated for a circular and a stadium-shaped scatterer. The approximation formulas have great importance in the field of infrared spectroscopy of biological materials, as they provide handy and computationally inexpensive tools for modelling Mie scattering in infrared spectra of cells and tissues.

2.2.4 Quantifying absorption of radiation in infrared spectroscopy

A unit-free measure of the quantity of electromagnetic radiation absorbed is the unit *absorbance*. This quantity is commonly used in absorption spectroscopy and is given by

$$A = -\log_{10}(\frac{I}{I_0}), \tag{2.37}$$

where I_0 is the intensity of the incident radiation and I is the intensity of the light that is transmitted through the sample. In the case where scattering can be neglected, we often refer to A given by Eq. 2.37 as the *pure absorbance*. Pure absorbance spectra in infrared spectroscopy can be obtained for example by thin film measurements of biological materials in macroscopic infrared spectroscopic measurements and where there is little backscattering from the film.

The absorption properties of a material can be modelled by including an imaginary part n_i in the refractive index, $m = n_r + in_i$, as decribed in Sec 2.1.1. n_r is the real part and describes the refractive properties of the material. n_i can be related to the pure absorbance A_{pure} by

$$A_{pure} = \frac{4\pi n_i d_{\text{eff}} \tilde{\nu}}{\ln(10)}, \tag{2.38}$$

where d_{eff} is the effective thickness and $\tilde{\nu}$ is the wavenumber [20, 44]. In the case of an infinite cylinder where the light is propagating perpendicular to the cylinder axis, $d_{\text{eff}} = \frac{\pi a}{2}$, where a is the radius of the cylinder. Eq. 2.38 can be obtained by considering the transmission of electromagnetic radiation through a thin film with negligible backscattering. Eq. 2.38 has high importance, since it connects the measured quantity absorbance with the imaginary part of the refractive index.

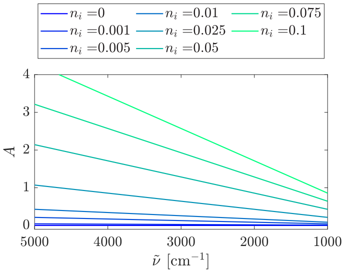

Figure 2.14: The absorbance, A, as a function of wavenumber for different choices of the imaginary part of the refractive index, n_i. A is related to n_i as indicated by Eq. 2.38. The effective thickness of cylinder of radius 10 μm was used.

In order to estimate relevant levels of the imaginary part of the refractive index, the relation between the imaginary part of the refractive index and the measured absorbance needs to be considered. Fig. 2.14 shows how the absorbance A depends on the imaginary part of the refractive index for a cylindrical scatterer of radius 10 μm. Absorbance values are usually obtained in a range between zero and 1.2 in infrared spectroscopy of cells and tissue. An absorbance value in the order of one means that 90% of the incoming radiation is absorbed.

In many situations as in infrared spectroscopy of cells and tissues, strong scattering signatures are visible in the measured spectra. This is illustrated in Fig. 2.1, where the incident light is partly scattered off the object. In this case, the absorbance that is calculated from the incoming and transmitted intensity according to Eq. 2.37 is often called the *apparent absorbance*. The measured apparent absorbance can be related to the calculated extinction efficiency by

$$A = -\log_{10}\left(1 - \frac{g}{G} Q_{ext}\right) \approx \frac{1}{\ln(10)} \frac{g}{G} Q_{ext}, \tag{2.39}$$

where g is the geometrical cross section of the sample and G is the geometrical cross section of the detector. The approximation is found by expanding the logarithm and assuming $G >> g$ [20].

2.2.5 The effect of the size of the numerical aperture on the extinction efficiency

In a real FTIR measurement, the detector has a finite size G and the scattered and transmitted radiation is collected over a numerical aperture. This needs to be taken into account when the absorbance-spectra are evaluated. The size of this detector is called the *numerical aperture*, NA, and is defined as

$$\mathrm{NA} = \sin(\theta_{\mathrm{NA}}), \tag{2.40}$$

where θ_{NA} is the angle defined by the size of the detector as shown in Fig. 2.15 [86]. While Figure 2.15 is a simplified model of the Schwarzschild optics in the infrared microscopic transmission measurements [55], it is sufficient for our discussion of how the NA affects the measured absorbance spectra.

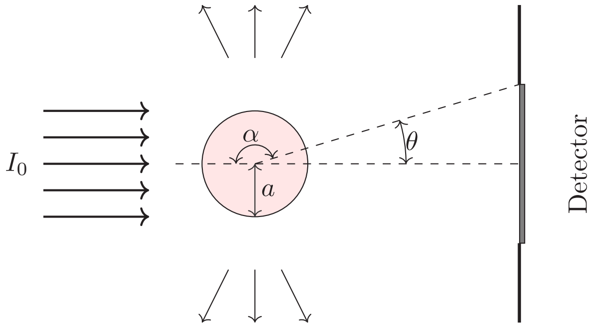

Figure 2.15: Infrared light of intensity I_0 is propagating towards a sample with a shape of an infinite cylinder of radius a in an FTIR spectrometer. The detector of the spectrometer is of a finite size, defined by the numerical aperture given by NA $= \sin\theta$. The scattered light that does not hit the detector is limited by the angle α on both sides of the center line.

The extinction efficiency, Q_{ext}, is the sum of the scattering efficiency and the absorption efficiency. In the case of a non-absorptive scatterer, $Q_{ext} = Q_{sca}$. For an infinite cylinder and in the case where the E-field is parallel with the cylinder axis, Q_{sca} can be found as a sum of the b_n's as described in Eq. 2.33. The scattering efficiency is calculated by evaluating the following integral

$$Q_{sca} = \frac{1}{\pi ka}\int_0^{2\pi} |T(\theta)|^2 d\theta = \frac{2}{\pi ka}\int_0^{\pi} |T(\theta)|^2 d\theta, \tag{2.41}$$

where k is the angular wavenumber, a is the radius of the cylinder and θ is the angle as shown in Fig. 2.15. The integral can be reduced due to symmetry. In the case where the E-field is parallel to the cylinder axis, the function T is given by

$$T(\theta) = \sum_{n=-\infty}^{\infty} b_n e^{in\theta}, \tag{2.42}$$

where b_n is given in Eq.2.35.

When radiation is collected over a numerical aperture, radiation which is scattered into the NA is collected by the detector. In order to quantify the radiation lost due to scattering, we need to evaluate the integral in Eq. 2.41 everywhere, except in the range of the numerical aperture, and obtain

$$Q_{sca}^{\mathrm{NA}} = \frac{2}{\pi ka} \int_{\theta_{\mathrm{NA}}}^{\pi} |T(\theta)|^2 d\theta, \tag{2.43}$$

where θ_{NA} is defined by the NA by Eq. 2.40 and the scattered light escapes over the angle α on both sides of the central line, as shown in Fig. 2.15

2.3 Description of electromagnetic radiation by use of rays

In classical ray tracing or geometric ray tracing approaches, the wave nature of the light is usually ignored. The light is assumed to travel along a straight path and the behavior at the boundaries is described through Fresnel's equations and Snell's law. Classical ray tracing is used in the field of structured thin-film solar cells to evaluate how long rays stay in certain structures, in order to estimate the efficiency of the structure to capture the rays. The absorption properties of such systems are determined through Beer-Lambert's law. The classical ray tracing approximation is only valid in the small wavelength regime, i.e. when the size of the structures are much larger than the wavelength of the light [63, 67, 86]. For situations, where the wavelengths of the incoming light are of the same order as the size of the structures at which the incoming light scatters, wave phenomena such as interference effects in films and whispering gallery mode resonances in spheres appear. The classical ray tracing approach fails to describe these resonances. While electromagnetic and scalar wave theory exhibit resonance phenomena (see Sec. 2.2), a semi-classical theory that connects resonances with specific rays is highly desired, since it may enhance our understanding of the phenomena considerably. While semi-classical approaches that attribute phases to rays are well established in the field of quantum chaos [87–89], they are not commonly used in the fields dealing with nano-structured solar cells or in spectroscopy of small particles. Paper I [1] and Paper II [2] introduce exact ray models for different electromagnetic model systems with planar boundaries between different materials.

Ray tracing is also commonly used to evaluate if systems show a chaotic behaviour or not. In such ray investigations, ray splitting may be included or not. It has been shown that ray splitting needs to be introduced to understand the wave-related properties of quantum chaos systems [88, 90]. Reflection and transmission probabilities can be found by evaluating Fresnel's equations, where only the real part of the refractive index is taken into account. When the rays are evaluated without taking ray splitting into account, using only so-called *Newtonian rays*, the rays are always transmitted through a boundary with the exception of total internal reflection. In Paper IV [4], ray tracing of Newtonian rays has been used to investigate the ray dynamics of a stadium-shaped billiard to decide if the system is chaotic or not. For this purpose it was not necessary to consider ray splitting. In the following we shortly introduce the methods used in this paper for applying ray dynamics in ray-splitting systems in electrodynamics.

2.3.1 Use of semi-classical rays to describe scattering systems

By attaching the correct phase to the ray, Feynman proved that an infinite number of rays can be used to solve the Schrödinger equation [91]. Since in this case, the ray theory solves the Helmholtz equation exactly, the ray theory can also correctly handle resonances caused by the wave nature of light. In Paper I [1] and Paper II [2], we show how an infinitely number of rays can be used to describe reflection, transmission and absorption properties of an infinite film exactly. Absorption properties of the film were included in the formalism by adding an imaginary part to the refractive index of the film.

2.3.2 Use of classical rays to determine the scattering properties

Classical rays can be used to evaluate the scattering properties of a system. Non-integrable systems can exhibit chaotic scattering. A part of this work was to evaluate how the extinction properties of a scatterer is affected by regular and chaotic scattering. When a classical ray hits a boundary, the refraction angle is decided by Fresnel's equations. If ray splitting is considered, the fraction of reflected and transmitted light is given by Fresnel's equations. Absorption can be included by use of Beer-Lambert's law [48]. In an open scattering system, the life time of the ray is defined as the time the ray stays in the system, i.e the length of the ray, before it leaves. In a chaotic system, the length of the ray is very sensitive to starting conditions, i.e. a small change of the start position may result in a big change in the length of the ray. In a regular system, a slight change in the start position is not related to a big change of the length of the ray. The classical ray tracing performed in this work was related to the evaluation of a two-dimensional system where Newtonian rays, i.e. non-ray-splitting rays, were sent straight downwards towards the scatterer. Reflection of rays was only possible when the condition for total internal reflection was fulfilled.

As a system that exhibits a chaotic ray dynamics, we investigated a stadium-shaped scatterer as shown in Fig. 2.16. The system is adopted from the Bunimovich billiard [92] which has been used as a model system for a chaotic resonator. The same system was investigated by Jensen as a scatter system [93]. For us, the main interest in investigating the stadium billiard as a scatterer was to understand if chaotic scattering is a mechanism that suppresses ripples in Mie scattering. Ripples are not modelled by the van de Hulst approximation, which is the main model used for Mie scattering in measured absorbance spectra in infrared spectroscopy. Below we describe the tools used to manifest if the system is chaotic or not.

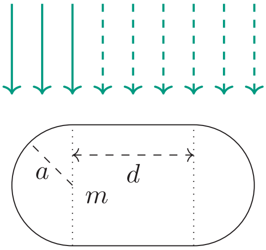

Figure 2.16: Newtonian rays are sent straight down towards the stadium. The rays are refracted according to Snell's law. Only the rays that hit the left end-cap of the stadium are investigated (solid line). Due to symmetry, the rays that hit the right end-cap behave in the same way as the rays that hit the left end-cap. Rays that hit the straight sections of the stadium are not long-lived: They transmit straight through the stadium.

In order to evaluate further if a system exhibits chaotic scattering or not, several factors can be investigated. In this work we considered (i) the fractal structure of the life time plot of rays in the system as a function of the start position, (ii) the fractal dimension and (iii) the Lyapunov exponent of the system.

Investigation of the fractal structure

The path length or life time of a ray that is sent towards a scatterer can be plotted as a function of the initial position. The path length or life time of the rays is calculated as the length of the ray as long as it travels inside the system or the time the ray stays inside the system before it escapes to infinity. By investigating the path length plots of rays on different scales, a fractal structure may be discovered. A fractal is a class of irregular structures that are not smooth. Fractals are indicators of chaos. When the magnification of the fractal yields several identical copies of the fractal itself, the fractal is self-similar. A well-known self-similar fractal is the Cantor set. Several objects in nature emerge as fractal structures, e.g., cumulus clouds, trees, and lungs [94].

Investigation of the fractal dimension by the box-counting method

Already in the 1930s, the concept of the box-counting method was introduced. In order to evaluate the ray dynamics in the stadium-shaped scatterer, as introduced in Fig. 2.16, rays were sent straight downwards towards the left end-cap of the stadium. We determined the number of intervals of a given size δ containing start positions which result in long-lived trajectory. The box-counting dimension, i.e. the fractal dimension, d, is found by

$$d = -\lim_{\delta \to 0} \frac{\log N(\delta)}{\log(\delta)} \tag{2.44}$$

where $N(\delta)$ is the number of intervals, which contain long-lived trajectories as a function of the interval size δ. The interval size δ is given as the width of the interval of start positions. The use of Eq. 2.44 is limited due to the limit $\delta \to 0$. In order to find d, the slope of the plot of $\log N(\delta)$ against $-\log(\delta)$ was evaluated. The slope needs to be determined in the linear region of the plot, i.e. before δ is too small and the amount of the rays in the interval δ becomes to small. The size of δ revealing useful data is therefore restricted by the resolution of the simulations [95–97].

2.3.3 Investigation of the Lyapunov exponent

The Lyapunov exponent, γ, is a measure of the instability of the system. The Lyapunov exponent γ indicates how quickly two rays, starting with a small distance between each other, diverge. In the case of a chaotic system, the distance between the two rays D grows exponentially with time t,

$$D(t) \sim D(0)e^{\gamma t}. \tag{2.45}$$

The Lyapunov exponent γ can be found by evaluating the slope of the plot of $\log(D)$ against t [97].

Chapter 3

Results and Discussions

3.1 Paper I

Exact ray theory for the calculation of the optical generation rate in optically thin solar cells

In Paper I, an exact ray theory was developed for one-dimensional systems consisting of thin layers. The thicknesses of the layers were of the same order as the wavelength of the light, i.e. the ray model needs to take the wave nature of light into account. By summing up infinitely many rays with phases attached, we were able to calculate the exact reflection amplitudes, transmission amplitudes and absorption efficiencies. The rays are found by including ray splitting at the boundaries.

Figure 3.1 shows the three simplest rays that are included in the ray model for a single film with a reflecting backside mirror. The thickness of the film is a and the refractive index of the film is m. The film may be an absorptive material, i.e. the refractive index m is complex. The material in front of the film is air, i.e. the refractive index $n_0 = 1$.

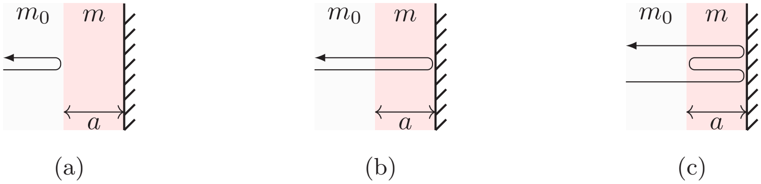

Figure 3.1: The three simplest rays encountered in a system consisting of a film and a backside reflecting mirror. The thickness of the film is a and the refractive index of the film is m. It is air in front of the film with a refractive index of $n_0 = 1$. Frame (a) show the simplest rays, which directly reflects from the surface. The simplest ray that contributes to the absorption efficiency is shown in frame (b). The ray enters into the film is reflected at the mirror and exits. Frame (c) shows the ray with two reflections at the mirror and one internal reflection from the film-air boundary.

By adding up the contributions from these three rays to the total reflection amplitude we obtain

$$r = r_l + t_l e^{imka} e^{i\pi} e^{imka} t_r + t_l e^{imka} e^{i\pi} e^{imka} r_r e^{imka} e^{i\pi} e^{imka} t_r, \qquad (3.1)$$

where the first term is the contribution of the ray illustrated in Fig. 3.1a, the second term is the contribution from the ray illustrated in Fig. 3.1b, and the third term is the contribution from the ray illustrated in Fig. 3.1c. r_l, r_r,t_l and t_r are reflection and transmission amplitudes the ray collected when it reflects at or transmits through the boundary between air and the film. The exact expressions are given in Paper I. e^{imka} is the phase the ray obtained by travelling a distance

a in the material with refractive index m. k is the angular wavenumber and the phase $e^{i\pi}$ is obtained due to the 180° phase shift at the mirror.

If we include all contributing rays, their total, exact contribution to r is given by

$$r = r_l + t_l t_r e^{i\pi} e^{2inka} \sum_{\nu=0}^{\infty} (e^{i\pi} r_r e^{2inka})^{\nu}. \tag{3.2}$$

By evaluating this geometric series and using the expressions for r_l, r_r, t_l and t_r, the exact expression found by electromagnetic theory for the reflection amplitude for an incident plane wave is found.

As shown in Fig. 3.2, the ray model found by Eq. 3.2 converges fast even if only a few of the shortest rays are included. The figure also shows that considering only the five simplest rays in the system, the analytically calculated absorption cross section can already be predicted nearly perfectly. Fig. 3.2 also illustrates another important aspect, namely that our ray theory can describe absorption of electromagnetic radiation by including a complex refractive index.

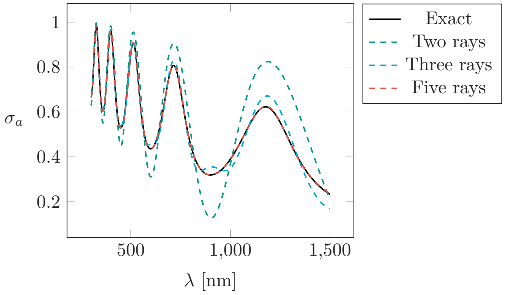

Figure 3.2: Absorption efficiency, σ_a, as a function of the wavelength, λ, for a system consisting of a single film with a reflecting backside mirror. The black line is calculated analytically with the exact expression for σ_a and the ray model with Eq. 3.2 is used when the two (green dashed), three (blue dashed line) and five (red dashed line) simplest rays are included. The refractive index of the film in this system is 1.8+0.05i and the thickness is 500 nm. The wavelength ranges from 300 nm to 1500 nm.

More realistic solar cell devices consist of several layers of films. In the paper, the absorption efficiency for a realistic solar cell device was evaluated with rays by the hierarchical summation scheme (HSS). The HSS was developed for film stacks with more than one layer. Since a numerical summation over all rays is not possible, a hierarchical summation scheme (HSS) was developed to approximate σ.

We further show how the measured reflection amplitude ($R = 1 - \sigma_a$) can be connected to rays by a Fourier transform. From the Fourier transform, the most important rays could be recovered. This obtained knowledge about the relation between rays and absorption efficiency of layered systems may in the future contribute to optimizing the absorption efficiency of multilayered systems.

3.2 Paper II

An Exact Ray Model for Oblique Incident Light on Planar Films

In Paper II, we extend the one-dimensional ray theory from Paper I to treat three-dimensional problems where a plane wave is propagating towards a film with an arbitrary angle of incidence. The ray model describes the scattering problem with oblique incidence at the absorptive films exactly. It further shows that it is essential that the path length of the ray and the phase are calculated with respect to the wave front as illustrated in Fig. 3.3. Basic physics text books often use ray models to describe the resonance structures of thin films. We highlighted that several basic text books do not calculate the contributions of the rays with respect to the incoming wave front, which leads to an inaccurate description which predicts wrong positions of the resonances.

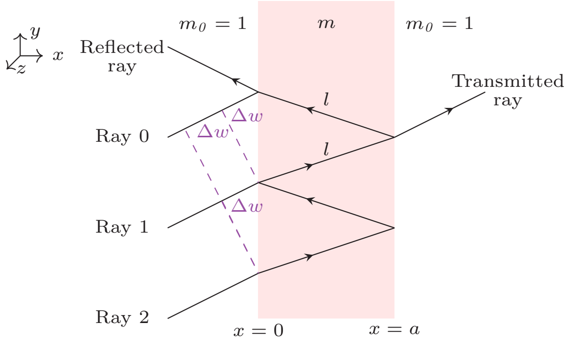

Figure 3.3: Three incoming rays (Ray 0, Ray 1 and Ray 2) that exit the system at the same position and contribute to the reflected ray. The two rays, Ray 1 and Ray 2, bounces inside the interior of the film, exit at the same position, and contribute to the transmitted ray. m_0 and m are the refractive indexes of air and the material in the film, respectively. a is the film thickness and l is the geometrical path length the rays travel from the front surface to the back surface of the film. Δw is the path length difference that Ray 0 and Ray 1 (Ray 1 and Ray 2, respectively) travel outside of the film.

An intriguing aspect of the developed ray model for a plane wave with oblique incidence to a boundary between air and an absorbing medium, is that it demonstrates that absorption only happens with respect to the direction perpendicular to the surface. By starting rays outside the film in the wave front and by taking into account absorption inside the film only in the direction of the axis perpendicular to the boundary we obtain the exact solutions for the electromagnetic problem. Since it is counter-intuitive that absorption of rays could only happen perpendicular to the boundary, we investigate the oblique incidence of a beam of finite width onto an absorbing material. We show that the absorption of a Gaussian beam takes place along its path in case of a beam of finite width, i.e. according to Beer-Lambert's law. Calculations were done by evaluating a Gaussian beam in Comsol for different angles of incidence.

In order to evaluate the different models, we make a comparison of the following models and experiments: We compare (i) a ray model (ray model A) which includes only the travelled length inside the film (only l in Fig. 3.3) (ii) the ray model (ray model B) with rays started in the wave front (i.e. including the distance Δw and l in Fig. 3.3) and absorption of all rays only along the axis perpendicular to the boundary, and (iii) the measured reflection amplitude of a SiN$_x$ film with a backside mirror.

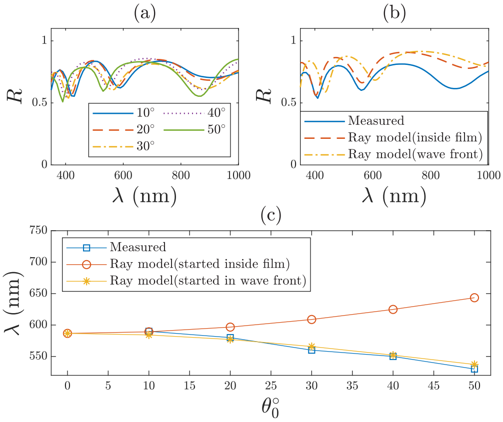

Figure 3.4: Frame (a) shows the measured reflection probability R for an optically thin SiN$_x$ film. With increased angle of incidence, the resonances are shifted towards shorter wavelengths. In frame (b), the blue line shows R for an angle of incidence of 30° and as a function of wavelength for the measurements, the red dashed line shows R for ray model A and the yellow dotted line shows R for a ray model B Frame (c) shows the position of an absorption resonance (dip in R) of the measured R between 500 and 600 nm [see frame (a)] (blue line, squares) as a function of the angle of incidence in comparison for ray model A (red line, circles) and for ray model B (yellow line, stars). The predictions of the ray model A (circles), clearly deviate from the predictions of the correct ray model B (stars), which agrees with our measurements (squares).

Figure 3.4 a shows the reflection probability R as a function of wavelength. The figure shows how the resonances are shifted towards shorter wavelengths as the angle of incidence increases. In Fig. 3.4b the measured data is compared with ray model A and ray model B. Fig. 3.4b shows that the ray models B is predicting the dips of R correctly. Figure. 3.4c follows the resonance between 500 and 600 nm from Fig. 3.4a for an increasing angle. We observe that the ray model B is following the same trend as the measured data.

3.3 Paper III

Investigation of resonance structures in optically thin solar cells

In Paper III, the effect of resonances on the absorption efficiency is evaluated for layered systems. This means that the systems could be evaluated by exact theory. Both resonances in the surface structures and the absorptive materials were investigated.

Intuitively, one would expect that a higher imaginary part of the refractive index of the absorptive film would result in higher levels of absorption efficiency. However, this is not always the case. As the imaginary part of the refractive index increases, the absolute value of the complex refractive index also increases, and hence the reflection probability increases according to Fresnel's equations. For a given wavelength interval, the optimal imaginary part of the refractive index is given when the absorptive layer absorbs the light for small wavelengths, while for longer wavelengths standing waves in the absorptive materials can still be observed. When evaluating a film with a thickness of 500 nm and a real part of the refractive index of 4.3 (the real part of the refractive index of silicon for light of wavelength 500 nm), the optimal imaginary part of the refractive index is found to be 0.27. The wave function for this optimal value is plotted in Figure 3.5, where the absolute square of the wave function in front of and inside a single film with a backside reflecting mirror is shown. As the figure shows, all the incident light is absorbed for the small wavelengths but not for the longer wavelengths.

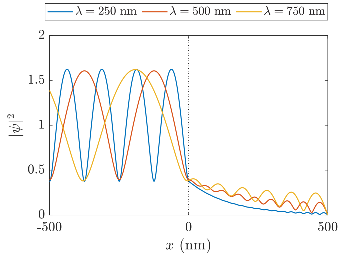

Figure 3.5: The figure shows the absolute square of the wave function for a system consisting of an absorptive film and a backside mirror. The thickness of the film is 500 nm and a refractive index equal to 4.3 + 0.27i. A plane wave of amplitude 1 is propagating from the left towards the film. The boundary of the film is at $x = 0$. The optimal imaginary part of the refractive index of 0.27i was found to result in maximum absorption efficiency.

Non-absorptive layers in front of the absorptive film act as surface structures in a one-dimensional system. By taking the integral over the wave function in the non-absorptive layer, the effect of resonance structures in the front layer can be evaluated. Figure 3.6 shows the absorption cross section σ_a (blue line and left

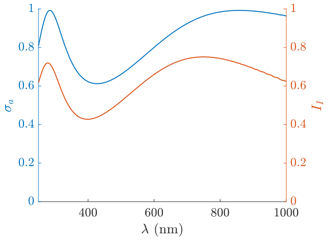

Figure 3.6: The absorption cross section σ_a (blue line, left y-axis) and the integral over the first layer (red line, right y-axis) as function of wavelength for a two-film system with a backside mirror. The first layer has a refractive index of 1.9 and a thickness of 112 nm and the second layer has a refractive index of 4.3+0.1i and a thickness of 5000 nm.

y-axis) and the integral over the absolute square of the wave function of the first layer I_I (red line and right y-axis) as a function of wavelength of the incoming light. I_I is evaluated in order to see whether resonances in the first layer lead to absorption enhancement in the second non-absorptive layer. The thickness of the absorptive layer is 5000 nm and the refractive index is 4.3+0.1i, i.e. all light entering the absorptive layer is absorbed. The oscillations are therefore due to resonances in the first layer which has a thickness of 112 nm and a refractive index of 1.9. Both σ_a and I_I are following the same trend, demonstrating that an enhanced field in the non-absorptive layer is associated with an enhanced field in σ_a.

In the case where a non-absorptive layer is placed on both sides of an absorptive film, the resonances in the first layer are mainly causing the absorption enhancement in the absorptive layer. We investigated further if coupling of resonances could enhance absorption in an absorptive layer which was located between to absorbing layers and could not find any effect. Based on the obtained results, we present a strategy for optimization of absorption enhancement by optimizing film thicknesses for experimentally realizable solar cells.

3.4 Paper IV

Potential pitfalls in interpretation of Mie-type signatures in infrared microspectroscopy

In Paper IV, we evaluate how the extinction efficiency of circular scatteres are affected by (i) deformation, (ii) absorption and (iii) the size of the numerical aperture. The extinction efficiency for a circular scatterer is described by Mie theory and displays wiggles and ripples, i.e. the broad and sharp oscillations.

By use of Comsol [74] we evaluated the electric near- and far field of a scatterer as it transits from a disk to (a) a stadium-shaped scatterer and (b) an elliptical scatterer. We observe that wiggles are stable, but ripples disappear as the deformation increases. The stadium-shaped scatterer is inspired by the Bunimovich stadium, which is a chaotic system. Investigations of the extinction efficiency show that the ripple structure of the two systems is suppressed for smaller deformation for a stadium-shaped scatterer compared with the elliptical scatterer.

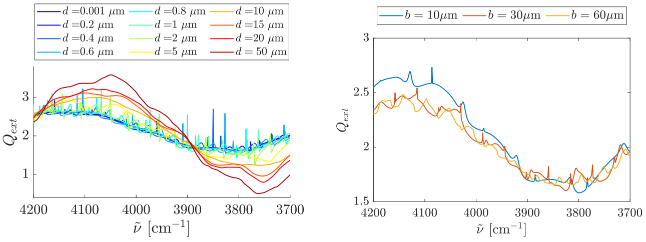

(a) (b)

Figure 3.7: The figure shows the extinction efficiency as a function of wavenumber for a scatterer which transits from a disk to (a) a stadium-shaped scatterer and (b) an elliptical scatterer. The refractive index of the scatterer is 1.8. For both cases, the radius of the disk is 10 μm. For the stadium shaped scatter, a straight section of length d is inserted between the to circular end-caps of radius 10 μm. d is increased from 0 to 50 μm. For the elliptical scatterer, one of the semi-major axes is kept constant to 10 μm and the other semi-major axis is increased up to 60 μm.

By evaluating the classical ray dynamics we show that the stadium-shaped scatterer exhibits chaotic scattering. Both the sensitivity to initial conditions, the fractal structure, the fractal dimension and the Lyapunov exponent were evaluated. The elliptical scatterer is an integrable system and does not exhibit chaotic scattering. We demonstrate that ripples are suppressed more efficiently in the chaotic scattering situation compared to the regular scattering situation at the elliptic scatterer.

Further, we evaluate the effect of absorption on the Mie wiggles and ripples. Figure 3.8 shows how the extinction efficiency for a circular scatterer is effected by increased absorption. The figure shows that the wiggle structure remains. In addition, the ripple structure is still present at relative high absorbance values. The exception are the sharp ripples which disappear as soon as the absorption is turned on.

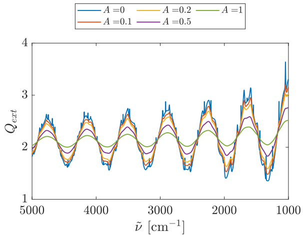

Figure 3.8: The extinction efficiency as a function of wavenumber for a circular scatterer for an increased absorbance, A. The real part refractive index of the scatterer is 1.8 and the imaginary part is found by use of Eq. 2.38. The radius of the disk is 10 μm.

The third part of the paper concerns the effect of the size of the numerical aperture on the extinction efficiency. Figure 3.9 shows that the extinction efficiency is reduced as the size of the numerical aperture increases. We further observe that both the wiggle and the ripple structure are preserved.

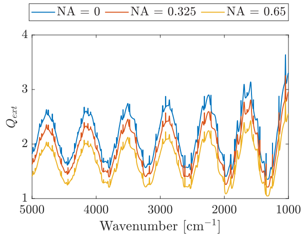

Figure 3.9: The extinction efficiency as a function of wavenumber for a circular scatterer for an increased numerical aperture, NA. The refractive index of the scatterer is 1.8 and the radius of the disk is 10 μm.

Chapter 4

Conclusion and Outlook

The overall goal for this thesis was to contribute to an increased understanding of scattering and absorption of radiation for scattering at small particles, using methods from the fields of semi-classical theory and electromagnetism.

In paper I, an exact ray model for a layered one-dimensional systems is presented, which is further extended to layered systems with oblique incidence in paper II. The ray models are motivated from ray models used in the field of semi-classics that has used ray models for achieving a better understanding of quantum systems. The absorption properties of the scatterers considered in this thesis have been incorporated by employing a complex index of refraction. While conventional ray models used for understanding absorption properties of solar cells that are employed in the short wavelength limit do not take into account phases, the thesis points out that the phase need to be taken into account when resonance structures are to be explained. Paper II shows further that the electromagnetic ray model for a plane wave scattering at a layered film requires to start all rays in the wave front and that resonant structures and absorption properties are solely governed by the component of the rays that is perpendicular to the layers. This is a remarkable result as it also shows that the enhancement related to the resonant structure of the layered film is only dependent of the component of the plane wave which is normal to the surface. Therefore all results of paper III, which deals with the optimization of the absorption properties by the resonant structure of a layered film with perpendicular incidence of light, are valid for oblique incidence, only adjusted to the component normal to the surface. Paper III considers several factors for enhancement of absorption of light due to resonances in optically thin layered solar cells. The layered film systems can be described exactly and both the refractive indices and thicknesses of layers were evaluated in order to optimize the absorption efficiency. It is shown that resonance in the non-absorptive layer is followed by an increased field inside the absorptive layer, hence an increased absorption is observed. The resulting absorption enhancement in the absorptive layer is expected each time a resonance appears and we expect as well that the absorption increases when anti-resonances appear. However, it could be shown that by optimizing the film thickness over a whole wavelength range, the resonant structure can be optimized for a whole wavelength range and absorption enhancement could be achieved globally. A similar effect could not be observed for coupling of resonances. The coupling of resonances did not show a global absorption enhancement, while absorption could be enhanced at certain wavelengths by coupling specific resonances. If the conclusions can be transferred to the coupling of resonances in spheres that are embedded in energy converting materials needs to be evaluated in future work.

While the three first papers deal with electromagnetic radiation in the visible region of light, paper IV considers scattering at small particles in the infrared region of the electromagnetic spectrum. Both the size of the scatterer and the wavelength range are in the micrometer range, i.e. the condition of scattering at small particles is fulfilled. We investigated how deformation of the scatterer affects the appearance of ripples in the extinction efficiency and found that deformation of the shape of a spherical scatterer results in suppression and disappearance of ripples, i.e. resonances, of quasi-spherical scatterers in IR-spectra. Further, classical ray dynamics was used to evaluate the scattering properties of the systems. We find that the appearance of chaos accelerates the disappearance of ripples compared with a non-chaotic scatterer. This has a direct implication for the scatter correction algorithms developed in the field of infrared microspectroscopy of single cells and tissues [42–44, 46, 47]. Biological cells are normally not perfect spheres and it is therefore not expected that their infrared spectra show ripples. The exact Mie theory exhibits ripples, which may yield modelling artefacts when exact Mie theory is use in the iterative algorithms developed for scattering corrections. For instance, the exact Mie theory for cylinders has been implemented in a scattering correction algorithm [47]. This algorithm is computationally expensive compared with scattering correction algorithms which use the approximation formulae developed by van de Hulst [18] to model scattering and absorption [42–47] of spherical and quasi-spherical scatterers. We recommend to use approximations that are developed along the same lines as the van de Hulst approximation for a sphere. Paper IV develops an approximation for a stadium-shaped scatterer. Similar approximations could be developed for other shapes and implemented in the Mie scatter correction algorithms. We show in this thesis that the approximations are sufficient for modelling the respective scatter and absorption signatures.

The work of this thesis was done in close collaboration with the thesis work of Eivind Seim. The paper [5] connected to the thesis work of Seim introduces chaotic scattering as a mechanism for enhancing absorption of light in surface-structured solar cells. The thesis at hand shows that the onset of chaos removes ripples from the extinction efficiency. Since the total number of resonances is expected to stay constant when the volume of the scatterer does not change, it would be interesting to investigate further how the absorption enhancement that is connected with the onset of chaos is related to the general field enhancement introduced through the distribution of resonances in the case of chaos.

Bibliography

[1] M.A. Brandsrud, E. Seim, R. Lukacs, A. Kohler, E.S. Marstein, E. Olsen, and R. Blümel. Exact ray theory for the calculation of the optical generation rate in optically thin solar cells. *Physica E: Low-dimensional Systems and Nanostructures*, 105:125–138, 2019.

[2] M.A. Brandsrud, R. Blümel, R. Lukacs, E. Seim, E.S. Marstein, E. Olsen, and A. Kohler. An exact ray model for oblique incident light on planar films. Submitted to *Physica E*, under review.

[3] M.A Brandsrud, R. Blümel, R. Lukacs, E. Seim, E.S. Marstein, E. Olsen, and A. Kohler. Resonance structures in layers of planar films. To be submitted to *Physica E.*

[4] M.A Brandsrud, R. Blümel, J. Solheim, and A. Kohler. Validity of mie theory for infrared spectroscopy of biological cells. Submitted to *Scientific Reports.*

[5] E. Seim, A. Kohler, R. Lukacs, M.A. Brandsrud, E.S. Marstein, E. Olsen, and R. Blümel. Chaos: A new mechanism for enhancing the optical generation rate in optically thin solar cells. *Chaos: An Interdisciplinary Journal of Nonlinear Science*, 29(9):093132, 2019.

[6] E. Seim, A. Kohler, R. Lukacs, M.A. Brandsrud, E.S. Marstein, E. Olsen, and R. Blümel. Wave chaos enhanced light-trapping in optically thin solar cells. *Journal not decided*, being written.

[7] M.A. Brandsrud, R. Lukacs, R. Blümel, E. Seim, E.S. Marstein, E. Olsen, and A. Kohler. Optimized solar cells based on changes in resonance structure as a function of the refractive index and the thickness. In *Physics, Simulation, and Photonic Engineering of Photovoltaic Devices VIII*, volume 10913, pages 109–130. International Society for Optics and Photonics, 2019.

[8] E. Seim, A. Kohler, R. Lukacs, M.A. Brandsrud, E.S. Marstein, E. Olsen, and R. Blümel. Chaos: a new mechanism for enhancing the optical generation rate in optically thin solar cells. In Alexandre Freundlich, Laurent Lombez, and Masakazu Sugiyama, editors, *Physics, Simulation, and Photonic Engineering*

of Photovoltaic Devices VIII, volume 10913, pages 213 – 221. International Society for Optics and Photonics, SPIE, 2019.

[9] M.A. Brandsrud, R. Blümel, J. Solheim, E.A. Magnussen, E. Seim, and A. Kohler. Does chaotic scattering affect the extinction efficiency in quasi-spherical scatterers? In *Biomedical Spectroscopy, Microscopy, and Imaging*, volume 11359, page 113590C. International Society for Optics and Photonics, 2020.

[10] M.A. Brandsrud, R. Lukacs, R. Blümel, E. Seim, E.S. Marstein, E. Olsen, and A. Kohler. Optimized solar cells based on changes in resonance structure as a function of the refractive index and the thickness. Presented at: *SPIE Photonics West* 2019-02-01–2019-02-06.

[11] E. Seim, A. Kohler, R. Lukacs, M.A. Brandsrud, E.S. Marstein, E. Olsen, and R. Blümel. Wave chaos: A new mechanism for enhancing the absorption cross section of optically thin solar cells. Presented at: *Norwegian Solar Cell Conference* 2019-05-20–2019-05-21.

[12] M.A. Brandsrud, R. Blümel, J. H. Solheim, E. Magnussen, E. Seim, and A. Kohler. Does chaotic scattering affect the extinction efficiency in quasi-spherical scatterers? Presented at: *SPIE Photonics Europe Digital Forum* 2020-04-06–2020-04-10.

[13] M.A. Brandsrud, A. Kohler, R. Blümel, E. Seim, and R. Lukacs. The importance of coupling between spheres for the efficiency enhancement of periodically structured solar cells. Presented at: *Norwegian Solar Cell Conference* 2017-05-09–2017-05-10.

[14] E. Seim, A. Kohler, R. Blümel, M.A. Brandsrud, and R. Lukacs. Light trapping by structured surfaces in the regular and chaotic scattering regime. Presented at: *Norwegian Solar Cell Conference* 2017-05-09–2017-05-10.

[15] E. Seim, A. Kohler, R. Lukacs, M.A. Brandsrud, E.S. Marstein, E. Olsen, and R. Blümel. Chaos: A new mechanism for enhancing the optical generation rate in thin-film solar cells. Presented at: *SPIE Photonics West* 2019-02-01–2019-02-06.

[16] M.A. Brandsrud, R. Lukacs, R. Blümel, E. Seim, E.S. Marstein, E. Olsen, and A. Kohler. Two-dimensional ray theory for optically thin solar cells. Presented at: *Norwegian Solar Cell Conference* 2019-05-20–2019-05-21.

[17] M.A. Brandsrud, E. Seim, J.H. Solheim, R. Blümel, and A. Kohler. Does chaotic scattering affect the extinction efficiency in quasi-spherical scatterers? Presented at: *BioSpecMLC* 2019-04-18–2019-08-21.

[18] Hendrik Christoffel Hulst and Hendrik C van de Hulst. *Light scattering by small particles*. Courier Corporation, 1981.

[19] Gustav Mie. Contribution to the optical properties of turbid media, in particular of colloidal suspensions of metals. *Ann. Phys.(Leipzig)*, 25:377–452, 1908.

[20] R Blümel, R Lukacs, B Zimmermann, M Bağcıoğlu, and A Kohler. Observation of mie ripples in the synchrotron fourier transform infrared spectra of spheroidal pollen grains. *JOSA A*, 35(10):1769–1779, 2018.

[21] Jonathan Grandidier, Dennis M Callahan, Jeremy N Munday, and Harry A Atwater. Light absorption enhancement in thin-film solar cells using whispering gallery modes in dielectric nanospheres. *Advanced Materials*, 23(10):1272–1276, 2011.

[22] Dimitrios Tzarouchis and Ari Sihvola. Light scattering by a dielectric sphere: perspectives on the mie resonances. *Applied Sciences*, 8(2):184, 2018.

[23] Jonathan Grandidier, Michael G Deceglie, Dennis M Callahan, and Harry A Atwater. Simulations of solar cell absorption enhancement using resonant modes of a nanosphere array. *Journal of Photonics for Energy*, 2(1):024502–1–024502–11, 2012.

[24] Marina Mariano, Francisco J. Rodríguez, Pablo Romero-Gomez, Gregory Kozyreff, and Jordi Martorell. Light coupling into the whispering gallery modes of a fiber array thin film solar cell for fixed partial sun tracking. *Scientific Reports*, 4(1), 2014.

[25] G. Kang, H. Park, D. Shin, S. Baek, M. Choi, D. H. Yu, K. Kim, and W. J. Padilla. Broadband light-trapping enhancement in an ultrathin film a-si absorber using whispering gallery modes and guided wave modes with dielectric surface-textured structures. *Adv Mater*, 25(18):2617–23, 2013.

[26] Erik Garnett and Peidong Yang. Light trapping in silicon nanowire solar cells. *Nano letters*, 10(3):1082–1087, 2010.

[27] A. Smets, K. Jäger, O. Isabella, R. van Swaaij, and M. Zeman. *Solar Energy: The Physics and Engineering of Photovoltaic Conversion, Technologies and Systems.* UIT Cambridge, 2016.

[28] Rolf Brendel. *Thin-film crystalline silicon solar cells: physics and technology.* John Wiley & Sons, 2011.

[29] Zachary C Holman, Miha Filipič, Antoine Descoeudres, Stefaan De Wolf, Franc Smole, Marko Topič, and Christophe Ballif. Infrared light management in high-efficiency silicon heterojunction and rear-passivated solar cells. *Journal of Applied Physics*, 113(1):013107, 2013.

[30] James R Nagel and Michael A Scarpulla. Enhanced absorption in optically thin solar cells by scattering from embedded dielectric nanoparticles. *Optics express*, 18(102):A139–A146, 2010.

[31] C. Battaglia, C. M. Hsu, K. Soderstrom, J. Escarre, F. J. Haug, M. Charriere, M. Boccard, M. Despeisse, D. T. L. Alexander, M. Cantoni, Y. Cui, and C. Ballif. Light trapping in solar cells: Can periodic beat random? *Acs Nano*, 6(3):2790–2797, 2012.

[32] KL Chopra, PD Paulson, and V Dutta. Thin-film solar cells: an overview. *Progress in Photovoltaics: Research and applications*, 12(2-3):69–92, 2004.

[33] Daniel Lockau, Tobias Sontheimer, Christiane Becker, Eveline Rudigier-Voigt, Frank Schmidt, and Bernd Rech. Nanophotonic light trapping in 3-dimensional thin-film silicon architectures. *Opt. Express*, 21(S1):A42–A52, Jan 2013.

[34] Lucio Claudio Andreani, Angelo Bozzola, Piotr Kowalczewski, Marco Liscidini, and Lisa Redorici. Silicon solar cells: toward the efficiency limits. *Advances in Physics: X*, 4(1):1548305, 2019.

[35] Peng Hui Wang, Regina-Elisabeth Nowak, Stefan Geißendörfer, Martin Vehse, Nies Reininghaus, Oleg Sergeev, Karsten von Maydell, Alexandre G Brolo, and Carsten Agert. Cost-effective nanostructured thin-film solar cell with enhanced absorption. *Applied Physics Letters*, 105(18):183106, 2014.

[36] Marina Mariano, Francisco J. Rodríguez, Pablo Romero-Gomez, Gregory Kozyreff, and Jordi Martorell. Light coupling into the whispering gallery modes of a fiber array thin film solar cell for fixed partial sun tracking. *Scientific Reports*, 4(1), 2014.

[37] M. Schmid. Review on light management by nanostructures in chalcopyrite solar cells. *Semiconductor Science and Technology*, 32(4), 2017.

[38] L. Brongersma Mark, Cui Yi, and Fan Shanhui. Light management for photovoltaics using high-index nanostructures. *Nature Materials*, 13(5):451, 2014.

[39] Brian Mohlenhoff, Melissa Romeo, Max Diem, and Bayden R Wood. Mie-type scattering and non-Beer-Lambert absorption behavior of human cells in infrared microspectroscopy. *Biophysical Journal*, 88(5):3635–3640, 2005.

[40] Paul Bassan, Hugh J Byrne, Franck Bonnier, Joe Lee, Paul Dumas, and Peter Gardner. Resonant Mie scattering in infrared spectroscopy of biological materials–understanding the ‘dispersion artefact’. *Analyst*, 134(8):1586–1593, 2009.

[41] Matthew J Baker, Júlio Trevisan, Paul Bassan, Rohit Bhargava, Holly J Butler, Konrad M Dorling, Peter R Fielden, Simon W Fogarty, Nigel J Fullwood, Kelly A Heys, et al. Using fourier transform ir spectroscopy to analyze biological materials. *Nature protocols*, 9(8):1771, 2014.

[42] A Kohler, J Sule-Suso, GD Sockalingum, M Tobin, F Bahrami, Y Yang, J Pijanka, P Dumas, M Cotte, DG Van Pittius, et al. Estimating and correcting Mie scattering in synchrotron-based microscopic Fourier transform infrared

spectra by extended multiplicative signal correction. *Applied Spectroscopy*, 62(3):259–266, 2008.

[43] Paul Bassan, Achim Kohler, Harald Martens, Joe Lee, Hugh J Byrne, Paul Dumas, Ehsan Gazi, Michael Brown, Noel Clarke, and Peter Gardner. Resonant Mie scattering (rmies) correction of infrared spectra from highly scattering biological samples. *Analyst*, 135(2):268–277, 2010.

[44] Tatiana Konevskikh, Rozalia Lukacs, Reinhold Blümel, Arkadi Ponossov, and Achim Kohler. Mie scatter corrections in single cell infrared microspectroscopy. *Faraday discussions*, 187:235–257, 2016.

[45] Tatiana Konevskikh, Rozalia Lukacs, and Achim Kohler. An improved algorithm for fast resonant mie scatter correction of infrared spectra of cells and tissues. *Journal of biophotonics*, 11(1):e201600307, 2018.

[46] Johanne H Solheim, Evgeniy Gunko, Dennis Petersen, Frederik Großerüschkamp, Klaus Gerwert, and Achim Kohler. An open-source code for mie extinction extended multiplicative signal correction for infrared microscopy spectra of cells and tissues. *Journal of biophotonics*, 12(8):e201800415, 2019.

[47] Ilia L. Rasskazov, Rajveer Singh, P. Scott Carney, and Rohit Bhargava. Extended multiplicative signal correction for infrared microspectroscopy of heterogeneous samples with cylindrical domains. *Applied spectroscopy*, 73(8):859–869, 2019.

[48] D.J. Griffiths. *Introduction to Electrodynamics*. Prentice Hall, 1999.

[49] Dario Cozza, Carmen M. Ruiz, David Duché, Sergio Giraldo, Edgardo Saucedo, Jean Jacques Simon, and Ludovic Escoubas. Optical modeling and optimizations of cu2znsnse4 solar cells using the modified transfer matrix method. *Optics Express*, 24(18):A1201–A1209, 2016.

[50] Luis L. Sánchez-Soto, Juan J. Monzón, Alberto G. Barriuso, and José F. Cariñena. The transfer matrix: A geometrical perspective. *Physics Reports*, 513(4):191–227, 2012.

[51] Urmita Sikder and Mohammad Asif Zaman. Optimization of multilayer antireflection coating for photovoltaic applications. *Optics & Laser Technology*, 79:88–94, 2016.

[52] Brynmor J Davis, P Scott Carney, and Rohit Bhargava. Theory of midinfrared absorption microspectroscopy: I. homogeneous samples. *Analytical chemistry*, 82(9):3474–3486, 2010.

[53] Rohit Bhargava. Infrared spectroscopic imaging: the next generation. *Applied spectroscopy*, 66(10):1091–1120, 2012.

[54] Rozalia Lukacs, Reinhold Blümel, B Zimmerman, M Bağcıoğlu, and Achim Kohler. Recovery of absorbance spectra of micrometer-sized biological and inanimate particles. *Analyst*, 140(9):3273–3284, 2015.

[55] Thomas Van Dijk, David Mayerich, P Scott Carney, and Rohit Bhargava. Recovery of absorption spectra from fourier transform infrared (ft-ir) microspectroscopic measurements of intact spheres. *Applied Spectroscopy*, 67(5):546–552, 2013.

[56] Ilia L. Rasskazov, Nicolas Spegazzini, P. Scott Carney, and Rohit Bhargava. Dielectric sphere clusters as a model to understand infrared spectroscopic imaging data recorded from complex samples. *Analytical Chemistry*, 89(20):10813–10818, 2017.

[57] Sebastian Berisha, Thomas van Dijk, Rohit Bhargava, P. Scott Carney, and David Mayerich. Bim-sim: Interactive simulation of broadband imaging using mie theory. *Frontiers in physics*, 5(5), 2017.

[58] Jonathan Grandidier, Raymond A Weitekamp, Michael G Deceglie, Dennis M Callahan, Corsin Battaglia, Colton R Bukowsky, Christophe Ballif, Robert H Grubbs, and Harry A Atwater. Solar cell efficiency enhancement via light trapping in printable resonant dielectric nanosphere arrays. *physica status solidi (a)*, 210(2):255–260, 2013.

[59] P. Spinelli and A. Polman. Light trapping in thin crystalline si solar cells using surface mie scatterers. *IEEE Journal of Photovoltaics*, 4(2):554–559, 2014.

[60] Brynmor J. Davis, P. Scott Carney, and Rohit Bhargava. Theory of mid-infrared absorption microspectroscopy: Ii. heterogeneous samples. *Analytical Chemistry*, 82(9):3487–3499, 2010.

[61] Eli Yablonovitch. Statistical ray optics. *JOSA*, 72(7):899–907, 1982.

[62] T Uematsu, M Ida, K Hane, Y Hayashi, and T Saitoh. A new light trapping structure for very-thin, high-efficiency silicon solar cells. In *Photovoltaic Specialists Conference, 1988., Conference Record of the Twentieth IEEE*, pages 792–795. IEEE, 1988.

[63] J. Gjessing and E. S. Marstein. An optical model for predicting the quantum efficiency of solar modules. *Ieee Journal of Photovoltaics*, 4(1):304–310, 2014.

[64] David Thorp and Stuart R. Wenham. Ray-tracing of arbitrary surface textures for light-trapping in thin silicon solar cells. *Solar Energy Materials and Solar Cells*, 48(1):295–301, 1997.

[65] J. Gjessing, A. S. Sudbo, and E. S. Marstein. Comparison of periodic light-trapping structures in thin crystalline silicon solar cells. *Journal of Applied Physics*, 110(3):8, 2011.

[66] Hakan Engin Tureci and A Douglas Stone. Deviation from snell's law for beams transmitted near the critical angle: application to microcavity lasers. *Optics letters*, 27(1):7–9, 2002.

[67] Eugene Hecht. *Optics*. Pearson, 2015.

[68] Grant R Fowles. *Introduction to modern optics*. Courier Corporation, 1989.

[69] Albert Einstein. Über einem die erzeugung und verwandlung des lichtes betreffenden heuristischen gesichtspunkt. *Annalen der physik*, 4, 1905.

[70] J.S. Townsend. *Quantum Physics: A Fundamental Approach to Modern Physics*. University Science Books, 2010.

[71] John J Hench and Zdenek Strakoš. The rcwa method-a case study with open questions and perspectives of algebraic computations. *Electronic Transactions on Numerical Analysis*, 31:331–357, 2008.

[72] Anders Bondeson, Thomas Rylander, and Pär Ingelström. *Computational electromagnetics*, volume 51. Springer Science & Business Media, 2005.

[73] Lumerical Inc. Lumerical. https://www.lumerical.com/products/fdtd., 2020.

[74] Sweden. COMSOL AB, Stockholm. COMSOL Multiphysics v. 5.4. www.comsol.com., 2020.

[75] R. G. Newton. *Scattering Theory of Waves and Particles*. Texts and Monographs in Physics. Springer-Verlag Berlin Heidelberg, New York, 1982.

[76] R. Blumel and U. Smilansky. A simple-model for chaotic scattering .2. quantum-mechanical theory. *Physica D*, 36(1-2):111–136, 1989.

[77] Felix Bloch. Über die quantenmechanik der elektronen in kristallgittern. *Zeitschrift für Physik*, 52(7):555–600, 1929.

[78] Jenő Sólyom. *Fundamentals of the Physics of Solids*, volume Volume 1: Structure and Dynamics. Springer-Verlag Berlin Heidelberg, 2007.

[79] Philip M. Morse and Herman Feshbach. *Methods of theoretical physics. Vol. I. II*, volume 22. New York, 1953.

[80] H. Kogelnik and T. Li. Laser beams and resonators. *Appl. Opt.*, 5(10):1550–1567, Oct 1966.

[81] V. E. Ferry, J. N. Munday, and H. A. Atwater. Design considerations for plasmonic photovoltaics. *Adv Mater*, 22(43):4794–808, 2010.

[82] Vivian E. Ferry, Albert Polman, and Harry A. Atwater. Modeling light trapping in nanostructured solar cells. *ACS Nano*, 5(12):10055–10064, 2011.

[83] Josefine K. Selj, David Young, and Sachit Grover. Optimization of the antireflection coating of thin epitaxial crystalline silicon solar cells. *Energy Procedia*, 77:248–252, 2015.

[84] D. Bouhafs, A. Moussi, A. Chikouche, and J. M. Ruiz. Design and simulation of antireflection coating systems for optoelectronic devices: Application to silicon solar cells. *Solar Energy Materials and Solar Cells*, 52(1):79–93, 1998.

[85] Tatiana Konevskikh, Arkadi Ponossov, Reinhold Blümel, Rozalia Lukacs, and Achim Kohler. Fringes in ftir spectroscopy revisited: understanding and modelling fringes in infrared spectroscopy of thin films. *Analyst*, 140(12):3969–3980, 2015.

[86] Paul A. Tipler and Gene Mosca. *Physics for scientists and engineers : with modern physics*. Freeman, New York, 6th ed. edition, 2008.

[87] Richard P. Feynman. *QED : the strange theory of light and matter*, volume [1] of *Alix G. Mautner memorial lectures*. Princeton University Press, Princeton, N.J, 1985.

[88] A Kohler, GHM Killesreiter, and R Blümel. Ray splitting in a class of chaotic triangular step billiards. *Physical Review E*, 56(3):2691, 1997.

[89] Reinhold Blümel, Jr T. M. Antonsen, Bertrand Georgeot, Edward Ott, and R. E. Prange. Ray splitting and quantum chaos. *Physical Review Letters*, 76(14):2476–2479, 1996.

[90] A Kohler and R Blümel. Test of semiclassical amplitudes for quantum ray-splitting systems. *Physical Review E*, 59(6):7228, 1999.

[91] Reinhold Blumel. *Advanced quantum mechanics: the classical-quantum connection*. Jones & Bartlett Publishers, 2011.

[92] Leonid A Bunimovich. On the ergodic properties of nowhere dispersing billiards. *Communications in Mathematical Physics*, 65(3):295–312, 1979.

[93] JH Jensen. Chaotic scattering of light by a dielectric cylinder. *JOSA A*, 10(6):1204–1208, 1993.

[94] Bruce J West and Ary L Goldberger. Physiology in fractal dimensions. *American Scientist*, 75(4):354–365, 1987.

[95] A Kohler, V Høst, and R Ofstad. Image analysis of particle dispersions in microscopy images of cryo-sectioned sausages. *Scanning*, 23(3):165–174, 2001.

[96] James Theiler. Estimating fractal dimension. *JOSA A*, 7(6):1055–1073, 1990.

[97] Angelo Vulpiani. *Chaos: from simple models to complex systems*, volume 17. World Scientific, 2010.

Appendix A

Paper I

Physica E: Low-dimensional Systems and Nanostructures 105 (2019) 125–138

Contents lists available at ScienceDirect

Physica E: Low-dimensional Systems and Nanostructures

journal homepage: www.elsevier.com/locate/physe

Exact ray theory for the calculation of the optical generation rate in optically thin solar cells

M.A. Brandsrud[a,1], E. Seim[a,*,1], R. Lukacs[a], A. Kohler[a], E.S. Marstein[c,d], E. Olsen[a], R. Blümel[b]

[a] Norwegian University of Life Sciences, Faculty of Science and Technology, Drøbakveien 31, 1432 Ås, Norway
[b] Wesleyan University, Department of Physics, 265 Church Street, Middletown, 06459, CT, USA
[c] Institute for Energy, Department of Solar Energy, Instituttveien 18, 2007, Kjeller, Norway
[d] University of Oslo, Department of Physics, Gunnar Randers vei 19, 2007, Kjeller, Norway

ABSTRACT

There is a profound duality between rays and waves. In fact, 70 years ago, in the context of quantum mechanics, Feynman showed that rays, properly equipped with phases and correctly summed, provide exact solutions of the quantum mechanical wave equation. In this paper, constructing explicit, exact ray solutions of the one-dimensional Helmholtz equation as a model for optically thin solar cells, we show that the ray-wave duality is also exact in the context of the electromagnetic wave equations. We introduce a complex index of refraction in order to include absorption. This have so far not been treated in the quantum ray-splitting literature. We show that inclusion of exact phases is mandatory and that a ray theory without phases may result in amplitude errors of up to 60%. We also show that in the case of multi-layered solar cells the correct summation order of rays is important. Providing support for the notion that rays provide the "skeleton" of electromagnetic waves, we perform a Fourier transform of the (experimentally measurable) solar cell reflection amplitude, which reveals the rays as peaks in the optical path length spectrum. An application of our exact ray theory to a silicon solar cell is also provided. Treating the one-dimensional case exactly, our paper lays the foundation for constructing exact ray theories for application to solar cell absorption cross section in two and three dimensions.

1. Introduction

In the quest for cheaper and cheaper solar cells, the solar cell community is continuously on the lookout for ways to decrease material costs. It is well known that in order to produce thinner solar cells with the same absorption properties as their thicker counterparts, absorption of optically thin solar cells may be enhanced by the use of nano-layering or by nano-structuring [1,2]. In order to investigate the nature of the absorption enhancement of optically thin solar cells by nano-layering or structuring, full wave calculations have been employed [3,4]. Shape resonances such as whispering gallery modes in spherical nanostructures have been considered as one possible cause for the absorption enhancement [5]. As another possible cause for the absorption enhancement, the coupling of modes in periodic nano-structures has been considered [6]. While absorption enhancement by nano-layering and nano-structuring has been demonstrated both experimentally [7] and numerically [8], the origins of the absorption enhancement mechanisms are not completely understood. Handy tools for investigating wave propagation and absorption properties of electromagnetic radiation in complex nano-structures are required for achieving a deeper understanding.

In the short wavelength limit, i.e., when the wavelength is small compared to the size of the structures used for absorption enhancement (e.g in micro-structured materials), ray tracing has been employed as an approach for investigating wave propagation and absorption enhancement in solar cells since the 1980s [9–11], when the optical performance of various solar cell designs was evaluated using ray-tracing techniques for the computation of the reflectance, transmittance and absorption. Since then, several numerical codes [12–19] and methods were developed, such as the Monte Carlo ray tracing method [20], the polarization ray tracing technique [21,22], the ray tracing combined with transfer matrix theory [23] and ray tracing combined with image processing [17]. Starting with one-dimensional modelling [24], these methods were later extended to two and three dimensions [25–28].

Ray tracing methods have been shown to explain the trapping of rays in solar cells. However, ray tracing fails to explain resonance effects in nano-structured materials such as whispering gallery modes. The reason for this deficiency is obvious: In order to describe resonance effects in layered thin films or films with nano-structures, the wave nature of the electromagnetic radiation needs to be taken into account, while the classical ray picture in electrodynamics is used to study the propagation of electromagnetic waves in terms of rays for cases where the wavelength of the electromagnetic radiation is short compared to changes of the media in which the electromagnetic radiation is

---

[*] Corresponding author.
E-mail address: e.seim.es@gmail.com (E. Seim).
[1] Contributions to the publication are considered equal.

https://doi.org/10.1016/j.physe.2018.08.018
Received 4 July 2018; Received in revised form 22 August 2018; Accepted 31 August 2018

propagating. This is not the case for optically thin solar cells with nano-layers and nano-structures, where the optical properties of the material change on a scale which is comparable to the wavelength of light.

In the field of quantum theory, a ray theory that takes into account the wave nature is readily available. In quantum mechanics, the ray-wave duality leads to the important field of semiclassical methods [29,30], which attempts to solve the quantum Schrödinger equation on the basis of classical particle trajectories. Using rays to solve the wave equations is tempting since it is usually much more straightforward to solve the ordinary differential equations determining the dynamics and geometry of rays, than solving the wave equations, which requires the solution of partial differential equations of continuous media. In order to obtain an exact result on the basis of rays, the rays need to be associated with phases; if for each ray the correct phases can be determined, the wave-ray duality is exact and the wave equations may be solved on the basis of rays. Since in this case, the ray theory solves the Helmholtz equation exactly, the ray theory can also correctly handle resonances caused by the wave nature of light. In addition, we introduced a complex refractive index in the ray theory allowing to treat absorption, which so far has not been introduced in quantum ray-splitting literature.

Only recently, in the field of solar cells, attempts that include phases have been reported [31].

In order to increase the understanding of the behavior of light in nano-layered and nano-structured solar cells, we present a ray theory that yields an exact description of the behavior of light in one-dimensional systems and allows to explain absorption enhancement due to nano-layering and nano-structuring.

In order to demonstrate the new theory, we study the optical generation rate of optically thin solar cells, modeled as vertical stacks of thin (absorbing) dielectric films, under normal incidence of light. In sections 2 and 3 we show that in this case, with or without a mirror behind the stack, Maxwell's vector equations are equivalent with a one-dimensional scalar Helmholtz equation, which we solve with our exact ray theory. We will use the scalar theory throughout this paper. In order to model absorption, we use a complex index of refraction. In section 4 we introduce a hierarchical scheme of summing rays as a convenient method of keeping track of rays bouncing off of and transmitting through different dielectric layers of the solar cell. We also show that including only the simplest rays already yields an excellent approximation of the exact solution of the wave equation. In Section 5 and 6 we show that both summation order and phases are important in our ray theory. We show in section 7 that the signature of the most important rays appears as peaks in the Fourier transform of the reflection amplitude of a flat solar cell. In section 8 we demonstrate how our ray theory can be used for materials with practical importance within the solar cell field. In Section 9 we discuss our results; we summarize and conclude our paper in Section 10.

Our method can be extended for use in two and three dimensions. The theory describes the optical properties of a device and is based on the imperative that phases need to be included to arrive at a useful ray theory.

2. The scalar wave model for a one-dimensional film

In order to develop a ray theory for studying absorption enhancement in optically thin solar cells, we consider one-dimensional systems in which electromagnetic radiation is propagating towards a region consisting of one or more parallel layers of different materials. In this section we will introduce one-dimensional model system that we will use for illustration throughout the paper. In all cases, we consider the propagation direction as normal to the surfaces of the materials. Since we want to develop model systems for optically thin solar cells, we study cases where one or more of the layers consist of energy-converting materials. We describe the incoming electromagnetic wave by a plane wave. Since we consider only normal incidence, the system can be fully described by a scalar wave function, ψ [32].

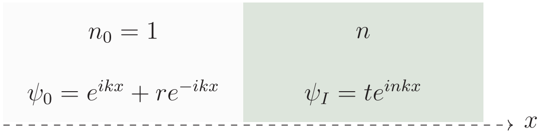

Fig. 1. Schematic description of a half-space problem, where the left half space is vacuum ($n_0 = 1$) and the right half space is material. A plane wave is propagating towards a boundary between vacuum ($n_0 = 1$) and an arbitrary dielectric material with refractive index $n = n_r + in_i$. The imaginary part n_i of the refractive index is set to zero if the dielectric material is non-absorptive. The waves are propagating in x-direction, normal to the surface. ψ_0 and ψ_I are the scalar wave functions in the two regions, $k = 2\pi/\lambda$ is the angular wave number in vacuum, and λ is the vacuum wavelength. r and t are here the reflection and transmission amplitudes for the plane wave in this system; the amplitude of the incoming plane wave is set to one.

The first and simplest system we will investigate is a system consisting of a single film. By evaluating the scalar wave function for one single film, where the material of the film is an energy-converting material with complex refractive index $n = n_r + in_i$, we can understand the occurrence of interference maxima and investigate how these are related to the enhancement of the absorption cross section. The interference maxima are resonances akin to the whispering gallery resonances that occur in spherical particles used for nano-structuring solar cells, which lead to an enhancement of the electric field and the absorption properties of the solar cells.

The reflection probability R at the boundary between two materials is calculated as $R_b = |r|^2$, where r is the amplitude of the reflected wave (see Fig. 1). By requiring a continuous scalar wave function and a continuous first derivative of the scalar wave function at the boundary, we can derive an expression for R_b for the case illustrated in Fig. 2 [33], i.e.,

$$R_b = \frac{(1 - n_r)^2 + n_i^2}{(1 + n_r)^2 + n_i^2}. \tag{2.1}$$

The probability for transmission at the boundary for the system in Fig. 1, T_b, is given by $T_b = |t|^2 = 1 - R_b$.

We start by evaluating two simple systems, namely a single film and a single film with a mirror, as shown in Fig. 2a and b, respectively.

We require that the wave function and its first derivative are continuous at the boundaries and that the wave function is zero at the surface of the mirror. We derive the transmission probability $T = |t|^2$ and the reflection probability $R = |r|^2$ for the systems, where t and r are the amplitudes of the transmitted and reflected plane waves, respectively. For the single-film case, shown in Fig. 2a, the reflection and transmission amplitudes are given by

$$r = \frac{i\sin(nka)[(nk)^2 - k^2]}{2nk^2\cos(nka) - i\sin(nka)[(nk)^2 + k^2)]}, \tag{2.2a}$$

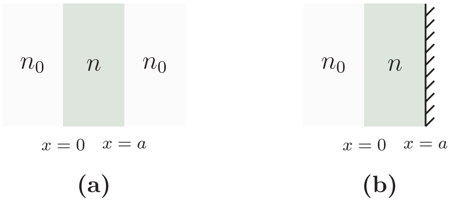

Fig. 2. Two simple single film systems. (a) A single film in vacuum and (b) a single film in vacuum with a mirror. The refractive index of the film is given by $n = n_r + in_i$. $n_0 = 1$ is the refractive index of vacuum, a is the thickness of the film.

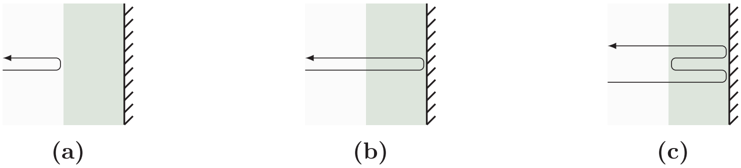

Fig. 3. Three types of rays encountered in a film-plus-mirror system. (a) The ray directly reflects from the surface. This ray does not contribute to the absorption cross section. (b) The simplest ray that contributes to the absorption cross section. The ray enters into the film is reflected from the mirror and exits. (c) A more complex ray contributing to the absorption cross section. This ray has two reflections from the mirror and one internal reflection from the film-vacuum boundary.

$$t = \frac{2nk^2 e^{-2ika}}{2nk^2\cos(nka) - i\sin(nka)[(nk)^2 + k^2]}, \tag{2.2b}$$

where $k = 2\pi/\lambda$ is the angular wave number in vacuum, λ is the vacuum wavelength, nk is the angular wave number in the film, n is the complex refractive index of the film, and a is the thickness of the film. If the film is non-absorptive, i.e., n is real, it is straightforward to show that Eqs. 2.2a and 2.2b lead to $R + T = |r|^2 + |t|^2 = 1$, i.e., all electromagnetic radiation entering the film is eventually leaving the film again.

In the case a mirror is present (see Fig. 2b), there is no transmission. Therefore the system can be characterized by the reflection amplitude alone, which in this case is given by

$$r = \frac{n\cos(nka) + i\sin(nka)}{n\cos(nka) - i\sin(nka)}. \tag{2.3}$$

If the film is non-absorptive, i.e., n is real, it follows immediately from Eq. (2.3) that $R = |r|^2 = 1$, i.e. again all electromagnetic radiation entering the film is eventually leaving the film.

We define the *absorption cross section* as the fraction of light that is absorbed and denote it by σ. In the two cases shown in Fig. 2, the film with and without the mirror, the expressions for σ are respectively given by

$$\sigma(\lambda) = 1 - R(\lambda), \tag{2.4a}$$

$$\sigma(\lambda) = 1 - (R(\lambda) + T(\lambda)). \tag{2.4b}$$

According to the definition of σ as the fraction of absorbed light, i.e., light that does not exit the solar cell, in addition to absorbed light that leads to beneficial photo current, σ contains all parasitic absorption processes, for instance the two-photon process [34,35].

The same procedure can be applied for film-systems without mirror. For a non-absorptive film, σ is zero. For the rest of this paper, we will focus exclusively on cases where a mirror is placed behind the film/films in order to model a solar cell system.

In an equivalent solar cell system the absorption cross section is the total amount of absorbed energy absorbed at a given wavelength λ. This is the maximal amount of energy that can potentially create electron-hole pairs at a given wavelength λ. Under normal operating conditions, if the total amount of absorbed energy is increasing, the number of the photo-electrons will also increase and this will lead to enhanced efficiency. When the absorption cross section is weighted by the AM1.5 solar spectrum, we obtain the *optical generation rate*, G_{opt}. The optical generation rate G_{opt} has been introduced to the solar cell field by Ferry et al. [36]. Since then it is used as the measure of the optical performance of various solar cell designs. In our case G_{opt} is given by

$$G_{opt}(\lambda) = \Gamma_{solar}(\lambda)\sigma(\lambda)A, \tag{2.5}$$

where $\Gamma_{solar}(\lambda)$ is the spectral weighting term and A is the surface area of the solar cell. In this paper we will evaluate $\sigma(\lambda)$ for our systems in order to get a fundamental understanding of how the optical resonances in the energy converting film increase the total amount of absorbed energy.

For a single film, or a stack of films, with different refractive indices, it is possible to analytically derive a formula for the absorption cross section from the probability current. This depends only on the absolute square of the scalar wave function inside of the film(s). To be specific, we consider the case of an array of films, described by a space-dependent complex refractive index $n(x) = n_r(x) + in_i(x)$. The complex refractive index $n(x)$ when the optical or the absorption properties of a material change. When a stack of films is illuminated from the front and backed by a mirror, the absorption cross section is given by

$$\sigma = 2k\int_0^w n_i(x)n_r(x)|\psi(x)|^2\,dx, \tag{2.6}$$

where the stack of films is assumed to be located in the interval $0 \le x \le w$ and the mirror is located at $x = w$. The details of the derivation are presented in Appendix B. Since for a single film with mirror both r and $\psi(x)$ are known explicitly (see Eq. (2.3) and Appendix B), it is straightforward in this case to show by explicit calculations that Eq. (2.6) holds (see Appendix C).

3. Exact ray theory for single films

In this section, we will show that it is possible to estimate the absorption cross section by considering and summing rays. Three examples of simple rays are shown in Fig. 3.

In order to calculate the total reflection amplitude r we need to sum up all possible rays in the film [37,38]. Every ray contributes to the total reflection amplitude and thereby to the absorption cross section with an amplitude and a phase. The reflection and transmission amplitudes of the ray depending on the side of the boundary the ray is hitting. Denoting by r_l and t_l the reflection and transmission amplitudes, respectively, for a ray originating from outside in the vacuum and transmitting into the film, and by r_r and t_r the reflection and transmission amplitudes, respectively, for a ray originating from inside of the film and traveling towards the vacuum, we obtain (see Appendix A):

$$r_l = \frac{1-n}{1+n}, \tag{3.1}$$

$$t_l = \frac{2}{1+n}, \tag{3.2}$$

$$r_r = -\left(\frac{1-n}{1+n}\right), \tag{3.3}$$

$$t_r = \frac{2n}{1+n}. \tag{3.4}$$

It is important to note that the amplitudes, eq. (3.1)–(3.4), remains exact if the refractive index, n, is complex. We hereby established a ray model that is able to describe absorption of electromagnetic radiation. In addition to the amplitudes, we need to include the phase that the ray collects when it transverses the film, i.e., each time it travels from the vacuum-film interface to the mirror or from the mirror to the interface. This phase collected when traveling through the distance a is given by e^{inka}. Further we have to include the phase $e^{i\pi}$ [39] caused by the mirror each time a ray is reflected by the mirror.

To introduce our procedure, we state the contribution to r from the three selected rays illustrated in Fig. 3. The result is

$$r = r_l + t_l e^{inka}e^{i\pi}e^{inka}t_r + t_l e^{inka}e^{i\pi}e^{inka}r_r e^{inka}e^{i\pi}e^{inka}t_r, \tag{3.5}$$

where the first term is the contribution of the ray illustrated in Fig. 3a,

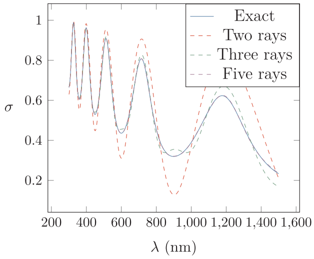

Fig. 4. Absorption cross section σ as a function of the wavelength λ for the system given in Fig. 2a. The blue line is calculated analytically with Eq. (2.3) and the ray model with Eq. (3.6) is used when the two (red dashed), three (green dashed line) and five (purple dashed line) simplest rays are included. The refractive index of the film in this system is 1.8 + 0.05i and the thickness is 500 nm. The wavelength ranges from 300 nm to 1500 nm. (For interpretation of the references to color in this figure legend, the reader is referred to the Web version of this article.)

the second term is the contribution from the ray illustrated in Fig. 3b, and the third term is the contribution from the ray illustrated in Fig. 3c. If we include all contributing rays, their total, exact contribution to r is given by

$$r = r_l + t_l t_r e^{i\pi} e^{2inka} \sum_{\nu=0}^{\infty} (e^{i\pi} r_r e^{2inka})^{\nu}. \tag{3.6}$$

By inserting the expressions for r_l, t_l, r_r and t_r, and with the help of the elementary summation formula for the geometric series, it turns out that r in Eq. (3.6) is equal to r in Eq. (2.3).

Whenever an energy-converting film is present, i.e., whenever $n_r > 1$, we have $|r_r| < 1$ and the expression for r in Eq. (3.6) converges absolutely. Fig. 4 shows σ for the single film system with a mirror behind. The solid line is the exact expression for σ, the dashed line is σ found by the ray model where only a few simple rays are included.

As shown in Fig. 4 very fast convergence is observed even if only a few of the shortest rays are included. The figure also shows that considering only the five simplest rays in the system, the analytically calculated absorption cross section can already be predicted near perfectly. Fig. 4 illustrates another important aspect, namely that our ray theory can describe absorption of electromagnetic radiation by including a complex refractive index.

4. Exact ray theory for multilayered films: hierarchical summation scheme

When a system has more than one layer, each ray, upon encountering a vacuum-film boundary or a boundary between two layers, will split into two rays, a reflected ray and a transmitted ray (except the mirror in our model system). This is called ray splitting [40–42]. With increasing geometric length, tracking splitting rays becomes an ever more complex task since each split ray, subsequently, will undergo splittings itself. Thus, the number of rays in the system increases exponentially with the number of splittings, i.e., with the geometric lengths of the rays.

In order to keep track of all the rays, we present a convenient bookkeeping system, called symbolic dynamics [43]. This system is widely used in the fields of non-linear dynamics and chaos. This symbolic language consists of an alphabet and simple grammatical rules which determine the path of a ray unambiguously. The symbolic dynamics of two film layers with a backside mirror (Fig. 5) has an alphabet that consists of the three letters (symbols) a, b, c. Each of the letters corresponds to a boundary where the ray will either split or simply reflect. The grammatical rules are:

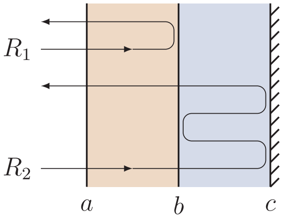

Fig. 5. Two rays, R_1 and R_2, in a system with a mirror and two film layers. R_1 and R_2 are labeled by the symbolic dynamics *aba* and *abcbcba*, respectively.

1. A word must start with the letter a. If the ray exits the system, the word must also end in the letter a.
2. Skipping letters is not allowed, i.e., unless the trajectory terminates, the letter a is always followed by the letter b, the letter b is always followed by letters a or c and the letter c is always followed by the letter b, indicating reflection off of the mirror.

Illustrating these rules, we construct the two sample rays R_1 and R_2 shown in Fig. 5. R_1 transmits at a and reflects at b before transmitting out of the system through a. Thus, the word labeling R_1 is *aba*. We may be tempted to label R_2 as *aca*, but this violates rule 2. The correct word, *abcbcba*, contains information about every boundary crossed.

To define the symbolic dynamics of systems with more films, we simply use a larger alphabet. If there is no mirror, i.e., transmission through the system is possible, rule 1 would allow words to end with the last letter of the alphabet.

The graph in Fig. 6 generates the part of the vocabulary that contains words with seven or less symbols for the two-film system in Fig. 5. The incoming ray will first hit node a. All a nodes are colored blue to emphasize that they mark the end of a word. The edges that are connecting the nodes are either black or red. A black edge signifies a ray traveling to the right and a red edge signifies a ray traveling to the left. A word can easily be read off Fig. 6 by writing down the successive letters starting from the first node to another blue node.

The computer implementation of this hierarchical summation scheme uses the number of ray splittings at the boundaries as a measure of the run time, not the number of rays explicitly. More splitting events generate exponentially more rays to approximate the reflectance R. About seven such splittings are needed to approximate the analytic expression reasonably well as seen in Fig. 7. These seven splittings generate a set of 64 contributing rays. Allowing more splittings, thus adding more rays, improves the approximation further.

If photons were classical, Newtonian particles, ray-splitting would not occur. The only ray allowed according to Newtonian mechanics would be the ray labeled *abcba*. Accordingly, this ray is also known as the “Newtonian ray” [44]. All other rays show ray splitting [40–42]. Since ray splitting is not allowed according to Newtonian mechanics, these split rays are called “non-Newtonian” [44]. Non-Newtonian rays have been proven theoretically [40,41,45,46] and experimentally [42,47–49].

To assess the importance of the (Newtonian forbidden) non-Newtonian rays compared with the (Newtonian allowed) non-split, Newtonian ray, we also show the contribution of the Newtonian ray to $R(\lambda)$ in Fig. 7. We see that the Newtonian ray alone, although in the vicinity of the exact result for $R(\lambda)$, produces a result with very poor accuracy. Conversely, Fig. 7 shows that the contribution of the split, non-Newtonian rays is substantial, and that only the added contribution of the split, non-Newtonian rays produces accurate results.

5. Importance of the correct summation order

As discussed in the previous section, in the case of a single film, the sum in Eq. (3.6) for the reflection amplitude r is absolutely convergent,

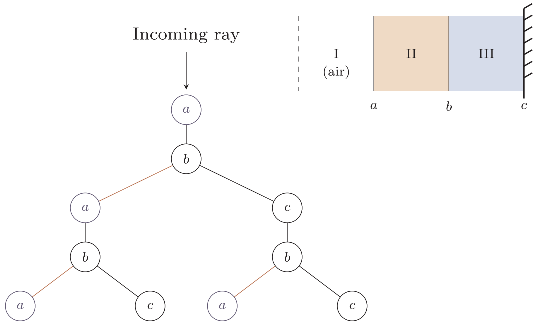

Fig. 6. Schematic of the ray tree algorithm. The interfaces between the materials II and III are labeled *a* and *b*, respectively, and the mirror is labeled *c*. An incoming ray always hits *a* first. At *a* the ray will split in two. One ray is reflected (ray labeled '*a*') and the other will travel to the right (black edge) towards *b*. At *b* it can either go to the left (red edge) and exit, or continue to travel to the right to the mirror, *c*. The inset shows the two-layered system that is considered in this example. (For interpretation of the references to color in this figure legend, the reader is referred to the Web version of this article.)

and the summation order of the rays is irrelevant. Any summation scheme, as long as all rays are included, will yield the exact value for *r*. However, if there is more than one film, the order of summation does matter. Let

$$r = \sum_{j=0}^{\infty} A_j \tag{5.1}$$

be the ray representation of the reflection amplitude. If Eq. (5.1) were a finite sum, the order in which we sum the rays would clearly not matter. However, this is not the case with infinite sums, such as Eq. (5.1). Only if

$$\sum_{j=0}^{\infty} |A_j| < \infty \tag{5.2}$$

is the summation order of the terms in Eq. (5.1) irrelevant and always yields the correct reflection amplitude. In this case, as discussed in the previous section, we call the sum in Eq. (5.1) absolutely convergent. If, however,

$$\sum_{j=0}^{\infty} |A_j| = \infty, \tag{5.3}$$

it was shown by Riemann [50] that, depending on the summation order of the terms in Eq. (5.1), the infinite sum in Eq. (5.1) can be made to have any prescribed value. This is known as Riemann's Rearrangement Theorem [51]. In this case the sum in Eq. (5.1) is called conditionally convergent, and it is necessary to sum it in some prescribed way in order to obtain correct results.

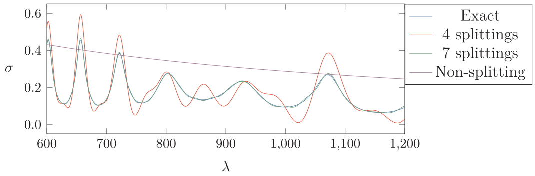

Fig. 7. Absorption cross section σ as a function of the wavelength λ, including various numbers of split rays, and the shortest non-splitting ray. The hierarchical summation scheme approximates the analytical result for the film with two layers (Fig. 5) almost perfectly with only 64 rays or, equivalently, seven splittings. Including more rays yields an even more accurate result. The non-splitting ray approximately defines the lower envelope of the exact result.

In Appendix D we show that for our two-film system, for a large range of dielectric constants, Eq. (5.3) holds, i.e., in these cases our ray sum in Eq. (5.1) is only conditionally convergent. The correct summation scheme in these cases is to sum the rays in the order of increasing path length, where the path length of the ray may either be its geometric length or its optical path length. This summation scheme is not dictated by mathematics, which does not help us beyond the fact of stating that in the case of conditional convergence different summation prescriptions produce different results [51], but interestingly is dictated by the physical situation. For actual realizations of solar cells there is always some absorption present, which naturally suppresses the importance of longer rays. Therefore, ordering the rays according to their importance for *r* means ordering them according to their path lengths.

We can numerically corroborate the importance of the summation order by testing for absolute convergence with the hierarchical summation scheme. We take the absolute value of each term, which is equivalent to removing the phase completely. Fig. 8 compares the absolute value of the difference between the analytical reflection probability R_A and the reflection probability R_{HSS}, computed according to the hierarchical summation scheme. Without the absolute value of each term, i.e., when phases are included, convergence is reached after a small number of splittings. Without phases, we see that the difference $|R_A - R_{HSS}|$ is diverging, numerically corroborating that the sum over rays is not absolutely convergent.

6. Importance of phases in the ray theory

In this section we emphasize the importance of phases, even in the case of absorption (which was not included in Sec. 5), by computing absorption cross sections, with and without phases included, using as an example the single film with mirror introduced in Secs. 2 and 3. Comparing the two cases, we show that the ray theory without phases produces results that contain unacceptably large errors.

In order to demonstrate the importance of the phases, we introduce the following ray model where phases are not included. Without phases, instead of being associated with an amplitude, every ray is associated with an intensity. We set the incoming intensity of the ray to I_0. The simplest ray model we consider retains only the directly reflected ray as illustrated in Fig. 3a. We call this ray *the ray of zero length*, since it does not enter the energy-converting film, and its optical path length inside of the film, therefore, is zero. We further assume that the probability given in Eq. (2.1) describes the amount of light reflected at the surface of the film. The rest of the light is absorbed in the film. In this case the absorption depends on the wavelength of the incoming light only through the wave number, *k*, as long as the refractive index of the film is constant for all wavelengths. When we evaluate rays that travel inside of the film, the intensity assigned to a particular ray decreases via Beer-Lambert's Law, and is expressed as

$$I = I_0 e^{-n_i k x}, \tag{6.1}$$

where I_0 is the incoming intensity of the light, which we set to 1, x is the distance travelled in the film [39,52], k is the wave number and n_i is the imaginary part of the refractive index of the film.

To find the amount of absorbed light, i.e., the absorption cross section, σ, we need to sum the contributions to the absorption from each ray. When the ray hit a boundary, a part of it will reflect and a part of it will transmit. The probability for reflection at a boundary, R_b is given in eq. (2.1) and the probability of transmission is $T_b = 1 - R_b$. Evaluating σ due to the rays in Fig. 3a and b, the result is

$$\sigma = 1 - \left(R_b + T_b^2 e^{-2n_i k a}\right), \tag{6.2}$$

where *a* is the width of the film. The expression inside the brackets is the sum of the intensities of these two reflected rays. When all possible rays are included (infinitely many), σ is given by

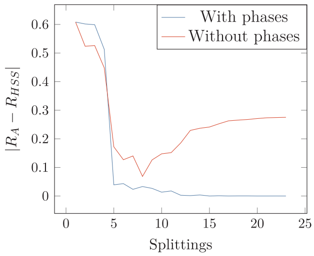

Fig. 8. Absolute value of the difference between the reflection calculated by the analytical expression, R_A, and the hierarchical summation scheme, R_{HSS}, is converging when the phase of the rays is included. The same calculation will diverge if it is done without phases.

$$\sigma = 1 - \left(R_b + \frac{T_b^2 e^{-2n_i ka}}{1 - R_b e^{-2n_i ka}} \right). \tag{6.3}$$

We arrive at this formula by summing up all possible rays and by using the elementary summation formula for the geometric series.

Fig. 9 shows a comparison of the absorption cross section evaluated with ray models that include and neglect phases, respectively. For the case in which phases are neglected, we present three different scenarios. (1) The horizontal blue line in Fig. 9 is σ computed by including only the ray of zero length (see Fig. 3a). (2) The red line in Fig. 9 is σ computed on the basis of the two rays in Fig. 3a and b (Eq. (6.2)). (3) The green line in Fig. 9 is σ obtained by including infinitely many rays (Eq. (6.3)). Contrasting these three cases, computed without including phases, we also show the exact result for σ in Fig. 9, where we have included infinitely many rays *with phases* (purple line). The exact result, with phases included, shows oscillations (purple line), which are not captured by either of the three cases that do not include phases. As seen in Fig. 9, σ without phases is monotonically decreasing when the wavelength increases (green and red lines), without any oscillations according to Eq. (6.1). The result without phases included underestimates the exact result with phases included, and, according to Fig. 9, the relative error can exceed 60% in the wavelength region shown in Fig. 9. In the context of absorption cross sections of typical solar cells, an error of this magnitude is not acceptable. We conclude that for accurate modelling of solar-cell efficiencies in terms of rays, inclusion of phases is absolutely essential. Any ray theory, whether applied in the electromagnetic, acoustic, or quantum domains, is exact only if phases are included. Neglecting phases may have serious consequences, ranging from incorrect results to divergent results as demonstrated in Fig. 8 of Sec. 5.

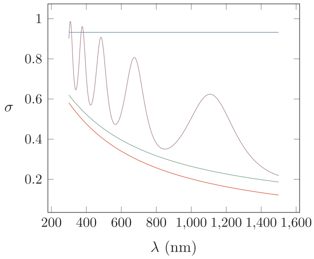

Fig. 9. Absorption cross section, σ, as a function of wavelength,λ, in the range $300\,\text{nm} \le \lambda \le 1500\,\text{nm}$, for a single film with refractive index $n = 1.8 + 0.05i$, a thickness of 500 nm, and a mirror on the backside of the film. The blue line is σ, including only the reflected ray of zeroth length (see Fig. 3a). The red line is σ, including only the two simplest rays (see Fig. 3a and b, calculated with Eq. (6.2). The green line is σ, including infinitely many rays without phases, calculated with Eq. (6.3), and the purple line is σ, including infinitely many rays with phases. The purple line is calculated with the ray theory presented in Sec. 3. (For interpretation of the references to color in this figure legend, the reader is referred to the Web version of this article.)

7. Signatures of rays in the Fourier transform of the reflection amplitude

A Fourier transform of the reflection amplitude $r(k)$ allows us to reveal the signatures of the rays whose combined contributions result in the exact functional form of $r(k)$. If the entire spectral range is accessible to us, we obtain this information in the form of the *length spectrum*

$$\mathscr{F}(L) = \frac{1}{2\pi} \int_{-\infty}^{\infty} r(k) e^{-iLk}\, dk. \tag{7.1}$$

To illustrate, let us use the exact, explicit formula 3.6 for the reflection amplitude r of a single film with mirror. We obtain

$$\mathscr{F}(L) = r_l \delta(L) + \frac{t_l t_r}{r_r} \sum_{\nu=1}^{\infty} e^{i\nu\pi} r_r^{\nu} \delta(L - 2na\nu), \tag{7.2}$$

where $\delta(x)$ is Dirac's delta function. We see that $\mathscr{F}(L)$ is a series of sharp peaks at integer multiples of the optical path length $2na$, where each peak corresponds to the optical path length of a certain ray inside of the film. Thus, every single ray that contributes to Eq. (3.6) is represented as a sharp peak in $\mathscr{F}(L)$. This even includes the "ray of zero length", which is the ray that reflects with amplitude r_l off of the front surface of the film. Since this ray does not enter the film, its optical path length in $\mathscr{F}(L)$, naturally, is zero. The weights of the δ terms in Eq. (7.2) correspond to the amplitudes that the rays pick up when crossing a boundary or being reflected from a boundary. Thus, the length spectrum of r contains the complete optical information of the system under consideration. This is not surprising, since the Fourier transform in Eq. (7.1), a function in L space, is complementary to the ray representation, Eq. (3.6), of r in k space. Unfortunately, ray information can be extracted so cleanly from $r(k)$ with Eq. (7.1) only if the integration range is infinite. In actual applications in solar cells, we are restricted to a finite spectral range, which turns the exact length spectrum $\mathscr{F}(L)$ into an approximate length spectrum

$$\widetilde{\mathscr{F}}(L) = \frac{1}{2\pi} \int_{k_1}^{k_2} r(k) e^{-ikL}\, dk. \tag{7.3}$$

Applied to our single-film example, this evaluates to

$$\begin{aligned} \widetilde{\mathscr{F}}(L) = {} & \tfrac{r_l}{2\pi} \exp\left[-i\left(\tfrac{k_1 + k_2}{2}\right)L\right](k_2 - k_1)\, \mathrm{sinc}\left[\tfrac{L}{2}(k_2 - k_1)\right] \\ & + \tfrac{t_l t_r}{2\pi r_r}(k_2 - k_1) \textstyle\sum_{\nu=1}^{\infty} e^{i\nu\pi} r_r^{\nu} \exp\left[i\left(\tfrac{2na\nu - L}{2}\right)(k_1 + k_2)\right] \\ & \times \mathrm{sinc}\left[\left(\tfrac{2na\nu - L}{2}\right)(k_2 - k_1)\right], \end{aligned} \tag{7.4}$$

where $\mathrm{sinc}(x) = \sin(x)/x$ is the "sinc-function". We see that in the case of a finite spectral range the sharp δ-function peaks are replaced by smooth, oscillatory sinc-functions, which produces "Gibbs ringing" [53] in $\widetilde{\mathscr{F}}(L)$ that produces copious "extra peaks" in $\widetilde{\mathscr{F}}(L)$ and may thus obscure the peaks that correspond to rays. The ringing may be reduced by the use of a window function [54], i.e., a function $w(k)$ that softly "switches on" and "switches off" the integration at k_1 and k_2 according to $w(k_1) = w(k_2) = 0$, $w'(k_1) = w'(k_2) = 0$, $w''(k_1)/k_1^2 \ll 1$, $w''(k_2)/k_2^2 \ll 1$.

As an illustrative example we present the Fourier transform of the reflection amplitude of a three-layered film with constant, non-dispersive indices of refraction, $n_1 = 1.5$, $n_2 = 1.9$, $n_3 = 2.3$, and film widths $a_1 = 500\,\text{nm}$, $a_2 = 2000\,\text{nm}$, and $a_3 = 1000\,\text{nm}$, respectively. In this example we chose $k_1 = 2\pi/1200\,\text{nm}$ and $k_2 = 2\pi/5\,\text{nm}$. We used the window function

$$w(m) = 1 - \left(\frac{m - \frac{N-1}{2}}{\frac{N-1}{2}} \right)^2, \tag{7.5}$$

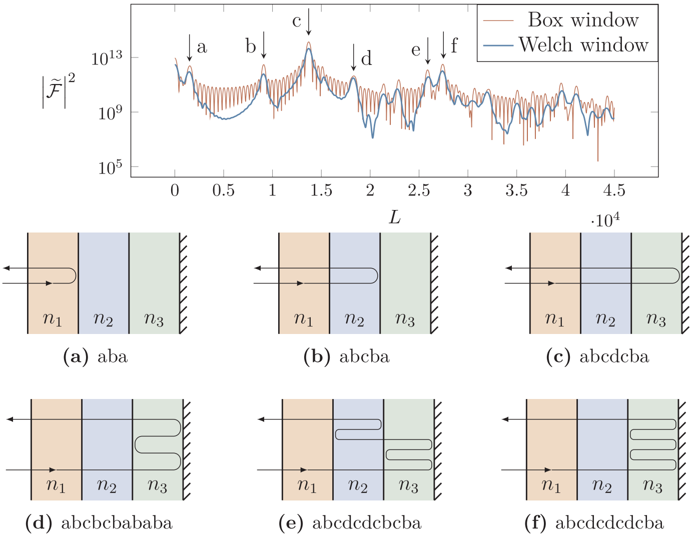

(a) aba **(b)** abcba **(c)** abcdcba

(d) abcbcbababa **(e)** abcdcdcbcba **(f)** abcdcdcdcba

Fig. 10. Top frame: Finite-range Fourier transform (approximate length spectrum) $\widetilde{\mathcal{F}}(L)$ of the exact $r(k)$ of a three-layer film system with mirror with parameters as specified in the text. $\widetilde{\mathcal{F}}(L)$ shows distinct peaks, labeled (a)–(f). The rays corresponding to these peaks, including their symbolic-dynamics labels, are illustrated in the six frames (a)–(f), below the top frame, respectively. These six rays make the most important contributions in the ray-representation of $r(k)$ of this system.

called the Welch window function. Here m is an integer variable that corresponds to the grid used in the calculations. If we are using M different values of k, m takes the values $0 \le m \le M-1$. Using no window (box window) shows Gibbs phenomenon very clearly. The resulting length spectrum of this three-layer system is displayed in Fig. 10. In general, a larger Fourier peak indicates a more important component in a Fourier series. Hence, the heights of the peaks in Fig. 10 directly relate to the importance of the contributions of the corresponding rays to r. The peaks labeled a-f in Fig. 10 correspond to the rays illustrated in (a) - (f) of Fig. 10, respectively. The six tallest peaks correspond to rays labeled by the words *aba*, *abcba*, *abcdcba*, *abcbcbababa*, *abcdcdcbcba*, and *abcdcdcdcdcba*, respectively. The peaks in Fig. 10 are located at the optical path lengths of the rays, i.e., they are located at the linear combinations $2\nu_1 n_1 a_1 + 2\nu_2 n_2 a_2 + 2\nu_3 n_3 a_3$, where ν_j, n_j, and a_j are the repetition number, index of refraction, and width of layer number j, respectively.

As shown in this section, whenever we have $r(k)$, either analytically or numerically calculated, or experimentally determined, a Fourier transform of $r(k)$ reveals the peaks of the corresponding multi-layer system, a technique we call *ray spectroscopy*. The peak heights will tell us which of the rays are the most important in determining the reflection amplitude r, which, in turn, determines the absorption cross section of the corresponding solar cell. As shown in Fig. 10, the peak height is an exponentially decreasing function of optical path length, which means that only a few of the shortest rays are necessary to determine $r(k)$ with sufficient accuracy to be useful for system optimization. This, in turn, enables us to design and optimize solar cells in a completely new way on the basis of a few important rays, which implies a very small parameter space to be searched for system optimization.

8. Example with silicon

To provide an example of the ray-wave equivalence and the hierarchical summation scheme, we analyzed a three-layer simplification of a five-layer optically thin, epitaxial crystalline silicon solar cell using experimentally determined indices of refraction [55–58]. Fig. 11 shows the layer structure for these two models. The intent with the simple three-layer design is to demonstrate the concepts described in this paper applied to a system with material constants of practical importance. However, it should be noted that solar cells with co-planar structure are mainly used to provide an example. Commercial solar cells usually have some kind of surface structure to lower the reflectivity.

Since both the two amorphous silicon (a-Si) layers and the two crystalline silicon (c-Si) layers in the experimentally realized solar cell

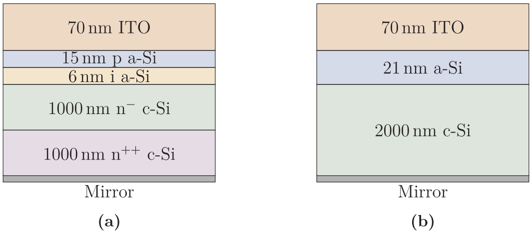

Fig. 11. Multilayer solar cells with mirror. (a) Experimentally realized thin epitaxial crystalline silicon solar cell consisting of five layers [55]. (b) Three-layer simplified model of the experimental system shown in (a), obtained by replacing layers with different doping but approximately the same index of refraction by a single layer. The three layers are, from top to bottom, 70 nm ITO, 21 nm amorphous silicon, and 2000 nm intrinsic silicon, respectively.

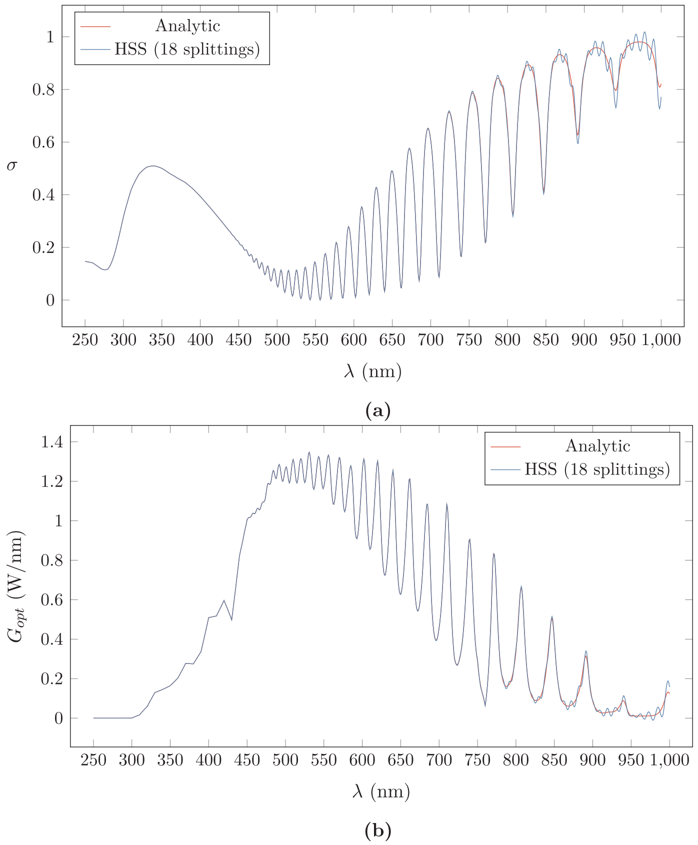

Fig. 12. a) A comparison of the absorption cross section σ calculated from an analytic expression and with a finite number of rays, using the hierarchical summation scheme (HSS). 18 splittings produce 65,537 rays and gives a good approximation to the analytic expression. b) When the AM1.5 solar spectrum [59] is taken into account, we get the optical generation rate, G_{opt}.

differ only in their doping, and since we for now neglect the doping-dependent free carrier absorption, we modeled this solar cell in terms of a three-layer system by collapsing the two a-Si layers and the two c-Si layers into a single layer, respectively.

Fig. 12a shows a comparison between the analytical result (red line) for the absorption cross section σ and the result produced by the hierarchical summation scheme (blue line). In the lower wavelength regime, σ is perfectly approximated by the hierarchical summation scheme including 18 splittings or 65,537 rays. Only from 750 nm on do we start to see some deviations. This demonstrates the complexity of a three-layer film in terms of its ray dynamics, and highlights the power of the hierarchical summation scheme even in the case of dispersive indices of refraction.

In order to obtain the optical generation rate [59], Eq. (2.5), we multiply σ with the AM1.5 solar spectrum, Γ. The result is displayed in Fig. 12b for both the analytical expression (red line) and the hierarchical summation scheme (blue line), corresponding to the two corresponding cases shown in Fig. 12a, respectively.

Once more, we see excellent agreement between optical generation rate obtained on the basis of the analytical and hierarchical summation scheme results.

9. Discussion

As shown in section 3, there is a profound duality between waves and rays. Rays are governed by ordinary differential equations, describing particle motion, while wave fronts are the solutions of continuous wave equations expressed in the language of partial differential equations. This duality is exploited in many fields of physics that deal with waves. In optics, e.g., it leads to the important field of geometric optics [60] in which one attempts to obtain an accurate description of the passage of light through various optical components by using a ray picture, side-stepping the more involved solution of Maxwell's wave equations [39,61]. There are many examples where the wave-ray duality is exact (see, e.g., [30]) and may be exploited to advantage. The most important example is Feynman's path integrals [62], which solve the full wave-mechanical problem of quantum mechanics exactly by summing over all possible classical rays. Another example of exact ray solutions to the corresponding wave problem is quantum mechanics with energy-scaling step potentials in one dimension [63–65]. Since the quantum step-potential problem and the electromagnetic (E&M) optically thin solar-cell problem are formally identical problems, one of the intentions of this paper is to transfer and adapt methodology from the quantum chaos community in the field of one-dimensional energy-scaling step potentials and dressed quantum graphs [64,65] to the solar-cell community, who is concerned with the solution of Maxwell's equations for stacks of layers of anti-reflection coatings on top of energy-converting materials. We note that, so far, only the bound-state problem has been studied extensively in the context of dressed, scaling quantum graphs, which, in the optical case, would correspond to the presence of two mirrors, one at the front and one at the back of the stack of films. The scattering problem, as studied in this paper, has to our knowledge not yet been studied in the context of dressed, scaling quantum graphs.

For the one-dimensional case we derived the exact expression for the *absorption cross section*, σ, of the energy-converting material. When σ is weighed by the solar spectrum as the spectral weighting term, the *optical generation rate* is obtained. This brings out the connection between the structure of the wave function ψ and the absorption. By evaluating σ we can engineer our system to increase the absorption, and thus the absorption cross section, of the system.

We showed the importance of including phases in our ray theory with the help of the following two-step method. First, we include the exact phases of the rays in our one-dimensional model, which we take as consisting of a single film. In section 3 we demonstrate that this yields the exact solution of the Helmholtz equation. Then, we evaluated the ray sum for this one-dimensional systems setting all phases to 1. We showed in Section 5 that the resulting, incorrect ray theory cannot handle the resonances and in addition predicts a spectral optical generation rate that is up to 60% off. We are convinced that this observation carries over to any ray tracing in two and three dimensions, which means that in order to be confident in the accuracy of a ray-tracing result, phases *must* be included. Otherwise, as shown in our paper in the one-dimensional case, one should be prepared for large errors in the predictions of a ray theory that omits phases.

For several of our model systems, including our example of the lab silicon cell discussed in section 8, we showed that including only a few rays in the ray sum already gives a good approximation of the absorption cross section (see, e.g., Fig. 4. This observation is important since, in principle, an infinity of rays needs to be summed over in order to obtain exact results, and if the convergence were slow, this would result in an enormous number of terms to be summed, partially, or totally, cancelling out the advantage in computational speed of rays over waves. That only a few dominant rays already determine the final result with good accuracy is particularly important in two and three dimensions, since, according to the increased dimension, the set of rays that needs to be summed over is much larger.

Since our ray theory is exact, it works for all refractive indices, n. This includes all n typically encountered in solar cells, where complex n indicates an absorptive material. A strength of the ray theory is that the refractive index can have any value and is not limited to only small values of real and imaginary parts. Our ray theory is therefore applicable to any solar cell material. Including the temperature dependence of its index of refraction. In linear approximation, as a function of temperature T, we can write

$$n(T) = n_0(T_0) + \beta(T - T_0), \tag{9.1}$$

where n_0 is the complex index of refraction at a reference temperature T_0 and β is the complex temperature coefficient, combining the two temperature coefficients for the real and imaginary parts of the index of refraction. Since our theory is exact for all indices of refraction, our theory can accommodate exactly the temperature dependence of the index of refraction, described by the temperature coefficients. In addition, since our complex index of refraction models the effects of the band gap and any gain and loss mechanisms, their temperature dependence, via the complex index of refraction, is included as well. We would also like to point out here that complex indices of refraction have so far not been treated in the quantum ray-splitting literature. Therefore our paper is the first to show that a complex index of refraction does not invalidate the exactness of the ray theory.

In our theory the boundary conditions between the vacuum and dielectric films, and between different dielectric films, are treated exactly, without any approximations. Only the boundary condition between the energy-converting dielectric film and the mirror is idealized, assuming 100% reflection. This assumption is not necessary since the mirror can be treated as another dielectric layer [39] for which our theory is exact.

Two-dimensional materials are of great current interest (see, e.g., [66,67]). Since the dielectric properties of these materials have already been measured [68], reflection and transmission amplitudes of these two-dimensional materials can be computed. Once these amplitudes are known, our theory is applicable to these materials and stays exact.

We do not hesitate to point out that for one-dimensional systems wave calculations are cheaper than ray calculations. For one-dimensional multi-layer systems, the transfer matrix method [69] can be used, which is fast and includes absorption. Even in two dimensions, solving the wave equation might still be cheaper and faster than applying the ray theory. In three dimensions, however, supported by the fact that an extensive literature on ray-tracing in three dimensions exists [15,16,27,28], we believed that ray methods will have an edge, in particular when constructed with phases included, which renders them exact.

In addition to paving the way toward an exact and efficient ray theory in three dimensions, the emphasis of this work is to present a ray theory that can be used to understand the different mechanisms that may be used to improve the absorption cross section. The fact that only a few rays describe the absorption cross section, σ, of the system is encouraging since only a few parameters (rays) need to be optimized for optimizing the entire system. Consequently, there are two ways in which classical ray calculations can be used in the context of solar cells: (1) As a predictive tool used to predict the outcomes of wave calculations (predictive direction; forward model) and (2) as a means to understand the results of wave calculations, in particular to illuminate and illustrate the mechanisms by which enhancement of the absorption cross section is achieved (analysis direction).

In the case of a single film, we showed in section 5 that the ray sum is absolutely convergent. Therefore, the terms in the sum may be summed in any order. In the case of stacks of two or more films, however, we showed in section 5 that the resulting ray sum is only conditionally convergent. In this case the order of summation is important, since, according to Riemann [50,70], any result can be obtained from a conditionally convergent sum by cleverly re-ordering the terms. In section 4 we present a hierarchical scheme according to which the rays in a multi-layer system can be summed in correct order.

The dominant rays describing the system can be found by performing the Fourier transform of σ, Thus, the Fourier transform provides us with the possibility of extracting ray information from σ. It is important to use a windowed Fourier transform (requiring a switching function) to eliminate the Gibbs ringing, which produces spurious peaks in the Fourier transform that do not correspond to rays. We found that rays are connected to the absorption cross section. The longer the rays, the larger the absorption cross section. The Fourier transform gives us the ability to study the dominant rays. By increasing the dominance of the long rays, which have the largest contribution to the absorption, it is possible to design solar cells to have an increased absorption cross section.

In section 8 we study a realistic system with a refractive index that exhibits dispersion. We showed at even dispersion is no obstacle to our theory; it still provides us with the correct absorption cross section.

Sunlight is incoherent and the question arises whether our results, derived for coherent light, are relevant for illumination of solar cells with incoherent light. We answer this question in the affirmative, since what we evaluate is the absorption cross section, which is defined for a sharp frequency, associated with an infinite coherence length. Another way to see this is the following. On the microscopic level, it is individual photons that strike the solar cell and interact with it. While different photons certainly have different frequencies, each individual photon has a sharp frequency and a corresponding wave function that is the solution of the optical Helmholtz equation. Thus, at each individual frequency, it is indeed the Helmholtz equation that governs the absorption of photons and thus determines the absorption cross section. The total optical generation rate is then obtained by a simple integral over the absorption cross sections weighted with the solar spectrum. Thus, our theory, despite the fact that sun light is incoherent, works for all film thicknesses.

10. Conclusions

In this paper we have shown that the ray theory is exact in one dimension. Our results are important since they pave the way to the use of exact ray tracing in three dimensions, which allows for both including textures and other scattering surfaces, as well as oblique incidences of sunlight.

We also showed several other facts that are important for the extension of the ray theory to three dimensions. We showed that the summation order of the rays is important and that it is dangerous, although tempting, to sum sub classes of rays to infinity, and then add the sub classes results. We showed explicitly that this will yield incorrect results.

An important result we obtained is that phases must be properly computed and included with each ray that is used to compute reflection probabilities and the absorption cross section. Without including the phases, as is sometimes done in current three-dimensional Monte-Carlo simulations of ray tracing in solar cells, we showed that an error of up to 60% and larger can be incurred.

We also showed that including only a few rays in the sum over rays gives quite accurate results, provided the phases are also correctly included. This is of the utmost importance for three-dimensional applications since, as a consequence of ray splitting, as we showed in Section 5, the number of rays explodes exponentially in the lengths of the rays that need to be included to obtain converged results with acceptable accuracy. We also showed that the rays are “real” in the sense that their signatures can readily be seen in the Fourier transform of the reflection probability as peaks in the length spectrum.

Since our theory is exact, it works for all refractive indices n, even if n is complex, which includes indices of refraction typical for solar cell materials. We showed this explicitly in Section 8, where we discuss the application of our exact ray theory to an example of a silicon solar cell. Extension of our theory to two and three dimensions is straightforward and provides the basis for future work on the application of exact ray theories for the computation of the absorption cross section of solar cells of practical importance.

Acknowledgement

This work was supported by the grant “Development of a new ray model for understanding the coupling between dielectric spheres for photovoltaics with higher efficiency” - No: 250678 financed by The Research Council of Norway.

The contributions from Maren Anna Brandsrud and Eivind Seim are considered to be equal, thus the first author and second author was decided by alphabetical order.

Appendix A. Reflection and transmission amplitudes

In order derive the exact ray model, we need to include the phases. The phases are described as below:

To obtain the proper phases for reflection and transmission of a ray at the left edge of a material, we consider the potential shown in Fig. A.1.

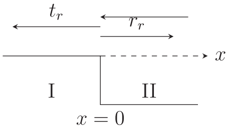

Fig. A.1. When a ray is coming from the left and goes from region I (vacuum) to region II (material with refractive index n), the ray will split into a transmitted and a reflected ray at the boundary. The amplitudes of this rays are given by the reflection and transmission amplitudes, r_l and t_l.

Coming from the left, out of region I ($x < 0$), a ray encounters the left edge of region II at $x = 0$. It gets reflected back into region I with reflection amplitude r_l, and gets transmitted into region II with amplitude t_l. The subscript l stands for “left”. In region I it is vacuum. In order to find the correct phase of the amplitude, we need to use the wavenumber of the corresponding wave and k is given by $\frac{2\pi}{\lambda}$, where λ is the wavelength. In region II, the wavenumber of the corresponding wave is given by $k_{II} = nk$ where n is the refractive index in region II. The wavefunction in region I and II are:

$$\Psi_I = e^{ikx} + r_l e^{-ikx}, \tag{A.1}$$

$$\Psi_{II} = t_l e^{ik_{II}x}. \tag{A.2}$$

Using the continuity of the wavefunction and its first derivative at $x = 0$, we obtain:

$$r_l = \frac{1-n}{1+n}, \tag{A.3}$$

$$t_l = \frac{2}{1+n}. \tag{A.4}$$

When the wave is coming from the right, the ray will encounter the boundary as shown in Fig. A.2.

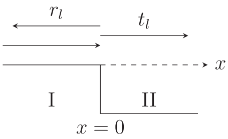

Fig. A.2. Reflection and transmission amplitudes, r_r and t_r, respectively, for a ray incident from the right (out of region II, i.e., $x > 0$).

The wavefunctions are

$$\Psi_I = t_r e^{-ikx}, \tag{A.5}$$

$$\Psi_{II} = e^{-ik_{II}x} + r_r e^{ik_{II}x}. \tag{A.6}$$

Again using continuity and the continuity of the first derivative gives us

$$r_r = -\left(\frac{1-n}{1+n}\right), \tag{A.7}$$

$$t_r = \frac{2n}{1+n}. \tag{A.8}$$

Appendix B. Integral formula for the spectral optical generation rate

In the scalar one-dimensional theory, the radiative flux, up to a constant, is defined by

$$j = \frac{1}{2i}\left(\psi^* \frac{d}{dx}\psi - \psi \frac{d}{dx}\psi^*\right). \tag{B.1}$$

Since, according to Fig. 1, the incident radiation is described by the plane wave $\psi_{in} = e^{ikx}$, the flux of the incident radiation is

$$j_{in} = \frac{1}{2i}\left(e^{-ikx}\frac{d}{dx}e^{ikx} - e^{ikx}\frac{d}{dx}e^{-ikx}\right) = k > 0. \tag{B.2}$$

Since, according to Fig. 1 the reflected radiation is described by $\psi_{refl} = re^{-ikx}$, a calculation analogous to Eq. (B.2) yields

$$j_{refl} = -|r|^2 k = -Rk < 0. \tag{B.3}$$

The total flux on the left-hand side of the boundary is thus

$$j = j_{in} + j_{refl} = k - Rk. \tag{B.4}$$

In terms of flux, the reflection probability R is defined as

$$R = \left|\frac{j_{refl}}{j_{in}}\right| = |r|^2, \tag{B.5}$$

which is consistent with our earlier definition Eq. (2.1) of the reflection probability above. We now turn to the wave equation, i.e.,

$$\frac{d^2\psi}{dx^2} = -n^2k^2\psi. \tag{B.6}$$

Taking the complex conjugate, we arrive at

$$\frac{d^2\psi^*}{dx^2} = -(n^2)^*k^2\psi^*. \tag{B.7}$$

From Eqs. (B.6) and (B.7) we obtain

$$\psi^*\frac{d^2\psi}{dx^2} - \psi\frac{d^2\psi^*}{dx^2} = [(n^*)^2 - n^2]k^2|\psi|^2. \tag{B.8}$$

We can also write the left-hand side of Eq. (B.8) as

$$\psi^*\frac{d^2\psi}{dx^2} - \psi\frac{d^2\psi^*}{dx^2} = \frac{d}{dx}\left[\psi^*\frac{d\psi}{dx} - \psi\frac{d\psi^*}{dx}\right] = 2i\frac{d}{dx}j(x), \tag{B.9}$$

where we used equation Eq. (B.1).

We now specialize to the situation shown in Fig. 2b, i.e., the film with mirror. For this situation, we now integrate Eq. (B.9) with Eq. (B.8) over the width of the film to obtain

$$\begin{aligned} 2i\int_0^a \tfrac{dj}{dx}dx &= 2i[j(a) - j(0)] \\ &= 2i[0 - k(1-R)] \\ &= \int_0^a [(n^*)^2 - n^2]k^2|\psi|^2 dx \\ &= \int_0^a (-4in_rn_i)k^2|\psi|^2 dx. \end{aligned} \tag{B.10}$$

Therefore, we now obtain

$$R = 1 - 2k\int_0^a n_in_r|\psi|^2 dx \tag{B.11}$$

and

$$\sigma = 1 - R = 2k\int_0^a n_in_r\ |\psi|^2 dx. \tag{B.12}$$

Appendix C. Equivalence of the 1-R with the spectral optical generation rate

In this appendix we demonstrate that the two different approaches presented in section 2 lead to the same formula for the absorption cross section σ. For a single film on a mirror (Fig. 2a) the wavefunction ψ inside the film is

$$\psi = \frac{-2\sin[nk(x-a)]}{\sin(nka) + in\cos(nka)}, \tag{C.1}$$

where a is the film thickness, n is the complex refractive index and k is the wavenumber. The absorption cross section is

$$\sigma = 2k\int_0^a |\psi|^2 n_i n_r dx. \tag{C.2}$$

This can also be written as

$$\sigma = 2kn_r n_i\left(\frac{2}{\eta^2+\theta^2}\right)\int_0^a \cosh[2n_i k(x-a)] - \cos[2n_r k(x-a)]dx, \tag{C.3}$$

where the prefactor contains

$$\begin{aligned} \eta &= \gamma - n_i\varepsilon + n_r\zeta \\ \theta &= \delta + n_i\zeta + n_r\varepsilon \\ \gamma &= \sin(n_r ka)\cosh(n_i ka) \\ \delta &= i\cos(n_r ka)\sinh(n_i ka) \\ \varepsilon &= \cos(n_r ka)\cosh(n_i ka) \\ \zeta &= i\sin(n_r ka)\sinh(n_i ka). \end{aligned} \tag{C.4}$$

Evaluation of the integral is straightforward and results in

$$\frac{2}{\eta^2+\theta^2}[n_r\sinh(2n_i ka) - n_i\sin(2n_r ka)]. \tag{C.5}$$

To complete our task, we have to show that $1-|r|^2$ from the scalar wave model produces the same result. The reflectivity $|r|^2$ is

$$|r|^2 = \left|-\frac{n\cos(nka) + i\sin(nka)}{n\cos(nka) - i\sin(nka)}\right|^2, \tag{C.6}$$

which can be rewritten as

$$|r|^2 = \frac{(n_r\varepsilon + n_i\zeta - \delta)^2 + (n_i\varepsilon - n_r\zeta + \gamma)^2}{\theta^2+\eta^2}. \tag{C.7}$$

Inserting this together with γ, δ, ε, and ζ into $1-|r|^2$ yields exactly the same result as in Eq. (C.5).

Appendix D. Proof of importance of the summation order

In this Appendix we show that for our two-film system and for a large range of dielectric constants, Eq. (5.3) holds, i.e., in these cases our ray sum in Eq. (5.1) is only conditionally convergent. We show this by observing that if the sum in Eq. (5.3) is already infinite for a subclass of rays, it is certainly infinite when summing over all rays, since all the terms not taken into account are positive. The subclass we focus on consists of rays that make p right reflections on the vacuum/film interface and make q right reflections on the film/film interface (see Fig. D.1). We also exclude any left reflections on the film/film interface, which uniquely defines our subclass of rays. Three examples of rays in our subclass are shown in Fig. D.1. All three rays have $p=1$ and $q=2$, and they contribute the same amplitude to r in Eq. (5.1). They differ only in their sequence of bounces. This induces degeneracy in our ray sum. In fact, any class of rays, characterized by a given p and q, is $\binom{p+q}{p}$ fold degenerate, where $\binom{p+q}{p}$ is the binomial coefficient [71]. The total contribution ρ of all of the rays of our subclass to the total reflection amplitude r is

$$\rho = \sum_{p=0}^{\infty}\sum_{q=0}^{\infty}\binom{p+q}{p} t_1^2 t_2^{2p+2} r_1^p r_2^q e^{ik[2(p+1)n_1a_1+2(p+q+1)n_2a_2]}, \tag{D.1}$$

where t_1 and r_1 are transmission amplitude and right-reflection amplitude at the vacuum/film interface, t_2 and r_2 are transmission amplitude and right-reflection amplitude at the film/film interface, a_1 is the width of film 1, a_2 is the width of film 2, and n_1 and n_2 are the refractive indices of films 1 and 2, respectively. To check whether the double sum in Eq. (D.1) is absolutely convergent, we need to check whether

$$\rho' = \sum_{p=0}^{\infty}\sum_{q=0}^{\infty}\binom{p+q}{p}|t_1|^2|t_2|^{2p+2}|r_1|^p|r_2|^q \tag{D.2}$$

is finite or infinite. Defining $x=|t_2|^2|r_1|$ and $y=|r_2|$, we may write Eq. (D.1) in the form

$$\rho' = |t_1|^2|t_2|^2\sum_{p=0}^{\infty}\sum_{q=0}^{\infty}\binom{p+q}{p}x^p y^q, \tag{D.3}$$

and since t_1 and t_2 are constants, it is sufficient to check the double sum

$$\rho'' = \sum_{p=0}^{\infty}\sum_{q=0}^{\infty}\binom{p+q}{p}x^p y^q > \sum_{p=0}^{\infty}\binom{2p}{p}(xy)^p > \sum_{p=1}^{\infty}\frac{(4xy)^p}{p}. \tag{D.4}$$

For the first inequality we used the fact that all terms in the sum are positive, and that, therefore, including only the diagonal terms in the sum provides a strict lower bound for the value of the sum, and for the second inequality we used the fact that $\binom{2p}{p} > 2^{2m}/m$, which is straightforward to show using the doubling formula for Euler's Γ function [71]. Analyzing the result in Eq. (D.4), we see that the sum over p converges for $xy < 1/4$. In this case, therefore, we cannot decide whether ρ'' is finite or infinite. For $xy = 1/4$, however, the last sum in Eq. (D.4) is the harmonic series, which diverges [71]. Therefore, for $xy = 1/4$, we definitely have $\rho'' = \infty$, which implies that in this case Eq. (5.1) is only conditionally convergent. Since for all $xy > 1/4$ the harmonic series provides a lower bound of the last sum in Eq. (D.4), we also have $\rho'' = \infty$ for all $xy > 1/4$. It follows that the ray sum in Eq. (5.1) is only conditionally convergent in all cases for which $z = |t_2|^2|r_1r_2| \geq 1/4$. Finally, we have to answer the question whether $z \geq 1/4$ is possible at all. We note that $|r_1|$ may freely range between 0 and 1, while $|t_2|^2|r_2|$ can range only between 0 and $2/(3\sqrt{3})$, which is obtained by observing that $|t_2|^2 = 1 - |r_2|^2$ and subsequently determining the maximum of the function $w = (1 - |r_2|^2)|r_2|$. This implies that z may range between 0 and $2/(3\sqrt{3}) > 0.38$, which overlaps with $z > 1/4$. Thus, we have proved that an entire range of cases exists in which Eq. (5.1) is only conditionally convergent. In these cases of conditional convergence we are not allowed to sum rays in arbitrary order. As discussed in Sect. 5, in order to obtain correct results, we have to sum the rays in the order of increasing path length.

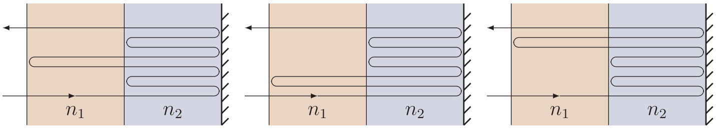

(a) $R_{1,2}$ (b) $R_{1,2}$ (c) $R_{1,2}$

Fig. D.1. Three ray trajectories that belong to the same class, $R_{1,2}$, and contribute with the same amplitude to the reflection amplitude of the film system. They differ only in the order of right-reflections on the vacuum/film and film/film interfaces. (a) The ray reflects inside the second film, then reflects inside the first film and reflects for the second time at the film/film interface and leaves the system. (b) The ray reflects once at the vacuum/film interface then enters the second film and reflects twice on the film/film interface. (c) The ray enters the second film, reflects twice on the film/film interface, enters the first film and reflects once on the vacuum/film interface.

References

[1] J. Krc, M. Zeman, S.L. Luxemburg, M. Topic, Modulated photonic-crystal structures as broadband back reflectors in thin-film solar cells, Appl. Phys. Lett. 94 (2009) 153501.
[2] P. Spinelli, A. Polman, Light trapping in thin crystalline si solar cells using surface mie scatterers, IEEE J. Photovolt. 4 (2) (2014) 554–559.
[3] Robin Vismara, Olindo Isabella, Miro Zeman, Back-contacted BaSi$_2$ solar cells: an optical study, Optic Express 25 (8) (2017) A402.
[4] Daniel Lockau, Tobias Sontheimer, Christiane Becker, Eveline Rudigier-Voigt, Frank Schmidt, Bernd Rech, Nanophotonic light trapping in 3-dimensional thin-film silicon architectures, Optic Express 21 (S1) (Jan 2013) A42–A52.
[5] Jonathan Grandidier, Dennis M. Callahan, Jeremy N. Munday, Harry A. Atwater, Light absorption enhancement in thin-film solar cells using whispering gallery modes in dielectric nanospheres, Adv. Mater. 23 (10) (2011) 1272–1276.
[6] M. Schmid, Review on light management by nanostructures in chalcopyrite solar cells, Semicond. Sci. Technol. 32 (4) (2017) 043003.
[7] C. Becker, P. Wyss, D. Eisenhauer, J. Probst, V. Preidel, M. Hammerschmidt, S. Burger, 5 by 5 cm^2 silicon photonic crystal slabs on glass and plastic foil exhibiting broadband absorption and high-intensity near-fields, Sci. Rep. 4 (2014) 5886.
[8] W.I. Nam, Y.J. Yoo, Y.M. Song, Geometrical shape design of nanophotonic surfaces for thin film solar cells, Optic Express 24 (14) (Jul 2016) A1033–A1044.
[9] Eli Yablonovitch, Statistical ray optics, J. Opt. Soc. Am. 72 (7) (1982) 899–907.
[10] Patrick Campbell, A. Martin, Green. Light trapping properties of pyramidally textured surfaces, J. Appl. Phys. 62 (1987) 243–249.
[11] T. Uematsu, M. Ida, K. Hane, Y. Hayashi, T. Saitoh, A new light trapping structure for very-thin, high-efficiency silicon solar cells, Photovoltaic Specialists Conference, 1988., Conference Record of the Twentieth IEEE, 1988, pp. 792–795.
[12] David Thorp, Stuart R. Wenham, Ray-tracing of arbitrary surface textures for light-trapping in thin silicon solar cells, Sol. Energy Mater. Sol. Cell. 48 (1997) 295–301.
[13] A.W. Smith, A. Rohatgi, S.C. Neel, Texture: a ray tracing program for the photovoltaic community, Photovoltaic Specialists Conference, 1990., Conference Record of the Twenty First IEEE, 1990, pp. 426–431.
[14] Rolf Brendel, Coupling of light into mechanically textured silicon solar cells: a ray tracing study, Prog. Photovoltaics Res. Appl. 3 (1995) 25–38.
[15] J.E. Cotter, Raysim 6.0 - a free geometrical ray tracing program for silicon solar cells, Photovoltaic Specialists Conference, 2005. Conference Record of the Thirty-first IEEE, 2005, pp. 1165–1168.
[16] Rudi Santbergen, Tomomi Meguro, Takashi Suezaki, Gensuke Koizumi, Kenji Yamamoto, Miro Zeman, Genpro4 optical model for solar cell simulation and its application to multijunction solar cells, IEEE J. Photovolt. 7 (2017) 919–926.
[17] Helmut Mäckel, Hendrik Holst, Mirko Löhmann, Eckard Wefringhaus, P. Pietro, Altermatt, Detailed analysis of random pyramidal surfaces with ray tracing and image processing, IEEE J. Photovolt. 6 (2016) 1456–1465.
[18] Hendrik Holst, Matthias Winter, Malte R. Vogt, Karsten Bothe, Marc Köntges, Rolf Brendel, P. Pietro, Altermatt, Applications of a new ray tracing framework to the analysis of extended regions in Si solar cell modules, Energy Procedia 28 (2013) 86–93.
[19] Keith R. McIntosh, Richard M. Swanson, Jeffrey E. Cotter, A simple ray tracer to compute the optical concentration of photovoltaic modules, Prog. Photovoltaics Res. Appl. 14 (2006) 167–177.
[20] Rolf Brendel, Simple prism pyramids: a new light trapping texture for silicon solar cells, Photovoltaic Specialists Conference, 1993., Conference Record of the Twenty Third IEEE, 1993, pp. 253–255.
[21] Garam Yun, Karlton Crabtree, Russell A. Chipman, Properties of the polarisation ray tracing matrix, Proc. SPIE 6682, Polarization Science and Remote Sensing III, 2007, p. 66820Z.
[22] Simeon C. Baker-Finch, Keith R. McIntosh, Reflection of normally incident light from silicon solar cells with pyramidal texture, Prog. Photovoltaics Res. Appl. 19 (2010) 406–416.
[23] Benjamin Lipovsek, Janez Krc, Marko Topic, Optical model for thin-film photovoltaic devices with large surface textures at the front side, Inf. MIDEM: J. Microelectron., Electron. Compon. Mater. 41 (4) (2011) 264–271.
[24] Janez Krc, Franc Smole, Marko Topic, Analysis of light scattering in amorphous si:h solar cells by a one-dimensional semi-coherent optical model, Prog. Photovoltaics Res. Appl. 11 (2003) 15–26.
[25] C. Zechner, P. Fath, G. Willeke, E. Bucher, Two- and three-dimensional optical Carrier generation determination in crystalline silicon solar cells, Sol. Energy Mater. Sol. Cell. 51 (1998) 255–267.
[26] Rolf Brendel, D. Scholten, Modeling light trapping and electronic transport of waffle-shaped crystalline thin-film si solar cells, Appl. Phys. A 69 (1999) 201–213.
[27] Simeon C. Baker-Finch, Keith R. McIntosh, One-dimensional photogeneration profiles in silicon solar cells with pyramidal texture, Prog. Photovoltaics Res. Appl. 20 (2012) 51–61.
[28] Keith R. McIntosh, Malcolm D. Abbotta, Ben A. Sudburya, Ray tracing isotextured solar cells, Energy Procedia 92 (2016) 122–129.
[29] M. Zworski, Semiclassical Analysis, Graduate Studies in Mathematics vol. 138, (2012).
[30] Reinhold Blümel, Advanced Quantum Mechanics: the Classical-quantum Connection, Jones & Bartlett Publishers, 2011.
[31] Janez Krc, Franc Smole, Marco Topic, One-dimensional semi-coherent optical model for thin film solar cells with rough interfaces, Inf. MIDEM: J. Microelectron., Electron. Compon. Mater. 32 (1) (2002) 6–13.
[32] Eugen Merzbacher, Quantum Mechanics, second ed. edition, Wiley, New York, 1970.
[33] L.D. Landau, Electrodynamics of Continuous Media, Volume 8 of Course of Theoretical Physics, second ed., Pergamon, Oxford, 1984 revised and enlarged by E.M. Lifshitz and L.P. Pitaevskii. edition.
[34] Jichi Ma, Jeff Chiles, Yagya D. Sharma, Sanjay Krishna, Sasan Fathpour, Two-photon photovoltaic effect in gallium arsenide, Optic Lett. 39 (18) (2014) 5297–5300.
[35] Sasan Fathpour, Kevin K. Tsia, Bahram Jalali, Two-photon photovoltaic effect in silicon, IEEE J. Quant. Electron. 43 (12) (2007) 1211–1217.
[36] V.E. Ferry, J.N. Munday, H.A. Atwater, Design considerations for plasmonic photovoltaics, Adv. Mater. 22 (43) (2010) 4794–4808.
[37] Richard Phillips Feynman, QED: the Strange Theory of Light and Matter, Princeton University Press, 2006.
[38] J.S. Townsend, Quantum Physics: a Fundamental Approach to Modern Physics, University Science Books, 2010.
[39] David J. Griffiths, Introduction to Electrodynamics, third ed. edition, Prentice Hall,

Upper Saddle River, N.J, 1999.
[40] R. Blümel, T.M. Antonsen, B. Georgeot, E. Ott, R.E. Prange, Ray splitting and quantum chaos, Phys. Rev. E 53 (Apr 1996) 3284–3302.
[41] A. Kohler, R. Blümel, Weyl formulas for quantum ray-splitting billiards, Ann. Phys. 267 (1998) 249–280.
[42] R. Blümel, P.M. Koch, L. Sirko, Ray-splitting billiards, Found. Phys. 31 (2001) 269–281.
[43] Martin C. Gutzwiller, Chaos in Classical and Quantum Mechanics, first ed. edition, Springer, 1990.
[44] L. Sirko, P.M. Koch, R. Blümel, Experimental identification of non-Newtonian orbits produced by ray splitting in a dielectric-loaded microwave cavity, Phys. Rev. Lett. 78 (Apr 1997) 2940–2943.
[45] Y. Hlushchuk, A. Kohler, Sz Bauch, L. Sirko, R. Blümel, M. Barth, H.-J. Stöckmann, Autocorrelation function of level velocities for ray-splitting billiards, Phys. Rev. E 61 (1) (2000) 366.
[46] N. Savytskyy, A. Kohler, Sz Bauch, R. Blümel, L. Sirko, Parametric correlations of the energy levels of ray-splitting billiards, Phys. Rev. E 64 (3) (2001) 036211.
[47] A. Kohler, R. Blümel, Annular ray-splitting billiard, Phys. Lett. A 238 (4–5) (1998) 271–277.
[48] A. Kohler, R. Blümel, Weyl formulas for quantum ray-splitting billiards, Ann. Phys. 267 (2) (1998) 249–280.
[49] A. Kohler, R. Blümel, Test of semiclassical amplitudes for quantum ray-splitting systems, Phys. Rev. E 59 (6) (1999) 7228.
[50] B. Riemann, Über die Darstellbarkeit einer Function durch eine trigonometrische Reihe, Dieterich, 1867.
[51] Stewart Galanor, Riemann's rearrangement Theorem, Math. Teach. 80 (8) (1987) 675–681.
[52] Seok-Joo Byun, Seok Yong Byun, Jangkyo Lee, Jae Wan Kim, Taek Sung Lee, Won Mok Kim, Young Kyu Park, Kyuman Cho, An optical simulation algorithm based on ray tracing technique for light absorption in thin film solar cells, Sol. Energy Mater. Sol. Cell. 95 (1) (2011) 408–411.
[53] H.S. Carslaw, A historical note on Gibbs' phenomenon in Fourier's series and integrals, Bull. Am. Math. Soc. 31 (8) (10 1925) 420–424.
[54] A. Nuttall, Some windows with very good sidelobe behavior, IEEE Trans. Acoust. Speech Signal Process. 29 (1) (Feb 1981) 84–91.
[55] Josefine K. Selj, David Young, Sachit Grover, Optimization of the antireflection coating of thin epitaxial crystalline silicon solar cells, Energy Procedia 77 (2015) 248–252 5th International Conference on Silicon Photovoltaics, SiliconPV 2015.
[56] A. Martin, Green. Self-consistent optical parameters of intrinsic silicon at 300K including temperature coefficients, Sol. Energy Mater. Sol. Cell. 92 (11) (2008) 1305–1310.
[57] D.T. Pierce, W.E. Spicer, Electronic structure of amorphous Si from photoemission and optical studies, Phys. Rev. B 5 (Apr 1972) 3017–3029.
[58] Tobias A.F. König, Petr A. Ledin, Justin Kerszulis, Mahmoud. A. Mahmoud, Mostafa A. El-Sayed, John R. Reynolds, Vladimir V. Tsukruk, Electrically tunable plasmonic behavior of nanocube–polymer nanomaterials induced by a redox-active electrochromic polymer, ACS Nano 8 (6) (2014) 6182–6192 PMID: 24870253.
[59] Reference solar spectral irradiance: Air mass 1.5. http://rredc.nrel.gov/solar/spectra/am1.5. (Accessed 19 April 2018).
[60] Max Born, E. Wolf, Principles of Optics: Electromagnetic Theory of Propagation, Interference and Diffraction of Light, fourth ed. edition, Pergamon Press, Oxford, 1970.
[61] John David Jackson, Classical Electrodynamics, second ed. edition, John Wiley & Sons, New York, 1970.
[62] Richard P. Feynman, Quantum Mechanics and Path Integrals, International Series in Pure and Applied Physics, McGraw-Hill, New York, 1965.
[63] R. Blümel, Yu. Dabaghian, R.V. Jensen, Explicitly solvable cases of one-dimensional quantum chaos, Phys. Rev. Lett. 88 (4) (January 2002).
[64] Yu. Dabaghian, R. Blümel, Explicit analytical solution for scaling quantum graphs, Phys. Rev. E 68 (Nov 2003) 055201.
[65] Yu. Dabaghian, R. Blümel, Explicit spectral formulas for scaling quantum graphs, Phys. Rev. E 70 (Oct 2004) 046206.
[66] Jiabao Zheng, Robert A. Barton, Dirk Englund, Broadband coherent absorption in chirped-planar-dielectric cavities for 2d-material-based photovoltaics and photodetectors, ACS Photonics 1 (9) (2014) 768–774.
[67] Jessica R. Piper, Shanhui Fan, Broadband absorption enhancement in solar cells with an atomically thin active layer, ACS Photonics 3 (4) (2016) 571–577.
[68] Yilei Li, Alexey Chernikov, Xian Zhang, Rigosi Albert, Heather M. Hill, Arend M. van der Zande, Daniel A. Chenet, En-Min Shih, James Hone, Tony F. Heinz, Measurement of the optical dielectric function of monolayer transition-metal dichalcogenides: Mos 2, mo s e 2, ws 2, and ws e 2, Phys. Rev. B 90 (20) (2014) 205422.
[69] Dario Cozza, Carmen M. Ruiz, David Duche, Sergio Giraldo, Edgardo Saucedo, Jean Jaques Simon, Ludovic Escoubas, Optical modeling and optimization of $Cu_2ZnSnSe_4$ solar cells using the modified transfer matrix method, Optic Express 24 (18) (2016) A1201–A1209.
[70] R. Blümel, Comment on 'quantum chaos in elementary quantum mechanics' by Yu. Dabaghian and R. Jensen, Eur. J. Phys. 27 (1) (2006) L1.
[71] I.S. Gradshteyn, I.M. Ryhzik, Table of Integrals, Series and Products, fifth ed., Academic Press, 1994.

Appendix B

Paper II

An Exact Ray Model for Oblique Incident Light on Planar Films

Maren Anna Brandsrud[a,*], Reinhold Blümel[b], Chang Chuan You[c], Erik Stensrud Marstein[c,d], Eivind Seim[a], Rozalia Lukacs[a], Espen Olsen[a] and Achim Kohler[a]

[a]Norwegian University of Life Sciences, Faculty of Science and Technology, Drøbakveien 31, 1432 Ås, Norway
[b]Wesleyan University, Department of Physics, 265 Church Street, Middletown, CT 06459, United States of America
[c]Institute for Energy Technology, Department of Solar Energy, Instituttveien 18, 2007 Kjeller, Norway
[d]University of Oslo, Department of Technology Systems, Gunnar Randers Vei 19, 2007 Kjeller, Norway

ARTICLE INFO

Keywords:
Exact ray model
Oblique incident light
Planar Films

ABSTRACT

During recent years, ray tracing has frequently been used to study the absorption characteristics of structured solar cells. However, wave properties such as absorption enhancement due to resonances in optically thin solar films, cannot be explained by pure classical ray models. Here we present an exact three-dimensional ray model for oblique incidence of a plane electromagnetic wave on a thin film and show that the resonant structure of the absorption cross section calculated from our ray model is identical to exact calculations by electromagnetic wave theory. Both parallel and perpendicular polarized light are described exactly by the ray model presented. We validate the resonant structure of the absorption cross section of our ray model by an experimentally realized layered film, where we obtain perfect agreement between experiment and theory. We demonstrate further that for a beam with a finite beam waist, in accordance with Beer-Lambert's law, absorption occurs along the path of the beam, while, in the case of a plane wave incident on an optically thin film, and contrary to Beer-Lambert's law, absorption occurs along the axis perpendicular to the surface of the film.

1. Introduction

In optical systems where the wavelength is smaller than the structures applied to the surfaces, geometrical optics approaches have been successfully applied for evaluating and understanding the absorption efficiency of materials. Geometrical optics approaches take into account the path length of optical rays, and absorption properties are estimated for a large number of rays calculating the decay of the intensity of the rays due to absorption. The intensity decay is achieved by attenuating the rays according to the Beer-Lambert's law. Efficient absorption is an important feature for solar cells: an efficiency increase is obtained when a large number of the incoming light rays can be trapped in the solar cell and be effectively absorbed by the cell before they leave it [1, 2, 3].

In systems with structures that are of the same size as the wavelength of the incoming light, wave resonance phenomena occur. Examples of such systems are optically thin solar cells, such as thin film solar cells, as well as solar cells made from epitaxially grown thin silicon foils. Since wave resonance phenomena are due to the wave nature of light, a simple geometrical ray-optics approach is not sufficient to model them. In the field of quantum chaos, an approach based on classical trajectories and rays in the corresponding classical systems has been used extensively to study and explain wave properties of quantum systems. Especially in the area of quantum chaos, where the phase space of the corresponding classical systems shows chaotic behavior, ray models have been used for understanding the inherent properties of the systems. Remarkably, the ray models of quantum chaos systems can explain quantum (wave) properties of the systems [4, 5]. In order to include the wave properties of the system in the ray model, each ray is assigned a phase in analogy to the Feynman formulation of quantum physics [6]. One-dimensional quantum problems can be described exactly by such ray models [7, 8, 9]. For two- and three-dimensional systems that show chaotic behavior, approximation formulas have been calculated based on semi-classical formulas that take into account special trajectories and rays of the systems including phase properties of the rays. For example, for so-called quantum ray-splitting billiards, the density of states can be calculated taking the phenomenon of ray-splitting fully into account [10, 11, 12, 13, 14].

When an electromagnetic wave front of a plane wave is perpendicularly incident on a plane ray-splitting surface, such as the surface of a solar cell or a ray-splitting boundary between layers in solar cells, we can consider the system as an effectively one-dimensional system. We have recently presented an exact ray model for the perpendicular incidence of electromagnetic radiation on a system of ray-splitting boundaries. Our ray model takes into account the phases and describes exactly the wave properties of the light in effectively one-dimensional systems, i.e. layered optically thin solar cells with perpendicular incidence [15]. The ray model describes the interference properties and the absorption efficiency of layered systems, such as layered solar cells, exactly. We presented an approach for calculating the optical generation rate of layered solar cells analytically and numerically for any layered system with perpendicular incidence.

The description of three-dimensional electromagnetic wave propagation in layered surfaces for the general case of oblique incidence is of high interest. Planar optical structures can be exactly described by electromagnetic wave theory or by the transfer matrix (S-matrix) method [15, 16, 17, 18, 19]. Ray simulations are frequently used

---

*Corresponding author
maren.brandsrud@nmbu.no (M.A. Brandsrud)
ORCID(s):

to evaluate the efficiency of solar cells, and oblique incidence is the generic case for most solar cells under most operating conditions. In the paper at hand, we present a ray model that describes exactly the absorption and resonance properties for the situation when a plane wave is incident on a three-dimensional layered system with plane surfaces and with an arbitrary angle of incidence. This three-dimensional system is translationally invariant in one dimension and can thus be simplified to a two-dimensional problem. The proposed model is an extension of the ray theory presented in [15], i.e., a ray theory for one-dimensional systems, which is equivalent with a three-dimensional system that is translationally invariant in two directions, with absorption. The model presented in this paper is valid for flat, three-dimensional, optically thin solar cells, where a plane wave propagates toward the system from an arbitrary incoming direction. Since the ray picture is frequently used to describe interference properties in physics text books, we take the opportunity to highlight general aspects related to the derivation of resonance patterns in thin films with oblique incidence that are often overlooked in physics text books.

In Section 2, we briefly review our theory of normal incident light in order to set the stage for our main topic, the case of oblique incident light. We discuss this case in two stages. In Section 3, we treat the case of real index of refraction (no absorption), followed by the case of complex index of refraction (absorption included), discussed in Section 4. Section 5 discusses absorption in the case of a Gaussian beam. In Section 6, we validate our ray model by comparison with measured data.

2. Ray theory for describing normal incident light

In the following, we develop a ray model for the general case of oblique incidence. To introduce the reader to the concept of a ray model that can describe wave properties of an optical system, we start the discussion by considering perpendicular incidence. As model systems we use the systems shown in Fig. 1. The model systems consist of (a) a single film with a mirror on the backside of the film and (b) a single film without a mirror. A ray model for perpendicular incidence is an effectively one-dimensional problem and can be described exactly by a scalar wave equation [15]. The scalar wave equation is equivalent to exact three-dimensional electromagnetic theory and independent of polarization since both polarization directions are equivalent for normal incident light. For system (a) the reflection amplitude, r_{1dfm}, can be calculated exactly as

$$r_{1dfm} = -\frac{n\cos(nka) + i\sin(nka)}{n\cos(nka) - i\sin(nka)}, \tag{1}$$

where n is the complex refractive index of the film, k is the angular wave number of the incoming plane wave, and a is the thickness of the film. The mirror is assumed to be perfect.

For the system in Fig. 1b, the reflection and transmission amplitudes, r_{1df} and t_{1df}, respectively, can be calculated exactly as

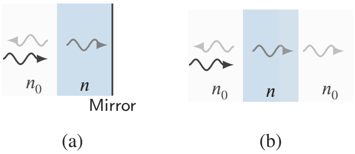

Figure 1: (a) When a plane wave is propagating towards a single film with a mirror behind all of the light will be reflected in case of a non-absorptive film. In the case of an absorptive film, the light is partly absorbed and partly reflected. (b) In the case where there is no mirror behind the film, the light is partly reflected at the surface and partly transmitted. If the film is absorptive, a part of the light is absorbed by the film as well. For both situations, the refractive index outside of the film is n_0 and the refractive index of the film is n, where $n > n_0$.

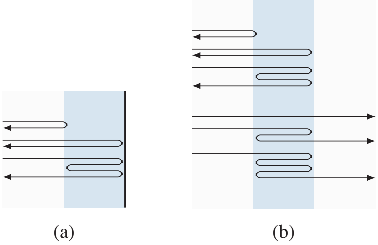

Figure 2: Frame (a) shows the three simplest rays that contribute to the reflection amplitude in Fig. 1a. Frame (b) shows the three simplest rays that contribute to the transmission and reflection amplitude for the system shown in Fig. 1b.

$$r_{1df} = \frac{i(n^2-1)\sin nka}{2n\cos nka - i(n^2+1)\sin nka}, \tag{2a}$$

$$t_{1df} = \frac{2ne^{-inka}}{2n\cos nka - i(n^2+1)\sin nka}, \tag{2b}$$

where n is the complex refractive index of the film, k is the angular wave number of the incoming plane wave, and a is the thickness of the film. We have previously shown that the reflection amplitude, r, of Eq. (1), i.e., for a plane wave propagating towards a system as shown in Fig. 1a with perpendicular incidence, can be evaluated exactly by a sum of rays, taking into account all possible rays of the system as shown in Fig. 2a, according to

$$r_{1dfm} = r_l + t_l t_r e^{i\pi} e^{2inka} \sum_{\nu=0}^{\infty} (e^{i\pi} r_r e^{2inka})^{\nu}, \tag{3}$$

where r_l, t_l, r_r, and t_r are the amplitudes of the respective rays that are reflected or transmitted at the boundary between air and film. The amplitudes depend only on the refractive index of the film. The subscripts of the amplitudes indicate if the respective rays are approaching the boundary from the left (l) or from the right (r). The exact expressions for the amplitudes are given in [15]. The factor $e^{i\pi}$ represents the phase that a ray acquires by reflection at the mirror, n is the refractive index of the film, k is the angular wave number, and a is the thickness of the film. The model shown in Eq. (3) is called a ray model since it is built on the summation of all possible rays in the system. While Eq. (3) is exact and equivalent to Eq. (1), its analytical strength lies in the fact that each ray contribution can be read directly from it.

In [15] we have shown that the inclusion of phases in the ray model is essential for describing the interference properties of the material. Interference properties lead to absorption resonances in the material when the film thickness matches multiples of the wavelength.

The same procedure can be used to establish a ray model for a single film without mirror, as shown in Fig. 1b, by summing up all possible rays that contribute to the total reflected and transmitted rays, respectively. The corresponding reflection and transmission amplitudes are given by

$$r_{1df} = r_l + t_l t_r r_r e^{2inka} \sum_{\nu=0}^{\infty} (r_r^2 e^{2inka})^{\nu}, \tag{4a}$$

$$t_{1df} = \left(t_l t_r e^{inka} \sum_{\nu=0}^{\infty} (r_r^2 e^{2inka})^{\nu} \right) e^{-ika}, \tag{4b}$$

where r_l, t_l, r_r, and t_r are the amplitudes as described above. n is the complex refractive index of the film with thickness a, and k is the wave number. The factor e^{-ika} outside the parentheses in Eq. 4b is included to remove the phase the ray would have obtained if it had passed the film without the mirror. The three simplest rays that contribute to the sums for the reflection and transmission amplitudes given in Eq. (4b) are shown in Fig. 2b.

Absorption properties of materials are taken into account by the imaginary part of the complex refractive index $n = n_r + in_i$. Thus n accounts for both the refraction and absorption properties of the material. In [15] it is shown that only a few rays are sufficient to describe system properties with high accuracy.

3. Exact ray theory for oblique incidence without absorption

Our ray model can be extended to a three-dimensional model for planar films. We consider the situation illustrated in Fig. 3, where a plane electromagnetic wave propagates towards a planar film. Reflection and transmission amplitudes can be obtained by solving the respective electromagnetic problem [16], taking into account the polarization of the incident radiation.

3.1. Exact electromagnetic description of the system

Figure 4 illustrates how the coordinate system and angles are chosen in order to evaluate the system by exact electromagnetic theory. The incoming wave is a plane wave with wavelength λ. The angular wave number of the wave outside the material is given by $k_0 = \frac{2\pi}{\lambda}$ and can be decomposed into x- and y-components according to

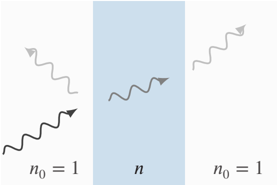

Figure 3: A plane wave is propagating with an arbitrary angle of incidence towards a single film. The wave is partly reflected at the first surface and partly transmitted through the film. The refractive index of the film is n and the refractive index of the area outside is $n_0 = 1$.

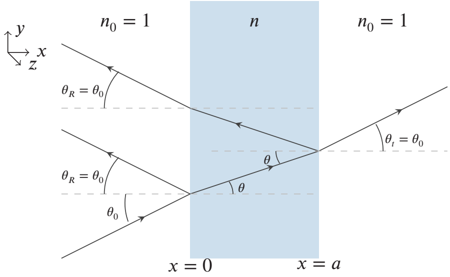

Figure 4: The model system consists of a single film with thickness a. The refractive index of the film is n. In front of the film, the refractive index is $n_0 = 1$, i.e. vacuum. A plane wave is propagating towards the film in the xy-plane with an angle of incidence θ_0. The angle of reflection, θ_R, is equal to θ_0. The angle of refraction, θ, can be found by Snell's law. For the transmitted ray behind the film, the direction of the angle of the transmitted ray is $\theta_t = \theta_0$.

$$k_{x,0} = k_0 \cos\theta_0, \tag{5a}$$

$$k_{y,0} = k_0 \sin\theta_0, \tag{5b}$$

where θ_0 is the angle of incidence as shown in Fig. 4.

The absolute value of the angular wavenumber inside the film is given by $k = nk_0$, where n is the refractive index of the film. Since the y-component of k is constant through the boundary, the components of the angular wavenumbers inside the film are given by

$$k_y = k_{y,0} = k_0 \sin\theta_0 = k \sin\theta \tag{6}$$

and

$$k_x = k\cos\theta = \sqrt{k^2 - k_y^2} = k_0\sqrt{n^2 - \sin^2\theta_0} \tag{7}$$

for k_x and k_y, respectively, where θ is the angle of refraction as shown in Fig. 4. Snell's law can be derived from Eq. (6) [16].

For a detailed presentation of the derivation of the expressions for the reflection amplitudes for oblique incidence on a plane surface, we refer to textbooks on electromagnetic theory such as [16]. By setting the surface charge to zero, the expressions for the transmission and reflection amplitude for the two polarizations for the system presented in Fig. 3 are given in Tab. 1.

Table 1
According to electromagnetic theory [16], the reflection and transmission amplitudes can be found for parallel and perpendicular polarized light for the system shown in Fig. 4. $k_{x,0}$ and k_x are given in Eqs. 5a and 7. n is the refractive index of the film and a is the thickness of the film.

	Parallel polarization
$r_\parallel$	$\frac{(k_x+n^2k_{x,0})\left[(n^2k_{x,0}-k_x)+e^{2ik_xa}(k_x-n^2k_{x,0})\right]}{(k_x+n^2k_{x,0})^2-e^{2ik_xa}(k_x-n^2k_{x,0})^2}$
$t_\parallel$	$\frac{4n^2k_{x,0}k_xe^{i(k_x-k_{x,0})a}}{(k_x+n^2k_{x,0})^2-e^{2ik_xa}(k_x-n^2k_{x,0})^2}$
	Perpendicular polarization
$r_\perp$	$\frac{(k_x+k_{x,0})\left[(k_{x,0}-k_x)+e^{2ik_xa}(k_x-k_{x,0})\right]}{(k_x+k_{x,0})^2-e^{2ik_xa}(k_x-k_{x,0})^2}$
$t_\perp$	$\frac{4k_{x,0}k_xe^{i(k_x-k_{x,0})a}}{(k_x+k_{x,0})^2-e^{2ik_xa}(k_x-k_{x,0})^2}$

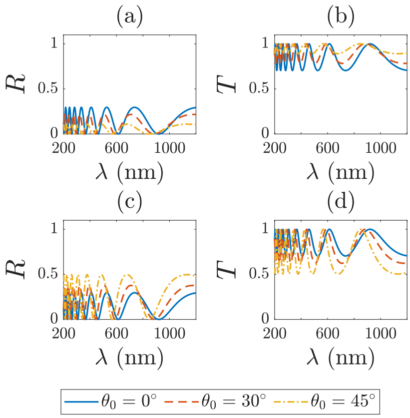

Figure 5: The reflection and transmission probability, $R = |r|^2$ ((a) and (c)) and $T = |t|^2$ ((b) and (d)), as a function of wavelength, λ, for a system as shown in Fig. 3. The angle of incidence is set to 0°, 30° and 45°. The incoming light is parallel polarized in (a) and (b) and perpendicular polarized in (c) and (d). r and t are found by the equations in Tab. 1. The thickness of the film is 500 nm and the refractive index of the film is $n = 1.84$.

Fig. 5 shows how the reflection and transmission probability, $R = |r|^2$ and $T = |t|^2$, change as the angle of incidence equal to 0°, 30° and 45° for a film with thickness of 500 nm and a refractive index of 1.84. We chose the refractive index as $n = 1.84$ since it corresponds to the refractive index of the SiN_x-film at 630 nm used for the measurements presented and discussed in Sec. 6.

We observe that the positions of the maxima depend on the angle of incidence of the incoming plane wave. The dependence on the angle of incidence can be seen in the expressions of the amplitudes for perpendicular and parallel polarized light in Tab. 1. As shown in Eqs. 5a and 7, $k_{x,0}$

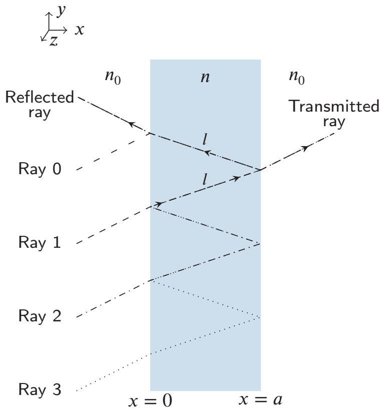

Figure 6: Schematic illustration of the ray model for the thin-film system of Fig. 3. By adding up the amplitudes from all possible rays that contribute to the reflected and transmitted ray, the reflection and reflection probability can be found. The path length of contribution to the reflection probability from $Ray1$ which transmitting through the front of the film and is reflected at the backside of the film is $d = 2l = \frac{2a}{\cos\theta}$. θ is the angle of refraction (see Fig. 3).

and k_x depend on the angle of incidence.

3.2. Ray model for oblique incident light - started inside the film

In order to build a ray model to describe the system, we need to add up all possible rays that contribute to the reflected and transmitted rays as shown in Fig. 6. In order to accomplish this, we study in this section a ray model that is suggested in two well-known text books [20, 21]. Implementing this model and comparing it with the results of exact E&M calculations, we will show at the end of this section that the model suggested in these two text books is not correct.

If we hypothesize that we can calculate the Eqs. (5a) and (7) for the reflection coefficient for oblique incidence based on a ray model, we would expect that not only the x-components of the rays contribute. We would expect that rays contribute according to their travelled path inside the film as in the case described in Sec. 2.

To illustrate this, we consider Fig. 6. We start by evaluating how the reflection amplitude can be described by rays. The simplest ray that contributes to the reflected ray is the one that only reflects at the first boundary between air and the material. This ray is named *Ray 0* in Fig. 6. The shortest possible ray that contributes to the reflected ray that transmits into the film and back travels a distance of $d = 2l$ through the film, where $l = \frac{a}{\cos\theta}$ and θ is the angle of refraction. The phase and attenuation collected inside the film by this ray (called *Ray 1* in Fig. 6), is given in Tab. 2 in the table entry for *Ray 1*. In order to develop a ray formula for oblique incidence, we have to take into account all possible rays. The four simplest rays are shown in Fig. 6. All rays

Table 2
The contribution to the reflected ray from the four simplest rays as illustrated in Fig. 6. Assuming that the rays are attenuated according to the actual travelled distance inside of the film turns out to give an incorrect description of the absorption properties of the system. The amplitudes r_l, r_r, t_l, and t_r can be found in Tab. 3, k is the angular wave number in the film, and $2l$ is the path length the ray travels during one reflection inside the film, as illustrated in Fig. 6.

Ray 0	r_l
Ray 1	$t_l t_r r_r e^{2ikl}$
Ray 2	$t_l t_r r_r^3 e^{4ikl}$
Ray 3	$t_l t_r r_r^5 e^{6ikl}$
Ray N	$t_l t_r r_r^{2N-1} e^{2Nikl}$
Sum of all rays	$r_l + t_l t_r r_r e^{2ikl} \sum_{v=0}^{\infty} (r_r^2 e^{2ikl})^v$

Table 3
In general, when light propagates towards the surface of a material, part of the incoming radiation is transmitted and part of the incoming radiation is reflected at the boundary between the two materials. The transmitted amplitude, t, and the reflected amplitude, r, are given by Fresnel's equations [16, 22] and depend on the angle of incidence, θ_0, the angle of refraction, θ, and the polarization of the light. The amplitudes also depend on the refractive index of the material, which, in our case, is $n_0 = 1$ for air and n for the film, as shown in Fig. 4. The subscripts of the amplitudes indicate if the respective rays are approaching the boundary from the left (l) or from the right (r).

	Parallel polarization	Perpendicular polarization
r_l	$\frac{\cos\theta - n\cos\theta_0}{\cos\theta + n\cos\theta_0}$	$\frac{\cos\theta_0 - n\cos\theta}{\cos\theta_0 + n\cos\theta}$
t_l	$\frac{2\cos\theta_0}{\cos\theta + n\cos\theta_0}$	$\frac{2\cos\theta_0}{\cos\theta_0 + n\cos\theta}$
r_r	$\frac{n\cos\theta_0 - \cos\theta}{\cos\theta + n\cos\theta_0}$	$\frac{n\cos\theta - \cos\theta_0}{\cos\theta_0 + n\cos\theta}$
t_r	$\frac{2n\cos\theta}{n\cos\theta_0 + \cos\theta}$	$\frac{2n\cos\theta}{n\cos\theta + \cos\theta_0}$

are listed in Tab. 2. r_l, r_r, t_l and t_r are the amplitudes for reflection and transmission at the boundary and are given by Fresnel's equations [16]. They are shown in Tab. 3 for parallel and perpendicular polarized electromagnetic radiation.

In analogy to how the amplitudes for the reflected rays are found (see Tab. 2), the amplitudes of the transmitted rays can be found. We need to include all possible rays that contribute to the transmitted ray. It is important to notice that we also need to multiply the sum with the phase $e^{-ik_0 l}$. This phase corresponds to the phase the ray would obtain by passing through the region of the film as if the film were not there. The explicit expression is given by

$$t = \left[t_l t_r e^{ikl} \sum_{v=0}^{\infty} (r_r^2 e^{2ikl})^v \right] e^{-ik_0 l}. \tag{8}$$

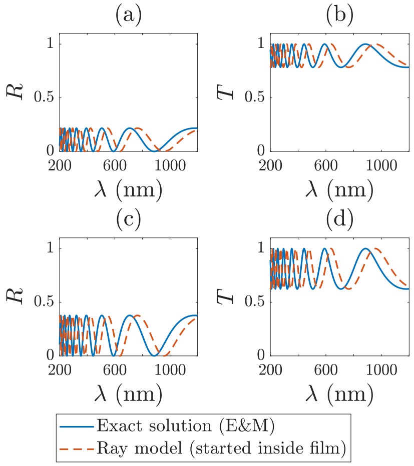

Figure 7: The reflection and transmission probabilities, $R = |r|^2$ and $T = |t|^2$, found by exact electromagnetic theory (blue solid lines) compared with R and T found by the incorrect ray model presented in Sec. 3.2 (red dashed line). The positions of the minima and maxima are not in agreement between the two models. The refractive index of the film is 1.84, and the thickness is 500 nm. The angle of incidence is 30°. (a) and (b) show R and T for parallel polarized light and (c) and (d) for perpendicular polarized light.

With the help of the expressions for r and t, the reflection and transmission probabilities can be found. Figure 7 shows R and T for a system as in Fig. 3, where the angle of incidence is 30° and the angle of refraction is 2.5. Frames 3a and b show the results for R and T for parallel polarized light, while Frames 3c and d show the results for perpendicular polarized light. In all frames we compare the exact E&M results (blue solid line) for the reflection and transmission probabilities with the results obtained by the ray model suggested in [20, 21] (red solid line).

We observe that the results obtained from the exact calculations (blue solid lines) do not agree with the results obtained from the ray model suggested in [20, 21]. For instance, the maxima and minima in all frames of Fig. 3 occur at different wavelength locations. While Fig. 3 shows the results for a specific incident angle of 30°, additional calculations show that the difference increases as the angle of incidence increases. Another remarkable observation is that for the exact E&M calculations the maxima and minima shift towards shorter wavelengths as we increase the angle of incidence. For the ray model implemented according to [20, 21] the opposite happens: the maxima and minima shift towards larger wavelengths. This shows that the ray theory suggested in [20, 21] is not viable as a method for obtaining an exact ray model. The correct procedure for obtaining an exact ray model is presented in the following section.

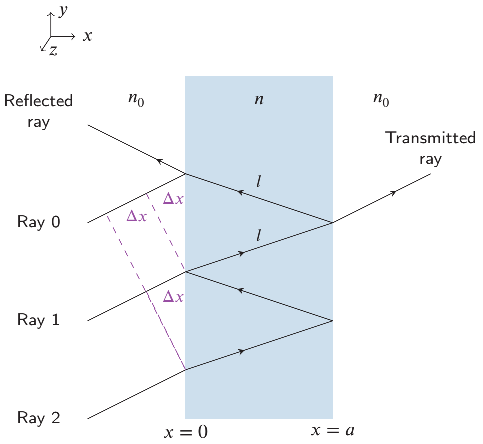

Figure 8: Three incoming rays (Ray 0, Ray 1 and Ray 2) that exit the system at the same position and contribute to the reflected ray. Two rays (Ray 1 and Ray 2) zig-zag in the interior of the film, exit at the same position, and contribute to the transmitted ray. n_0 and n are the refractive indexes of air and the material in the film, respectively. a is the film thickness and l is the geometrical path length the rays travel from the front surface to the back surface of the film. Δx is the path length difference that Ray 0 and Ray 1 (Ray 1 and Ray 2, respectively) travel outside of the film.

3.3. Ray model for oblique incident light - started according to the wave front

Correcting the ray model discussed in the previous section, we demonstrate in this section that we need to consider the phase difference of rays with respect to the wave front of the incoming and outgoing plane waves in order to obtain an exact ray model, i.e., a ray model that reproduces the exact electromagnetic results for oblique incidence. This procedure is in agreement with theory presented, e.g., by Fowles [22] and Hecht [23].

Let us consider the wave front of a plane wave as illustrated by the red dashed line in Fig. 8. When comparing the two incoming rays (Ray 1 and Ray 0) that merge into the same outgoing ray in Fig. 8, we find the path difference Δx due to the shorter propagation distance of ray 0 outside the film. Therefore, the difference in optical path length between *Ray 1* and *Ray 0*, as shown in in Fig. 8, is

$$2nl - \Delta x, \tag{9}$$

where n is the refractive index of the film and l is the geometrical length the ray travels inside the film. Compared to the ray model presented in the previous section, where we only took into account the path length inside the film, we obtain an additional term Δx by which the path difference is reduced.

By evaluating the contribution to the phase and the attenuation of the radiation caused by the difference in the travelled distance, simple geometrical considerations give an additional phase to Ray 1 in Fig. 8 equal to

Table 4
The contribution to the reflected ray from the four simplest rays as illustrated in Fig. 6. The phase collected according to the travelled distance is found by Eq. 10, which starts the ray at the wave front (see Fig. 8). r_l, r_r, t_l and t_r can be found in Tab. 3, k_x is the x-component of the angular wave number in the film given by Eq. (7), and a is the thickness of the film.

Ray 0	r_l
Ray 1	$t_l t_r r_r e^{2ik_x a}$
Ray 2	$t_l t_r r_r^3 e^{4ik_x a}$
Ray 3	$t_l t_r r_r^5 e^{6ik_x a}$
Ray N	$t_l t_r r_r^{2N-1} e^{2Nik_x a}$
Sum of all rays	$r_l + t_l t_r r_r e^{2ik_x a} \sum_{\nu=0}^{\infty} (r_r^2 e^{2ik_x a})^\nu$

$$e^{ik_0(2nl-\Delta x)} = e^{2ink_0 a\cos\theta} = e^{2ik_x a}, \tag{10}$$

where k_0 is the angular wave number in vacuum and k_x is the x-component of the angular wave number in the film described by Eq. (7). The quantities l, a, and θ are illustrated in Fig. 8 and Fig. 4. They are the geometrical path length inside the film, the thickness of the film, and the angle of refraction, respectively. Equation (10) shows that by evaluating the rays correctly, it turns out that the total reflection amplitude, as described by our ray theory, should only depend on the x-component of the wave number.

Therefore, a ray model that takes into account the phase difference collected by considering only the x-components of rays inside the film is equivalent to the exact ray model that uses the phase differences with respect to the incoming and outgoing wave fronts. The expressions for the four simplest rays and the Nth ray of the exact ray model are listed in Tab. 4.

The transmission amplitudes are found in analogy to the reflection amplitudes (see Tab. 4). Multiplying the factors in the ray sum by the phase $e^{-ik_{x,0}a}$, corrects for the phase the ray would have gained in the absence of a film. The sum of all possible rays that contribute to the transmission amplitude is therefore given by

$$t = \left[t_l t_r e^{ik_x a} \sum_{\nu=0}^{\infty} (r_r^2 e^{2ik_a x})^\nu \right] e^{-ik_{x,0}a}. \tag{11}$$

It can be shown that the sum of all possible rays in Tab. 4 and the sum given in Eq. 11 are in fact identical with the expressions in Tab. 1. This equivalence is obtained by performing the sum over the infinitely many rays using the summation formula for geometric series and by including the correct expressions for r_l, t_l, r_r, and t_r.

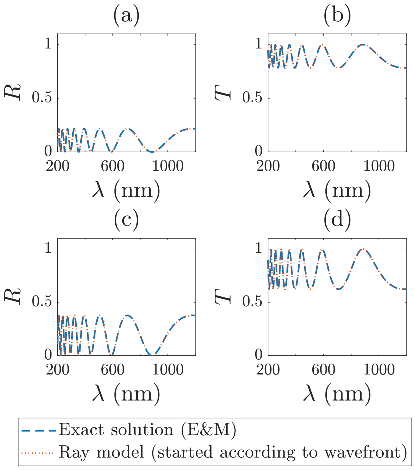

Figure 9: The reflection and transmission probabilities, $R = |r|^2$ and $T = |t|^2$, found by exact electromagnetic theory (blue solid line), compared with R and T found by the ray model presented in Sec. 3.3 (red dotted line). Both models yield identical spectra for R and T. The refractive index of the film is 1.84, and the thickness is 500 nm. The angle of incidence is 30°. (a) and (b) show R and T for parallel polarized light, and (c) and (d) for perpendicular polarized light.

Figure 9 shows that, contrary to the incorrect ray model discussed in Sec. 3.2, the ray model presented in this section agrees completely with the results of exact electromagnetic theory and yields the same resonance structure. The system underlying the results in Fig. 9 consists of a film of thickness 500 nm and a refractive index equal to 1.84. The angle of incidence is 30°. To produce the results in Fig. 9 it was necessary to include only 10 rays in the ray sum. Based on this fact, we conclude that, in general, only a few rays are needed to describe the system with close to perfect accuracy. This is in agreement with the observations for the one-dimensional ray model [15].

4. Exact ray theory for oblique incidence with absorption

When the film is absorptive, part of the light entering the film is absorbed. In order to construct a ray model for an absorptive film, a system as in Fig. 10 is considered. The system consists of a film with a perfect mirror behind it. In this case, no light is transmitted. In the absence of absorption this system would have reflection probability equal to 1.

In order to evaluate how the system behaves in this case, we consider how reflection and refraction are described at a boundary of an absorptive medium. The approach presented by Fowles [22] describes how a plane wave behaves at a boundary.

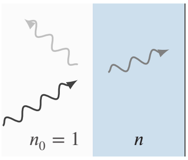

Figure 10: Oblique incident radiation is propagating from air, with refractive index $n_0 = 1$, towards a material with refractive index n. When the material is absorptive, i.e., $n \in \mathbb{C}$, a part of the radiation is absorbed by the material, while the rest is back-reflected.

For an absorptive material, the refractive index is a complex number given by

$$n = n_r + i n_i. \tag{12}$$

In addition, the wave propagation vector inside the film is also complex and given by

$$\vec{k} = \vec{k}_r + i\vec{k}_i. \tag{13}$$

The plane wave inside the material with amplitude A is denoted by

$$A e^{i\vec{k}\cdot\vec{r}} = A e^{-\vec{k}_i\cdot\vec{r}} e^{i\vec{k}_r\cdot\vec{r}}. \tag{14}$$

For a film infinitely extended in the y direction, the field needs to be translationally invariant along the boundary. From this it follows that $\vec{k}_r$ and $\vec{k}_i$ have different directions. The wave is said to be *inhomogeneous*. $\vec{k}_i$ is normal to the boundary. From this it follows that the wave is attenuated in the same direction.

From the argumentation in Fowles [22] it follows that the components of the wave vector are given by

$$k_x = k_0\sqrt{n^2 - \sin^2\theta_0}, \tag{15a}$$

$$k_y = k_{y,0} = k_0 \sin\theta_0. \tag{15b}$$

The equations stated above are identical to the expressions for the components given in Sec. 3 (Eqs. 7 and 6, respectively). When absorption is present, k_x is complex.

The exact expression for the reflection amplitude can be found by electromagnetic theory. By setting the surface charge to zero, and the free surface current to zero, the reflection amplitude for a plane wave that is propagating with an oblique angle of incidence is given by

$$r_{perp} = -\frac{k_x + i k_{x,0}\tan(k_x a)}{k_x - i k_{x,0}\tan(k_x a)}, \tag{16}$$

for perpendicular polarized light, and by

$$r_{par} = -\frac{n^2 k_{x,0} + i k_x \tan(k_x a)}{n^2 k_{x,0} - i k_x \tan(k_x a)}, \tag{17}$$

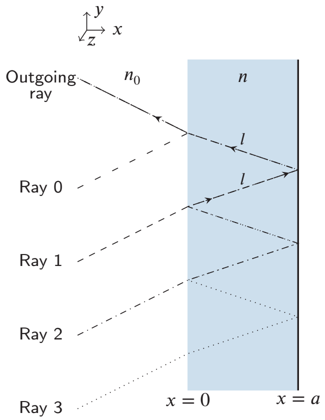

Figure 11: Schematic illustration of the ray model for the thin-film system of Fig. 4. By adding up the amplitudes from all possible rays that contribute to the outgoing ray, the absorption cross section can be found. The path length of the shortest ray that is transmitting through the front of the film and is reflected at the mirror on the backside of the film is $d = 2l = \frac{2a}{\cos\theta}$. θ is the angle of refraction as shown in Fig. 4.

for parallel polarized light, where n is the complex refractive index of the film, a is the thickness of the film and $k_{x,0}$ and k_x are the x-components of the angular wave numbers in air and inside the material, respectively.

Naïvely, according to Beer-Lambert's law, one would expect the rays to lose intensity along their trajectory. However, it turns out, by following the argumentation in Sec. 3.3, that only the x-component of the wave vector is needed in order to evaluate the system in terms of rays.

By summing over all rays that contribute to the reflected ray, as shown in Fig. 11, we can build an exact ray model that includes absorption in analogy to the way we built a ray model without absorption in Sec. 3.3.

In Tab. 5 the expressions for the four simplest rays and the Nth ray of the exact ray model, including absorption, are listed.

Summing over all rays, we obtain an expression for the reflection amplitude as

$$r = r_l + t_l t_r e^{i\pi} e^{2ik_x a} \sum_{\nu=0}^{\infty} (e^{i\pi} r_r e^{2ik_x a})^{\nu}, \tag{18}$$

where r_l, t_l, r_r and t_r are the amplitudes (computed according to Fresnel's equations given in Tab. 3) that the rays incur along their paths due to reflection or transmission at the boundary between air and film. The term $e^{i\pi}$ is the phase caused by reflection at the mirror, and $e^{2ik_x a}$ is the phase collected according to the travelled distance for the different rays.

It can be shown that Eq. (18) is in fact identical with the expressions in Eqs. (16) and (17). This equivalence is obtained by performing the sum over the infinitely many rays using the summation formula for geometric series and by including the correct expressions for r_l, t_l, r_r, and t_r.

Table 5
The exact absorption cross section for oblique incidence can be found by taking into account the phases and the attenuation of rays that start in the incoming wave front and end in the outgoing wave front. This is equivalent to considering only the x-components of the rays inside the film. r_l, r_r, t_l, and t_r are the amplitudes for reflection and transmission at the boundary at $x = 0$ according to whether the ray is approaching the boundary from the left or the right, respectively. The amplitudes can be found by use of Fresnel equations [16] and are shown in Tab. 3. $e^{i\pi}$ is the phase shift caused by reflection at the mirror.

Ray 0	r_l
Ray 1	$t_l t_r e^{2ik_x a} e^{i\pi}$
Ray 2	$t_l t_r r_r e^{4ik_x a} e^{2i\pi}$
Ray 3	$t_l t_r r_r^2 e^{6ik_x a} e^{3i\pi}$
Ray N	$t_l t_r r_r^{N-1} e^{2Nik_x a} e^{Ni\pi}$
Sum of all rays	$r_l + t_l t_r e^{2ik_x a} e^{i\pi} \sum_{\nu=0}^{\infty} (r_r e^{2ik_x a} e^{i\pi})^{\nu}$

5. Beams absorb according to Beer-Lambert law

In order to simulate a beam, we used the COMSOL Multiphysics® software to perform the modelling [24]. A Gaussian beam was sent towards a single film as in Fig. 3 with different angles of incidence (0°-50°). The spot radius of the beam is 5.0 μm, where the beam radius is defined as the distance from the center of the beam with maximum value E_0 to where the value of the electric field has dropped to $\frac{E_0}{e}$ or $\sim 0.37 E_0$ [23]. The beam has an energy corresponding to a wavelength of 500 nm. We compared two film thicknesses for the same width of the beam spot: In the first case the thickness of the film is chosen to be of the same size as the film, in the second case the thickness of the film is much larger than the width of the beam spot. The real part of refractive index of the film is set to 1.84.

Figure 12 shows the Gaussian beam in case of a non-absorptive film. In case of a thin film (5μm), the standing waves that are created are parallel to the film boundary. For the thicker film (75μm), we observe that the beam behaves as we would expect for a classical ray, except for the interference pattern in front of boundaries where the waves corresponding to an incoming and a reflected ray interfere.

In order to evaluate how radiation is absorbed inside the film as a function of the path, we evaluate the absorbance. The absorbance is given by

$$A = -\log_{10}(T_f), \tag{19}$$

where $T_f = \frac{I}{I_0}$. I_0 is the intensity of the beam when it enters the film and I is the intensity after a given path length [25].

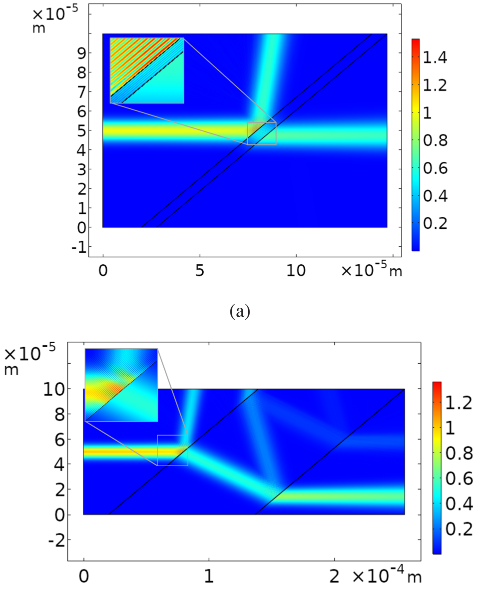

(a)

(b)

Figure 12: A Gaussian beam of spot radius 5μm is sent from the left towards a film of thickness (a) 5 μm and (b) 75 μm. The angle of incidence is 50° in both cases. The film is non-absorptive and has a refractive index of 1.84. Both frames, (a) and (b), show the norm of the electric field. In case (a) (thin film), the standing waves inside the film are parallel to the film boundary. Frame (b) (thick film) shows that the beam is reflected several times inside the film. We observe an interference pattern in areas where an incoming beam meets a reflected beam.

T_f can also be found by

$$T_f = \frac{|E|^2}{|E_0|^2} = e^{-2kn_i l}, \tag{20}$$

where E_0 and E are the electric fields when the beam enters the film and after a given path length, l, respectively; k is the angular wave number and n_i is the imaginary part of the refractive index [16]. The absorbance can therefore be found analytically by

$$A = 2kn_i l \log_{10}(e). \tag{21}$$

Therefore, the loss of energy is expected to follow Beer-Lambert's law (Fig. 13).

Let us first consider Beer-Lamberts law in the case of a thick film. Figure 13 shows the intensity of the electric field along the center of the beam as a function of path length. Figure 13a shows that the intensity decreases exponentially and Fig. 13b shows the trend by means of a logarithmic y-axis.

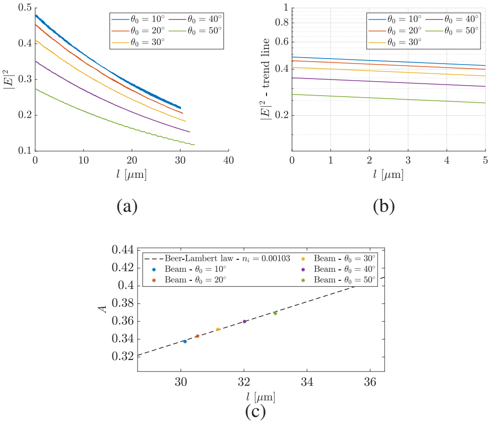

(a)

(b)

(c)

Figure 13: Intensity of the electric field $|E|^2$ along the path of the ray inside the film. The refractive index of the film is $1.84 + 0.001i$. The thickness of the film is 75 μm. Frame (a) shows how the intensity decreases along the central line of the beam inside the film from the point of entry into the film to a distance l inside of the film, terminating at $l \approx 30$ μm. This termination point is chosen to avoid areas with strong interference inside of the film. Frame (b) shows a log-plot of the average intensity inside of the film. Frame (c) shows the absorbance calculated by COMSOL for five different angles of incidence as shown in (a) and (b). The dashed line is the fitted line through the absorbance values for the five angles of incidence, resulting in an imaginary part of the refractive index of 0.00103, according to Eq. 21.

Figure 13c shows the absorbance, computed according to Eq. 19, for the five angles of incidence in Fig. 13a. The black, dashed line is the fitted line through the absorbance values for the five angles of incidence, resulting in $n_i = 0.00103$, according Eq. 21. Therefore, unlike in the case of oblique plane-wave incidence, where we saw that absorption only happens in x-direction, the simulation of the beam predicts that, in accordance with Beer-Lambert's law, the absorption is along the path of the beam.

The situation is different for a thin film. The behavior of the electric field in a thin film is shown in Fig. 12a. Locally, in the center of the beam, the electric field behaves as a plane wave and the standing waves are normal to the boundary. In Fig. 14a the absolute square of the electric field is plotted inside of the film as a function of the distance along the normal of the boundary at the center of the beam shown in Fig. 12a.

In Fig. 14b, the solid line is the trend of the absolute square of the electric field, $|E|^2$, in the center of the beam as a function of the distance along the normal of the boundary, plotted with a logarithmic y-axis. The dashed lines in Fig. 14b indicate how we would expect the absorption to take place as described in Sec.4.

Figure 14c shows the trend (blue solid line) and the expected absorption (red dashed line) in the case of an angle of incidence equal to 50°. The yellow solid line indicates how $|E|^2$ decays if we assume that the absorption decreases as a function of the full path length of the classical ray. For

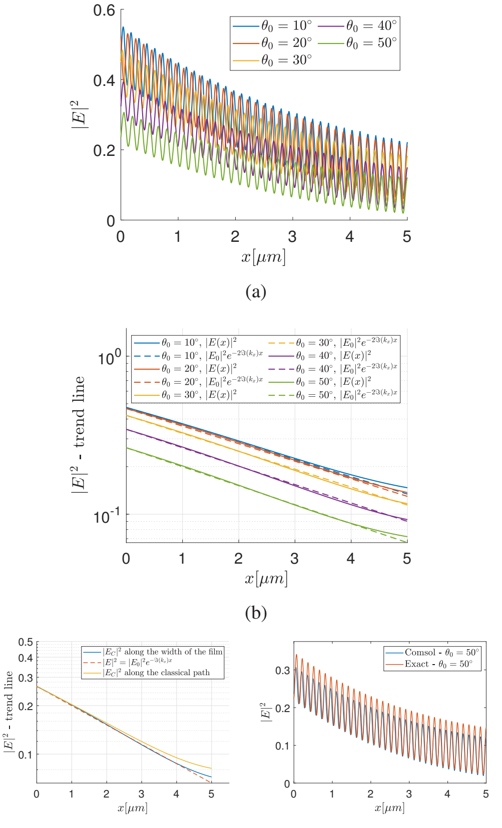

(a)

(b)

(c) (d)

Figure 14: Frame (a) shows the absolute square of the electric field, $|E|^2$, in the center of the beam along the normal of the boundary of the film. In frame (b), the solid line shows the trend of $|E|^2$ (without the resonances) with a logarithmic y-axis. The dashed lines in (b) indicates the expected absorption in the case of absorption along the normal of the film, as described in Sec. 4. Frame (c) shows the trend of $|E|^2$ in the case of an angle of incidence equal to 50°. The blue solid line is the trend as shown in (b), the red dashed line is the expected absorption as in frame (b). The yellow solid line is the absorption along the classical path of the Gaussian beam as a function of x. ($x = l\cos(\theta)$, where l is the travelled length along the classical path and θ is the refraction angle.) The blue line in frame (d) shows $|E|^2$ along the normal of the boundary in the center of the beam. The red line indicates the exact behavior of $|E|^2$ for a plane wave with a wavelength of 500 nm along the normal.

comparison this decrease is projected on the x-component. We see that the absorption actually decreases along the x-component for a thin film. We observe further that the deviation increases as x increases.

In Fig 14d, $|E|^2$ is plotted together with the exact description of $|E|^2$ in the case where an infinite plane wave hits the film. The angle of incidence is 50°. We observe that the resonances occur at the same x-positions for both models.

It is straightforward to explain this result. In the case of plane-wave incidence, the system, which includes the incident, reflected, and transmitted waves, as well as the film itself, is translationally invariant in the y-direction. Therefore, there is no possibility of absorption in the y-direction, since any exponential decay in y-direction would break translational invariance.

In addition to this mathematical explanation, there is a physical explanation: In a situation with a plane incident wave on an infinitely extended film in the y-direction, the y direction is continuously fed by incoming radiation with components in the y-direction, all along the boundary of the film. Therefore, because of this continuous power input along the boundary, decay in the direction of the boundary cannot happen. This is very different for a beam with a beam spot that is small with respect to the film thickness. In this case, from the perspective of the beam, the material looks homogeneous, which means that absorption also happens in the y-direction. Since the beam breaks the translational symmetry in the y-direction, there is also no formal symmetry argument that would prevent dissipation in y-direction. In other words, because of the localization of the beam, and unlike in the incident plane-wave situation, energy dissipated in the y-direction is not replenished. Therefore, absorption happens in both x- and y-directions, i.e., along the path of the beam, in accordance with Beer-Lambert's law.

The above arguments also give rise to the prediction of a transition from pure x-absorption in the case of incident plane waves to pure Beer-Lambert's law in the case of thin, sharply localized beams: If the beam waist is much smaller than the film thickness, then we expect Beer-Lambert's law to hold. In the opposite case, where the beam waist is much larger than the film thickness, we expect the case of pure x-absorption to hold. Since optically thin solar-cell structures are typically of the order of the wavelengths of the incident light, and since the widths, i.e., the illumination areas of solar cells are typically much larger than a wavelength, we expect the case of pure x-absorption to be the relevant case for optically thin solar cells in practical applications.

6. Resonances in an optically thin SiN_x film

In order to demonstrate experimentally how the resonance structures change as a function of the angle of oblique incidence, we measured the reflection probability R as a function of the angle of incidence for a thin, layered film. We fabricated a sample consisting of a thin layer of SiN_x on top of a 270-nm-thick aluminum layer. The SiN_x/Al stack was prepared on top of a 273-μm-thick, mechanically polished (i.e. co-planar), single-crystalline Si substrate. SiN_x can be used as an anti-reflection coating layer for solar cells. The thickness of the SiN_x layer was $\sim$ 400 nm, as determined by ellipsometry measurements carried out on a SiN_x film deposited on bare Si substrate using a VASE ellipsometer from J. A. Woollam Co., Inc. The SiN$_x$ film was prepared by plasma-enhanced chemical vapor deposition (PECVD) in an Oxford Plasmalab 133 system. The Al film was sputter-deposited on Si substrate in an inline sputter-coating system from Leybold Optics (model A550V7).

Although the complex index of refraction n of SiN$_x$ is wavelength dependent, for our purposes it can be assumed to be constant. Moreover, since n was not specifically measured for our particular sample (SiN$_x$/Al/Si), but to be able to compare the measured resonance structures qualitatively with our theoretical ray models, we assume a generic, constant value for the complex index of refraction of $n = 1.84 + 0.012i$ [26]. The reflection probability R was measured using a home-built spectral response measurement system consisting of a Newport Oriel Apex illuminator with a Cornerstone 260 monochromator, a set of collimating and focusing lenses, and an integrating sphere with center-mounted sample holder from Labsphere (model RTC-060-SF). An achromatic depolarizer (Thorlabs model DPU-25) was used to convert the beam of light from the monochromator into a pseudo-random polarized beam of light. The reflected beam from the sample was collected by a silicon photodiode detector (Hamamatsu model S1336-5BQ). The measurements were performed with an angle of incidence equal to 10°, 20°, 30°, 40°, and 50°. The sample was illuminated by a partly coherent, monochromatic light. The exact bandwidth (spectral resolution) of the monochromatic light in our experiment was not explicitly measured, but according to the specifications for this monochromator with a slit width manually set at 1.002 mm in the Oriel TracQ basic software, the bandwidth typically varies from $\Delta\lambda = 3.2$ nm and 3.1 nm at blaze wavelengths of 350 nm and 750 nm, respectively, to $\Delta\lambda = 6.4$ nm at blaze wavelength of 1000 nm in the spectral range of interest in our experiment, i.e., 350 to 1100 nm. Thus, the coherence length, l_c, of our light source/monochromator combination can be found according to

$$l_c = \frac{\lambda^2}{\Delta\lambda}, \tag{22}$$

where λ is the wavelength and $\Delta\lambda$ is the bandwidth [22]. Thus, the coherence length in our experiments is at least $(350\,\text{nm})^2/3.2\,\text{nm} \approx 38\,\mu$m, which, compared to the thickness of our film, is large. Therefore, we can assume that our sample is irradiated by a coherent light source that allows us to see resonance structures in the reflection probability R as a function of λ.

Figure 15(a) shows the measured reflection probability R as a function of the wavelength. In Fig. 15(c) we trace the position of an absorption resonance , i.e., a dip in the R, in our measured data (squares in Fig. 15(c)) as a function of the angle of incidence. At 10° this resonance occurs at approximately 600 nm and, as shown in Fig. 15(c), shifts toward lower wavelengths as a function of increasing angle of incidence. The predictions of our correct ray theory (presented in Seg. 3.3), stars in Fig. 15(c), follow this trend. The predictions of the incorrect ray theory, discussed in Sec. 3.2, show an incorrect upward trend and strongly disagree with both our measured results and our exact ray model. Thus, from this three-way comparison, we conclude that a ray model built on only considering rays inside the film, gives wrong predictions of the wavelengths at which film resonances will occur. As shown in Fig. 15(c)), the error increases as the angle of incidence increases.

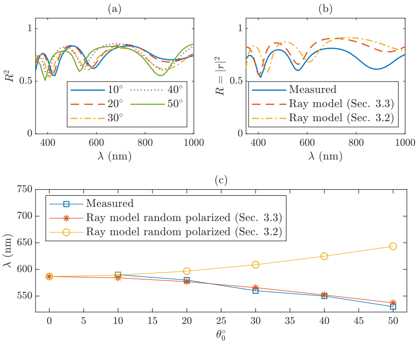

Figure 15: Frame (a) shows the measured reflection probability R for an optically thin SiN$_x$ film. With increasing wavelength, the resonances are shifted towards shorter wavelengths as expected from Fig. 5. In frame (b) R is plotted as a function of wavelength for the measurements and the two ray models for an angle of incidence of 30°. Frame (c) shows the position of an absorption resonance (dip in R) of the measured R between 500 and 600 nm [see frame (a)] (squares) as a function of the angle of incidence in comparison with the positions predicted by our exact ray model of Sec. 3.3 (stars) and by the incorrect ray model of Sec. 3.2 (circles). The predictions of the incorrect ray model (circles) clearly deviate from the predictions of the correct ray model (stars), which, in turn, agree with our measurements (squares).

There are many instances where a resonance structure such as the one illustrated in Figure 15(a), can be observed directly in nature. An example is the colorful pattern that can be seen in thin oil films floating on top of water puddles or on the surface of soap bubbles. If the angle of illumination changes, the color changes. The color change is caused by the change in the position of the resonances as illustrated in Figure 15(a). In summary, as we showed in this section, constructing a ray model that describes the positions of resonances quantitatively and accurately needs to be build on rays that are started in the wave front.

7. Discussion

Basic physics textbooks (see, e.g. [20, 21]) describe and evaluate the resonance structures of thin-film wave systems on the basis of rays. We have earlier showed the importance of associating phases with the rays [15]. If this is done correctly, the rays will also describe the resonances caused by the wave nature of light. Several basic textbooks base their ray models on evaluating the path differences inside the film only (see, e.g., [20, 21]). A ray model which is based on this set-up is presented in Sec. 3.2. As Fig. 7 shows, this approach gives an incorrect description of the system. The ray model presented in Sec. 3.3 shows how we also have to include the travelled distance outside the film when we evaluate how different rays contribute to an outgoing ray. We need to evaluate the rays from one common ray front as shown in Fig. 8. In the present paper we have shown that an exact description of the absorption cross section can be obtained by summing all possible rays in a wave front that are propagating with oblique incidence through boundaries. We have shown that it is important to compute the phases of contributing rays with respect to the incoming wave front.

The ray model for the general case of oblique incidence is expected to be valid for any situation where the ray splitting surfaces are planar; they do not need to be parallel. Corners and edges are expected to introduce small errors. The strategy for a general situation where the ray model is used is to consider an incoming wave front and a defined outgoing direction. The Fresnel equations are used to calculate the reflection and transmission amplitudes each time rays hit a boundary between two materials and are split into a transmitting and reflecting ray. Additional phases collected by the rays along their paths need to be taken into account and the phases collected by reflection at a mirror.

Ray tracing is a frequently used approach for estimating the absorption efficiency of solar cells. Ray models that describe solar cells are often used to investigate systems where the system dimensions are much larger than the wavelength of the incident radiation [2, 27, 28, 29, 30, 31]. In these cases the phases are not included in the models at all. However, some models have already been presented that use the phases of rays, but they are not taking the wave front into account [32].

Only a few simple rays are necessary to describe the absorption properties of the investigated system. This is an advantage of our ray theory compared with time consuming numerical calculations of the electric field of the systems. As the complexity of the system increases, it is expected that more rays need to be included [15]. The system investigated is a single film with mirror. This system can be extended to a system consisting of several layers using the hierarchical summation scheme (HSS) [15]. HSS needs to be applied in conjunction with the angle-dependent Fresnel equations and the x-components of the angular wave number. HSS is summing up the contributing rays in the correct order. A further adjustment of the presented ray theory and the HSS method makes it possible to use the ray theory to include the investigation of surface-structured systems.

In the way of additional support for our exact ray model, we presented experimental measurements of R for a SiN_x-layer with a thickness of 400 nm. We obtained excellent agreement between our exact ray theory and the experiments, but noted a marked deviation of the results of the incorrect ray theory presented in some text books. This shows that the phase corrections that distinguish our exact theory from alternative, inexact theories are not small effects, but are sizable effects that can easily be observed in practice. Since ray methods are frequently used for designing better solar-cell geometries for improved light trapping, using an incorrect ray method may result in a failed solar-cell design and thus has practical consequences. Thus, in summary, we conclude that both in view of theoretical and practical considerations, it is important for the construction of exact ray models to evaluate the optical path lengths of rays starting from the wave front in order to obtain a correct results that agree with exact electromagnetic theory, in particular to obtain the correct positions of resonances in optically thin solar cells.

8. Conclusion

In this paper we presented an extension of the ray theory that is capable of describing the exact absorption properties for a film system where a plane wave is propagating towards the system with an arbitrary angle of incidence. This is done by summing up all possible rays that are contributing to an outgoing ray. Fresnel's equations are used to determine the reflection and transmission amplitudes for each ray splitting. The extended ray theory works for both perpendicular and parallel polarized light. We showed that it is important to carefully include the phases of the rays based on their travelled distances, and to include both travelled distance inside and outside of the film. If this is not done correctly, one obtains incorrect results for solar-cell properties, such as reflection probabilities and resonance structures. On the other hand, a correct ray description, as shown in this paper, provides a powerful ray-based tool that in some applications, for instance in solar-cell design, may rival equivalent E&M-based wave simulations in computational efficiency.

Acknowledgement

This work was supported by the grant *Development of a new ray model for understanding the coupling between dielectric spheres for photovoltaics with higher efficiency* - No: 250678 financed by The Research Council of Norway.

References

[1] C. Ulbrich, M. Peters, B. Bläsi, T. Kirchartz, A. Gerber, U. Rau, Enhanced light trapping in thin-film solar cells by a directionally selective filter, Optics Express 18 (2010) A133–A138.

[2] E. Seim, A. Kohler, R. Lukacs, M. A. Brandsrud, E. S. Marstein, E. Olsen, R. Blümel, Chaos: a new mechanism for enhancing the optical generation rate in optically thin solar cells, in: Physics, Simulation, and Photonic Engineering of Photovoltaic Devices VIII, volume 10913, International Society for Optics and Photonics, 2019, p. 109131O.

[3] E. Seim, A. Kohler, R. Lukacs, M. A. Brandsrud, E. S. Marstein, E. Olsen, R. Blümel, Chaos: A new mechanism for enhancing the optical generation rate in optically thin solar cells, Chaos: An Interdisciplinary Journal of Nonlinear Science 29 (2019) 093132. URL: `https://doi.org/10.1063/1.5111042`. doi:`10.1063/1.5111042`. `arXiv:https://doi.org/10.1063/1.5111042`.

[4] F. Haake, Quantum Signatures of Chaos, 4th ed., Springer Berlin Heidelberg, Cham, Switzerland, 2018.

[5] H.-J. Stöckmann, Quantum chaos: an introduction, 2000.

[6] R. P. Feynman, QED : the strange theory of light and matter, volume [1] of *Alix G. Mautner memorial lectures*, Princeton University Press, Princeton, N.J, 1985.

[7] R. Blümel, Y. Dabaghian, R. V. Jensen, Explicitly solvable cases of one-dimensional quantum chaos, Phys.Rev.Lett. 88 (2002) 044101.

[8] Y. Dabaghian, R. Blümel, Explicit spectral formulas for scaling quantum graphs, Phys.Rev.E 70 (2004) 046206.

[9] A. S. Bhullar, R. Blümel, P. M. Koch, Ray splitting with ghost orbits: explicit, analytical and exact solution for spectra of scaling step potentials with tunneling, J. Phys. A: Math. Gen. 38 (2005) L563–L569.

[10] R. Blümel, J. T. M. Antonsen, B. Georgeot, E. Ott, R. E. Prange, Ray splitting and quantum chaos, Physical Review Letters 76 (1996) 2476–2479. doi:10.1103/PhysRevLett.76.2476.

[11] A. Kohler, G. Killesreiter, R. Blümel, Ray splitting in a class of chaotic triangular step billiards, Physical Review E 56 (1997) 2691.

[12] A. Kohler, R. Blümel, Annular ray-splitting billiard, Physics Letters A 238 (1998) 271–277.

[13] A. Kohler, R. Blümel, Weyl formulas for quantum ray-splitting billiards, Annals of Physics 267 (1998) 249–280.

[14] A. Kohler, R. Blümel, Signature of periodic lateral-ray orbits in a rectangular ray-splitting billiard, Physics Letters A 247 (1998) 87–92.

[15] M. Brandsrud, E. Seim, R. Lukacs, A. Kohler, E. Marstein, E. Olsen, R. Blümel, Exact ray theory for the calculation of the optical generation rate in optically thin solar cells, Physica E: Low-dimensional Systems and Nanostructures 105 (2019) 125–138.

[16] D. J. Griffiths, Introduction to Electrodynamics, 3rd ed., Prentice Hall, Upper Saddle River, N.J, 1999.

[17] D. Cozza, C. M. Ruiz, D. Duché, S. Giraldo, E. Saucedo, J. J. Simon, L. Escoubas, Optical modeling and optimizations of cu2znsnse4 solar cells using the modified transfer matrix method, Opt. Express 24 (2016) A1201–A1209. URL: http://www.opticsexpress.org/abstract.cfm?URI=oe-24-18-A1201. doi:10.1364/OE.24.0A1201.

[18] L. L. SÃąnchez-Soto, J. J. MonzÃşn, A. G. Barriuso, J. F. CariÃśena, The transfer matrix: A geometrical perspective, Physics Reports 513 (2012) 191–227. doi:10.1016/j.physrep.2011.10.002.

[19] B. LipovsÌŇek, J. KrcÌŇ, M. TopicÌŇ, Optical model for thin-film photovoltaic devices with large surface textures at the front side = opticÌŇni model za tankoplastne fotonapetostne strukture z velikimi povrsÌŇinskimi teksturami na sprednji strani, Informacije MIDEM (2011) 264–271.

[20] P. A. Tipler, G. Mosca, Physics for scientists and engineers : with modern physics, 6th ed. ed., Freeman, New York, 2008.

[21] M. Alonso, E. J. Finn, Fundamental university physics, Reading, Mass. : Addison-Wesley Publishing Company, 1967.

[22] G. R. Fowles, Introduction to modern optics, Courier Corporation, 1989.

[23] E. Hecht, Optics, Pearson, 2015.

[24] S. COMSOL AB, Stockholm, COMSOL Multiphysics v. 5.4. www.comsol.com., 2020.

[25] R. Blümel, M. Bağcioğlu, R. Lukacs, A. Kohler, Infrared refractive index dispersion of polymethyl methacrylate spheres from mie ripples in fourier-transform infrared microscopy extinction spectra, Journal of the Optical Society of America A 33 (2016) 1687–1696.

[26] D. N. Wright, E. S. Marstein, A. Rognmo, A. Holt, Plasma-enhanced chemical vapour-deposited silicon nitride films; the effect of annealing on optical properties and etch rates, Solar energy materials and solar cells 92 (2008) 1091–1098.

[27] S.-J. Byun, S. Y. Byun, J. Lee, J. W. Kim, T. S. Lee, K. Cho, D. Sheen, S. J. Tark, D. Kim, W. M. Kim, Analysis of light trapping effects in Si solar cells with a textured surface by ray tracing simulation, Current Applied Physics 11 (2011) S23–S25. doi:10.1016/j.cap.2011.01.048.

[28] J. Gjessing, A. S. Sudbo, E. S. Marstein, Comparison of periodic light-trapping structures in thin crystalline silicon solar cells, Journal of Applied Physics 110 (2011) 8. URL: <GotoISI>://WOS:000293956600005. doi:10.1063/1.3611425.

[29] T. Uematsu, M. Ida, K. Hane, Y. Hayashi, T. Saitoh, A new light trapping structure for very-thin, high-efficiency silicon solar cells, in: Conference Record of the Twentieth IEEE Photovoltaic Specialists Conference, IEEE, 1988, pp. 792–795.

[30] H. Holst, M. Winter, M. R. Vogt, K. Bothe, M. Köntges, R. Brendel, P. P. Altermatt, Application of a new ray tracing framework to the analysis of extended regions in Si solar cell modules, Energy Procedia 38 (2013) 86–93.

[31] E. Yablonovitch, Statistical ray optics, Journal of the Optical Society of America A 72 (1982) 899–907.

[32] B. Lipovšek, J. Krč, M. Topič, Optical model for thin-film photovoltaic devices with large surface textures at the front side, Informacije Midem 41 (2011) 264–271.

Appendix C

Paper III

Highlights

Investigation of resonance structures in optically thin solar cells

Maren Anna Brandsrud,Reinhold Blümel,Rozalia Lukacs,Eivind Seim,Erik Stensrud Marstein,Espen Olsen,Achim Kohler

- Resonance enhancement of conversion efficiency in thin-film solar cells.
- Optimization of film thicknesses of layered optically thin solar cells optimizes the resonances structure and absorption efficiency.
- Contrary to intuition, coupling of resonances does not always lead to increased conversion efficiency.

Investigation of resonance structures in optically thin solar cells

Maren Anna Brandsrud[a,*], Reinhold Blümel[b], Rozalia Lukacs[a], Eivind Seim[a], Erik Stensrud Marstein[c,d], Espen Olsen[a] and Achim Kohler[a]

[a] Norwegian University of Life Sciences, Faculty of Science and Technology, Drøbakveien 31, 1432 Ås, Norway
[b] Wesleyan University, Department of Physics, 265 Church Street, Middletown, CT 06459, United States of America
[c] Institute for Energy Technology, Department of Solar Energy, Instituttveien 18, 2007 Kjeller, Norway
[d] University of Oslo, Department of Technology Systems, Gunnar Randers Vei 19, 2007 Kjeller, Norway

---

ARTICLE INFO

Keywords:
Optically thin solar cells
Resonance enhancement
Conversion efficiency
Coupling of resonances

ABSTRACT

In order to reduce costs, the solar cell industry is aiming at producing ever thinner solar cells. Structuring the surfaces of optically thin solar cells is important for avoiding excessive transmission-related losses and, hence, to maintain or increase their efficiency. Light trapping leading to longer optical path lengths within the solar cells is a well established field of research. In addition to this, other possible benefits of structured surfaces have been proposed. It has been suggested that nanostructures on the surface of thin solar cells function as resonators, inducing electric-field resonances that enhance absorption in the the energy-converting material. Further, coupling of electric field resonances in periodically structured solar cells may couple with each other thereby increasing the absorption of energy. A deeper understanding of the nature of the energy-conversion enhancement in surface-structured and thin solar cells would allow to design more targeted structures.

Generally, efficiency enhancement may be evaluated by investigating the electric field and optimizing the optical generation rate. Here, we establish a model system consisting of multi-layered solar cells in order to study resonances and coupling of resonances in a one-dimensional system. We show that resonances in energy-converting and non-energy converting layers exist. The coupling of resonances in the non-energy converting material and the energy-converting material is only possible for certain parameter ranges of thickness of the energy converting material and the imaginary part of the refractive index. We evaluate the resonances and the coupling of resonances in different thin-film systems and show how they affect the total absorption of energy in the energy converting layer. We show how resonances in non-absorbing layers can contribute to increasing the resonances in the absorbing layers. We optimize the parameters of the multilayered thin-film systems to achieve an increase in the amount of the absorbed energy. The optimization is also evaluated for an experimentally realizable thin-film solar cell.

1. Introduction

The solar-cell industry is continuously on the lookout for ways to reduce material usage in the production of solar cells while maintaining conversion efficiency in order to increase the cost-efficiency of solar-cell devices [1, 2]. While thin, crystalline silicon solar cells exhibit lower absorption than thicker, traditionally crystalline silicon wafer cells [1], absorption in optically thin solar cells can be enhanced by surface structuring, e.g., by adding surface structures to the top layer of thin solar cells [3, 4]. The most established approach is light trapping, wherein the path length of light in the absorber is increased because of the surface structures. Light trapping is common in surface-structure solar cells where the surface structures are larger than the wavelength employed, i.e. in the short wavelength limit. It has also been shown that nano-structured surfaces cause resonances in the electric field which increase the absorption in the absorptive material below [3]. Coupling of resonances into the nano-structures has also be discussed as a mechanism for absorption enhancement in structured thin-film solar cells [5, 6]. A different mechanisms that has been used to address enhancement of absorption efficiency of thin solar cells is to minimize the energy losses due to reflection [7]. A possible way to achieve this is to add one or more thin dielectric layers on the top of the solar cell as anti-reflection coatings (ARC). While single layer ARCs are standard in the industry today, many studies have been carried out to optimize thin-film solar cells consisting of two different layers in order to find an optimal combination of the refractive indexes and thicknesses of the materials [8].

---

[*] Corresponding author
✉ `maren.brandsrud@nmbu.no` (M.A. Brandsrud)
ORCID(s):

The aim of the current study is to study absorption efficiency in the energy converting layer of a solar cell as a function of the appearance of resonances in the absorbing and non-absorbing layers of a thin-film solar cell. For this purpose we developed a simple model system that exhibits resonances and allows to investigate the implication of these resonances on absorption in the energy-converting material. A simple system that can exhibit resonances is a multilayered film system. A multilayered film system can be set up by absorbing and non-absorbing layers. It can be used to investigate how resonances in the non-absorbing layers affect the absorption in the absorbing layers. It can be further used to investigate how absorption can be enhanced by tuning the refractive index and the thicknesses of the absorbing and non-absorbing layers involved. Therefore, our work is strongly related to optimization of anti-reflection coatings [7], but it focuses on a different aspect, namely the effect of resonances in layered films on the absorption in the energy-converting film.

In order to study the effectiveness of the device, we evaluate the absorption efficiency, σ_a [9, 10, 11]. In order to take into account the characteristics of the solar spectrum, absorption efficiency can be weighted by the solar spectrum. The resulting quantity is called the optical generation rate [12]. The systems evaluated in this study are three-dimensional systems where the incoming light is a plane wave propagating towards the system and where the propagation direction is perpendicular to the surfaces. Because of normal incidence, the systems are invariant in two dimensions and effectively one-dimensional systems.

The paper is organized as follows: In Sec. 2, we present the systems that we evaluate and relevant theory. The first part of Sec. 3 (Sec. 3.1-Sec. 3.3), evaluates systems with wavelength-independent refractive indices. We investigate how the absorption efficiency and the resonance structure in the layered films depend on the size of the imaginary part of the refractive index. We show that our results agree with the Fresnel equations [13] for non-magnetic dielectric materials. We investigate further if the thickness of the layers can be optimized with respect to absorption efficiency and material usage. We show how resonances in the non-absorptive material enhance the absorption of light in the energy converting film. Section 3.3 evaluates how two non-absorptive layers can be used to increase the absorption efficiency. We evaluate the effect of coupling of resonances between non-absorptive layers, when the absorptive layer is between two non-absorptive films. We evaluate how the coupled resonances of the two non-absorptive layers and resonances in the absorptive layer can affect the absorption efficiency. In Sec. 3.4, we further demonstrate that our approach can be useful in the optimization of real solar-cell material by optimizing the thickness of the layers of an experimentally realizable solar cell in Sec. 3.4.

2. Theory

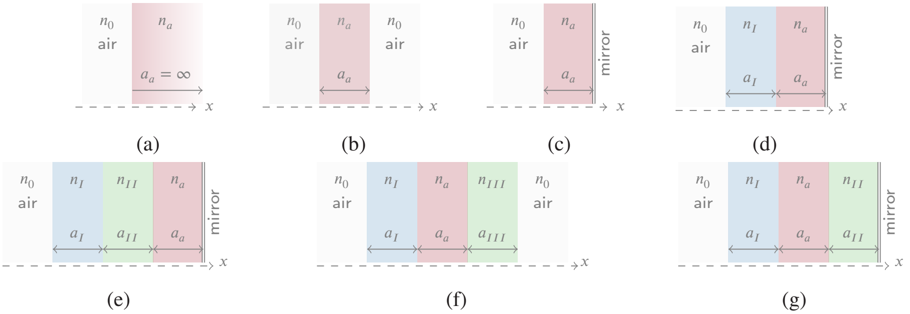

Figure 1: The systems evaluated are one-dimensional systems. The incident light is a plane wave of amplitude equal to 1 propagating from the left where the refractive index is $n_0 = 1$. In (a) the system consisting of a boundary between n_0 and the absorptive material with an refractive index of n_a and an infinite thickness. The system in (b) consist of a finite absorptive film with refractive index n_a and a thickness a_a. System (c) is identical to system (b) except that a perfect mirror i placed behind the film. The systems (d) and (e) have the absorptive film placed behind one or two non-absorptive layers. A mirror i placed behind the absorptive film. The thicknesses of the non-absorptive films are a_I and a_{II} and refractive indices of n_I and n_{II}. System (f) has the non-absorptive layer between to non-absorptive layers with thicknesses a_I and a_{III} and refractive indices n_I and n_{III}. System (g) is equivalent with system (f) but has a backside mirror behind the third layer.

Optically thin solar cells consisting of layers with normal incidence light can be treated as one-dimensional systems and are therefore simple to handle numerically. The model system chosen in the current paper represents a one-dimensional system consisting of several thin layers with different absorbing and non-absorbing materials. Both the non-absorbing and the absorbing materials can function as resonators as we will see later. The systems that will be investigated are shown in Fig. 1. For all the systems, a plane wave with an amplitude equal to one is propagating towards the layers from the left. Figure 1a shows the simplest system, only consisting of a boundary between air and the absorptive material of refractive index n_a. The absorption properties of the absorptive film is described by the imaginary part of n_a. In Fig. 1a, the thickness of the absorptive material is assumed to be infinitely thick. In the system presented in Fig 1b, a single absorptive film of thickness a_a and refractive index n_a is shown. For Figs. 1c-1e, we assume a backside mirror behind the layers, reflecting back all the radiation perfectly. The thickness of the absorptive layer is a_a and has a refractive index of n_a. The refractive indices of the non-absorptive layers are n_I and n_{II} with a thickness of a_I and a_{II}. The system presented in Fig. 1f is the system used to evaluate coupling between a non-absorptive layer on each side of the absorptive layer. Figure 1g show an identical system to the one presented in Fig. 1f, but with a backside mirror behind the third layer.

Since we only consider normal incidence and thus treat the model system in one dimension, we do not need to consider the polarization. The model system can therefore be described by scalar wave theory, which provides an exact description of the wave mechanics in the film structures. The one-dimensional model is completely equivalent to the three-dimensional film system with normal incident light.

We set the first boundary from the left for the systems shown in Fig. 1 at $x = 0$ and obtain the wave functions given in Tab. 1. The amplitudes of the wave functions in Tab. 1 can be found by requiring that the wave functions and their first derivatives are continuous across the boundary [14].

For layered systems, the amount of absorbed light can be calculated via the absorption efficiency σ_a, given by

$$\sigma_a = 1 - |r|^2 - |t|^2, \tag{1}$$

where r is the amplitude of the reflected plane wave and t is the amplitude of the transmitted wave [9, 10, 15]. The reflection probability of the system is given by $|r|^2 = R$ and the transmission probability is given by $T = |t|^2$. When the refractive index is real for all films involved, $|r|^2 + |t|^2 = 1$ and the absorption efficiency $\sigma_a = 0$. If a mirror is placed behind the system, there is no transmitted wave, i.e. $t = 0$, and the absorption efficiency is given by

$$\sigma_a = 1 - |r|^2 \tag{2}$$

The amplitude of the reflected wave can be found by requiring a continuous scalar wave function and a continuous first derivative of the scalar wave function at all interfaces [14, 15]. For simple systems with a few layers of materials, the calculation of σ_a is straightforward. For systems consisting of several layers, the transfer matrix method [16] may be used. Alternatively, a hierarchical summation scheme suggested by Brandsrud et. al. [9] can be employed.

The absorption efficiency is also related to the absolute value of the scalar wave function, $\psi(x)$, in a one dimensional system by

$$\sigma_a = 2k \int n_r(x) n_i(x) |\psi(x)|^2 dx, \tag{3}$$

where k is the angular wave number in vacuum of the incoming wave and the refractive index of the system is given by $n(x) = n_r(x) + i n_i(x)$ [9]. When the wave function has higher absolute values, we expect that the absorption efficiency increases. Since resonances appear locally and lead therefore locally to increased absorption efficiencies, it is interesting to evaluate if the absorption efficiency increases over the whole solar spectral range for a given system as well. In order to evaluate if the absorption properties of a layered system are enhances, the averaged absorption efficiency, $\bar{\sigma_a}$, needs to be considered for whole wave length interval. In order to take into account the characteristics of the solar spectrum, the integral in Eq. 3 can be weighted by the solar spectrum.

The refractive index n is in general wavelength dependent [17]. In the first part of the paper, we consider thin-film systems with an index of refraction that is independent of the wavelength. In the second part of the paper, we evaluate an experimentally realizable solar cell. The refractive indices of the materials is found experimentally and are wavelength dependent.

Table 1
The wave functions for the systems shown in Fig. 1. The first boundary from the left is assumed to be at $x = 0$. The amplitude of the incoming plane wave is 1, r is the amplitude of the reflected wave and t is the amplitude of the transmitted wave. A, B, C, D, E and F are amplitudes of of the wave functions inside the films. k is the angular wave number given by $k = \frac{2\pi}{\lambda}$. n_I, n_{II}, n_{III} and n_a are the refractive indeces and a_I, a_{II}, a_{III} and a_a are the thicknesses of the films as indicated in the figure.

System a (Fig. 1a)	$\psi_a(x) = \begin{cases} e^{ikx} + re^{-ikx} & \text{for } x < 0 \\ Ae^{in_a kx} & \text{for } x > 0 \end{cases}$
System b (Fig. 1b)	$\psi_b(x) = \begin{cases} e^{ikx} + re^{-ikx} & \text{for } x < 0 \\ Ae^{in_a kx} + Be^{-in_a kx} & \text{for } 0 < x < a_a \\ te^{ikx} & \text{for } x > a_a \end{cases}$
System c (Fig. 1c)	$\psi_c(x) = \begin{cases} e^{ikx} + re^{-ikx} & \text{for } x < 0 \\ A\sin(n_a k(x - a_a)) & \text{for } 0 < x < a_a \end{cases}$
System d (Fig. 1d)	$\psi_d(x) = \begin{cases} e^{ikx} + re^{-ikx} & \text{for } x < 0 \\ Ae^{in_I kx} + Be^{-in_I kx} & \text{for } 0 < x < a_I \\ C\sin(n_a k(x - (a_I + a_a))) & \text{for } a_I < x < (a_I + a_a) \end{cases}$
System e (Fig. 1e)	$\psi_e(x) = \begin{cases} e^{ikx} + re^{-ikx} & \text{for } x < 0 \\ Ae^{in_I kx} + Be^{-in_I kx} & \text{for } 0 < x < a_I \\ Ce^{in_{II} kx} + De^{-in_{II} kx} & \text{for } a_I < x < (a_I + a_{II}) \\ E\sin(n_a k(x - (a_I + a_{II} + a_a))) & \text{for } (a_I + a_{II}) < x < (a_I + a_{II} + a_a) \end{cases}$
System f (Fig. 1f)	$\psi_f(x) = \begin{cases} e^{ikx} + re^{-ikx} & \text{for } x < 0 \\ Ae^{in_I kx} + Be^{-in_I kx} & \text{for } 0 < x < a_I \\ Ce^{in_a kx} + De^{-in_a kx} & \text{for } a_I < x < (a_I + a_a) \\ Ee^{in_{II} kx} + Fe^{-in_{III} kx} & \text{for } (a_I + a_a) < x < (a_I + a_a + a_{III}) \\ te^{ikx} & \text{for } x > (a_I + a_a + a_{III}) \end{cases}$
System g (Fig. 1g)	$\psi_g(x) = \begin{cases} e^{ikx} + re^{-ikx} & \text{for } x < 0 \\ Ae^{in_I kx} + Be^{-in_I kx} & \text{for } 0 < x < a_I \\ Ce^{in_a kx} + De^{-in_a kx} & \text{for } a_I < x < (a_I + a_a) \\ E\sin(n_{II} k(x - (a_I + a_a + a_{II}))) & \text{for } (a_I + a_a) < x < (a_I + a_a + a_{II}) \end{cases}$

3. Results

In this section we evaluate the different systems presented in Fig. 1.

3.1. Single film

We start with the system in Fig.1a which consists of an infinitely thick absorptive material with a wavelength-independent refractive index. The system is shown in Fig.1a. The real part of the refractive index of the absorptive layer n_a is set to 4.3. This is the real part of refractive index of silicon at a wavelength equal to 500 nm. We consider a range for the imaginary part of the refractive index, which we vary between 0 and 5. The wavelength interval evaluated is from 250 to 1000 nm. Since the absorptive layer is infinitely deep, all light that is entering the absorptive material will be absorbed. $\sigma_a(\lambda)$ is shown in Fig. 2a. For the system containing only one single boundary, the reflection and transmission coefficient r and t do not depend on the wavelength [9]. Figure 2a indicates that $\sigma_a(\lambda)$ decrease as n_i increases. This is expected since the absolute value of n increases, which results in an increased probability for reflection [9, 15]. In Fig. 2b, the averaged absorption efficiency, $\bar{\sigma}_a$ is showed as a function of n_i. As in Fig. 2a, we observe that an increased n_i is followed by a reduced $\bar{\sigma}_a$

When the absorptive material has a finite thickness which is in the order of the wavelength, standing waves can occur in the film. Figure 2c shows $\sigma_a(\lambda)$ for a single absorptive film as shown in Fig. 1b. The different graphs of

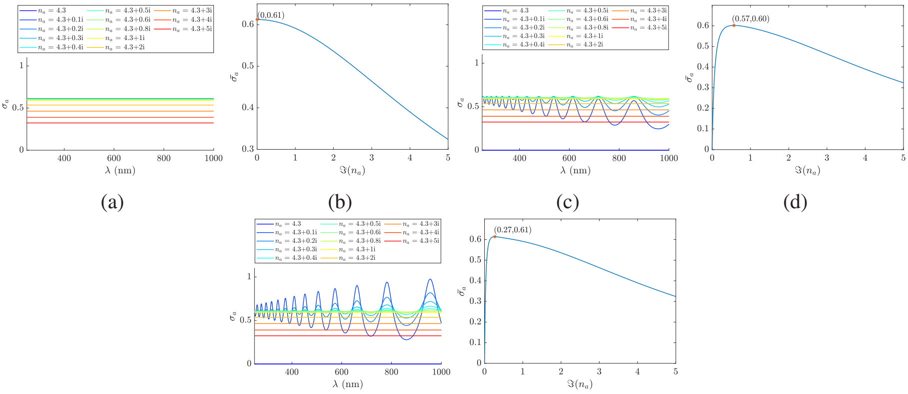

(a) (b) (c) (d)

(e) (f)

Figure 2: Frame (a) shows σ_a as a function of wavelength for an infinitely thick film for increasing $\Im(n_a)$. In frame (b) the averaged absorption efficiency, $\bar{\sigma_a}$, as a function of $\Im(n_a)$ is evaluated. Frame (c) σ_a as a function of wavelength of a absorptive film without mirror behind and frame (d) shows $\bar{\sigma_a}$ as a function of $\Im(n_a)$. Frame (e) and (f) show $\sigma_a(\lambda)$ and $\bar{\sigma_a}(\Im(n_a))$ for a system consisting of a single film with mirror. For all the systems the real part of the refractive index is set to 4.3, which is the real part of the refractive index of silicon at $\lambda = 500$ nm. The investigated wavelength interval is from 250 nm to 1000 nm. For frame (c)-(f) the thickness of the absorptive film is set to 500 nm.

$\sigma_a(\lambda)$ correspond to increasing values for n_i. We observe that resonances are present when n_i is sufficiently low. As n_i increases, the resonances are damped and, finally when n_i is large enough all light is absorbed before reaches the second boundary and no standing waves can be observed. Figure 2d shows how the absorption efficiency averaged over the wavelength range $\bar{\sigma_a}(n_i)$ increases before it reaches a maximum at $n_i = 0.57$.

The system in (Fig. 1c) can be considered as a simplified model of a solar cell as it considers one absorptive layer and a mirror on the backside. Figure 2e shows the corresponding absorption efficiency $\sigma_a(\lambda)$ for a range of constant imaginary parts of the refractive index. We observe that the resonance structure of $\sigma_a(\lambda)$ is changing as we increase the imaginary part of the refractive index. The real part of the refractive index is kept constant, $n_r = 4.3$. As n_i increases we observe the same tendency as for the single film without mirror. The amplitudes of the resonances are reduced and at one point, all the light is absorbed before it reach the mirror and no standing waves are created. Figure 2e shows how the averaged absorption efficiency changes as n_i increases.

Since the absorption efficiency is expected to increase when the absolute value of the wave function increases (see Eq. 3), it is interesting to consider the wave function for maxima and minima of the absorption efficiency. The system consisting of a single film with a reflecting backside mirror (Fig. 1c), exhibits several maxima for the absorption efficiency in Fig. 2e, e.g. for the imaginary part of the refractive index of 0.1i. We consider the maximum that appears at 662 nm and the minimum that appears at 717 nm. The corresponding wave functions ψ_c (Tab. 1) are plotted in Fig. 3 outside and inside the film for two selected wavelengths, 662 nm (red line) and 717 nm (blue line). The refractive index for the film is 4.3 + 0.1i and the thickness is 500 nm.

We see that the red line in Fig. 3, corresponds to a peak, a resonance, in $\sigma_a(\lambda)$ Fig. 2c. We observe that the absolute square of $|\psi|^2$ is larger in the case where the wavelength corresponds to a maximum in $\sigma_a(\lambda)$.

We turn now back to the averaged absorption efficiency shown in Fig. 2f. We observed that we obtained a maximum for an imaginary part of the refractive index of $\Im(n_a) = 0.27$. The thickness of the film was 500 nm, the real part of the refractive index was $\Re(n_a) = 4.3$ and there was a mirror behind the absorptive layer (see Fig. 1c). We want to consider wave functions for this maximum in the absorption efficiency at $\Im(n_a) = 0.27$. Since the maximum corresponds to a spectral range, we selected wave functions from this range: at 250 nm, at 500 nm and at 750 nm. Figure 4 shows the wave functions in front of and inside the absorptive film for the case where $n_a = 4.3 + 0.27i$. The thickness of the absorptive film is 500 nm. The wave functions in Fig. 4 indicate that the optimum of $\Im n_a$ is found for the case where the wave is completely absorbed for small wavelengths and where standing waves are present for lager wavelengths.

Up to now we considered absorption enhancement for an absorptive layer of thickness 500nm, both for different wavelengths and for a total wavelength range. We want to consider now the absorption properties of layered systems

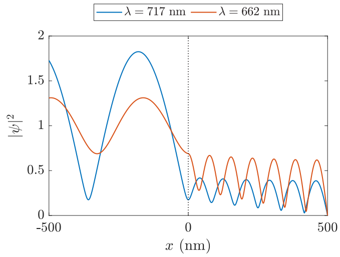

Figure 3: The figure shows the wave function in front of and inside the film where a plane wave is propagating from the left towards a single film of thickness 500 nm and refractive index 4.3 + 0.1i. A perfect mirror is placed behind the film. The system is shown in Fig. 1c. The wavelength of the plane wave is 717 nm (blue line) and corresponds to a dip and the wavelength 662 nm (red line) corresponds to a peak in Fig. 2c for the case where the refractive index of the film is 4.3 + 0.1i.

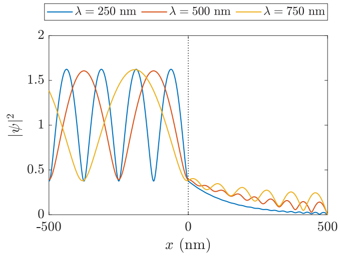

Figure 4: The figure shows the absolute square of the wave function for a system consisting of an absorptive film with a thickness of 500 nm and a refractive index equal to 4.3 + 0.27i. This value of the imaginary part of the refractive index was to be the optimum in the average absorption efficiency in Fig. 2d. At the optimum value no resonant structure is visible in the wave functions at lower wavelengths, while it is present in the wave functions for higher wavelengths.

for a changing film thickness. For the film thickness of 500nm, we found an optimal refractive index of $4.3 + 0.27i$. Figure 5 shows how the absorption efficiency is affected by changing the thickness of the film. The pattern of the absorption efficiency as a function of the wavelength is shown for several film thicknesses in Fig. 5a. It changes strongly when the film thickness is changed. The strong changes occur, since the standing waves occur only when a multiple wavelength matches the thickness of the film. This creates oscillations in the average absorption efficiency $\bar{\sigma}_a(a_a)$ which is plotted as a function of the wavelength (Fig. 5b).

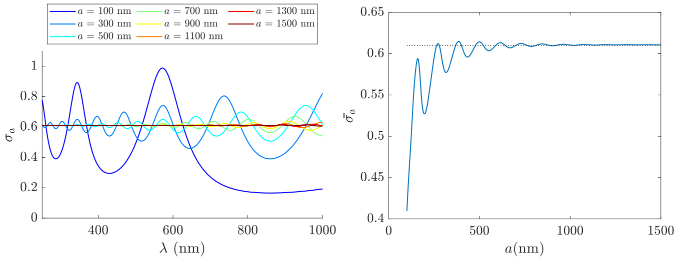

(a) (b)

Figure 5: Frame (a) shows the absorption efficiency, σ_a, as a function of the wavelength, λ, for a system consisting of a single film with a mirror behind (Fig. 1c). The thickness of the film, a_a, is increased from 50 nm (dark blue line) to 1500 nm (dark red line). The refractive index of the film is $n = 4.3 + 0.27$. Frame (b) shows the averaged absorption efficiency for the same system as a function of film width.

We now want to investigate how the peaks and dips in the average absorption efficiency in Fig. 5b are related to the appearance and disappearance of standing waves in the film as a function of the film thickness. We consider two peaks and two dips in the average absorption efficiency in Fig. 5b, namely the peaks $a = 162$ nm and $a = 273$ nm and the dips at $a = 199$ nm and $a = 316$ nm. In Fig. 6 the corresponding absorption efficiencies are shown for the whole wavelength region. We observe that at thicknesses that correspond to peaks, $a = 162$ nm (blue line) and $a = 273$ nm (yellow line), correspond to the cases where the thicknesses is just large enough that a new resonance is included into the $\sigma_a(\lambda)$ range considered. The thicknesses which corresponds to dips, $a = 199$ nm and $a = 316$ nm (red and purple line), correspond to the cases where the thickness is just large enough that an anti-resonance is included.

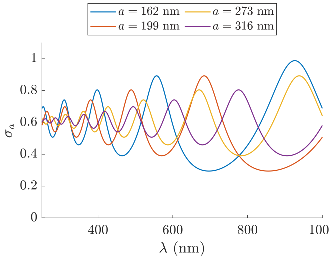

Figure 6: The absorption efficiency as a function of wavelength for a single film with refractive index $n = 4.3 + 0.27i$. The thickness of the film is changed and corresponds to the two first peaks ($a = 162$ nm and $a = 273$ nm) and two first dips ($a = 199$ nm and $a = 316$ nm) from the left in $\bar{\sigma}_a(a)$ in Fig. 5b.

3.2. Two films with mirror

In order to come closer to a real solar cell device, a system consisting of two films and a mirror as shown in Fig. 1d was investigated. The first film is a non-absorptive layer with a refractive index n_I and a thickness a_I. The refractive index n_I is in this layer was set to 1.9 which is the refractive index of ITO at 500 nm, as presented in [18].

In order to evaluate how the resonances in the front layer affect the absorption efficiency, two cases were evaluated: (i) A two-film system where the absorptive film has a thickness that is small enough that light is not completely absorbed in this layer and that resonances can occur and (ii) a two-film system where all the light is absorbed in the second layer before it reaches the mirror. The refractive index of the second layer is chosen to be $4.3 + 0.1i$ and the thicknesses are chosen to be (i) 500 nm and (ii) 5000 nm.

In order to evaluate the resonance structure of the first layer, we will consider the integral of the absolute square of the wave function ($|\psi_I(x)|^2$) in the first film according to

$$I_I = \frac{1}{a_I} \int_0^{a_I} |\psi_I(x)|^2 dx, \tag{4}$$

where a_I is the thickness of the first film and ψ_I is given in Tab. 1. We refer to the integral over I_I as the total intensity of the wave function $\bar{I}_I$. We start by evaluating case (i), i.e. where the absorbing layer has a thickness of 500 nm and where light is not completely absorbed by the absorbing layer such that resonances can occur in the absorbing layer. The absorption efficiency as a function of the wavelength $\sigma_a(\lambda)$ for this system is shown in Fig. 7a for different thicknesses of the first layer. The averaged absorption efficiency $\bar{\sigma}_a$ for the same system as a function of the thickness of the first layer is shown as the blue line in Fig. 7b. We compare now the averaged absorption efficiency $\bar{\sigma}_a$ in the absorbing layer with the total intensity of the wave function in the non-absorbing layer in order to understand if resonances in the non-absorbing layer have an effect on the absorption efficiency of the absorbing layer. The red line in Fig. 7b, shows the integral of the absolute square of the wave function ($|\psi_I(x)|^2$) (see Eq. 4) averaged with respect to the wavelength, i.e. the total intensity of the wave function in the non-absorbing layer. The units are shown as the right y-axis which is labeled by $\bar{I}_I(a_I)$. Both the red and the blue line follows the same trend showing that resonances in the non-absorbing layer lead to an increase of the absorption efficiency in the absorbing layer.

In the case of a thick totally absorbing second layer with $a_a = 5000$ nm we observe the same tendency as for the thin absorbing layer: Figure 7c and Fig. 7d are the plots that correspond to Fig. 7a and Fig. 7b, respectively but this time for case (ii), i.e. a thick absorbing layer with $a_a = 5000$ nm: Figure 7c shows the absorption efficiency $\sigma_a(\lambda)$ for the case where all the light entering the absorptive film is absorbed. The absorption efficiency $\sigma_a(\lambda)$ is less oscillatory compared to the corresponding graphs for the thin absorbing film in Fig. 7a. The reason for this is that in the case of total absorption in the second layer, resonances are only generated in the non-absorbing layer. Figure 7d shows the average absorption efficiency $\bar{\sigma}_a(a_I)$ in the non-absorbing layer as before as the blue line with units on the left y-axis) and the total intensity of the wave function $\bar{I}_I(a_I)$ as the red line and units on the right y-axis. Again it is obvious that the increased field in the non-absorbing layer is leaking into the absorbing layer and creating an enhanced absorption efficiency.

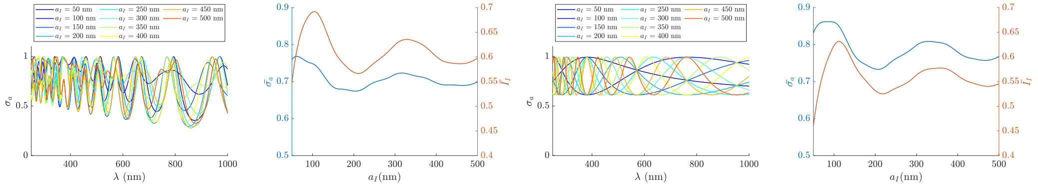

(a) (b) (c) (d)

Figure 7: In frame (a) is the absorption efficiency is plotted as a function of the wavelength for a system consisting of two films with a mirror behind. The thickness of the first film is increased from 50 nm to 500 nm and has a refractive index of 1.9. The second film has a thickness of 500 nm and has a refractive index equal to $4.3 + 0.1i$. Frame (b) shows the averaged absorption efficiency as a function of a_I for the same system. Frame (c) and (d) shows the same plots for a system where the thickness of the absorptive layer is 5000 nm.

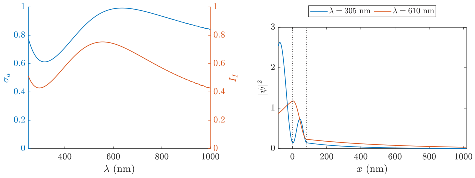

(a) (b)

Figure 8: Frame (a) shows the absorption efficiency (σ_a) and the integral over the absolute square of the wave function ($|\psi_I(x)|^2$) in the first film (I_I) as a function of wavelength for a system consisting of two films and a mirror behind. The refractive index of the second film is $4.3 + 0.1i$ and the thickness is 5000 nm, i.e. all the light is absorbed before it reaches the mirror. The first film has a refractive index of 1.9 and a thickness of 83 nm. This thickness corresponds to a maximum in $\bar{\sigma}_a(a_I)$ in Fig. 7d. A maximum in $\bar{\sigma}_a(a_I)$ is associated with an enhancement of the absorption in the absorbing layer. Frame (b) shows the absolute square of the wave function for the system for a wavelength corresponding to a top and a dip in frame (a), respectively. The wave function is shown for the non-absorbing layer and for the first 1000 nm of the absorbing layer which is in total 5000nm thick.

We now want to have a closer look at the system with two layers and a mirror with the totally absorbing layer for the situation where the absorption in the absorbing layer is enhanced by the resonances in the first layer. Inspecting the graph of $\bar{\sigma}_a$ in Figure 7d (blue line), we see that the absorption properties are enhanced for low thicknesses of the non-absorbing layer. We select the thickness of $a_I = 83$ nm which leads to enhancement. In Fig. 8 the absorption efficiency $\sigma_a(\lambda)$ is plotted as a function of the wavelength for the maximum of $\bar{\sigma}_a$ at $a_I = 83$ nm as the blue line with units on the left y-axis. The corresponding intensity of the wave function I_I is plotted as a function of the wavelength λ as the red line with units on the right y-axis. We see that the absorption efficiency $\sigma_a(\lambda)$ and and the intensity of the wave function $I_I(\lambda)$ have a minimum and a maximum in the wavelength range considered which can be further investigated. The absolute squares $|\psi|^2$ of the wave functions that correspond to the maximum and minimum, respectively, are shown in Fig. 8b for the non-absorbing film and the first 1000nm of the absorbing film. The wavelengths of the wave function corresponding to the minimum and the maximum were selected to be (i) 305 nm showing a dip in $\sigma_a(\lambda)$ in Fig. 8a (blue line), and (ii) 610 nm showing a peak in in $\sigma_a(\lambda)$ (red line). We observe that for the case where the wavelength corresponds to a dip $\sigma_a(\lambda)$ in Fig. 8a (blue line), $|\psi|^2$ has lower values in the absorptive film than for the case where the wavelength which corresponds to a peak in $\sigma_a(\lambda)$.

3.3. Coupling of resonances of non-absorptive layers

When the systems consist of three layers, two non-absorptive layers and an absorptive layer, we can investigate coupling of resonances in two non-absorbing layers. This is the one-dimensional equivalent to a thin film solar cell with coupling of e.g. nano-spheres on its surface. The coupling of resonances in spherical nano-structures on thin-film solar cells has been discussed in the literature as a cause for enhancement of absorption in the absorbing layers below [6, 5]. We start by evaluating how the thicknesses and refractive indices of two non-absorbing front layers of different materials affect the absorption in the third, absorptive layer. The system is shown in Fig. 1e. As for the two-film systems, we assume that the refractive indices of the films are constant for all wavelengths. This is to highlight the effect of the thickness of the first two layers on the average of the absorption efficiency, σ_a. The thickness of the third, absorptive film is chosen such that the wave function in this film is totally absorbed.

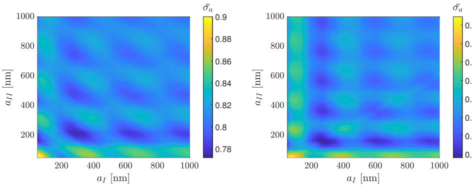

(a) (b)

Figure 9: The average absorption efficiency, $\bar{\sigma}_a$, for a three layer system as shown in Fig. 1e is displayed as a heat map for varying thicknesses of the two first non-absorbing layers. The thicknesses of the two first layers were varied between 50 nm and 1000 nm. The thickness of the third layer is kept constant at 5000 nm. The refractive indices of the layers are for frame (a) $n_I = 1.5$ (refractive index of SiO_2 at 500 nm), $n_{II} = 1.9$ (refractive index of ITO at 500 nm) and $n_{III} = 4.3+0.01i$ (where the real part of n_{III} is the real part of the refractive index of Si at 500 nm and the imaginary part of n_{III} is chosen so that all light which enters the absorptive film is absorbed). For frame (b) the refractive indices are given as $n_I = 1.5$, $n_{II} = 2.5$ (selected to be substantially above n_I) and $n_{III} = 4.3 + 0.01i$. The wavelength range that is investigated is 250 nm - 1000 nm.

In Fig. 9a, the average absorption efficiency is shown for the three film system, where the refractive indices of layer I, II and III in Fig. 1e are set to 1.5 (refractive index of SiO_2 at 500 nm), 1.9 (refractive index of ITO at 500 nm) and 4.3 + 0.01i, respectively. The thickness of the third layer is set to 5000 nm, i.e. all light which enters the third layer is absorbed. The thicknesses of the two first layers in the system were varied between 50 nm and 1000 nm in order to optimize the thicknesses of the two films with respect to the absorption efficiency of the third film. Figure 9a shows $\bar{\sigma}_a$ for different combinations of the thicknesses of the two first layers. We consider the wavelength range from 250 nm to 1000 nm. In Fig. 9b corresponding results for the same system with an increased refractive indices of the second layer are shown. The refractive indices of the layers I, II and III are now set to 1.5, 2.5 and 4.3 + 0.01i, respectively. As before, the wavelength range is evaluated in the region 250-1000 nm. The thicknesses of the two first layers are changed between 50 nm and 1000 nm and the thickness of the third layer is 5000 nm. A comparison between Fig. 9a and Fig. 9b shows that in the case where the two first layers have relatively close refractive indices, the pattern in the heat map is a skewed grid pattern while in Fig. 9b a non-skewed grid pattern is obtained. When the refractive indices of the two first layers are at a similar level, the resonances couple and the grid pattern is skewed. In the case where the difference between the refractive indices in the two layers is large, the resonances in the layers are independent of each other and the grid pattern of $\bar{\sigma}_a$ is not skewed.

In order to evaluate coupling of the resonances further, we consider the three-layer system shown in Fig. 1f where the first and third layer are the non-absorptive layers and the second layer is the absorptive layer. The backside mirror is removed in order to avoid the effect of an increased σ_a caused by the fact that all light is forced to travel back and forth in the third film.

In Fig. 10a and Fig. 10b, the averaged absorption efficiency, $\bar{\sigma}_a$, is shown as a heat map as a function of the thickness of the non-absorptive layers, a_I and a_{III}. For the system in Fig. 10a, the refractive indices of the layers I, II and III are wavelength independent as before and set to 1.9, 4.3+0.1i and 1.5, respectively. The thickness of the absorptive layer is 500 nm.

In Fig. 10b, the system parameters are identical to the situation shown in Fig. 10a, except that the refractive index of the third layer is set to 1.9, i.e. the refractive index of the two non-absorptive layers are identical. It is therefore expected that the resonance in the two non-absorptive layers occur at the same thicknesses and wavelengths.

The grid patterns observed in Fig. 10a and Fig. 10b indicate that both of the two layers affect $\bar{\sigma}_a$. But the differences are more distinguished for changes of thicknesses of the first layer that of the third.

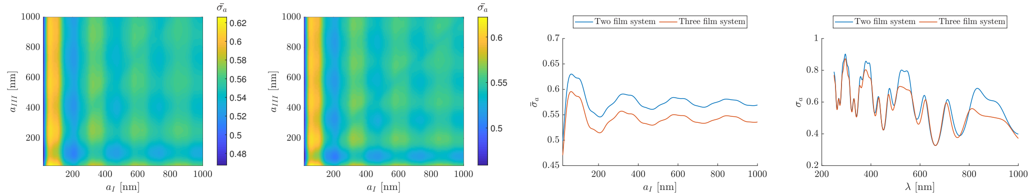

(a) (b) (c) (d)

Figure 10: Frame (a) and (b) show a heat map of the averaged absorption efficiency $\bar{\sigma}_a$ for a three-film system (see Fig. 1f). The averaged absorption efficiency $\bar{\sigma}_a$ is shown as a function of the thicknesses of the first and third layer a_I and a_{III}. The refractive index of the layers are for (a) $n_I = 1.9$, $n_{II} = 4.3 + 0.01i$ and $n_{III} = 1.5$ and (b) $n_I = 1.9$, $n_{II} = 4.3 + 0.01i$ and $n_{III} = 1.9$, respectively. The thickness of the second layer is 500 nm. Frame (c) shows the average absorption efficiency $\bar{\sigma}_a$ as a function of a_I for a two- (blue line) and a three-film (red line) system. For both systems, the refractive index of the first layer are set to 1.9 and for the second layer to 4.3 + 0.1. The thickness of the second layer is 500 nm. For the three-film system, the third film has a refractive index of 1.9 and a thickness 350 nm. Frame (d) shows $\sigma_a(\lambda)$ for the same systems as in frame (c) when the thickness of the first layer is 350 nm.

The blue line in Fig. 10c shows the averaged absorption efficiency $\bar{\sigma}_a$ as a function of the thickness of the first layer in a two-film system (without a backside mirror), i.e. $n_{III} = 1$ in the system shown in Fig. 1f. The refractive index of the first layer is 1.5, the refractive index of the second layer is $n_a = 4.3 + 0.1i$ and the thickness of the second layer is 500 nm. The red line shows the averaged absorption efficiency $\bar{\sigma}_a$ as a function of a_I for an equivalent three-film system where the refractive index of the third layer is $n_{III} = 1.9$ and the thickness of the third film is $a_{III} = 350$ nm. In Fig. 10d, the absorption efficiencies $\sigma_a(\lambda)$ for the two- and three-film systems are compared as a function of λ. For both systems, the first two layers are identical with thicknesses and refractive indices of the two first layers set to 350 nm and 500 nm and $n_I = 1.9$ and $n_a = 4.3 + 0.1i$, respectively. For the three-film systems, the refractive index and the thickness of third film are $n_{III} = 1.9$ and 350 nm, respectively. Both Fig. 10c and Fig. 10d show that a two-film system has a higher absorption efficiency than a corresponding three-layer system, where a third layer is added. This indicates that the coupling of resonances in this case does not have any enhancement effect.

In order to return to a system which is closer to a real solar cell device, the system in Fig. 1g was evaluated to further describe the effect of coupling in the case where a backside mirror is present. The refractive indices were selected as above and the three-layer system was compared with an equivalent two-layer system where the third layer is removed as in Fig. 1d. Figure 11a and Fig. 11b show the averaged absorption cross section as a function of the thickness of the non-absorptive layers, a_I and a_{III}. The thickness of the absorptive mid layer is 500 nm. The refractive indices are chosen as $n_I = 1.9$, $n_{II} = 4.3 + 0.1i$ and $n_{III} = 1.5$ for the results shown in Fig. 11a and as $n_I = 1.9$, $n_{II} = 4.3 + 0.1i$ and $n_{III} = 1.9$ for the results shown in Fig. 11b. We observe that the maximum $\bar{\sigma}_a$ is higher than for the system without mirror (Fig. 10). This is due to the fact that light was reflected at the mirror on the backside which was effectively doubling the effective thickness of the absorbing layer. Further, we observe the same trend that we discussed for Fig. 10: adding a third layer with an identical refractive index, which is expected to lead to coupling of resonances, does not enhance $\bar{\sigma}_a$.

The blue line in Fig. 11c shows the averaged absorption efficiency $\bar{\sigma}_a$ as a function of the thickness of the first layer in the two-film system (shown in Fig. 1d). The refractive index of the first layer is 1.5, the refractive index of the second layer is $n_a = 4.3 + 0.1i$ and the thickness of the second layer is 500 nm. The red line shows the averaged absorption efficiency $\bar{\sigma}_a$ as a function of a_I for an equivalent three-film system where the refractive index of the third layer is $n_{III} = 1.9$ and the thickness of the third film is $a_{III} = 350$ nm. We observe that with the backside mirror present, the third film reduces $\bar{\sigma}_a$. The same trend as what we observed for the case without a mirror. Compared to the system without a mirror on the backside in Fig. 10c, $\bar{\sigma}_a$ is less reduced in the system with a mirror on the backside.

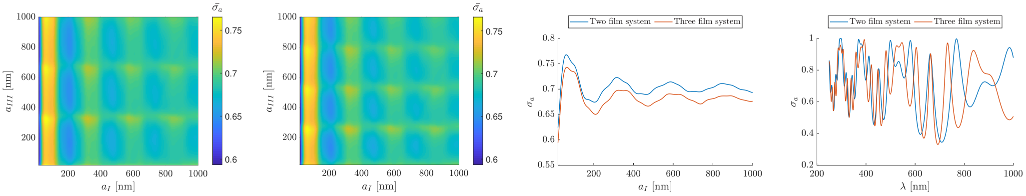

(a) (b) (c) (d)

Figure 11: Frame (a) and (b) show a heat map of the averaged absorption efficiency $\bar{\sigma}_a$ for a three-film system with a backside mirror (see Fig. 1g). The averaged absorption efficiency $\bar{\sigma}_a$ is shown as a function of the thicknesses of the first and third layer a_I and a_{III}. The refractive index of the layers are for (a) $n_I = 1.9$, $n_{II} = 4.3 + 0.01i$ and $n_{III} = 1.5$ and (b) $n_I = 1.9$, $n_{II} = 4.3 + 0.01i$ and $n_{III} = 1.9$, respectively. The thickness of the second layer is 500 nm. Frame (c) shows the average absorption efficiency $\bar{\sigma}_a$ as a function of a_I for a two-film system (blue line) and a three-film system (red line). For both systems, the refractive index of the first layer are set to 1.9 and for the second layer to 4.3 + 0.1. The thickness of the second layer is 500 nm. For the three-film system, the third film has a refractive index of 1.9 and a thickness 350 nm. Frame (d) shows $\sigma_a(\lambda)$ for the same systems as in frame (c) when the thickness of the first layer is 350 nm.

In Fig. 11d, the absorption efficiencies $\sigma_a(\lambda)$ as a function of λ are compared for the two- and three-film systems. The thicknesses and refractive indices of the two first layers are set to 350 nm and 500 nm and $n_I = 1.9$ and $n_a = 4.3 + 0.1i$, respectively for both systems. For the three-film systems, the refractive index and the thickness of third film are $n_{III} = 1.9$ and 350 nm.

As predicted by Eq. 3, the absorption efficiency is enhanced, when the field in the absorptive material is increased. From Fig. 11c we learn that a two-film yields a higher average absorption efficiency. However, as Fig. 11d indicates, the absorption efficiency is this wavelength dependent. In Fig. 12, the absolute square of two selected wave functions is shown for the two- and three-film system. For the two-film system with the mirror on the backside(see Fig. 1d), the wave function is plotted as a blue line in Fig. 12. As for the case without mirror, we chose $a_I = 350$ nm and $a_a = 500$ nm. For the three-film systems with the mirror placed behind the third film (see Fig. 1g), is $a_I = 350$ nm, $a_a = 500$ nm and $a_{III} = 350$ nm. The refractive indices are selected to be $n_I = 1.9$, $n_{II} = 4.3 + 0.01i$ and $n_{III} = 1.9$, respectively. The parameters are again chosen analog to the system without mirror. The wavelength of the incoming plane wave is selected to be 732 nm in Fig. 12a. This wavelength corresponds to the second peak from right in Fig. 11d for the three-film system. In Fig. 12b the wavelength is selected to be 769 nm. This corresponds to the second peak from right in Fig. 11d for the two-film system.

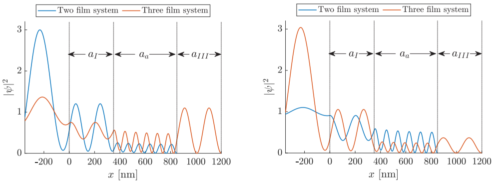

(a) (b)

Figure 12: The figure shows the absolute square of the wave functions (given in Tab. 1) as a function of position. The thicknesses is selected to be $a_I = 350$ nm, $a_a = 500$ nm and $a_{III} = 350$ nm and the refractive indices are $n_I = 1.9$, $n_{II} = 4.3 + 0.01i$ and $n_{III} = 1.9$. The blue line shows $|\psi|^2$ for the two-film system (Fig. 1d), where the backside mirror is placed behind the absorptive film of thickness a_a. The red line shows$|\psi|^2$ for a three-film system (Fig. 1g), where the backside mirror is placed behind the third, non-absorptive layer of thickness a_{III}. Frame (a) shows the behavior of the wave function in the case where the wavelength of the incoming light is 732 nm (corresponding to second peak from right in Fig. 11d for the three-film system). Frame (b) shows the behavior of the wave function in the case where the wavelength of the incoming light is 769nm (corresponding to second peak from right in Fig. 11d for the two-film system).

The wave functions in Fig. 12 confirm Eq. 3 that when the wave function has increased absolute values in the absorptive film, increased absorption efficiency is obtained.

However, the striking result is that coupling of resonances in thin films does not overall increase the absorption efficiency. This can be seen both for two and three-layer systems with an without mirror in Fig. 10 and Fig. 11, respectively.

3.4. Optimization of absorption of thin-film solar cells

In this section we will demonstrate how considering resonances in thin-film systems can help to optimize experimentally realizable solar cells. We consider the system shown in Fig 13b, which is a simplification of a five-layer epitaxial crystalline silicon solar cell, which is optically thin as shown in Fig. 13a [18]. The experimentally realized system consists of three different materials: ITO, amorphous silicon and crystalline silicon. The two silicon layers consist of p-doped and one n-doped layers as shown in the figure. In order to simplify the system, we treat the amorphous silicon as one layer with the same wavelength-dependent refractive index. The same assumption is used for the crystalline silicon. The absorption efficiency is calculated by Eq. 2. The refractive index of the three layers that are used are experimentally determined [19, 20, 21]. By evaluating the absorption efficiency for different choices of thickness for the three layers, the system can be optimized to absorb as much radiation as possible.

(a) (b)

Figure 13: A multi-layer thin-film solar cell, consisting of five thin layers and a mirror, are shown in (a). This solar cell has been experimentally realized [18] and consists of ITO, n- and p-doped amorphous and crystalline silicon. The thicknesses of the layers of the experimentally realized system are shown in the model. The system has been simplified into a three-layered system with mirror (b) [9]. The system has been simplified by replacing the layers with different doping with one single layer with experimentally determined refractive index [19, 20, 21]. n_0 indicates the refractive index of vacuum and is given by $n_0 = 1$. Behind the layers of the different materials, a perfect mirror is placed. In order to optimize the system, the thicknesses of the three layers are changed. The result is shown in Fig. 14.

The system in Fig. 13b is evaluated for several thicknesses of the layers. The average absorption efficiency $\bar{\sigma_a}$ is shown for systems with c-Si film thickness equal to 0.5 µm, 2 µm, 8 µm, 32 µm, 100 µm and 200 µm in Fig. 14. The thicknesses of the two first layers are varied between 20 nm and 500 nm. As Fig. 14 indicates, certain combinations of thicknesses of the two first layers give higher $\bar{\sigma_a}$ values than others.

As Fig. 14 indicates, 60 nm and 150 nm are optimal thicknesses for the first and the second layer, respectively. We therefore set the thicknesses of the first and second layers to 60 nm and 150 nm, and vary now the thickness of the third layer. By continuously increasing the thickness of the third layer from 0.5 µm to 200 µm, the findings of Sec. 3.2 are confirmed: When the thickness of the energy converting layer is increased, the average absorption efficiency $\bar{\sigma_a}$ stabilizes at a certain value. This is shown in Fig. 15, where the average absorption efficiency $\bar{\sigma_a}$ is shown as a function of the thickness of the third layer. We observe that the $\bar{\sigma_a}$ stabilizes at a maximum value of approximately $\bar{\sigma_a} = 0.8$. The stabilization takes place when the thickness of the third layer is approximately 50 µm. For larger thicknesses no further enhancement of the absorption of the c-Si layer can be obtained. A further investigation of the material cost versus the absorption efficiency is needed in order to decide if a thickness of 50 µm is an optimum, since already a thickness of the c-Si layer of around 20 µm is close to the optimum value for the average absorption efficiency $\bar{\sigma_a}$.

4. Discussion

The results presented in Sec. 3.1 show that when the imaginary part of the refractive index of the absorptive material is changed, the resonance structure of the absorption efficiency and the absorption properties of the material change. For a large imaginary part of the refractive index, all radiation entering the absorptive material is absorbed before it reaches the backside boundary or mirror. Therefore, standing waves do not occur in the absorptive material for a large imaginary part of the refractive index. One might assume an increasing imaginary part of the refractive index results in an increased absorption efficiency. However, as confirmed by the Fresnel equations [13], the reflection from the absorbing film's surface increases when the imaginary part of the refractive index increases. Therefore, less

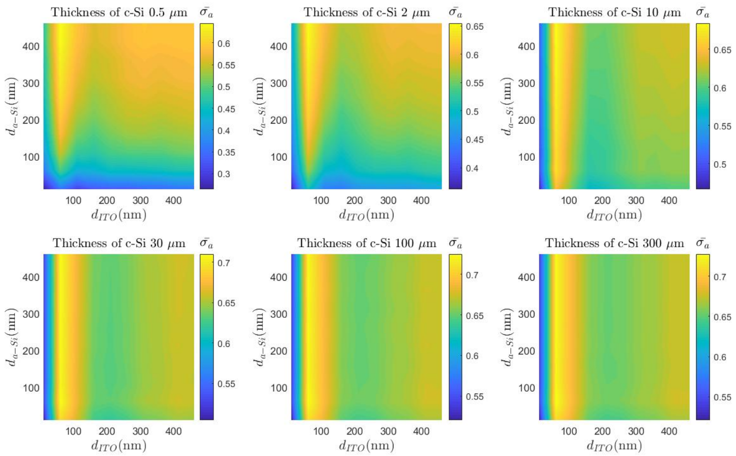

Figure 14: The average absorption efficiency $\bar{\sigma_a}$ for a three film system with the same materials as shown in Fig. 13b with experimentally determined refractive indices [19, 20, 21]. The thicknesses of the two first layers are varied between 20 nm and 500 nm. The thickness of the c-Si layer is set to 0.5 μm, 2 μm, 8 μm, 32 μm, 100 μm and 200 μm respectively. The wavelength range that is investigated is from 250 nm to 1000 nm.

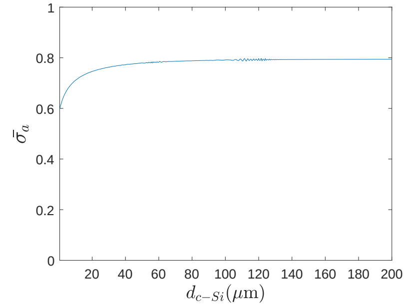

Figure 15: The average absorption efficiency, $\bar{\sigma_a}$, as function of the thickness of the c-Si layer. The system is equivalent to the system shown in Fig. 13b where the thicknesses of ITO and a-Si are set to 60 nm and 150 nm, respectively. Further, the thickness of the c-Si layer, d_{c-Si}, is increased from 0.5 μm to 200 μm. The refractive indices of the layers are experimentally determined [19, 20, 21].

radiation is transmitted into the absorptive material, which results in lower absorption. As Figs. 2d and 2f show, there is an optimal size of the imaginary part of the refractive index of the absorptive material, where the wave function is just totally absorbed before it reaches the mirror. Since we consider the average absorption efficiency for a whole wavelength region, this condition of optimal imaginary part of the refractive index is achieved, when the standing wave in the absorbing material has just disappeared for small wavelengths, while it is present for large wavelengths as showed in Fig. 4. When investigating the absorption properties of the film system as a function of the thickness of the absorbing film, we observe that the absorption increases with increasing thickness of the absorbing layer until a maximum is reached and stays constant for larger thicknesses. Before we reach this point, the average absorption efficiency $\bar{\sigma}_a$ oscillates as shown in Fig. 5. The peaks of the oscillatory pattern correspond to a thickness of the absorptive material which includes a new resonance, while the dips correspond to a thickness of the absorptive material which includes a new anti-resonance. This mechanism can be potentially used as a mechanisms to enhance absorption efficiency of thin-film solar cells within a desired wavelength range. In general we see that absorption in the absorbing layer is enhanced by resonances in the non-absorptive material, which lead to a field enhancement in the absorbing material.

This is shown in Sec. 3.2. In this section we also learn that the resonance in the absorption efficiency follows the same trend as the averaged integral over the non-absorptive film. An increase in the integral over the absolute square of the wave function is followed by an increased $\sigma_a(\lambda)$.

When considering a system consisting of three layers, we find that it is important to investigate first all combinations of thicknesses of the first two layers in order to optimize the thicknesses of the first two layers. The optimal thickness of the third layer is then found, where the wave function is just totally adsorbed.

A three-film system without a mirror is also considered in order to evaluate the effect of coupling between two non-absorptive films on each side of the absorptive film. From Fig. 10a and Fig. 10b, we conclude that mainly the resonances in the front layer affect the averaged absorption efficiency $\bar{\sigma}_a$. When we compare a two- and three-film system without a backside mirror in Fig. 10c and Fig. 10d, we observed that the absorption efficiency was lower for the three-film system. This can be understood, when considering the refractive index changes at the boundary: The refractive index in the third film is closer to the refractive index of air at the outside, which results in more light being transmitted out of the system. This is expected from Fresnel's equations. We further investigated a three-layer system with the absorbing layer in the middle and a mirror on the backside in order to avoid more leakage of radiation from the third film to the outside. Strikingly, also in the case of a three-film system with a mirror on the backside the absorption efficiency was not increased compared to the corresponding two layer-system without the third non-absorbing layer. The results are shown in Fig. 11. This indicates that the coupling of resonances itself is not a mechanism that increases the absorption efficiency of solar cells in layered system. Coupling of resonances has been suggested as a mechanism for resonance enhancement in surface structured thin film solar cells [5, 6]. We would therefore expect that when spheres are embedded into the energy converting material [22], it is rather the field enhancement due to resonances in each sphere than the coupling of the resonances that would lead to an absorption enhancement.

In section 3.4, the absorption efficiencies for experimentally realizable thin-film solar cells are investigated. An experimentally realized solar cell was used as a template, and wavelength-dependent, experimentally determined refractive indices were used in the system. The observations were comparable to the results found in Sec. 3.1 where systems with wavelength-independent refractive indices are investigated.

In all systems considered, we were studying the average absorption efficiency, $\bar{\sigma}_a$. It is important to notice that $\bar{\sigma}_a$ changes if we change the wavelength range. It is therefore essential to optimize the system according to the proper wavelength range. In our study, the results presented were not weighted with the solar spectrum. If the absorption efficiency is weighted with the solar spectrum, the optical generation rate [12] is obtained. In order to further evaluate a thin-film solar cell system, the average optical generation rate should be evaluated.

Our model is exact for situations with coherent light, which is a common assumption for simulations of thin-film solar cells where the thickness of the films is smaller then the coherence wavelength [23]. Sunlight, however, is incoherent, so the assumption of coherent light in our model is not strictly applicable to the case of incoherent sunlight. Indeed, it is known that there is a difference in conversion efficiency between illumination with coherent and incoherent light [24]. Since the spatial coherence area of sunlight is about 60 μm × 60 μm [25], and resonant solar-cell surface structures are of the order of a micron, the effects of spatial coherence may be neglected. However, since the temporal coherence length of sunlight is about 600 nm [26], and the thicknesses of our films are about of this order of magnitude, the temporal incoherence of sunlight cannot be neglected. Therefore, while our results are rigorous for coherent incident light, we have to be careful when using these results to make predictions for the case of incoherent sunlight. On the upside, a two-step method exists that takes the results of coherent calculations as input for a folding step that then obtains conversion efficiencies for incoherent illumination directly from the coherent input [24, 27]. Therefore, our results presented here are the first step in this two-step process. The investigation of the our systems for the use of incoherent light is beyond the scope of this study and will be addressed in a follow up work.

For monochromatic light, our results indicate that the optimum in conversion efficiency is reached when the layers in front of the energy-converting material are around the same size as the coherence length of the light [26]. We could therefore expect resonances in the first layers. Further, we show that it is optimal that the energy converting material should have a thickness so that the wave function is totally absorbed before it reaches the mirror. In this cases we will not have resonances in the layer closest to the mirror. We expect that these predictions, based on a coherent, monochromatic model are robust and will also hold in the case of illumination with incoherent light.

Our model only evaluates the optical properties of the system. Effects linked to losses other than reflection are not included in our models.

5. Conclusion

In this paper we have shown that simple calculations of the absorption efficiency can give an indication of a proper choice of thickness of the layers in a thin-film solar cell. We find that a resonance in the front layers can result in an increased absorption efficiency. This is caused by the enhanced wave function in the front layers. Due to the continuity of the wave function this also results in an enhanced absorption of radiation in the absorptive material. In the case of a non-absorptive layer on both sides of the absorptive layer, the resonances in the first layer are the most important. We investigated further if coupling of resonances could enhance absorption in an absorptive layer which was located between to absorbing layers and could not find any effect.

We have also shown that the absorption efficiency decreases when the imaginary part of the refractive index of the absorptive material increases. This is because the reflection probability increases according to Fresnel's equations. An optimal imaginary part of the refractive index is therefore obtained when the absorption is high enough such that standing waves just disappear in the absorbing material for a large part of the wavelength region considered, but not too high so that not a too large part of the radiation is reflected in the energy-converting material. We have applied our findings with success to the optimization of an experimentally realizable solar-cell system.

Acknowledgement

This work was supported by the grant *Development of a new ray model for understanding the coupling between dielectric spheres for photovoltaics with higher efficiency* - No: 250678 financed by The Research Council of Norway.

References

[1] R. Brendel, Thin-film crystalline silicon solar cells: physics and technology, John Wiley & Sons, 2011.

[2] T. D. Lee, A. U. Ebong, A review of thin film solar cell technologies and challenges, Renewable and Sustainable Energy Reviews 70 (2017) 1286–1297.

[3] J. Grandidier, D. M. Callahan, J. N. Munday, H. A. Atwater, Light absorption enhancement in thinâĂŘfilm solar cells using whispering gallery modes in dielectric nanospheres, Advanced Materials 23 (2011) 1272–1276.

[4] G. Kang, H. Park, D. Shin, S. Baek, M. Choi, D. H. Yu, K. Kim, W. J. Padilla, Broadband light-trapping enhancement in an ultrathin film a-si absorber using whispering gallery modes and guided wave modes with dielectric surface-textured structures, Adv Mater 25 (2013) 2617–23. URL: `https://www.ncbi.nlm.nih.gov/pubmed/23529900`. doi:`10.1002/adma.201204596`.

[5] C. Becker, P. Wyss, D. Eisenhauer, J. Probst, V. Preidel, M. Hammerschmidt, S. Burger, 5x5 cm2 silicon photonic crystal slabs on glass and plastic foil exhibiting broadband absorption and high-intensity near-fields, Scientific Reports 4 (2014) 5886. URL: `https://doi.org/10.1038/srep05886`. doi:`10.1038/srep05886`.

[6] M. Schmid, Review on light management by nanostructures in chalcopyrite solar cells, Semiconductor Science and Technology 32 (2017) 043003. URL: `http://stacks.iop.org/0268-1242/32/i=4/a=043003`.

[7] H. ElAnzeery, O. El Daif, M. Buffière, S. Oueslati, K. Ben Messaoud, D. Agten, G. Brammertz, R. Guindi, B. Kniknie, M. Meuris, J. Poortmans, Refractive index extraction and thickness optimization of cu2znsnse4 thin film solar cells, physica status solidi (a) 212 (2015) 1984–1990. URL: `https://onlinelibrary.wiley.com/doi/abs/10.1002/pssa.201431807`. doi:`10.1002/pssa.201431807`. `arXiv:https://onlinelibrary.wiley.com/doi/pdf/10.1002/pssa.201431807`.

[8] S. Saylan, T. Milakovich, S. A. Hadi, A. Nayfeh, E. A. Fitzgerald, M. S. Dahlem, Multilayer antireflection coating design for gaas0.69p0.31/si dual-junction solar cells, Solar Energy 122 (2015) 76 – 86. URL: `http://www.sciencedirect.com/science/article/pii/S0038092X15004302`. doi:`https://doi.org/10.1016/j.solener.2015.07.049`.

[9] M. Brandsrud, E. Seim, R. Lukacs, A. Kohler, E. Marstein, E. Olsen, R. Blümel, Exact ray theory for the calculation of the optical generation rate in optically thin solar cells, Physica E: Low-dimensional Systems and Nanostructures 105 (2019) 125–138.

[10] H. C. Hulst, H. C. van de Hulst, Light scattering by small particles, Courier Corporation, 1981.

[11] E. Seim, A. Kohler, R. Lukacs, M. A. Brandsrud, E. S. Marstein, E. Olsen, R. Blümel, Chaos: A new mechanism for enhancing the optical generation rate in optically thin solar cells, Chaos: An Interdisciplinary Journal of Nonlinear Science 29 (2019) 093132.

[12] V. E. Ferry, J. N. Munday, H. A. Atwater, Design considerations for plasmonic photovoltaics, Adv Mater 22 (2010) 4794–808. URL: `http://www.ncbi.nlm.nih.gov/pubmed/20814916`. doi:`10.1002/adma.201000488`.

[13] M. N. Sadiku, Elements of electromagnetics, Oxford university press, 2014.

[14] J. Townsend, Quantum Physics: A Fundamental Approach to Modern Physics, University Science Books, 2010. URL: `https://books.google.no/books?id=7PxAAQAAIAAJ`.

[15] D. J. Griffiths, Introduction to electrodynamics, 3rd ed. ed., Prentice Hall, Upper Saddle River, N.J, 1999.

[16] D. Cozza, C. M. Ruiz, D. Duché, S. Giraldo, E. Saucedo, J. J. Simon, L. Escoubas, Optical modeling and optimizations of cu 2 znsnse 4 solar cells using the modified transfer matrix method, Optics express 24 (2016) A1201–A1209.

[17] P. A. Tipler, G. Mosca, Physics for scientists and engineers : with modern physics, 6th ed. ed., Freeman, New York, 2008.

[18] J. K. Selj, D. Young, S. Grover, Optimization of the antireflection coating of thin epitaxial crystalline silicon solar cells, Energy Procedia 77 (2015) 248–252.

[19] M. A. Green, Self-consistent optical parameters of intrinsic silicon at 300 k including temperature coefficients, Solar Energy Materials and Solar Cells 92 (2008) 1305–1310.
[20] D. Pierce, W. E. Spicer, Electronic structure of amorphous si from photoemission and optical studies, Physical Review B 5 (1972) 3017.
[21] T. A. König, P. A. Ledin, J. Kerszulis, M. A. Mahmoud, M. A. El-Sayed, J. R. Reynolds, V. V. Tsukruk, Electrically tunable plasmonic behavior of nanocube–polymer nanomaterials induced by a redox-active electrochromic polymer, ACS nano 8 (2014) 6182–6192.
[22] J. R. Nagel, M. A. Scarpulla, Enhanced absorption in optically thin solar cells by scattering from embedded dielectric nanoparticles, Optics express 18 (2010) A139–A146.
[23] J. Puhan, B. Lipovšek, A. Bűrmen, I. Fajfar, An accurate representation of incoherent layers within one-dimensional thin-film multilayer structures with equivalent propagation matrices, IEEE Photonics Journal 9 (2017) 1–12. doi:10.1109/JPHOT.2017.2728535.
[24] A. Herman, M. Sarrazin, O. Deparis, The fundamental problem of treating light incoherence in photovoltaics and its practical consequences, New Journal of Physics 16 (2014) 013022.
[25] G. S. Agarwal, G. Gbur, E. Wolf, Coherence properties of sunlight, Optics letters 29 (2004) 459–461.
[26] A. Donges, The coherence length of black-body radiation, European journal of physics 19 (1998) 245.
[27] M. Sarrazin, A. Herman, O. Deparis, First-principle calculation of solar cell efficiency under incoherent illumination, Optics express 21 (2013) A616–A630.

Appendix D

Paper IV

Potential pitfalls in interpretation of Mie-type signatures in infrared microspectroscopy

Maren Anna Brandsrud[1, *], **Reinhold Blümel**[2], **Johanne Solheim**[1], **and Achim Kohler**[1]

[1]Faculty of Science and Technology, Norwegian University of Life Sciences, Ås, Norway
[2]Department of Physics, Wesleyan University, Middletown, Connecticut, United States of America
[*]maren.brandsrud@nmbu.no

ABSTRACT

Mie-type scattering features such as ripples and wiggles are frequently observed scattering phenomena in infrared microspectroscopy of cells and tissues. They appear in general when the wavelength of electromagnetic radiation is of the same order as the size of the scatterer. By use of approximations to the Mie solutions, iterative algorithms have been developed to retrieve pure absorbance spectra. However, the question remains to what extent the Mie solutions, and approximations thereof, describe the extinction efficiency in practical situations where the shapes deviate considerably from spheres. The aim of the current study is to investigate how deviations from a spherical scatterer, can change the extinction properties of the scatterer in the context of chaos in wave systems. For this purpose, we investigate a scatterer that is shaped like a Bunimovich billiard, which is shown to be chaotic. An elliptically shaped scatterer, which exhibits only regular scattering is compared with a stadium-shaped chaotic scatterer. We find that chaotic scattering has an accelerating effect on the disappearance of Mie ripples. We further show that the presence of absorption alone does not explain the absence of ripples in most measurements of biological samples.

Infrared microspectroscopy is a technique that is well established in the biological sciences[1,2]. It allows investigating for example cells, tissues and bio-fluids in their native forms. When combining infrared microscopy with synchrotron radiation, a spatial resolution close to the diffraction limit can be achieved[3]. In infrared transmission microscopy of cells and tissues, purpose-built microscopes are used that allow to operate with radiation in the mid-infrared region. These systems are operated in two main modes. In one type of systems, infrared radiation is transmitted through cells and thin tissues, and the transmitted radiation is collected by a single-element detector after passing, e.g., through a Schwarzschild optics. Alternatively, imaging systems are used, where the transmitted radiation is mapped onto an imaging detector in forward direction. Since the size of the cell structures is of the same order as the wavelength of the infrared radiation, i.e., typically in the range of 2.5μm to 25μm, infrared spectra of cells and tissues exhibit a variety of scattering phenomena. The most intriguing scattering phenomena that have been observed are so-called Mie-type scattering phenomena[4–6] and studied intensively in the literature during recent years[4–11].

Mie-type scattering occurs in spherical- and nearly spherical-shaped scatterers. When the size of the scatterer is of the same order as the wavelength employed, neither the long-wavelength Rayleigh limit nor the geometric-optics, short-wavelength limit yield accurate results. The scattering of electromagnetic radiation at an ideal dielectric sphere was solved analytically by Gustav Mie already in 1908[12]. In Mie scattering, two main scatter contributions appear in the infrared spectra of spherically-shaped particles. (i) Broad oscillatory structures, so-called wiggles, which are due to the interference of the undisturbed, incoming radiation with the scattered radiation. (ii) Sharp scattering features, which are due to standing waves, for instance, whispering gallery modes that are resonances in the spherical scatterer. These sharp features are called ripples. The broad oscillatory structures are well described by an approximation formula developed by van de Hulst[13], which has been used extensively to establish algorithms that allow retrieving pure absorbance spectra[5,7,11].

The broad Mie wiggles are observed in more or less any type of infrared microscopy of cells and tissues. Pre-processing approaches have been developed to remove Mie wiggles from infrared spectra with the goal of obtaining pure chemical absorbance spectra[5]. Newer and more advanced approaches deal even with cases where strong dispersive effects due to absorption resonances are present in spectra[11]. While wiggles are omni-present in infrared spectra of cells and tissues, sharp ripples are rarely observed. They are observed mainly in cases where the scatterers represent perfect spheres such as PMMA spheres[6,14], or shapes that are close to perfect spheres, such as pollen[15,16]. In most other infrared spectra of cells and tissues, the ripples are absent, while the wiggles are present.

Both ripples and wiggles are related to shape characteristics[17]. However, while wiggles are due to a robust interference process that does not rely on the intricacies of resonances, ripples, due to delicate resonance processes, were shown to be affected by absorption[16,18]. Ripples, if present, and wiggles are both strongly influencing the apparent absorbance spectra. It is known that they can lead to non-Beer-Lambert absorption behavior in the infrared spectroscopy of cells and tissues. For instance, chemical absorption lines may be affected by ripples, since ripples are caused by resonant enhancement of the electric field in the sphere. It is also clear that, because they are resonances, the strengths of the ripples may depend strongly on the actual shape of the scatterer. In the context of chaos in wave systems, it was shown that chaotic scattering behaviour may enhance absorption properties of a scatterer considerably[19]. Small deviations from perfect spherical scatterers that involve changes in the shape or the refractive index, may easily lead to a transition between regular and chaotic scattering[19]. The aim of the current study is to investigate how ripples and wiggles, observed in the scattering of cells and tissues, are influenced by the shape of the scatterer and the actual absorption properties of the scatterer. A deeper understanding of these properties may help to improve Mie-scatter correction algorithms. For this purpose, we investigate a scatterer that is shaped like a Bunimovich billiard[20]. A Bunimovich-billiard shaped scatterer has been shown to be chaotic[21], and it allows to study the gradual transition between a regular scatterer (sphere) and a chaotic scatterer (billiard). The Bunimovich-billiard shaped scatterer[20] is a ray-splitting system. Chaotic ray-splitting billiard systems have been investigated in the field of quantum chaos[22–25]. They provide model systems for investigating implications of interfaces between two dielectric media on the wave and ray dynamics of such systems. For completeness we also investigated in addition to the chaotic Bunimovich-billiard shaped scatterer the effects of deformation into an integrable scatterer, i.e., a scatterer which does not show a transition to chaotic scattering as a function of deformation. We find that under increased deformation chaotic scattering accelerates the destruction of shape-resonance phenomena, such as, e.g., Mie ripples in absorbance spectra, while resonance phenomena tend to be more robust under deformation in the case of integrable deformations, such as deformation into ellipsoids. This has important consequences, e.g., for infrared microspectroscopy: The effects of shape resonances, such as Mie ripples, may be important in the analysis of absorbance spectra of quasi-spherical/ellipsoidal samples, such as pollen and PMMA spheres, and may lead to serious errors in the analysis of spectra if not properly taken into account. However, in general, biological cells and tissues have structures that are very different from perfect spheres and ellipsoids, and in these cases, in addition to absorption, the effects of shape resonances are suppressed due to chaotic scattering.

Methods

Figure 1 illustrates a typical infrared transmission measurement. Infrared radiation of intensity I_0 is directed towards a sample and the transmitted radiation I hits the detector. The background intensity, I_0, is measured by moving the sample out of the beam. The absorbance A is obtained by

$$A = -\log_{10}\left(\frac{I}{I_0}\right). \tag{1}$$

In an ideal measurement, the measured absorbance A consists solely of absorption bands caused by chemical bonds that absorb in the sample. The infrared spectrum is known to be a highly reproducible fingerprint of the biochemical composition of cells and tissues that are under investigation. However, often scattering phenomena lead to scattering signatures in the absorbance spectrum A in addition to the chemical absorption signatures. When scattering signatures are mixed with chemical absorption features in the measured absorbance spectrum, we call the measured absorbance, *apparent absorbance*[11,16]. In the case of a perfectly spherical scatterer, the scattering can be described exactly by Mie Theory[13,16]. Examples of such samples are some biological samples and PMMA spheres[15,16]. In order to retrieve and estimate pure absorbance spectra from highly scatter-disturbed measured infrared microspectroscopic measurements of single cells and tissues, the Mie extinction extended multiplicative signal correction (ME-EMSC) algorithm can be applied[11].

The apparent absorbance can be related to the extinction efficiency, Q_{ext}, by

$$A = -\log_{10}\left(1 - \frac{g}{G}Q_{ext}\right) \approx \frac{1}{\ln(10)}\frac{g}{G}Q_{ext}, \tag{2}$$

where G is the geometrical cross section of the detector and g is the geometrical cross section of the sample as shown in Fig. 1. Q_{ext} is a commonly, dimensionless quantity used to describe the amount of light which is extinguished from the forward direction (I)[13]. The approximation is found by expanding the logarithm and assuming that $G >> g$[15].

The expression for Q_{ext} for a sphere is given exactly by Mie Theory. Q_{ext} for a sphere with refractive index 1.3 and a radius of 10 μm is shown in Fig. 2. A refractive index of 1.3 is approximately the same as for water, and the refractive indexes of biological samples are often in the vicinity of this value.

We observe that Q_{ext} consists of long-range oscillations and sharp, narrow resonance structures. The long-range oscillations are called *wiggles* and are well described by the *van de Hulst approximation*, shown as the red line in Fig. 2. The van de Hulst approximation is based on the phase difference a ray experiences, as it travels in a straight line through the scatterer, compared to the undisturbed ray[13]. The narrow, sharp resonance structures are the *ripples*. They are caused by standing waves, i.e., resonances, inside the scatterer and are further described below.

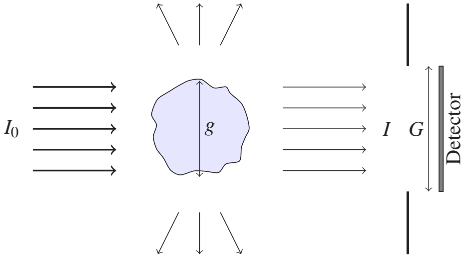

Figure 1. Infrared radiation of intensity I_0 is sent towards a sample with a geometrical cross section of g. Part of the radiation is scattered off or absorbed by the sample. The radiation that is transmitted through the sample has an intensity of I and hits a detector with a geometrical cross section equal to G.

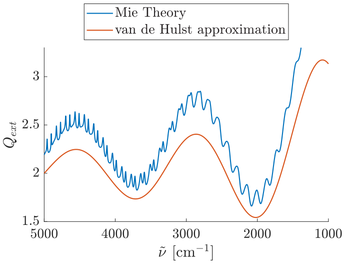

Figure 2. The extinction efficiency for a sphere of radius 10 μm and a refractive index of 1.3. The blue line indicates the exact extinction efficiency (described by Mie Theory) and the red line is the van de Hulst approximation for Q_{ext}.

While real cells are not perfectly spherically shaped, Mie extinction extended multiplicative scattering correction (ME-EMSC) has been proven useful for scatter corrections in many practical situations. The ME-EMSC algorithm uses the van de Hulst approximation for scattering off spheres. The van de Hulst approximation predicts the wiggle structure of the scattering, but not the ripples.

In order to evaluate what causes the disappearance of ripples, three mechanisms are investigated. First, we investigate how the wiggle and ripple structures are affected by a transition into a non-spherical shape. Then, we investigate how absorption is affecting the ripples and wiggles.We also evaluate how the numerical aperture and its size affects the extinction efficiency. The investigations are carried out for effectively two-dimensional systems.

The effect of a distortion of shape on Q_{ext}

In order to investigate the effect of shapes different from spheres and the validity of the van de Hulst formula, we investigate a model system that allows to perform the transition from a sphere to a system that shows irregular scattering features.

For this purpose, we study the transition from a circular scatterer to a stadium-shaped scatterer. The stadium-shaped scatterer is inspired by the Bunimovich stadium, which is an irregular, chaotic system[20,21]. In this work we investigate this model system by (1) deriving an approximation formula for the extinction efficiency for the stadium-shaped scatterer based on the van de Hulst approach, i.e., the approximation for the extinction efficiency for a sphere, (2) evaluating numerically exact electromagnetic calculations and (3) classical ray tracing. For calculating the electromagnetic near- and far-field, COMSOL Multiphysics® software was used[26]. The model system allows the transition from a disk to a stadium-shaped scatterer by changing a parameter d as shown in Fig. 3. We were especially interested in how the transition from a regular to a chaotic system affects the extinction efficiency, Q_{ext}, and the apparent absorbance spectra.

The effect of absorption on Q_{ext}

Samples investigated by FTIR spectroscopy are often highly absorptive in several wavenumber intervals. Therefore, the second step is to evaluate how Q_{ext} is affected by an increasing absorbance of the scatterer.

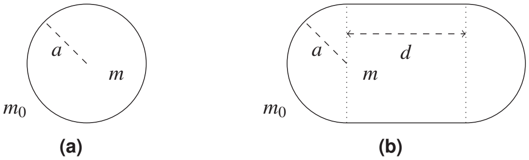

Figure 3. We are evaluating a system that transforms from a disk with a radius a, as shown in frame (a), into a stadium, as shown in frame (b), by increasing d. a is kept constant. The refractive index of the scatterer is m and the refractive index of the surroundings is $m_0 = 1$. The system is an open system, i.e., light can enter the system from the outside and can leave the system to the outside.

Extinction efficiency

The quantity Q_{ext} is dimensionless and related to the scattering efficiency Q_{sca} and the absorption efficiency Q_{abs} according to

$$Q_{ext} = Q_{sca} + Q_{abs}. \tag{3}$$

For perfectly spherical scatterers, Q_{ext}, Q_{abs} and Q_{sca} are described exactly by the Mie Theory[12,13].

In this work we are evaluating two-dimensional systems, or systems which are translationally invariant in the third dimension. We are therefore evaluating infinitely long cylinders. The infinitely long cylinders can also be described exactly by electromagnetic theory[13]. Figure 4 shows the extinction efficiency Q_{ext} for a sphere (black line) and an infinite cylinder with the E-field parallel to the cylinder axis (blue line) and the E-field perpendicular to the cylinder axis (red line). The radius of the sphere and cylinder is 10μm and the refractive index is 1.3.

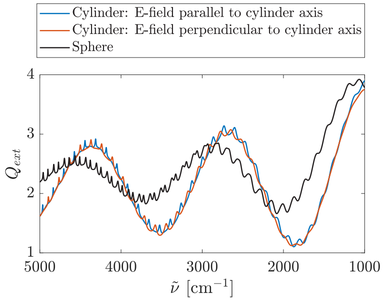

Figure 4. The extinction efficiency Q_{ext} for an infinite cylinder (red and blue line) and for a sphere (black line) with radius 10 μm and a refractive index of 1.3.[13]

We have further restricted our work to the case where the propagation direction of the incoming plane wave is perpendicular to the cylinder axis, and the electric field is parallel to the cylinder axis (blue line in Fig. 4). In this case, the extinction, scattering and absorption efficiencies are given by

$$Q_{ext} = \frac{2}{ka} \sum_{n=-\infty}^{\infty} \Re(b_n), \tag{4}$$

$$Q_{sca} = \frac{2}{ka} \sum_{n=-\infty}^{\infty} |b_n|^2, \tag{5}$$

and

$$Q_{abs} = Q_{ext} - Q_{sca}. \tag{6}$$

k is the angular wavenumber of the incoming plane wave and a is the radius of the cylinder. The coefficient b_n is given by

$$b_n = \frac{\tan\beta_n}{\tan\beta_n - i}, \tag{7}$$

and $\tan\beta_n$ is given by

$$\tan\beta_n = \frac{mJ_n'(mka)J_n(ka) - J_n(mka)J_n'(ka)}{mJ_n'(mka)N_n(ka) - J_n(mka)N_n'(ka)}. \tag{8}$$

m is the refractive index of the cylinder, J_n is the nth order Bessel function of the first kind and N_n is the nth order Bessel function of second kind (Neumann function).

In the case where the electric field is parallel to the cylinder axis the situation is equivalent to a two-dimensional scalar wave problem where a plane wave is propagating towards a circular scatterer and an exact description of the field inside and outside the scatterer can be found. Details are given in the supplementary materials Sec. A. The electric field of arbitrary shaped scatterers can be computed numerically. In this work we use Comsol Mulitiphysics and the wave optics module, which uses the finite element method to compute the electric near- and far-field of non-circular scatterers[26].

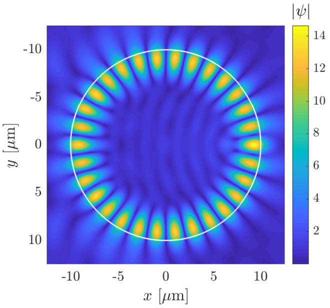

Figure 5. The norm of the wavefunction, equivalent with the norm of the electric field, for a disk of radius 10 μm and index of refraction 1.8. The incident radiation is a plane wave with wavenumber 1643.5 cm^{-1}, amplitude equal to one, and propagating from the left. The wavenumber of the incident plane wave is chosen to coincide with the wavenumber of a ripple.

Figure. 5 shows the norm of the wavefunction at a resonance at 1643.5 cm^{-1}. In this case the refractive index is 1.8 and the radius is 10 μm. As the figure shows, the resonance is caused by a standing wave around the circumference of the cylinder. The standing wave is called a whispering gallery mode. It can be associated with a classical ray that bounces around the circumference of the cylinder due to total internal reflection. It is noteworthy that the ray cannot leave the cylinder since it always bounces off the circumference from the inside of the cylinder with an incident angle larger than the critical angle for total internal reflection. Therefore the ray cannot be reached from the outside of the cylinder. The whispering gallery modes, i.e. the ripples, can also be found in the cases of a lower refractive index as indicated in Fig. 4. But the well recognizable patterns as shown in Fig. 5 are more distinct in the case of a lager ratio between the refractive indices inside and outside the circular scatterer.

Ray Tracing and classical chaotic scattering

In order to decide if the system is chaotic or not, we study the behavior of classical rays. Chaotic scattering systems have been studied for quantum wave systems and the corresponding classical ray systems[19,21]. Using the theory from this field, we evaluate if the system is chaotic or regular. The shape of the scatterer in this study is inspired by the *Bunimovich stadium*, which is a chaotic system. However, this system is a closed system, i.e., the rays cannot leave the system[19,20]. A chaotic scattering system is extremely sensitive to initial conditions. In a regular scattering system, a slight change in initial conditions of the rays, i.e., their starting positions, will be followed by only small differences in the paths of the corresponding rays. In the case of a chaotic system, small changes in starting conditions will be followed by large differences in the paths of the corresponding rays.

In our case of an open scattering system, rays are sent in from the top of the scatterer and are refracted into the system. The rays are treated as Newtonian rays, so when a ray hits a boundary it will either be transmitted or stay in the system due to total internal reflection. We can qualitatively show the occurrence of chaos by evaluating the lengths of the rays inside the scatterer. When the lengths are rapidly changing for a slight change in starting conditions, this is an indication of chaos.

In this work we evaluate the behavior of the classical rays for a system where the ripples have disappeared, i.e. we do not observe the standing waves in the scatterer. This system corresponds to systems without ripples in the absorbance spectra that we observe in FTIR experiments.

Several factors may be considered in order to decide whether the scattering behavior of the system is chaotic. In this work we consider (1) the fractal structure of path-length plots, (2) the fractal dimension, and (3) the Lyapunov exponent of the system.

By magnifying the path length plots several times, fractal structure may emerge. A fractal is a class of irregular structures that are not smooth. In our case if the starting position of a ray coincides with the fractal, a slight change in this starting position results in a considerable change in path length of the ray. The presence of a fractal indicates the presence of chaos. In the case where a magnification of the fractal yields several identical copies of the fractal itself, the fractal is *self-similar*. A well-known self-similar fractal is the Cantor set. Several objects in nature have a fractal structure, e.g., cumulus clouds, trees, and lungs[27].

In order to evaluate the fractal dimension of the system, the box-counting method is applied. By dividing the set of rays into smaller and smaller subsets and counting the number of sets that contain long-lived rays, the fractal dimension can be obtained as the slope of a logarithmic plot of the number of subsets with at least one long-lived trajectory and minus the width of the subset[28]. A non-integer fractal dimension is an indication of chaos[29–32].

The Lyapunov exponent can be found by evaluating the distance between two neighboring long-lived rays as a function of time. A positive Lyapunov exponent is an indication of chaos[29–32].

Relation between the imaginary part of the refractive index and absorbance

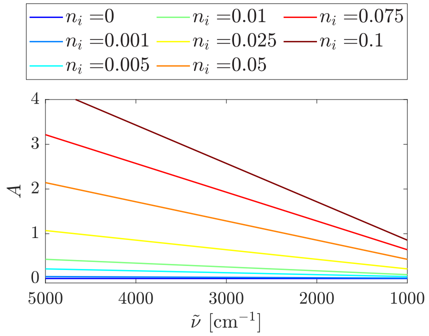

Figure 6. The absorbance, A, as a function of wavenumber for different choices of the imaginary part of the refractive index, n_i. A is related to n_i as indicated by Eq. 9. The effective thickness if found for a cylinder of radius 10 μm.

The absorption properties of a material can be modelled by including an imaginary part n_i in the refractive index, $m = n_r + in_i$. n_r is the real part and describes the refractive properties of the material. n_i can be related to the pure absorbance A_{pure} by

$$A_{pure} = \frac{4\pi n_i d_{\text{eff}} \tilde{\nu}}{\ln(10)}, \tag{9}$$

where d_{eff} is the effective thickness and $\tilde{\nu}$ is the wavenumber[9, 16]. In the case of an infinite cylinder where the light is propagating perpendicular to the cylinder axis, $d_{\text{eff}} = \frac{\pi a}{2}$ where a is the radius of the cylinder. Figure 6 shows how the absorbance is related to different choices of the imaginary part of the refractive index, n_i, within the wavenumber interval 5000-1000 cm^{-1}.

Relation between the size of the numerical aperture and the extinction efficiency

In FTIR measurements the detector has a finite size, G, as indicated in Fig. 1. The size of this detector is related to the *numerical aperture*, NA, which is defined as

$$\text{NA} = \sin(\theta), \tag{10}$$

where θ is the angle defined by the size of the detector as showed in Fig. 7[33]. Figure 7 is a simplified model of, e.g., a Schwarzschild optics for transmission IR measurements[8], that illustrates the general principle of how θ is related to NA.

The extinction efficiency, Q_{ext}, is the sum of the scattering efficiency and the absorption efficiency. In the case of a non-absorptive scatterer we have $Q_{ext} = Q_{sca}$. In the case where the E-field is parallel with the cylinder axis, Q_{sca} can be found

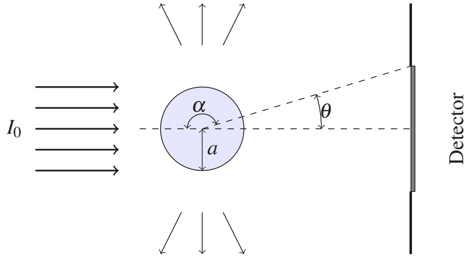

Figure 7. Infrared light of intensity I_0 is propagating towards a sample with a shape of an infinite cylinder of radius a in a FTIR spectrometer. The detector of the spectrometer is of a finite size, defined by the numerical aperture given by $\mathrm{NA} = \sin\theta$. The scattered light that does not hit the detector is limited within the angle α on both sides of the center line.

as a sum of b_n's as described in Eq. 5. This expression is found by evaluating the following integral

$$Q_{sca} = \frac{1}{\pi ka}\int_0^{2\pi} |T(\theta)|^2 d\theta = \frac{2}{\pi ka}\int_0^{\pi} |T(\theta)|^2 d\theta, \tag{11}$$

where k is the angular wavenumber, a is the radius of the cylinder and θ is the angle as shown in Fig. 7. The integral can be reduced as showed above due to symmetry. The function T in the case where the E-field is parallel to the cylinder axis is given by

$$T(\theta) = \sum_{n=-\infty}^{\infty} b_n e^{in\theta}, \tag{12}$$

where b_n is given in Eq.7.

When a numerical aperture is present, some of the scattered light is scattered in forward direction and hits the detector. In order to evaluate the amount of light which does not hit the detector, we need to evaluate how the Q_{sca} is affected by an increased θ. The scattering efficiency (Eq. 11) is then evaluated over the angle α on both sides of the center line.

Results

In order to corroborate the theoretical results presented in this paper, FTIR raw spectra of PMMA-spheres, pollen, and human cells were measured and analyzed. Three of the spectra are shown in Fig. 8.

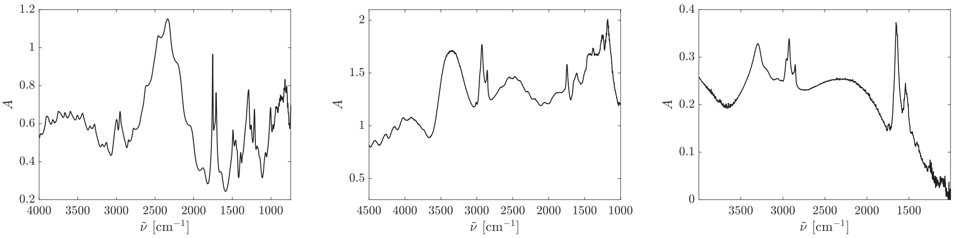

(a) **(b)** **(c)**

Figure 8. Absorbance spectra of (a) a PMMA-sphere[15] (b) a Juniperus Excelsa pollen grain[15] and (c) a human lung cancer cell[5]. In order not to introduce spurious features into the spectra that may result from using a correction algorithm, and in order to highlight the original appearance of the spectra, all three spectra shown are uncorrected, raw spectra. The tiny, sharp features seen in the spectrum in frame (c) are mostly due to noise and counting statistics; they are not reproducible ripples.

The absorbance spectrum for a PMMA-sphere (Fig. 8a) shows both ripples and wiggles, which confirms the fact that perfectly spherical scatterers are well described by Mie theory. The spectrum of the Juniperus Excelsa pollen grain (Fig. 8b) also shows both wiggles and ripples. This is expected since the shape of the pollen grains whose spectrum is shown in Fig. 8b, is close to spherical. In the case where the scatterer has a non-spherical shape, e.g., a biological cell (Fig. 8c), the corresponding spectrum only shows the wiggles, i.e., the broad oscillations, but not the ripples.

The PMMA (polymethylmatecrylate) spectrum shown in Fig. 8a was recorded at the SMIS infrared beamline at the SOLEIL synchrotron in France. Microspheres of PMMA with a diameter of approximately 15 μm, deposited on ZnSe slides, were measured in transmission mode. A Nicolet 5700 FTIR spectrometer with a Nicolet Continuum XL IR microscope, coupled with the synchrotron infrared beam, was used for the measurements. The Juniperus Excelsa pollen samples were collected at the Botanical Garden of the Faculty of Science of the University of Zagreb in 2012, and were measured at the same infrared beamline, with the same instrumental setup. The diameter of the pollen grains was estimated to be between 10 to 40 μm. More detailed information about measurement and analysis of the PMMA and pollen spectra can be found in reference[15]. The human lung cancer cell spectrum shown in Fig. 8c was recorded at the European Synchrotron Radiation Facility (ESRF) in Grenoble, at the ID 21 beamline. For these measurements, a Nicolet Nexus 870 spectrometer coupled with a Continuum-Thermo Nicolet microscope was used. More details of the experimental setup can be found in reference[5].

Distortion of the circular shape

Developement of an approximation for Q_{ext} for stadium-shaped scatterers

As presented above, the van de Hulst approximation for Q_{ext} for a sphere is used in the ME-EMSC algorithm. In order to derive an analytical van-de-Hulst-type extinction formula for our stadium system, we start by looking at an approximation for a disk and follow the same procedure as presented by van de Hulst for a sphere[13]. For a sphere, the extinction efficiency is given by[13]

$$Q_{ext} = \frac{4\pi}{k^2}\frac{1}{g}\Re[S(0)], \tag{13}$$

where k is the angular wavenumber, $g = \pi a^2$ is the geometrical cross section of the sphere (see Fig. 1) and $S(0)$ is the amplitude function in forward direction.

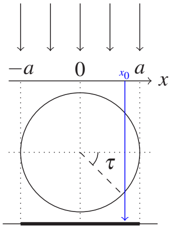

Figure 9. System investigated for the evaluation of the extinction efficiency of a disk.

In order to derive the approximation for a circular disk, we evaluate how the rays, assumed to propagate straight through the scatterer, affect the wave in the geometrical shadow of the disk (the shaded area in Fig. 9). The disk has a radius a and a refractive index m. The blue ray at $x = x_0$ has a phase lag equal to $2a\sin(\tau)(m-1)k$, where k is the angular wavenumber and $2a\sin(\tau)$ is the length of the ray inside the disk.

In the case of the two-dimensional system shown in Fig. 9, $S(0)$ is given by

$$S(0) = \frac{k^2}{2\pi}\int_{-a}^{a}[1 - e^{-i\rho\sin(\tau)}]dx, \tag{14}$$

where k is the angular wavenumber, a is the radius of the disk, τ is the angle as indicated in Fig. 9 and $\rho = 2ka(m-1)$.

In the geometrical shadow below the disk, the field that is added to the original plane wave is the expression inside the brackets of Eq. 14. The integral of $S(0)$ can be written in terms of Bessel functions, which then results in

$$Q_{ext}(\rho) = 2 - 2J_0(\rho) + 4\sum_{n=1}^{\infty} J_{2n}(\rho)\frac{1}{4n^2-1}, \tag{15}$$

where J_0 is the 0th order Bessel function of the first kind and J_{2n} are Bessel functions of the first kind and order $2n$.

Figure 10 shows the result of Eq. 15 together with the exact Mie solutions for an infinite cylinder (Eq. 4). As for the sphere in Fig. 2, the approximation predicts the positions of the wiggles, but not the ripples. The graph of the approximation

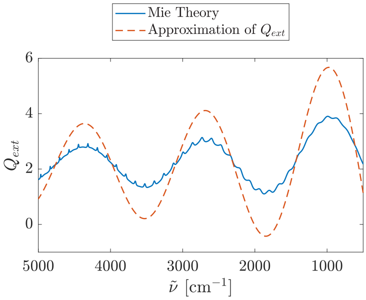

Figure 10. The blue line is the exact expression for Q_{ext} in the case where the E-field is parallel to the axis of the cylinder. The radius of the cylinder is 10μm and the refractive index is 1.3. The red dashed line is the approximation of Q_{ext} given by Eq. 15.

formula of Eq. 15 is scaled with respect to the exact result. This is not a problem for state of the art Mie scatter corrections in infrared spectroscopy, since the Mie scatter correction is scaling invariant with respect to the theoretical model used for the correction[5,7,9,11].

When we extend our circular scatterer to a stadium-shaped scatterer, as in Fig. 11, we also need to include rays that are propagating through the rectangular mid-section of the stadium. The phase lag in this case is given by $2a(m-1)k$. The amplitude function in forward direction is given by

$$S_{stadium}(0) = \frac{k^2}{2\pi}\left(\int_{-a}^{0}[1-e^{-i\rho\sin(\tau)}]dx + \int_{0}^{d}[1-e^{-i\rho}]dx + \int_{d}^{d+a}[1-e^{-i\rho\sin(\tau)}]dx\right), \tag{16}$$

where k is the angular wavenumber and a and d are the radius of the stadium's end caps and the lengths of the straight sections as indicated in Fig. 11.

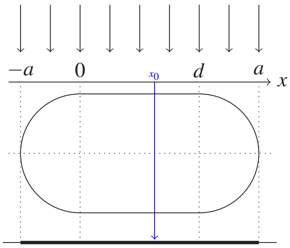

Figure 11. System investigated for the evaluation of the van de Hulst approximation of the extinction efficiency of a stadium.

With the result in Eq. 16, we arrive at the following explicit formula for the extinction efficiency

$$Q_{ext}(\rho) = \frac{2a}{2a+d}\left(2-2J_0(\rho)+4\sum_{n=1}^{\infty}J_{2n}(\rho)\frac{1}{4n^2-1}\right)+\frac{2d}{2a+d}(1-\cos(\rho)). \tag{17}$$

In Fig. 12, we compare the results of Eq. 17 with electromagnetic COMSOL simulations. The figure shows that both the van de Hulst formula in Eq. 17 and the COMSOL simulations predict that for a stadium the positions of the wiggles are shifted to the right as d increases.

Investigation of the electromagnetic field for stadium-shaped scatterers

To evaluate the scattering properties of a stadium further, the extinction coefficient and the electric field were calculated using COMSOL[26]. Figure 12 shows the results of these simulations. The refractive index was set to 1.3 and the radius of the half disks at the end of the stadium was set to 10 μm.

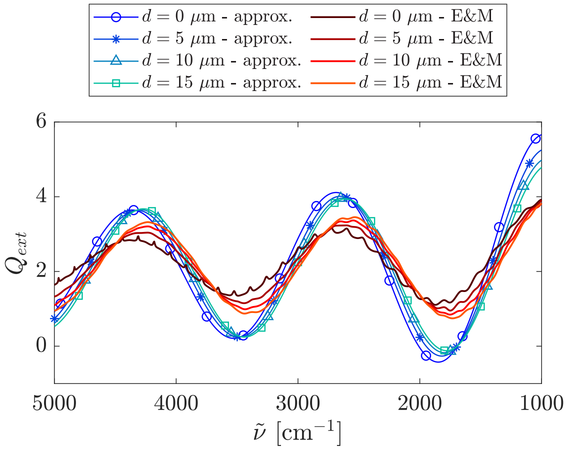

Figure 12. Q_{ext} of a stadium with a refractive index of 1.3 and a radius of the circular end caps equal to 10 μm. The length of the straight sections is changed from 0 μm (dark blue line and dark red line) to 15 μm (turquoise line and orange line). The figure shows that the wiggles are shifted to the right both according to the COMSOL simulations of the electromagnetic field (reddish, thick lines) and according to the approximation of Q_{ext} (bluish, thin lines) given by Eq. 17.

Figure 12 shows the extinction efficiency Q_{ext} as a function of the wavenumber found by COMSOL (reddish, thick lines) together with the approximation for Q_{ext} according to Eq. 17 (bluish, thin lines), where the darkest blue and red curves show the respective extinction efficiencies for a disk. In the exact result for a disk (darkest red color in Fig. 12), the familiar patterns of wiggles and ripples are present. As we increase d, the sharp ripples disappear. However, we still observe some remnants of ripples at the smallest wavenumbers.

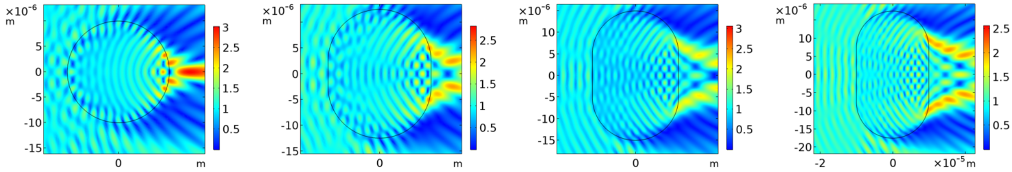

(a) $d = 0\mu$m. **(b)** $d = 5\mu$m. **(c)** $d = 10\mu$m. **(d)** $d = 15\mu$m.

Figure 13. For all the frames, the radius of the circular end caps is 10 μm and the refractive index of the scatterer is 1.3. Frames (a)-(d) show the norm of the E-field in the case where a plane wave is incident from the left with wavenumber $\tilde{\nu} = 2600$ cm^{-1}.

In Fig. 13a-13d, the norm of the E-field is shown for wavenumber $\tilde{\nu} = 2600$ cm^{-1}. In the case of a circular scatterer (Fig. 13a), we clearly see the focusing effect and the photonic jet behind the scatterer. As d increases, we observe that the photonic jet behind the scatterer divides into two. These two jets emerge from the scatterer at the points where the straight sections of the stadium meet the circular end caps of the stadium. This observation is well-known from the field of micro-disk lasers[34].

In order to further evaluate how the transition to chaos affects the system, the refractive index of the scatterer was increased to 1.8. An increased refractive index results in sharper ripples. Figure 14 shows Q_{ext}, found from simulations of the electromagnetic field (by Comsol), for this case. The wavenumber interval is between 4200 and 3700 cm^{-1}. The colors indicate the size of d, which ranges from 0.001 μm (dark blue line) to 50 μm (dark red line).

For the cases where d is equal to 2 μm or less, the ripple structure is present. Investigating the near field at wavenumbers that correspond to sharp peaks in $Q_{ext}(\tilde{\nu})$, we observe that they correspond to standing waves. Figure 15 shows some selected

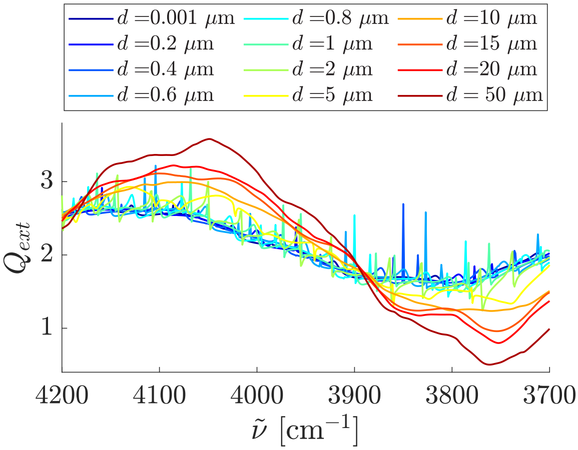

Figure 14. Extinction efficiency as a function of wavenumber. Illustrated is the change in Q_{ext} as a function of the length d of the straight sections of the stadium as we change d from 0.001 (dark blue), which is close to a disk, to a stadium with $d = 50\,\mu$m (dark red). The radius of each of the endcaps is 10 μm and the refractive index of the stadium is 1.8. The simulations are done by Comsol.

plots of the norm of the E-field. Supplementary materials Sec. B shows additional field plots. On the way to a fully developed stadium we observe that for a weakly deformed disk the circular standing-wave pattern transforms into a diamond-shaped pattern (see Figs. 15b and 15c).

At $d = 5$ μm, nearly all the ripples have disappeared. Some small peaks are still observed; they correspond to the wave functions equal and similar to the ones shown in Fig. 15d.

As the figure indicates, the sharp ripples disappear when d is 10 μm and larger. For the cases where the sharp resonances have disappeared, we observe scarlets[35,36], which are an indication of chaos. The scarlets are rigde-structures that show how the waves are locally guided.

The ratio between the wavelength and the size of the scatterer is important in order to observe wave chaos. It is therefore possible to observe classical chaos in cases where we still have standing waves in the wave picture. On the other hand, in cases where $d = 10$ μm and larger, this ratio is so small that the simulations of the electromagnetic field indicate chaotic behavior.

Behavior of classical rays for a stadium-shaped scatterer

In order to evaluate if the system is chaotic or not, a ray tracing code was written. The code simulates the evolution of rays sent straight down towards the scatterer as shown in Fig. 16. In order to look for an indication of chaos, the path lengths of the rays are evaluated for systems with different lengths of the straight sections d and different refractive indices. Only rays sent towards the left half disk of the stadium are considered. The reason is that (i) rays incident on the straight sections of the stadium pass straight through and are therefore uninteresting in the context of chaos, and (ii) because of symmetry, rays incident on the right end cap behave exactly the same as rays incident on the left end cap.

In Fig. 14 we observe that in the case where the length of the straight sections of the stadium, d, is 5 times larger than the radius, a (see Fig. 16), the ripples disappear and we observe scarlets in the corresponding electric-field plots. In this case, the refractive index of the scatterer is 1.8. Since classical rays are independent of wavelength, a was set to 1 and d was set to 5. Figure 17a shows the resulting behavior of the simulated rays and Fig. 17b shows the lengths of the rays inside the scatterer as a function of starting position. For rays incident on the very left of the stadium, long-lived trajectories are observed. This is an indication of chaos.

In order to investigate whether the life-time plot of the rays exhibits fractal structure, one tenth of the range of starting positions in Fig. 17b was magnified. This was repeated seven times. The resulting path length plots are shown in Fig. 18. Fractal structure is present in all seven stages of magnification. The magnifications also show that new structure appears at each stage of magnification. This indicates that the life-time fractal is not self-similar. Additional magnifications are displayed in the supplementary materials Sec. C.

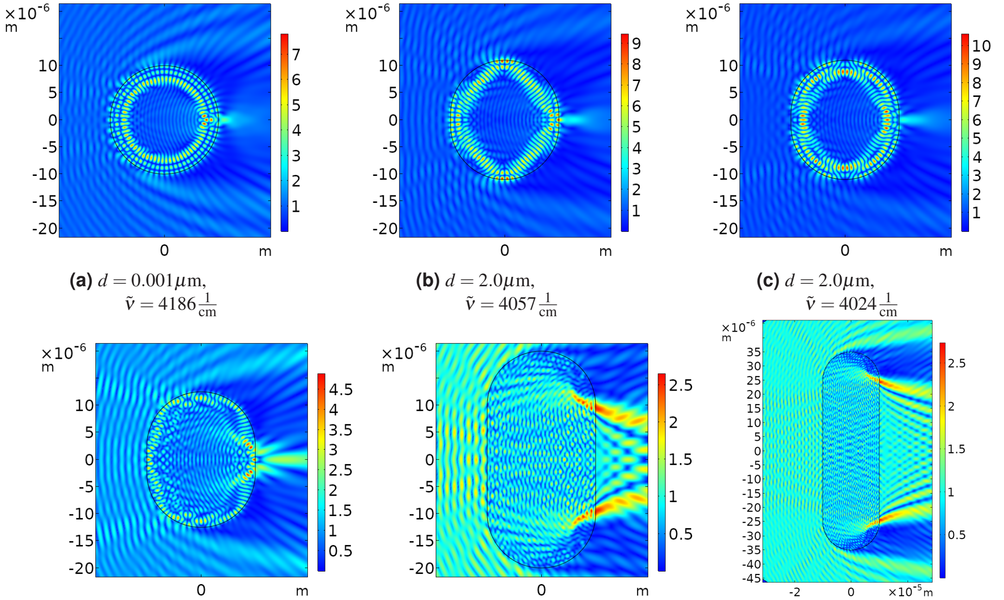

(a) $d = 0.001\mu$m, $\tilde{\nu} = 4186\frac{1}{\text{cm}}$

(b) $d = 2.0\mu$m, $\tilde{\nu} = 4057\frac{1}{\text{cm}}$

(c) $d = 2.0\mu$m, $\tilde{\nu} = 4024\frac{1}{\text{cm}}$

(d) $d = 5.0\mu$m, $\tilde{\nu} = 3943\frac{1}{\text{cm}}$

(e) $d = 20.0\mu$m, $\tilde{\nu} = 3797\frac{1}{\text{cm}}$

(f) $d = 50.0\mu$m, $\tilde{\nu} = 4048\frac{1}{\text{cm}}$

Figure 15. The plots show the norm of the electric field for selected wavenumbers. The incoming wave is a plane wave entering from the left. The stadium shaped scatterer has a radius of the end-caps equal to 10 μm and a refractive index of 1.8. The lengths of the straight sections of the stadium, d, and the corresponding selected wavenumbers are stated below each of the different panels

The fractal dimension of the system was found by evaluating a system where 10 million rays were sent straight downwards and incident on the left end-cap. A long-lived ray was defined as a ray with a length longer that 1 000 000. This set of starting positions was divided into subsets of length equal to δ. The blue line in Fig. 19 shows a plot of $\ln(N)$ as a function of $-\ln(\delta)$, where N is the number of subsets that contain at least one long-lived ray at resolution δ. The fractal dimension is then found as the slope of $\ln(N)$ as a function of $-\ln(\delta)$.

Figure. 19 shows $\ln(N)$ in the case where in total 10 million (blue line) and 100 million (red line) rays are started in the interval from $x_0 = -3.5$ and $x_0 = -3.4$. The yellow line is a straight-line fit to the data and shows that the slope, i.e., the fractal dimension, is approximately 0.65. As the figure shows, $\ln(N)$ deviates from a straight line when δ becomes too small. This is due to the fact that the resolution of the life-times (i.e., 10 million rays or 100 million rays) is still not enough for the corresponding δ where the bending-over of $\ln(N)$ vs. $-\ln(\delta)$ occurs.

In order to find the Lyapunov exponent, the distance between two long-lived rays was evaluated. The starting positions of the two rays are given as "Pair 1" in Tab. 2. The Lyapunov exponent was found by evaluating the distance between these two rays as a function of travelled path length. The logarithm of distance between the two rays, D, was plotted against the distance travelled. The result is shown in Fig. 20a as the blue line. The slope of the blue line is indicated by the red line, and indicates a Lyapunov exponent equal to 0.36. In order to evaluate the Lyapunov exponent in another region of starting positions we evaluated the average of the Lyapunov exponent for 10 rays. This is shown in Fig. 20c. This is the mean of the 10 rays in Fig. 20b and the starting positions of these ten rays are given in Tab. 2. The slope of this averaged line is also found to be 0.36.

The dips in the blue line in Fig 20 correspond to the fact that the rays are crossing each other. The slope of the blue line in Fig 20 (ignoring the dips) is the Lyapunov exponent. The red line indicates that the slope is approximately 0.36.

Elliptic deformation

The following question arises: Is the disappearance of the ripples of the system *caused* by the chaotic behavior or is the reason for the disappearance of the ripples primarily caused by the deformation into a stadium, and the chaotic scattering is merely

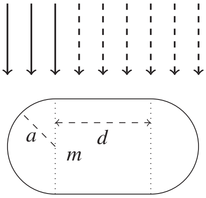

Figure 16. Newtonian rays are sent straight down towards the stadium-shaped scatterer. The rays are refracted according to Snell's law. Only the rays that hit the left end-cap of the scatterer are investigated (solid line). Due to symmetry, the rays that hit the right end-cap behave the same as the rays that hit the left end-cap. Rays that hit the straight sections of the stadium are not long-lived: They transmit straight through the scatterer.

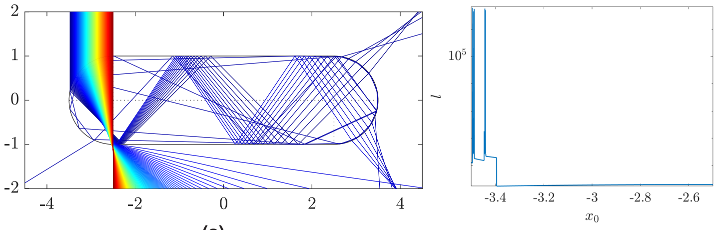

(a)

(b)

Figure 17. Frame (a) shows how rays sent straight downwards toward the left end cap refract when hitting the scatterer. Frame (b) indicates the length of the each ray, l, inside the scatterer as a function of start position x_0 with a logarithmic y-axis. The refractive index of the scatterer is 1.8. Classical ray tracing investigations are wavelength independent and the length of straight part of the stadium is 5 times the radius of the end caps. This corresponds to a system as in Fig. 15f where $d = 50\mu$m and $r = 10\mu$m.

a by-product of deformation, i.e., the disappearance of the ripples is *correlated* with the onset of chaotic scattering, but not *caused* by chaotic scattering. In order to conclusively answer this question, we also considered the deformation of the disk into an ellipse, which is an integrable system that has no chaotic scattering at any deformation. Therefore, if the ripples disappear under deformation into an ellipse, we have conclusively shown that the cause for the disappearance of the ripples is deformation, and that chaotic scattering, a consequence of deformation, is merely correlated with the disappearance of the ripples, but not the cause. To investigate this point, we studied how the ripple structure is changing as we deform our disk-shaped scatterer into an elliptical scatterer as shown in Fig. 21.

An ellipse is described by the two semi-major axes a and b as shown in Fig. 21. In our deformation studies, we increase the width of the ellipse in x-direction, i.e., we increase the semi-major axis b; the incident light illuminates the scatterer from above. The semi-major axis, a, is selected to be 10 μm, and b is increased from 10 μm (i.e. a disk-shaped scatterer) to 60 μm. Figure 22 shows how the extinction efficiency changes as we increase b. We observe that the ripple structure disappears when b becomes large enough. However, we also see that compared to the stadium, the ripples are more resilient in the case of the ellipse, i.e., an integrable system, and disappear only at a much larger deformation compared to the stadium, which exhibits chaotic scattering. This shows conclusively that the deformation is the reason for the disappearance of the ripples. However, we also see that chaotic scattering has an accelerating effect on the disappearance of the ripples, i.e., the ripples disappear more quickly in the presence of chaotic scattering. The calculations were done with COMSOL[26]. Contrary to the sensitivity of the ripples we observe that the wiggle structure is robust with respect to deformation. This is analogous to our observations in the case of the stadium-shaped scatterer (Fig 12).

Figure 23 shows the norm of the electric field for the selected wavenumbers for the systems evaluated in Fig. 22. The wavenumbers correspond to peaks (ripples) in the Q_{ext}.

Absorption properties of the scatterer

As mentioned above, the extinction, scattering, and absorption efficiency for an infinite cylinder can be described exactly by Mie theory.

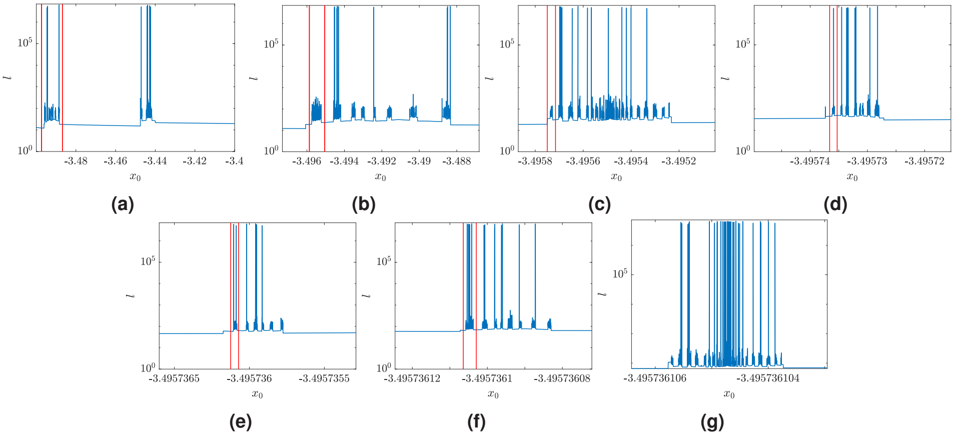

(a) (b) (c) (d)

(e) (f) (g)

Figure 18. The figures indicate the length of each ray as a function of start position. In frame (a) the start position is chosen to be a magnification of one tenth of the very left of Fig. 17b. Then the system is magnified as indicated by the two red lines seven times. For each magnification, 100 000 rays are started. All the figures have a logarithmic y-axis. The refractive index of the stadium shaped scatterer is 1.8. Classical ray tracing investigations are wavelength independent and the length of the straight sections of the stadium is 5 times the radius of the end caps. This corresponds to a system as in Fig. 15f where $d = 50\mu$m and $r = 10\mu$m. The magnification factor for each generation is given in Tab. 1

Table 1. The table indicates the magnification factor for the generation plots in Fig. 18.

Generation	Magnification factor
1	10
2	9.5
3	12.8
4	23.9
5	26.2
6	25.0
7	15.1

Figure 24 shows how Q_{ext} changes as the absorbance of the sample is increased. The absorbance is kept constant for all wavenumbers and is related to the imaginary part of the refractive index by Eq. 9. The real part of the refractive index in Fig. 24a is 1.3, and in Fig. 24b it is 1.8. For both cases, the wiggle structure remains when increasing A, but the amplitudes of the wiggles decrease as A increases. In Fig. 24b, the very sharp ripples disappear immediately when the absorbance is turned on. But the broader ripples are present until the the absorbance is equal to 0.5 for both cases.

Equation 4 shows how Q_{ext} and Q_{sca} are composed of a sum of b_n's. The b_n are given in Eq. 7, and by evaluating $\Re(b_n(\tilde{\nu}))$, how the ripples in Q_{ext} correspond to peaks $\Re(b_n(\tilde{\nu}))$. The figures in supplementary materials Sec. D. show how b_{15} and the corresponding ripple in Q_{ext} are attenuated as the absorbance of the sample increases. The figures further shows how the wave function for two of the ripples changes as A increases.

The effect of the numerical aperture

As mentioned above, the size of the numerical aperture decides the amount of scatted light that hits the detector. In order to evaluate how much of the light is extinguished from the forward direction, we evaluate the scattering efficiency of an infinite cylinder, where a plane wave is propagating perpendicular to the cylinder axis and the E-field is parallel to the cylinder axis. The investigation is done for a non-absorptive scatterer, i.e. $Q_{ext} = Q_{sca}$.

The extinction efficiency in the case where a numerical aperture is present is found by Eq. 11, where the integral is taken over the angle α as described in Fig. 7. The numerical apertures NA selected are NA$=0$ (which corresponds to the exact expression for Q_{ext} (Eq. 4)), NA$=0.325$, and NA$=0.65$[8,37]. The value of NA$=0.325$ was chosen to lie midway between 0 and 0.65. Figure 25 shows the result. The system investigated has a radius of 10 μm and a refractive index of 1.3 (Fig. 25a) and

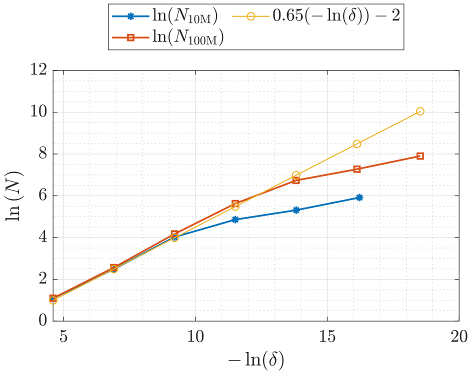

Figure 19. Determination of the fractal dimension of the set of long-lived rays based on the box-counting method. The blue line shows $\ln(N)$ as a function of $-\ln(\delta)$ where N is the number of intervals that contain at least one long-lived trajectory and δ is the width of the interval. The slope of the blue line is indicating the fractal dimension. The yellow line indicates that the slope is 0.65. $N_{10\mathrm{M}}$ indicates N for the case where 10 million rays were started in the interval and $N_{100\mathrm{M}}$ where 100 million rays were started in the same interval.

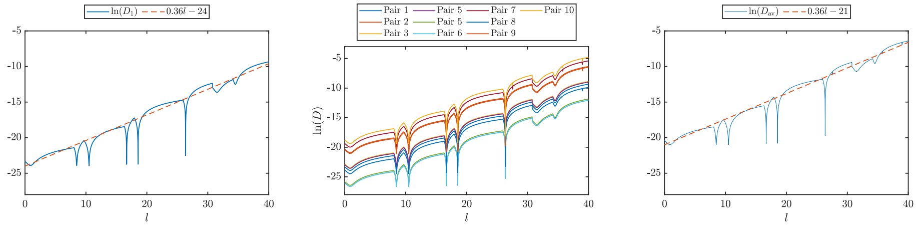

(a) **(b)** **(c)**

Figure 20. Frame (a) The blue line is $\ln(D)$ where D is the distance between the two rays as a function of path length, l. The start position of the two rays is given as pair 1 in Tab. 2. The red line indicates a straight line with the same trend as $\ln(D)$. The slope of this line, 0.41, is the Lyapunov exponent. Frame (b) shows $\ln(D)$ for 10 pairs of rays from Fig. 18g. The start positions of the rays are given in Tab. 2. Frame (c) shows the average of $\ln(D)$ for the 10 pairs of rays and the line which indicates the slope, i.e. the Lyapunov exponent, which in this case 0.36.

1.8 (Fig. 25b).

As NA is increased, Q_{ext} decreases. This is expected, due to the reduced angle, α, that the integral is taken over. We see that both the ripples and their positions are preserved as NA increases.

Discussion

The aim of this study has been to evaluate (i) how the extinction efficiency changes as we deform our circular-shaped scatterer into an elliptical- or stadium-shaped scatterer, (ii) how the absorbance of the scatterer affects the extinction efficiency and (iii) how the extinction efficiency is affected by the size of the numerical aperture. Figure 8 shows how the ripples are present in measurements of perfectly spherical scatterers (PMMA-spheres) and nearly perfectly spherical scatteres (pollen). In the case of a non-spherical scatterer (biological cell) we observed that the ripples completely disappeared, even in non-absorptive spectral regions.

For our study of the influence of sample shape on FTIR spectra, the choice of our system is natural, since it allows us to study the transition between regular scattering on a system whose scattering properties are known analytically, to a chaotic scattering system, which is no longer accessible analytically, i.e., its scattering properties have to be investigated numerically.

Table 2. The start position of the ten pairs of rays shown in Fig. 20b. The ten pairs of rays are selected as neighbouring long-lived rays ($l \approx 10^5$) in Fig. 18g.

	$x_{0,1}$	$x_{0,2}$
Pair 1	-3.495736105547581	-3.495736105546853
Pair 2	-3.495736105540718	-3.495736105530007
Pair 3	-3.495736105420616	-3.495736105420269
Pair 4	-3.495736105409732	-3.495736105409420
Pair 5	-3.495736105399923	-3.495736105399680
Pair 6	-3.495736105399368	-3.495736105399264
Pair 7	-3.495736105398918	-3.495736105398814
Pair 8	-3.495736105045579	-3.495736105043326
Pair 9	-3.495736105041593	-3.495736105041246
Pair 10	-3.495736104905339	-3.495736104904680

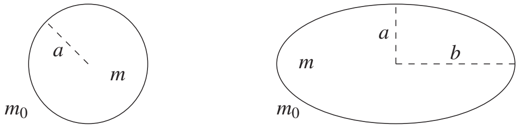

(a) **(b)**

Figure 21. We are evaluating a system that transforms from a disk with radius a, as shown in (a), into an ellipse, as shown in (b). The parameter that describes the height of the ellipse is its semi-major axis, a, which is kept constant and equal to the radius of the disk. We deform the scatterer by increasing the semi-major axis, b, of the ellipse. The refractive index of the scatterer is m and the refractive index of the surroundings is $m_0 = 1$. The light is entering the system from above.

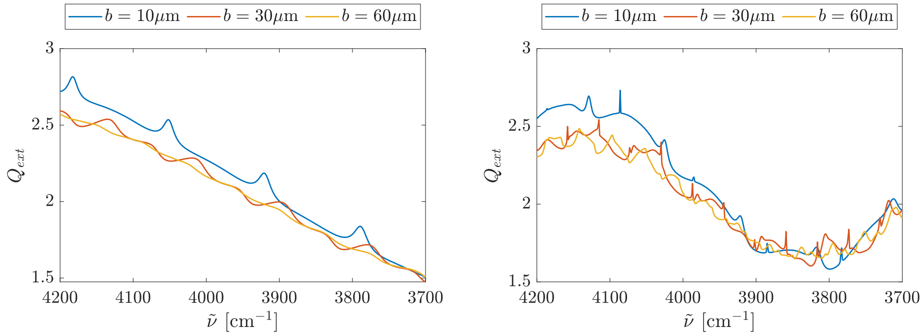

(a) **(b)**

Figure 22. The figure shows how Q_{ext} changes as the deformation of the ellipse increases. The semi-major axis, a, of the ellipse (see Fig. 21b) is kept constant at $a = 10\,\mu$m, and b is selected to be 10 μm (blue line, i.e., a disk-shaped scatterer), 30 μm (red line) and 60 μm (yellow line). The refractive index is (a) 1.3 and (b) 1.8.

The commercially available software package COMSOL Wave Optics allows us to extend previous knowledge accumulated in the domain of regular Mie scattering into the domains of regular scattering on an elliptic cylinder and chaotic scattering on a stadium-shaped cylinder. In both systems, the smooth transition from the disk system to the ellipse and stadium systems allows us to follow the evolution of the known Mie features, such as wiggles and ripples, into the domains of deformed, regular scattering in the case of elliptic deformations and chaotic scattering in the case of stadium-shaped deformations. In both cases we also looked at the dependence on the index of refraction. As one of our main observations we found that the ripples present in the scattering from a disk are suppressed by deformation, and faster in the presence of chaotic scattering (see Figs. 12 and

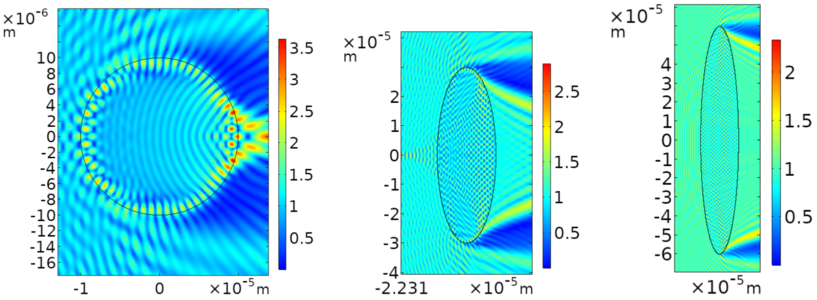

(a) $b = 10\mu$m, $\tilde{\nu} = 4181\,\frac{1}{\text{cm}}$
(b) $b = 30\mu$m, $\tilde{\nu} = 4133\,\frac{1}{\text{cm}}$
(c) $b = 60\mu$m, $\tilde{\nu} = 4144\,\frac{1}{\text{cm}}$

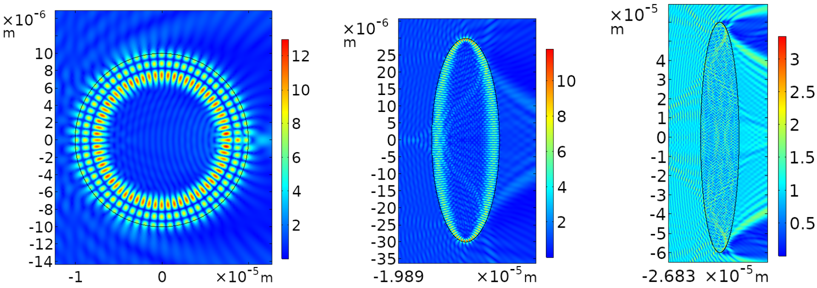

(d) $b = 10\mu$m, $\tilde{\nu} = 4086\,\frac{1}{\text{cm}}$
(e) $b = 30\mu$m, $\tilde{\nu} = 4115\,\frac{1}{\text{cm}}$
(f) $b = 60\mu$m, $\tilde{\nu} = 4052\,\frac{1}{\text{cm}}$

Figure 23. The plots show the norm of the electric field for selected wavenumbers. The incoming wave is a plane wave entering from the left. The ellipse-shaped scatterer as showed in Fig. 21, a is equal to 10.0μm and a refractive index of 1.3 (panel a-c) and 1.8 (panel d-f). The parameter b is shown in the sub-caption. The selected wavenumber is also shown in the sub-caption, the wavenumber corresponds to ripples/peaks in Fig. 22.

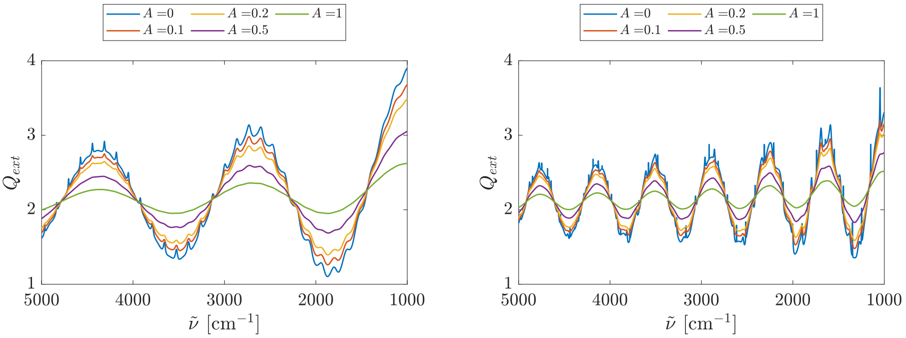

(a) **(b)**

Figure 24. The figure shows how Q_{ext} (Eq. 4) changes as the absorbance of the sample increases. The radius of the sample is 10 μm and the real part of the refractive index is (a) 1.3 and (b) 1.8. The imaginary part of the refractive index is found by Eq. 9.

14) compared to the case of regular scattering (see Fig. 22).

Despite the fact that the real world is three-dimensional, in order to keep our systems simple, allowing us to focus on

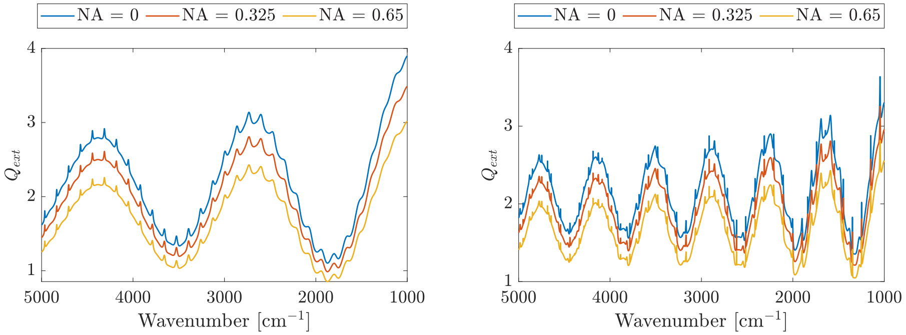

(a) **(b)**

Figure 25. The extinction efficiency, which is equivalent with the scattering efficiency in the case of a non-absorptive circular scatterer as found by Eq. 11. The refractive index of the scatterer is (a) 1.3 and (b) 1.8, and the radius is 10 μm. As described in Fig. 7, Q_{ext} is evaluated for the light that does not hit the detector with an angle larger than α. Q_{ext} is found for different sizes of the numerical aperture (NA). NA is related to θ in Fig. 7 by Eq. 10.

the essential mechanisms without cumbersome numerical ballast, we focused in this study on effectively two-dimensional (cylindrical) systems. This is justified since, as shown in Fig. 4 for a circular scatterer, qualitatively, and to some approximation even quantitatively, the same phenomena can be observed in two- and three-dimensional systems. Furthermore, a two-dimensional system is equivalent to a cylindrical three-dimensional system, i.e., a system which is translationally invariant in the third dimension.

Figure 10 shows how the van de Hulst approximation, derived in Eq. 15, compares with the exact Mie solution of the system. In the case of a disk, our approximation of the extinction efficiency of a disk reproduces the positions of the wiggles, but misses the ripples. When we use this approximation, we need to have in mind that the amplitudes of the resulting, approximate wiggles are too large. As the length of the straight sections of the stadium, d, increases, the COMSOL calculations show (see Fig. 12) that the positions of the wiggles are shifted towards the right. The same shift to the right is observed if we evaluate the extinction efficiency using our approximation of the extinction efficiency according to Eq. 17. This is also illustrated in Fig. 12.

We also observed some interesting structures in the electric field itself. A plot of the norm of the electric field shows how the photonic jet splits into two as the length of the straight sections of the stadium increases (see Fig. 13). The two jets emanate from points in the circumference of the stadium where the end caps merge with the straight sections. Similar effects have first been observed in the field of micro-disk lasers[34] and are used technically for coupling radiation in and out of these lasers. We also saw whispering gallery modes of higher than first order forming concentric rings in the E-field patterns located close to the perimeter. We also saw the manifestation of a "scar"[38], i.e., the local enhancement of the electric field in the vicinity of the diamond orbit of the Bunimovich stadium. Lastly, we also observed the phenomenon of "scarlets"[35,36] in the region of deeply chaotic scattering.

In order to further evaluate the stadium-shaped system we evaluated the behavior of the classical rays in the system. For the system where we observe scarlets in the electric field, we also observe that the length of the rays are very sensitive to their initial positions, which is an indication of chaos. In order to further evaluate the classical scattering properties of the system we found indications of chaos in terms of (i) the emergence of a fractal structure, which we traced through seven generations of magnification (see Fig. 18), (ii) a non-integer fractal dimension (see Fig. 19), and (iii) a positive Lyapunov exponent (see Fig. 20). Figure 18 also indicates that the fractal structure of the system is not self-similar. This contrasts with the self-similar structure found in[21]. However, we were able to reproduce the self-similar fractal structure in[21]. So, we are sure that our numerical codes are correct and the different fractal structure is a consequence of vertical versus horizontal incidence of rays and an increased refractive index.

Deformation is a new mechanism of ripple suppression that is now added to the mechanism of ripple suppression in the presence of damping[16]. We found that ripples are suppressed for deformations that lead to either integrable or non-integrable, chaotic systems. We also found that in integrable systems, the ripples are more resilient to deformation compared with systems that exhibit chaotic scattering. Intuitively it is clear why the ripples are suppressed more efficiently in the chaotic scattering situation. As shown in Fig. 15, whispering gallery modes, the origins of ripples, are not well, if at all, supported in the chaotic scattering situation, accounting for their fast disappearance. It has been shown (see, e.g.,[16]) that the sharp ripples, i.e., the needle-shaped resonances in the spectrum, start to disappear as soon as we turn on absorbance. But as Fig. 24 shows, the broader ripples, which correspond to higher-order Mie resonances[16], are still present until $A = 0.5$ is reached. Figure 25 indicates that the ripples are present also when we take the numerical aperture into account. Due to this fact, we would expect to observe the broader-type ripples in the non-absorptive regions in FTIR measurements. This is indeed confirmed by Fig. 8a and Fig. 8b, which are the spectra of spherical and quasi-spherical systems. However, the absorbance spectrum of the biological cell, shown in Fig. 8c, does not show a ripple-structure in the non-absorptive regions. This supports our hypothesis that the non-spherical shape of this scatterer results in a suppression of ripples combined with, possibly, chaotic scattering behavior.

The result of this study also supports the ME-EMSC method of analysis, which uses the van de Hulst approximation in order to Mie-correct FTIR spectra. Although ME-EMSC is based on the Mie-wiggle structure and does not take the Mie ripples into account, neglecting the ripple structure is justified in most cases of biological significance, since the shape of most biological samples is non-spherical, resulting in an absence of ripples. This follows from the fact that integrable deformations, which would support the manifestation of ripples even for relatively large deformations (see Fig. 22) are rare analytical oddities, while generic deformations result in chaotic scatterers with high probability[30–32] and consequently fast destruction of ripples for relatively small deformations (see Figs. 12 and 14). Still, it is important to be aware of the occurrence of ripples in the case of near-spherical samples, which definitely also occur in FTIR spectroscopic applications, as shown, e.g., in Figs. 8a and 8b.

Conclusion

In this paper, studying scattering on a disk that can be smoothly transformed into either an integrable elliptic scatterer or a Bunimovich stadium scatterer, we showed that deformation of the scatterer has a profound influence on the extinction efficiency. While regular scattering on a disk is accompanied by sharp resonances, i.e., whispering gallery modes that manifest themselves as “ripples” in the extinction efficiency, and integrable elliptical deformed scatterer support the ripples up to relatively large deformations, the ripples are nearly completely destroyed, even for relatively modes deformations in the presence of chaotic scattering. This is an important observation, since ripples may change both the locations and amplitudes of chemical absorption bands. While it is known that ripples are eliminated from FTIR spectra by sufficiently large absorption[16], the fast end efficient destruction of ripples by chaotic scattering is both a new result and of immense practical importance for spectroscopic applications such as FTIR spectroscopy of biological cells and tissues. While ripples are certainly eliminated in the presence of both chaotic scattering and sufficiently large absorption, we observed that even in the absence of absorption, for instance in chemically inert spectral regions, the presence of chaotic scattering caused by sample deformation, is sufficient to suppress Mie ripples in FTIR spectra. While this validates current correction methods for Infrared absorbance spectra, such as ME-EMSC in most situations of practical spectroscopic interest, in particular as applied to the correction and analysis of biological samples, great care has to be exercised when investigating quasi-spherically or quasi-elliptically deformed samples in which case Mie ripples may interfere with chemical absorption bands and may cause large errors in the analysis of spectra if Mie ripples are not properly taken into account.

References

1. Kwiatkoski, J. & Reffner, J. FT-IR microspectrometry advances. *Nature* **328**, 837 (1987).
2. Wetzel, D. L. & LeVine, S. M. Imaging molecular chemistry with infrared microscopy. *Science* **285**, 1224–1225 (1999).
3. Reffner, J. A., Martoglio, P. A. & Williams, G. P. Fourier transform infrared microscopical analysis with synchrotron radiation: the microscope optics and system performance. *Rev. Sci. Instruments* **66**, 1298–1302 (1995).
4. Mohlenhoff, B., Romeo, M., Diem, M. & Wood, B. R. Mie-type scattering and non-Beer-Lambert absorption behavior of human cells in infrared microspectroscopy. *Biophys. J.* **88**, 3635–3640 (2005).
5. Kohler, A. *et al.* Estimating and correcting Mie scattering in synchrotron-based microscopic Fourier transform infrared spectra by extended multiplicative signal correction. *Appl. Spectrosc.* **62**, 259–266 (2008).
6. Bassan, P. *et al.* Resonant Mie scattering in infrared spectroscopy of biological materials–understanding the ‘dispersion artefact’. *Analyst* **134**, 1586–1593 (2009).
7. Bassan, P. *et al.* Resonant Mie scattering (rmies) correction of infrared spectra from highly scattering biological samples. *Analyst* **135**, 268–277 (2010).
8. Van Dijk, T., Mayerich, D., Carney, P. S. & Bhargava, R. Recovery of absorption spectra from fourier transform infrared (ft-ir) microspectroscopic measurements of intact spheres. *Appl. Spectrosc.* **67**, 546–552 (2013).
9. Konevskikh, T., Lukacs, R., Blümel, R., Ponossov, A. & Kohler, A. Mie scatter corrections in single cell infrared microspectroscopy. *Faraday Discuss.* **187**, 235–257 (2016).

10. Konevskikh, T., Lukacs, R. & Kohler, A. An improved algorithm for fast resonant Mie scatter correction of infrared spectra of cells and tissues. *J. Biophotonics* **11**, e201600307 (2018).

11. Solheim, J. H. *et al.* An open-source code for Mie extinction extended multiplicative signal correction for infrared microscopy spectra of cells and tissues. *J. Biophotonics* **12**, e201800415 (2019).

12. Mie, G. Contribution to the optical properties of turbid media, in particular of colloidal suspensions of metals. *Ann. Phys.(Leipzig)* **25**, 377–452 (1908).

13. Hulst, H. C. & van de Hulst, H. C. *Light scattering by small particles* (Courier Corporation, 1981).

14. Blümel, R., Bağcioğlu, M., Lukacs, R. & Kohler, A. Infrared refractive index dispersion of polymethyl methacrylate spheres from Mie ripples in Fourier-transform infrared microscopy extinction spectra. *J. Opt. Soc. Am.* **33**, 1687–1696 (2016).

15. Lukacs, R., Blümel, R., Zimmerman, B., Bağcıoğlu, M. & Kohler, A. Recovery of absorbance spectra of micrometer-sized biological and inanimate particles. *Analyst* **140**, 3273–3284 (2015).

16. Blümel, R., Lukacz, R., Zimmermann, B., Bağcioğlu, M. & Kohler, A. Observation of Mie ripples in the synchrotron Fourier transform infrared spectra of spheroidal pollen grains. *J. Opt. Soc. Am. A* **35**, 1769–1779 (2018).

17. Brandsrud, M. A. *et al.* Does chaotic scattering affect the extinction efficiency in quasi-spherical scatterers? In *Biomedical Spectroscopy, Microscopy, and Imaging*, vol. 11359, 113590C (International Society for Optics and Photonics, 2020).

18. Chỳlek, P., Ngo, D. & Pinnick, R. Resonance structure of composite and slightly absorbing spheres. *JOSA A* **9**, 775–780 (1992).

19. Seim, E. *et al.* Chaos: A new mechanism for enhancing the optical generation rate in optically thin solar cells. *Chaos: An Interdiscip. J. Nonlinear Sci.* **29**, 093132 (2019).

20. Bunimovich, L. A. On ergodic properties of certain billiards. *Funct. Analysis Its Appl.* **8**, 254–255 (1974).

21. Jensen, J. H. Chaotic scattering of light by a dielectric cylinder. *J. Opt. Soc. Am. A* **10**, 1204–1208 (1993).

22. Kohler, A., Killesreiter, G. & Blümel, R. Ray splitting in a class of chaotic triangular step billiards. *Phys. Rev. E* **56**, 2691 (1997).

23. Kohler, A. & Blümel, R. Annular ray-splitting billiard. *Phys. Lett. A* **238**, 271–277 (1998).

24. Kohler, A. & Blümel, R. Weyl formulas for quantum ray-splitting billiards. *Annals Phys.* **267**, 249–280 (1998).

25. Kohler, A. & Blümel, R. Test of semiclassical amplitudes for quantum ray-splitting systems. *Phys. Rev. E* **59**, 7228 (1999).

26. COMSOL Multiphysics® v. 5.4. www.comsol.com. COMSOL AB, Stockholm, Sweden.

27. West, B. J. & Goldberger, A. L. Physiology in fractal dimensions. *Am. Sci.* **75**, 354–365 (1987).

28. Kohler, A., Høst, V. & Ofstad, R. Image analysis of particle dispersions in microscopy images of cryo-sectioned sausages. *Scanning* **23**, 165–174 (2001).

29. Blümel, R. & Reinhardt, W. P. *Chaos in Atomic Physics* (Cambridge University Press, 2005).

30. Lichtenberg, A. J. & Lieberman, M. A. *Regular and Chaotic Dynamics* (Springer, New York, 1983).

31. Gutzwiller, M. C. *Chaos in Classical and Quantum Mechanics* (Springer, New York, 1990).

32. Ott, E. *Chaos in Dynamical Systems* (Cambridge University Press, 1993).

33. Tipler, P. A. & Mosca, G. *Physics for scientists and engineers : with modern physics* (Freeman, New York, 2008), 6th ed. edn.

34. Nöckel, J. U., Stone, A. D. & Chang, R. K. Q spoiling and directionality in deformed ring cavities. *Opt. Lett.* **19**, 1693–1695 (1994).

35. O'Connor, P., Gehlen, J. & Heller, E. J. Properties of random superpositions of plane waves. *Phys. Rev. Lett.* **58**, 1296–1299 (1987).

36. Blümel, R., Davidson, I. H., Reinhardt, W. P., Lin, H. & Sharnoff, M. Quasilinear ridge structures in water surface waves. *Phys. Rev. A* **45**, 2641–2644 (1992).

37. Bhargava, R. Infrared spectroscopic imaging: the next generation. *Appl. spectroscopy* **66**, 1091–1120 (2012).

38. Heller, E. J. Bound-state eigenfunctions of classically chaotic hamiltonian systems: Scars of periodic orbits. *Phys. Rev. Lett.* **53**, 1515–1518 (1984).

Acknowledgements

- This work was supported by the grants "Development of a new ray model for understanding the coupling between dielectric spheres for photovoltaics with higher efficiency" - No: 250678 and by "Combining spectral and image information in the analysis of hyperspectral imaging data" - No: 289518, both financed by the Research Council of Norway.

- We thank Eirik Magnussen and Dr. Eivind Seim for helpful discussions.

- The simulations of extinction efficiency for different numerical apertures is based on the code presented in Simen Eriksen's Master thesis.

- The measurements of absorbance spectra of the PMMA-sphere and the pollen grain were supported by the SOLEIL, French national synchrotron facility (project No. 20120345). We thank Paul Dumas and Christophe Sandt from the SMIS beamline at SOLEIL.

- We thank Dr. Boris Zimmermann for useful discussions and for providing the measured absorbance spectra.

Author contributions statement

M.A.B., J.H. and A.K. developed together the initial idea. Author M.A.B., R.B. and A.K developed the concept of the paper. R.B. and A.K. supervised the research. M.A.B. carried out the simulations and analyzed the data being assisted by J.S. M.A.B. was the main writer of the paper with contributions from the other authors.

Additional information

Competing interests: The author declare no competing interests.

Figure Legends

*

Supplementary Material

Potential pitfalls in interpretation of Mie-type signatures in infrared microspectroscopy

A Scattering from a soft disk

A plane wave with a wavelength equal to λ is propagating from the left towards a circular scatterer as shown in Fig. A.1. The wave function of the incoming wave is given by ψ_0,

$$\psi_0 = e^{ikx} = e^{ikr\cos\theta}, \tag{1}$$

where k is the angluar wavenumber of the incoming plane wave, given by $\frac{2\pi}{\lambda}$. The x-position can be re-written in polar coordinates. ψ_0 can be written in terms for Bessel functions

$$\psi_0 = \sum_{l=-\infty}^{\infty} i^l J_l(kr) e^{il\theta}, \tag{2}$$

where J_l is the Bessel function of the first kind and order l.

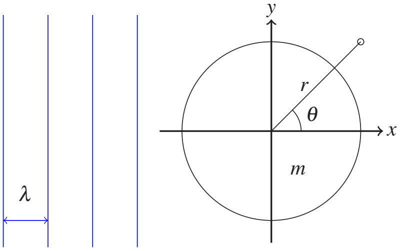

Figure A.1. The model circular scatterer with refractive index n. A plane wave is incident from the left with a wavelength equal to λ.

The scattered wave, ψ_s, can be written in terms of outgoing Hankel functions

$$\psi_s(r,\theta) = \sum_{l=-\infty}^{\infty} A_l H_l^{(+)}(kr) e^{il\theta}, \tag{3}$$

where $H^{(+)}$ is the Hankel function of the first kind and order l, and A_l is the scattering amplitude. The wave function outside the scatterer is therefore given by

$$\psi_{out}(r,\theta) = \psi_0 + \psi_s = \sum_{l=-\infty}^{\infty} i^l J_l(kr) e^{il\theta} + \sum_{l=-\infty}^{\infty} A_l H_l^{(+)}(kr) e^{il\theta}, \quad \text{for } r > R\,. \tag{4}$$

The wavefunction inside the scatterer is given by ψ_{in} and can be written as

$$\psi_{in}(r,\theta) = \sum_{l=-\infty}^{\infty} B_l J_l(\kappa r) e^{il\theta}, \quad \text{for } r < R\,, \tag{5}$$

where κ is the angular wave number inside the scatterer, given by $\kappa = kn$, where n is the refractive index of the scatterer.

By requiring a continuous ψ and ψ' for ψ_{in} and ψ_{out} at the boundary of the scatterer, we can derive an expression for the coefficients A_l and B_l:

$$A_l = \frac{-i^l\left[\kappa J_l'(\kappa r) J_l(kr) - k J_l'(kr) J_l(\kappa r)\right]}{\kappa J_l'(\kappa r) H_l^{(+)}(kr) - k J_l'(\kappa r) H_l'^{(+)}(kr)}, \tag{6}$$

$$B_l = \frac{i^l\left[k H_l^{(+)}(kr) J_l'(kr) - k H_l'^{(+)} J_l(kr)\right]}{\kappa J_l'(\kappa r) H_l^{(+)}(kr) - k J_l(\kappa r) H_l'^{(+)}(kr)}. \tag{7}$$

B Electric near field of a stadium shaped scatterer

Figure B.2 shows how the norm of the electric field inside a stadium-shaped scatterer changes as we increase the length, d, of the straight sections of the stadium. The extinction efficiency Q_{ext} is given in Fig. 14.For d less or equal to 2μm, the selected wave numbers correspond to peaks in $Q_{ext}(\tilde{\nu})$.

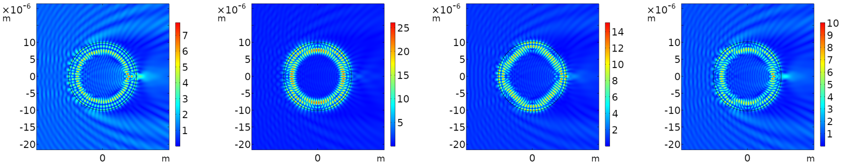

(a) $d = 0.001\mu$m, $\tilde{\nu} = 4186\frac{1}{\text{cm}}$

(b) $d = 0.2\mu$m, $\tilde{\nu} = 4159\frac{1}{\text{cm}}$

(c) $d = 0.4\mu$m, $\tilde{\nu} = 4139\frac{1}{\text{cm}}$

(d) $d = 0.4\mu$m, $\tilde{\nu} = 4132\frac{1}{\text{cm}}$

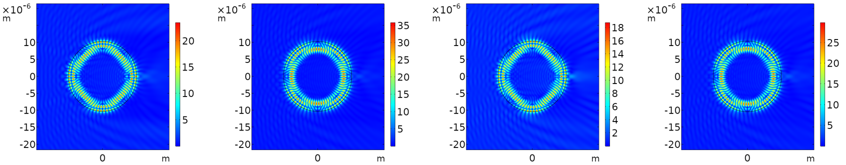

(e) $d = 0.6\mu$m, $\tilde{\nu} = 4115\frac{1}{\text{cm}}$

(f) $d = 0.6\mu$m, $\tilde{\nu} = 4104\frac{1}{\text{cm}}$

(g) $d = 0.8\mu$m, $\tilde{\nu} = 4091\frac{1}{\text{cm}}$

(h) $d = 0.8\mu$m, $\tilde{\nu} = 4077\frac{1}{\text{cm}}$

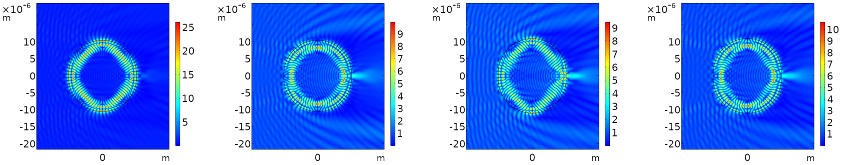

(i) $d = 1.0\mu$m, $\tilde{\nu} = 4068\frac{1}{\text{cm}}$

(j) $d = 1.0\mu$m, $\tilde{\nu} = 4051\frac{1}{\text{cm}}$

(k) $d = 2.0\mu$m, $\tilde{\nu} = 4057\frac{1}{\text{cm}}$

(l) $d = 2.0\mu$m, $\tilde{\nu} = 4024\frac{1}{\text{cm}}$

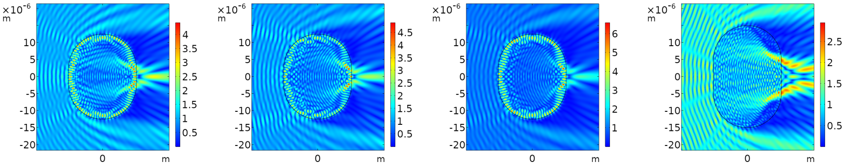

(m) $d = 5.0\mu$m, $\tilde{\nu} = 4103\frac{1}{\text{cm}}$

(n) $d = 5.0\mu$m, $\tilde{\nu} = 3943\frac{1}{\text{cm}}$

(o) $d = 5.0\mu$m, $\tilde{\nu} = 3780\frac{1}{\text{cm}}$

(p) $d = 10.0\mu$m, $\tilde{\nu} = 4115\frac{1}{\text{cm}}$

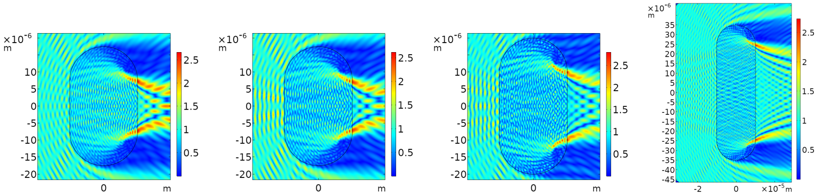

(q) $d = 15.0\mu$m, $\tilde{\nu} = 4028\frac{1}{\text{cm}}$

(r) $d = 15.0\mu$m, $\tilde{\nu} = 3807\frac{1}{\text{cm}}$

(s) $d = 20.0\mu$m, $\tilde{\nu} = 4086\frac{1}{\text{cm}}$

(t) $d = 50.0\mu$m, $\tilde{\nu} = 4048\frac{1}{\text{cm}}$

Figure B.2. The frames show the norm of the electric field for selected wave numbers. The stadium-shaped scatterer has a radius of the end-caps equal to 10.0 μm and a refractive index of 1.8. The length, d, of the straight sections of the stadium and the associated selected wave number are stated below each of the frames.

C Generation plots

In order to further evaluate the fractal structure of the system, more subsets of the set of long-lived trajectories of the stadium system were magnified. In Fig. 18only the very left of the brushes was magnified in each generation. In the figures below all fractals in the two first generations are evaluated. As the figures below indicate, we have a spectrum of different fractal structures appearing at the different levels.

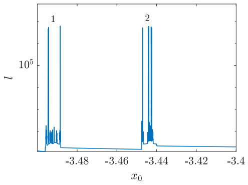

(a)

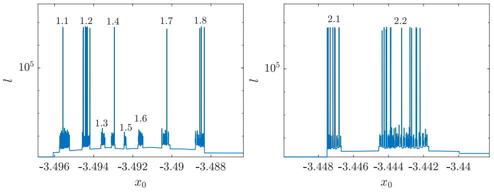

(b) 1 **(c)** 2

Figure C.3. Frame (a) is identical to Fig. 18 and consists of two brushes, numbered from the left, **1** and **2**. Then each of these two brushes is magnified. Frame (b) shows the magnification of **1**, and frame (c) shows the magnification of **2**. As the figures below show, the next generation of brushes is numbered from the left.

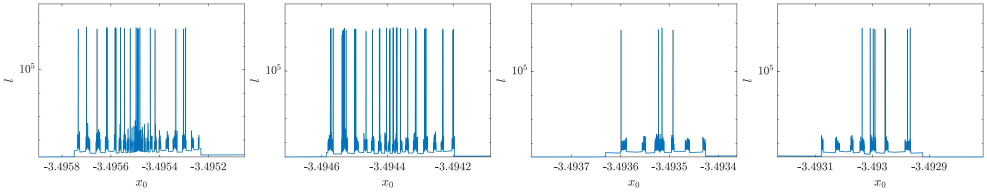

(a) 1.1 **(b)** 1.2 **(c)** 1.3 **(d)** 1.4

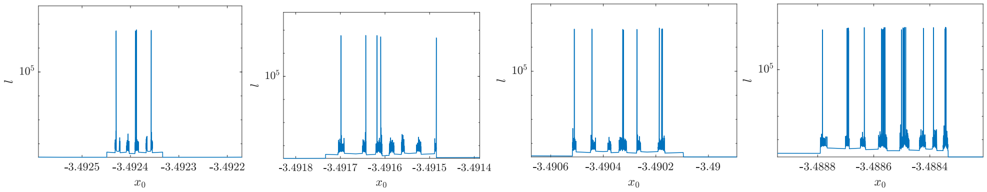

(e) 1.5 **(f)** 1.6 **(g)** 1.7 **(h)** 1.8

Figure C.4. Magnification of all fractal structures in Fig. C.3b. The sub-captions indicate which of the brushes in the previous generation a particular frame is associated with.

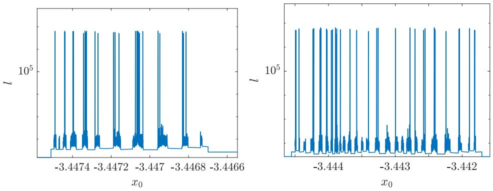

(a) 2.1 **(b)** 2.2

Figure C.5. Magnification of both fractal structures in Fig. C.3c. The sub-captions indicate which of the brushes in the previous generation a particular frame is associated with.

D How b_n's are connected to Q_{ext}

Figure D.6 shows Q_{ext} (Eq. 4) and b_{15} (Eq. 7) for an increasing absorbance. The first sharp peak from the right in b_{15} in Fig D.6a at $\tilde{\nu} = 1643.5 \frac{1}{\text{cm}}$ corresponds to a sharp ripple in Q_{ext}. The peak corresponds to a whispering gallery mode of first order. The second peak in b_{15} from the right is at $\tilde{\nu} = 2003.3\ \frac{1}{\text{cm}}$ and corresponds to a broader peak in Q_{ext}. This peak is a whispering gallery mode of second order. The wave function of the two ripples are shown in Fig. D.7. Notice the scale on the color bar.

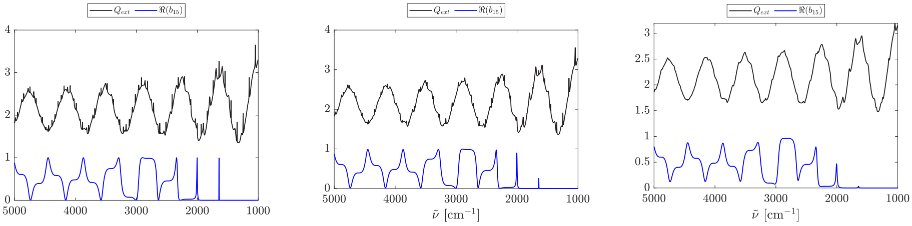

(a) $A = 0$ **(b)** $A = 0.01$ **(c)** $A = 0.1$

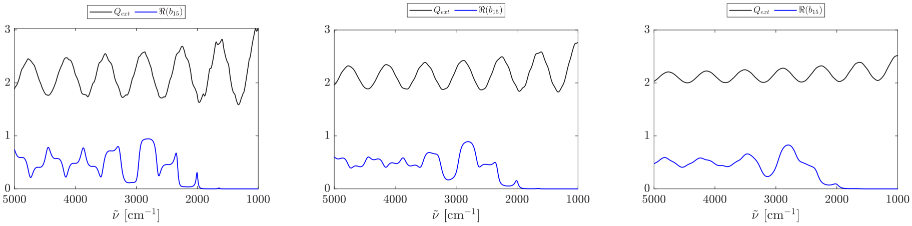

(d) $A = 0.2$ **(e)** $A = 0.5$ **(f)** $A = 1$

Figure D.6. The frames show how Q_{ext} (Eq.4) and b_{15} (Eq. 7) are changing as the absorbance (A) is increased. The radius of the cylinder is 10 μm, and the refractive index is given by $m = n_r + in_i$, where n_r = 1.8, and n_i is related to A (given in the respective sub-captions) by Eq. 9

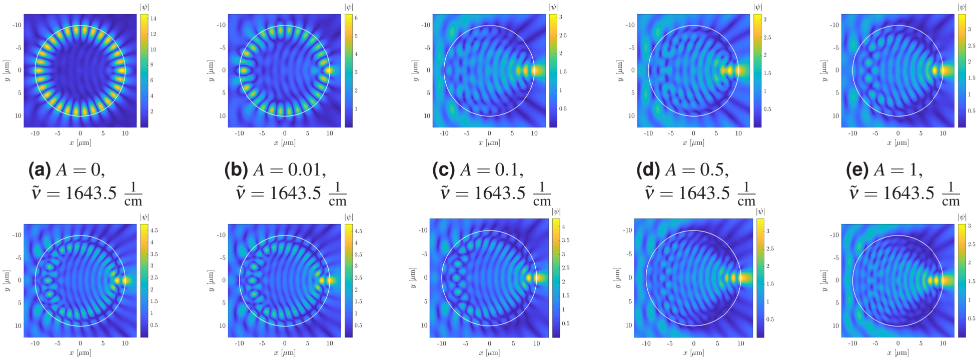

(a) $A = 0$, $\tilde{\nu} = 1643.5\ \frac{1}{\text{cm}}$ **(b)** $A = 0.01$, $\tilde{\nu} = 1643.5\ \frac{1}{\text{cm}}$ **(c)** $A = 0.1$, $\tilde{\nu} = 1643.5\ \frac{1}{\text{cm}}$ **(d)** $A = 0.5$, $\tilde{\nu} = 1643.5\ \frac{1}{\text{cm}}$ **(e)** $A = 1$, $\tilde{\nu} = 1643.5\ \frac{1}{\text{cm}}$

(f) $A = 0$, $\tilde{\nu} = 2003.3\ \frac{1}{\text{cm}}$ **(g)** $A = 0.01$, $\tilde{\nu} = 2003.3\ \frac{1}{\text{cm}}$ **(h)** $A = 0.1$, $\tilde{\nu} = 2003.3\ \frac{1}{\text{cm}}$ **(i)** $A = 0.5$, $\tilde{\nu} = 2003.3\ \frac{1}{\text{cm}}$ **(j)** $A = 1$, $\tilde{\nu} = 2003.3\ \frac{1}{\text{cm}}$

Figure D.7. The frames show the norm of the wave function, i.e., the electric field, for the first two ripple structures contained in b_{15}. The wave function is calculated as described in Appendix A. The incident plane wave is propagating from the left with a wavelength corresponding to the wave number in the respective sub-captions of each frame. The real part of the refractive index of the circular scatterer is 1.8 and the imaginary part is found by Eq. 9from the absorbance given in the respective sub-captions. The radius of the scatterer is 10 μm. The color bar is not kept constant.

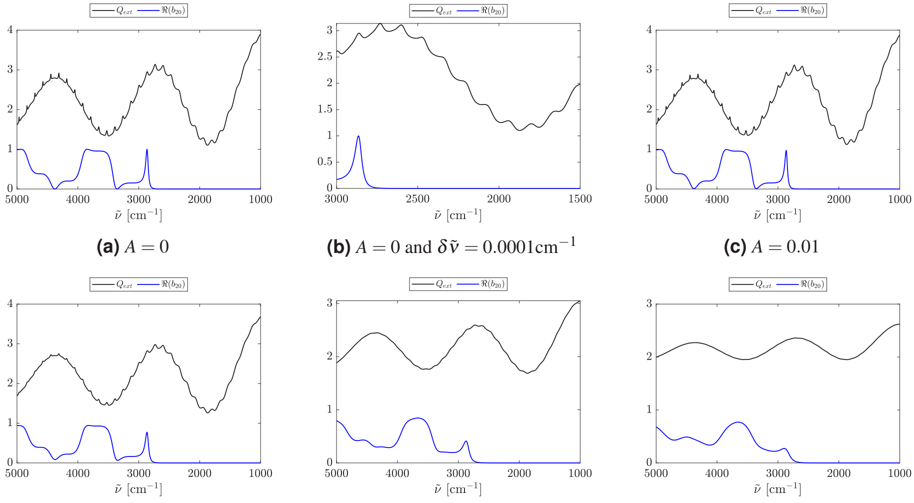

(a) $A = 0$ **(b)** $A = 0$ and $\delta\tilde{\nu} = 0.0001\text{cm}^{-1}$ **(c)** $A = 0.01$

(d) $A = 0.1$ **(e)** $A = 0.5$ **(f)** $A = 1$

Figure D.8. The frames show how Q_{ext} (Eq. 4) and b_{15} (Eq. 7) are changing as the absorbance (A) is increased. The radius of the cylinder is 10 μm, and the refractive index is given by $m = n_r + in_i$ where n_r = 1.3 and n_i is related to A (given in the respective sub-captions) by Eq. 9. Frame (b) shows the behavior of Q_{ext} in a smaller wavenumber interval with a very fine resolution. We observe that there is no needle-sharp resonance to the right of the resonance at $\tilde{\nu} = 2865.1\frac{1}{\text{cm}}$.

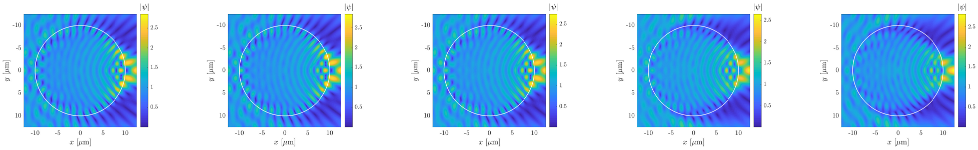

(a) $A = 0$,
$\tilde{\nu} = 2865.1\ \frac{1}{\text{cm}}$

(b) $A = 0.01$,
$\tilde{\nu} = 2865.1\ \frac{1}{\text{cm}}$

(c) $A = 0.1$,
$\tilde{\nu} = 2865.1\ \frac{1}{\text{cm}}$

(d) $A = 0.1$,
$\tilde{\nu} = 2865.1\ \frac{1}{\text{cm}}$

(e) $A = 1$,
$\tilde{\nu} = 2865.1\ \frac{1}{\text{cm}}$

Figure D.9. The frames show the norm of the wave function, i.e., the electric field, for the first ripple structure contained in b_{20}. The wave function is calculated as described in Appendix A. The plane wave is incident from the left with wave number $\tilde{\nu} = 2865.1\frac{1}{\text{cm}}$. The real part of the refractive index of the circular scatterer is 1.3 and the imaginary part is found by Eq. 9from the absorbance given in the respective sub-captions. The radius of the scatterer is 10μm. The color bar is not kept constant.

ISBN: 978-82-575-1717-5
ISSN: 1894-6402

Norwegian University
of Life Sciences

Postboks 5003
NO-1432 Ås, Norway
+47 67 23 00 00
www.nmbu.no

108185 / ANDVORDGRAFISK.NO